[redacted]

40186

National Library of Canada
Bibliothèque nationale du Canada

CANADIAN THESES ON MICROFICHE
THÈSES CANADIENNES SUR MICROFICHE

NAME OF AUTHOR/*NOM DE L'AUTEUR* TERENCE JOHN HUGHES

TITLE OF THESIS/*TITRE DE LA THÈSE* A COMPREHENSIVE MODEL OF
IONOSPHERIC-MAGNETOSPHERIC CURRENT SYSTEMS
DURING PERIODS OF MODERATE MAGNETOSPHERIC ACTIVITY

UNIVERSITY/*UNIVERSITÉ* ALBERTA

DEGREE FOR WHICH THESIS WAS PRESENTED/ *GRADE POUR LEQUEL CETTE THÈSE FUT PRÉSENTÉE* Ph.D.

YEAR THIS DEGREE CONFERRED/*ANNÉE D'OBTENTION DE CE GRADE* 1978

NAME OF SUPERVISOR/*NOM DU DIRECTEUR DE THÈSE* DR. G. ~~Ros~~ ROSTOKER

Permission is hereby granted to the NATIONAL LIBRARY OF CANADA to microfilm this thesis and to lend or sell copies of the film.

The author reserves other publication rights, and neither the thesis nor extensive extracts from it may be printed or otherwise reproduced without the author's written permission.

L'autorisation est, par la présente, accordée à la BIBLIOTHÈQUE NATIONALE DU CANADA de microfilmer cette thèse et de prêter ou de vendre des exemplaires du film.

L'auteur se réserve les autres droits de publication; ni la thèse ni de longs extraits de celle-ci ne doivent être imprimés ou autrement reproduits sans l'autorisation écrite de l'auteur.

DATED/*DATÉ* 30 March 1978 SIGNED/*SIGNÉ* Terence J. Hughes

PERMANENT ADDRESS/*RÉSIDENCE FIXE* RADIOLOGICAL RESEARCH LABS
MEDICAL SCIENCES BLDG., UNIV. OF TORONTO
TORONTO, ONTARIO M5S 1A8

NL-91 (3-74)

National Library of Canada

Cataloguing Branch
Canadian Theses Division

Ottawa, Canada
K1A 0N4

Bibliothèque nationale du Canada

Direction du catalogage
Division des thèses canadiennes

NOTICE

The quality of this microfiche is heavily dependent upon the quality of the original thesis submitted for microfilming. Every effort has been made to ensure the highest quality of reproduction possible.

If pages are missing, contact the university which granted the degree.

Some pages may have indistinct print especially if the original pages were typed with a poor typewriter ribbon or if the university sent us a poor photocopy.

Previously copyrighted materials (journal articles, published tests, etc.) are not filmed.

Reproduction in full or in part of this film is governed by the Canadian Copyright Act, R.S.C. 1970, c. C-30. Please read the authorization forms which accompany this thesis.

THIS DISSERTATION
HAS BEEN MICROFILMED
EXACTLY AS RECEIVED

AVIS

La qualité de cette microfiche dépend grandement de la qualité de la thèse soumise au microfilmage. Nous avons tout fait pour assurer une qualité supérieure de reproduction.

S'il manque des pages, veuillez communiquer avec l'université qui a conféré le grade.

La qualité d'impression de certaines pages peut laisser à désirer, surtout si les pages originales ont été dactylographiées à l'aide d'un ruban usé ou si l'université nous a fait parvenir une photocopie de mauvaise qualité.

Les documents qui font déjà l'objet d'un droit d'auteur (articles de revue, examens publiés, etc.) ne sont pas microfilmés.

La reproduction, même partielle, de ce microfilm est soumise à la Loi canadienne sur le droit d'auteur, SRC 1970, c. C-30. Veuillez prendre connaissance des formules d'autorisation qui accompagnent cette thèse.

LA THÈSE A ÉTÉ
MICROFILMÉE TELLE QUE
NOUS L'AVONS REÇUE

NL-339 (3/77)

THE UNIVERSITY OF ALBERTA

A COMPREHENSIVE MODEL OF IONOSPHERIC-MAGNETOSPHERIC CURRENT SYSTEMS DURING PERIODS OF MODERATE MAGNETOSPHERIC ACTIVITY

by

Ⓒ TERENCE JOHN HUGHES

A THESIS

SUBMITTED TO THE FACULTY OF GRADUATE STUDIES AND RESEARCH

IN PARTIAL FULFILMENT OF THE REQUIREMENTS FOR THE DEGREE

OF DOCTOR OF PHILOSOPHY

DEPARTMENT OF PHYSICS

EDMONTON, ALBERTA

SPRING, 1978

THE UNIVERSITY OF ALBERTA

FACULTY OF GRADUATE STUDIES AND RESEARCH

The undersigned certify that they have read, and recommend to the Faculty of Graduate Studies and Research, for acceptance, a thesis entitled A Comprehensive Model of Ionospheric-Magnetospheric Current Systems During Periods of Moderate Magnetospheric Activity submitted by Terence John Hughes in partial fulfilment of the requirements for the degree of Doctor of Philosophy

....
Supervisor

F. S. Vermeulen
....

....

....

....

....
External Examiner

DATE 27 March, 1978

ABSTRACT

The earth's magnetosphere is coupled to the ionosphere by large scale electric current systems. Knowledge of the geometry and characteristics of these current systems can lead to an understanding of the solar-terrestrial interaction through which energy from the interplanetary medium is transmitted into the magnetosphere and eventually dissipated. In this thesis is developed a comprehensive model of the magnetosphere-ionosphere current systems whose character is consistent with present knowledge of ionospheric electric field and conductivity distributions. The model is designed to reproduce the average magnetic perturbation pattern at high latitudes as derived from a study of 42 days of magnetometer array data recorded over three months in late 1971 and early 1972. The model is representative of winter conditions in the northern hemisphere. However, it is shown how the model current system must be modified to allow it to be used to describe magnetosphere-ionosphere coupling in the summer months. The model studies show the importance of considering the magnetic effects at the earth's surface of the Birkeland current sheets and the north-south ionospheric currents which link them. The major current systems in the model are the eastward and westward electrojets; both of these systems are fed by downward field-aligned current in the noon sector, with most of the current returning to the magnetosphere along field lines in the pre-midnight quadrant. A small portion of the current in the pre-noon quadrant flows to low latitudes, across the noon meridian, and returns to high latitudes in the dusk sector. A small portion of the electrojet current diverges up magnetic field lines at the dawn and dusk terminators which separate the sunlit and dark ionospheres. In this context, it is shown that, at quiet times, the electrojet resulting from the ionospheric electric field being superposed on the sunlit ionosphere (viz., the UV electrojet) produces significant magnetic perturbations at the earth's surface. Finally, it is shown that the model can be perturbed in the evening sector, in a manner consistent with known substorm phenomenology, to produce magnetic perturbation patterns in excellent agreement with observations of polar magnetic substorms.

ACKNOWLEDGEMENTS

A large number of friends, teachers and colleagues have contributed, either directly or indirectly, to the completion of this thesis. Among these are Dennis Ryan who first showed me the excitement of learning; Ernie Edmonds who first showed me that physics was fun and over the years has offered continued encouragement; Dr H. E. Johns and Dr. Bob Bruce who first got me started in research, and Dr. Ken Taylor, who kept me at it.

In recent years, Dr. Doug Oldenburg has offered unending encouragement, even from afar, and introduced me to inversion theory; Dr. John Olson has been of inestimable assistance as a friend and physicist; and Dr. Don Wallis, Dr. Koji Kawasaki and Dr. Jerry Kisabeth have provided me with many hours of valuable discussion.

I owe my supervisor, Dr. Gordon Rostoker, a debt of thanks for the continued stimulation, encouragement, and votes of confidence with which he has supplied me. A special thanks to Mr. Lou Rostoker, for introducing me to his son.

Finally, I wish to thank my wife, Lorna, for her continual, unshakeable confidence in me. Without her patience and understanding, I would not have completed this work.

Throughout most of this research, I have received financial support from the National Research Council of Canada. The research has been funded, in part, by the

National Research Council, and by the Department of Energy, Mines, and Resources (Earth Physics Branch) under contract numbers OSQ5-0019 and OSQ-7600019.

TABLE OF CONTENTS

CHAPTER PAGE

1. INTRODUCTION 1

   1.1 The Magnetosphere 1

   1.2 Magnetosphere-Ionosphere Interactions 9

   1.3 Large-scale Current Systems 17

      1.3.1 The Sq and L Current Systems 17

      1.3.2 The Dst and DP1 Current Systems 20

      1.3.3 The S_q^p and DP-2 Current Systems 20

      1.3.4 The Electrojets and the Interplanetary Magnetic Field 22

   1.4 Ionospheric Current Models 28

   1.5 The Objectives of this Thesis 33

2. DATA PROCESSING AND ANALYSIS 34

   2.1 Data Handling 34

   2.2 Data Processing 39

      2.2.1 Latitude Profiles 39

      2.2.2 Polar Plots 53

   2.3 Discussion of Inversion Theory 56

   2.4 Superposed Epoch Analysis 66

3. RESULTS OF DATA ANALYSIS 70

   3.1 Description of the Data 70

   3.2 Statistical Characterization of the Data Suite .. 71

TABLE OF CONTENTS continued

3.2.1 The 2200-0200 MLT Regime 71

3.2.2 The 0200-1000 MLT Regime 73

3.2.3 The 1000-1400 MLT Regime 80

3.2.4 The 1400-1900 MLT Regime 82

3.2.5 The 1900-2200 MLT Regime 86

3.2.6 Summary of the Five Regimes 89

3.3 Interpretation of the Data Suite 94

3.4 Inversion of Latitude Profile Data Near Dusk 117

4. A WORLDWIDE CURRENT MODEL 132

4.1 Introduction 132

4.2 Elementary Considerations 132

4.2.1 The Auroral Oval 132

4.2.2 Location of Currents 134

4.2.3 The Electric field and Conductivity Model ..144

4.3 The Approach to Current Modelling 147

4.4 The Basic Current Systems 151

4.4.1 The Westward Current System 151

4.4.2 The Eastward Current System 180

4.4.3 The North-South Current System 199

4.4.4 Other Contributing Current Systems 209

4.5 The Global Current Model 226

4.5.1 Qualitative Comparison of Model Latitude Profiles with SPEA Profiles 229

4.5.2 Quantitative Evaluation of the Model 253

4.5.3 Preliminary Summary and Discussion 264

4.6 Specific Events and the Average Current Model ...268

TABLE OF CONTENTS continued

4.6.1 Modelling of Two Unusual Dusk Sector Latitude Profiles 268

4.6.2 The Substorm of Day 23, 1972 281

4.7 Comparison of the Model for Average Conditions with Satellite Observations of Field-Aligned Currents 300

4.7.1 An Hypothesis to Explain the Post-Noon Discrepancy 302

5. POSSIBLE SOURCE MECHANISMS 315

5.1 Sources of Field-Aligned Currents 315

5.2 Concluding Remarks 333

REFERENCES 336

APPENDIX I: MODELLING OF THE CURRENT SYSTEMS 348

APPENDIX II: LINEAR INVERSE THEORY 357

LIST OF TABLES

Table	Description	Page
2.1	Coordinates of Magnetometer Line Sites	35
2.2	The Angle θ for the Observatories used in this Thesis.	40
3.1	Correspondence between Net Field-Aligned Current Flow and Auroral Zone Electric Field.	105
3.2	Summary of the Results of Inverting Hourly Averaged Latitude Profiles.	130
4.1	Boundaries of the Model Auroral Oval.	135
4.2	Statistical Analysis of the Comparison of the Global Model Profiles with the SPEA Profiles.	265
4.3(a)	Model Parameters for Day 38,1972.	279
4.3(b)	Model Parameters for Day 19,1972.	280
4.4	Model Parameters for the Substorm of Day 23,1972. ..	294

LIST OF FIGURES

Figure Page

1.1 A schematic drawing of the magnetosphere. 4

1.2 Current streamlines in a closed magnetosphere. 7

1.3 A model of the open magnetosphere. 11

1.4(a) Pedersen conductivity as a function of altitude. 14

1.4(b) Hall conductivity as a function of altitude. 14

1.5 The Sq current system. 15

1.6 The DP1 current system. 21

1.7 The S_q^p horizontal magnetic perturbation field. 23

1.8 The DP-2 current system. 24

1.9 A theoretical ionospheric current model. 32

2.1 A map of the magnetometer chain. 37

2.2(a) A model latitude profile for a uniform east-west current density. 42

2.2(b) A model latitude profile for a variable east-west current density. 42

2.2(c) Complete three-dimensional east-west current system. 43

2.3 Complete three-dimensional north-south current system. 45

2.4 A model latitude profile for a north-south current system. 47

2.5 A model latitude profile for a long north-south current system. 48

2.6 A model latitude profile for current constrained to flow along the model auroral oval. 50

2.7 A model latitude profile for an unbalanced downward field-aligned current. 52

LIST OF FIGURES continued

2.8 Model latitude profiles showing the effect of a superconductor at depth. 55

2.9 A model latitude profile for demonstrating the linear inversion technique. 58

2.10 The inversion of the data shown in Figure 2.9. 59

2.11 The inversion of the data shown in Figure 2.9, with a relaxed constraint on the latitudinal extent of the current. 61

2.12 The inversion of the data shown in Figure 2.9, assuming a purely ionospheric current forward model. 62

2.13 Comparison of the data in Figure 2.9 with the results of the flattest model. 65

2.14 A model SPEA profile. 68

3.1 Representative hourly averaged latitude profiles for the interval 2200-0200 MLT. 72

3.2 SPEA profiles for the interval 2200-0200 MLT. 74

3.3 Representative hourly averaged latitude profiles for the interval 0200-1000 MLT. 75

3.4 SPEA profiles for the interval 0200-1000 MLT. 78

3.5 Representative hourly averaged latitude profiles for the interval 1000-1400 MLT. 81

3.6 SPEA profiles for the interval 1000-1400 MLT. 83

3.7 Representative hourly averaged latitude profiles for the interval 1400-1900 MLT. 85

3.8 SPEA profiles for the interval 1400-1900 MLT. 88

3.9 Representative hourly averaged latitude profiles for the interval 1900-2200 MLT. 91

3.10 SPEA profiles for the interval 1900-2200 MLT. 93

3.11 Schematic drawing showing the magnetic effect of a vertical current diverging uniformly in the horizontal plane. 96

3.12 Histograms showing the diurnal distribution of net field-aligned current. 99

LIST OF FIGURES continued

3.13 (a) The diurnal variation in the high latitude ionospheric electric field. 101

3.13(b) Average high latitude ionospheric electric field vectors. 102

3.14 The ratio of $\Delta Y'_{step}$ to $\Delta X'_{peak}$ as a function of magnetic local time. 107

3.15 $\Delta Y'_{step}$ and $\Delta X'_{peak}$ as a function of magnetic local time. 108

3.16 Histogram showing the net field-aligned current flow as determined from the Triad satellite. 111

3.17 $\Delta Y'_{step}$ as a function of the vertical component of the IMF. 114

3.18 The inversion of a profile from the hour 1500-1600 MLT. 120

3.19 The inversion of a profile from the hour 1600-1700 MLT. 121

3.20 The inversion of a profile from the hour 1700-1800 MLT. 122

3.21 The inversion of an additional profile from the hour 1700-1800 MLT. 123

3.22 The inversion of a profile from the hour 1800-1900 MLT. 124

3.23 The inversion of a profile from the hour 1900-2000 MLT. 125

3.24 The inversion of a profile from the hour 2000-2100 MLT. 126

3.25 The inversion of a profile from the hour 2100-2200 MLT. 127

3.26 The inversion of a profile from the hour 2200-2300 MLT. 128

4.1 Polar plot of the model auroral oval. 137

4.2 The location of field-aligned current sheets as deduced from the Triad satellite data. 140

4.3 The extreme positions of the terminator for the period from Day 332, 1971 to Day 24, 1972. 143

LIST OF FIGURES continued

4.4 Polar plot of the model electric field. 146

Indentation

4.5 The model height-integrated current densities for the east-west current systems. 154

4.6 The model unbalanced field-aligned current densities. 157

4.7 The field-aligned current strength for the north-south current systems. 160

Variable indentation

4.8 The set of model latitude profiles due to the westward current system. 163

4.9 The set of model latitude profiles due to the westward current system plus the appropriate north-south current system. 172

4.10 The set of model latitude profiles due to the eastward current system. 183

4.11 The set of model latitude profiles due to the eastward current system plus the appropriate north-south current system. 191

4.12 The set of model latitude profiles due to the complete north-south current system. 201

4.13(a) A schematic drawing to demonstrate the equivalent current for a balanced three-dimensional current system. 213

4.13(b) A schematic drawing to demonstrate the equivalent current for an unbalanced three-dimensional current system. 215

4.14 The set of model latitude profiles due to the low-latitude current system. 218

4.15 A schematic drawing of the complete model current system. 228

4.16 Comparison of the model latitude profiles with the SPEA profiles. 231

4.17 Latitude profiles from 1000-1300 MLT resulting from a modification of the model current system. ..250

4.18(a) Polar plot of the model equivalent currents. ...252

4.18(b) Polar plot of the average high-latitude horizontal magnetic perturbation vectors. 255

LIST OF FIGURES continued

4.18(c) Overhead ionospheric current vectors for Day 290,1970. 256

4.19 Comparison of $\Delta X'_{peak}$ and $\Delta Y'_{step}$ from the model and the SPEA analysis. 258

4.20(a) Correlation between the model $\Delta X'_{peak}$ and the SPEA $\Delta X'_{peak}$ for the interval 0200-1000 MLT. 260

4.20(b) Correlation between the model $\Delta Y'_{step}$ and the SPEA $\Delta Y'_{step}$ for the interval 0200-1000 MLT. 260

4.20(c) Correlation between the model $\Delta X'_{peak}$ and the SPEA $\Delta X'_{peak}$ for the interval 1400-2200 MLT. 262

4.20(d) Correlation between the model $\Delta Y'_{step}$ and the SPEA $\Delta Y'_{step}$ for the interval 1400-2200 MLT. 262

4.20(e) Correlation between the model $\Delta X'_{peak}$ and the SPEA $\Delta X'_{peak}$ for the interval 1800-2200 MLT. 262

4.21(a) Model latitude profile for 0332 UT, Day 19, 1972. 270

4.21(b) The observed latitude profile for 0332 UT, Day 19, 1972. 270

4.22(a) Model latitude profile for 0214 UT, Day 38, 1972. 272

4.22(b) The observed latitude profile for 0214 UT, Day 38, 1972. 272

4.23 Schematic of the current model used to model the profiles shown in Figure 4.21 and 4.22. 278

4.24 Magnetograms for Day 23, 1972, 0000 to 0200 UT. ...283

4.25 Latitude profiles for Day 23, 1972. 285

4.26 Linear mappings of ASCA pictures from Day 23, 1972. 286

4.27 College magnetogram, Day 23, 1972. 287

4.28 A schematic of the currents used to model the event of Day 23, 1972. 291

4.29 Comparison of the differential profiles with the model calculations for Day 23, 1972. 296

4.30 The diurnal distribution of average field-aligned current densities. 301

LIST OF FIGURES continued

4.31 Polar plot of average high-latitude horizontal magnetic perturbation vectors for summer months. ..305

4.32 Average ionospheric electric field vectors for times when $B_y<0$. 307

Variable inclination

4.33 Polar plot of the magnetic field vectors due to the polar cap current system. 311

4.34 Model latitude profiles for the polar cap current system. 313

5.1 A schematic diagram of the solar wind - magnetospheric dynamo. 318

5.2 A schematic diagram showing the connection of the solar wind dynamo to the ionosphere. 321

5.3 A schematic diagram of the field-aligned current flow driven by the inertial dynamo of Rostoker and Bostrom. 327

5.4 A schematic diagram of the model ionospheric Hall and Pedersen currents 328

5.5 A schematic diagram of magnetospheric convection flow 330

AI.1 Diagram defining the vectors used in magnetic field calculations. 349

AI.2 Schematic of the cross polar cap current system. ..354

CHAPTER 1 INTRODUCTION

1.1 The Magnetosphere

Early in this century it was believed that the earth was surrounded by the vacuum of interplanetary space, and that the magnetic field was normally that of a pure dipole. However, the work of Birkeland (1908,1913) led to the suggestion that solar flares caused bursts of solar gas to be emitted by the sun and that, at these times, the earth's magnetic field would carve out a cavity in the streaming solar gas. Chapman and Ferraro (1931) considered the interaction of the solar gas with the earth's magnetic field configuration under the circumstances associated with solar flares, and they were able to estimate the position of the boundary between the earth's magnetic field cavity and the interplanetary medium. Biermann (1951), noting that comet tails were always directed away from the sun, independent of the direction of motion of the comet, inferred that there was a continual streaming of matter away from the sun. Parker (1958,1963) developed extensive theoretical arguments in which it was assumed that a continuous solar wind existed and, with the advent of space probes, it has been proven that interplanetary space is filled with a plasma streaming away from the sun. Due to this continuous presence of the solar wind, it became apparent that the magnetic cavity, termed the magnetosphere, is a permanent feature of the earth's environment.

A schematic drawing illustrating most of the features of the magnetosphere is shown in Figure 1.1 . It is apparent that present knowledge has lead to the realization that the magnetosphere is a complicated configuration of particles and fields. It is not the purpose of this thesis to provide a detailed understanding of the entire magnetosphere, but a brief description of it is in order.

The earth with its magnetic field acts as an obstacle to the flow of the solar wind. Average solar wind bulk velocities are of the order of 300 to 500 km s^{-1}, with number densities of 5 to 10 cm^{-1}, and temperatures in the range of 10^4 °K to 10^6 °K. These values give an Alfven velocity of 50 to 100 km s^{-1}, and a sound velocity of 100 to 200 km s^{-1} so that the solar wind is thus both supersonic and super-Alfvenic. Consequently, a standing mgnetohydrodynamic (MHD) shock wave is set up, typically about 14 earth radii (Re) upstream from the earth, as shown in Figure 1.1. Immediately interior to this is the region called the magnetosheath, which is a region of thermalized plasma. The surface along which the solar wind plasma pressure is balanced by the earth's magnetic field pressure is called the magnetopause.

The solar wind blowing past this cavity distorts it such that it is blunt on the sunward side of the earth, and extended in the anti-solar direction to form the so-called magnetotail. It is now known that the magnetotail extends beyond the orbit of the moon (about 60 Re) (Ness et al,

Figure 1.1 A schematic drawing of the magnetosphere (after Heikkila, 1972) modified by Rostoker to include the plasma mantle.

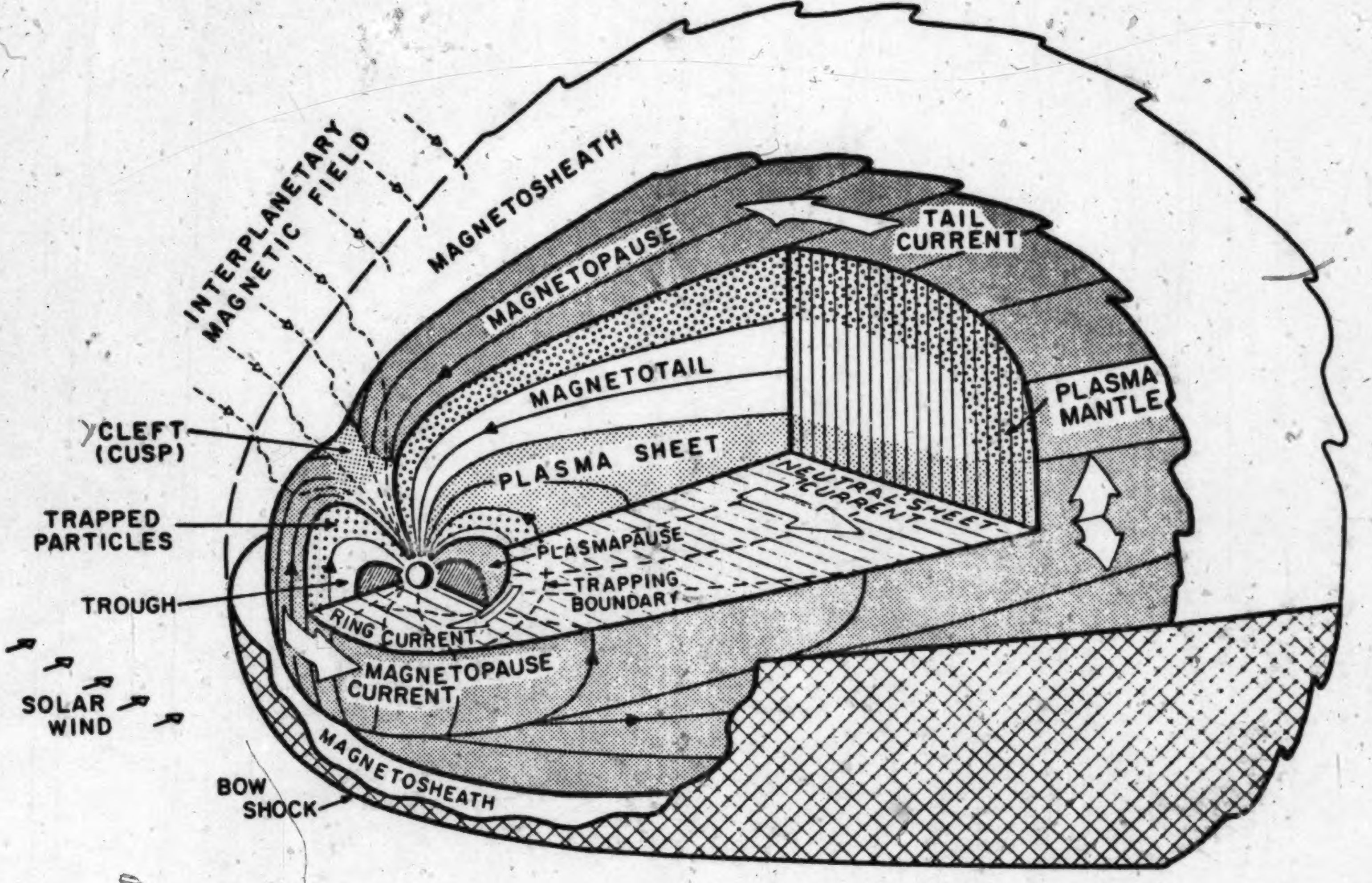
INTERPLANETARY MAGNETIC FIELD
MAGNETOSHEATH
MAGNETOPAUSE
TAIL CURRENT
MAGNETOTAIL
PLASMA MANTLE
CLEFT (CUSP)
PLASMA SHEET
NEUTRAL SHEET CURRENT
TRAPPED PARTICLES
PLASMAPAUSE
TRAPPING BOUNDARY
TROUGH
RING CURRENT
MAGNETOPAUSE CURRENT
SOLAR WIND
MAGNETOSHEATH
BOW SHOCK

1967), although its actual length is not known at the present time. Axford and Hines (1961) proposed the idea of plasma convection within the magnetosphere, but their magnetosphere was a closed, tear-drop shaped cavity. They suggested a "viscous-like" interaction between the solar wind and the magnetospheric plasma in the neighbourhood of the magnetopause. This interaction would result in plasma flowing down-tail, and eventually returning along the sun-earth line to give a closed circulation pattern. This motion is shown in Figure 1.2. Close to the earth, there exists a region of stably trapped particles, the plasmasphere, which is bounded by the plasmapause. Beyond the plasmapause, on the nightside of the earth, there is a region of plasma symmetrically distributed on either side of a mid-plane, and extending along the length of the tail (see Figure 1.1). On average, this so-called plasma sheet has a thickness of about 5 Re at the center, and widens to about double this at the flanks (near the magnetopause). The magnetic field along the central plane of the plasma sheet is weak and normal to this plane. This region of weak field is called the neutral sheet at higher latitudes. Outside the plasma sheet are the tail lobes, in which the plasma density is very low (<0.01 cm^{-3}) compared to densities of about 0.1 to 10 cm^{-3} in the plasma sheet itself.

Figure 1.2 depicts convection mapped onto the equatorial plane. However, if this motion is mapped to ionospheric altitudes, it corresponds to anti-sunward

Figure 1.2 Streamlines of plasma convection flow in the equatorial plane of the magnetosphere (After Axford and Hines, 1961).

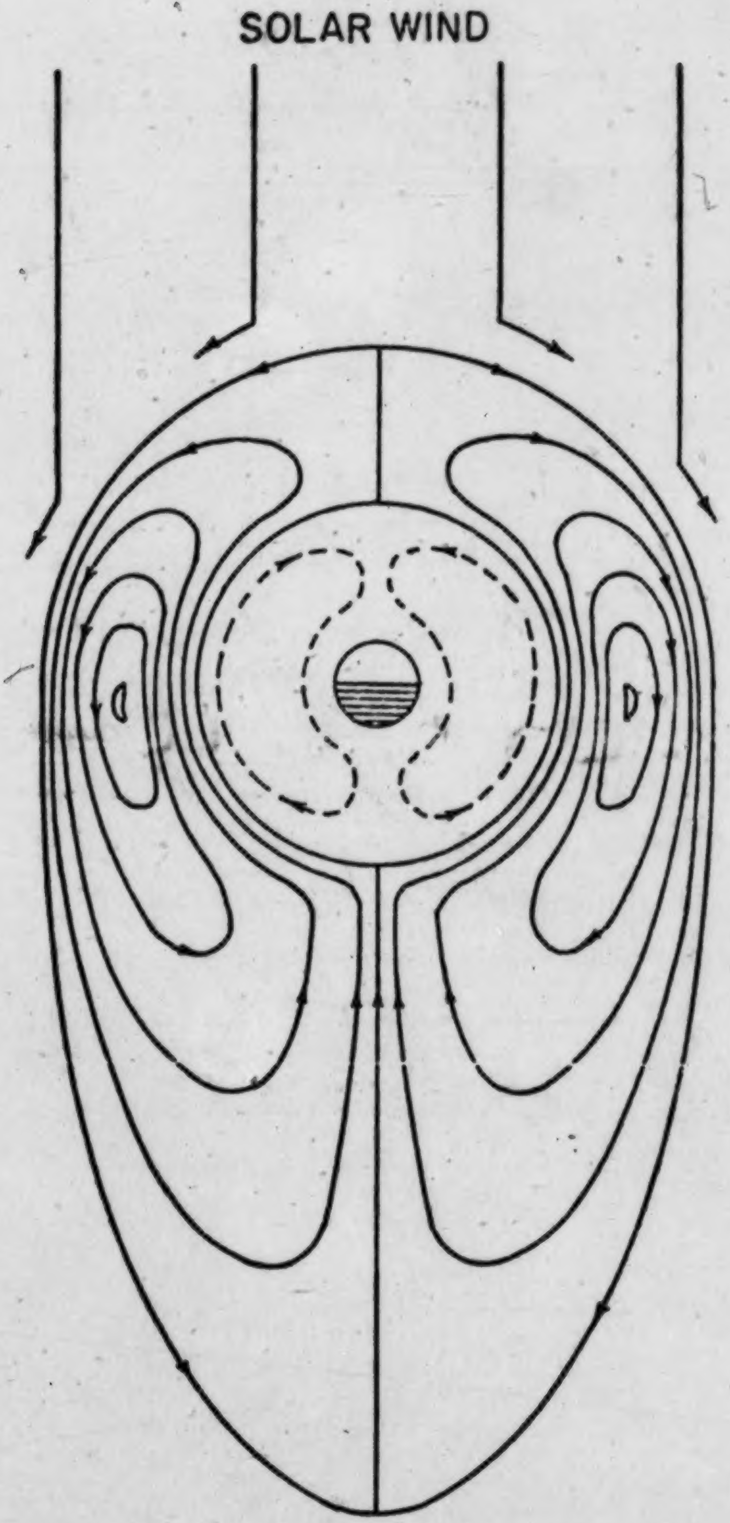
SOLAR WIND

convection across the polar cap regions, and sunward convection at lower latitudes. In a collisionless plasma, both ions and electrons would follow the convection pattern. However, in the lower ionosphere, ions undergo many collisions with neutral atoms, so that the ions remain almost stationary in comparison with the electrons. This differential motion of electrons and ions produces Hall current in the direction opposite to that of the convecting plasma. The convection pattern of Axford and Hines then corresponds approximately to westward flowing Hall current in the pre-noon sector, at sub polar cap latitudes, and eastward flowing current in the post-noon sector. This basic convection pattern is an oft-repeated observation (see the review by Cauffman and Gurnett (1972), and the references therein) and the currents associated with it correspond in large part to those to be discussed later in this thesis.

Although the basic convection pattern derived by Axford and Hines (1961) has withstood the test of extensive observations, the concept of the closed magnetosphere has not. Observations of solar electrons and low energy solar protons (identified by their energy spectra) at high latitudes, indicate an essentially uniform flux of these particles (Stone, 1964; Fennel, 1973; Vampola, 1971; McDiarmid and Burrows, 1970; among others). It has been concluded that, since solar particles have free access to the high latitude regions of the earth, that the high latitude field lines are directly connected to the interplanetary magnetic field (IMF). It is therefore believed that the magnetosphere is "open". Dungey (1961) proposed magnetic field line merging as a means by which the magnetosphere could become open. Figure 1.3 is a schematic depicting this process. The IMF merges with the earth's dipolar field at the magnetopause, and the merged field lines then are convected in the anti-sunward direction by the solar wind. This convection of field lines occurs because, in the solar wind, field lines are "frozen-in" to the plasma. This convective motion results in field lines moving across the polar cap from the dayside to the nightside,and returning at sub-polar cap latitudes. Recently, Rosenbauer et al, (1975) have suggested that solar wind plasma may enter the magnetosphere directly in the polar cleft (Figure 1.1) to form the plasma mantle streaming away from the earth. The existen e of the plasma also indicates a direct coupling of the interplanetary medium with the magnetosphere.

1.2 Magnetosphere-Ionosphere Interactions

Particles in the plasma are subject to drift motions due to electric fields, pressure gradients (Siscoe, 1966), magnetic field gradients and magnetic field curvature (see, for example, Roederer, 1970). Some of these drifting particles precipitate into the upper atmosphere, where due to ionization and excitation of neutral atoms and molecules, a region of enhanced conductivity is created. It is in this

Figure 1.3 Noon-midnight meridian section of the open magnetosphere showing field line merging at the nose of the magnetopause. The numbers represent the motion of field lines, with motion proceeding to the higher numbers. Note that in this figure, the north pole has been placed at the bottom of the figure. (After Hess, 1968),

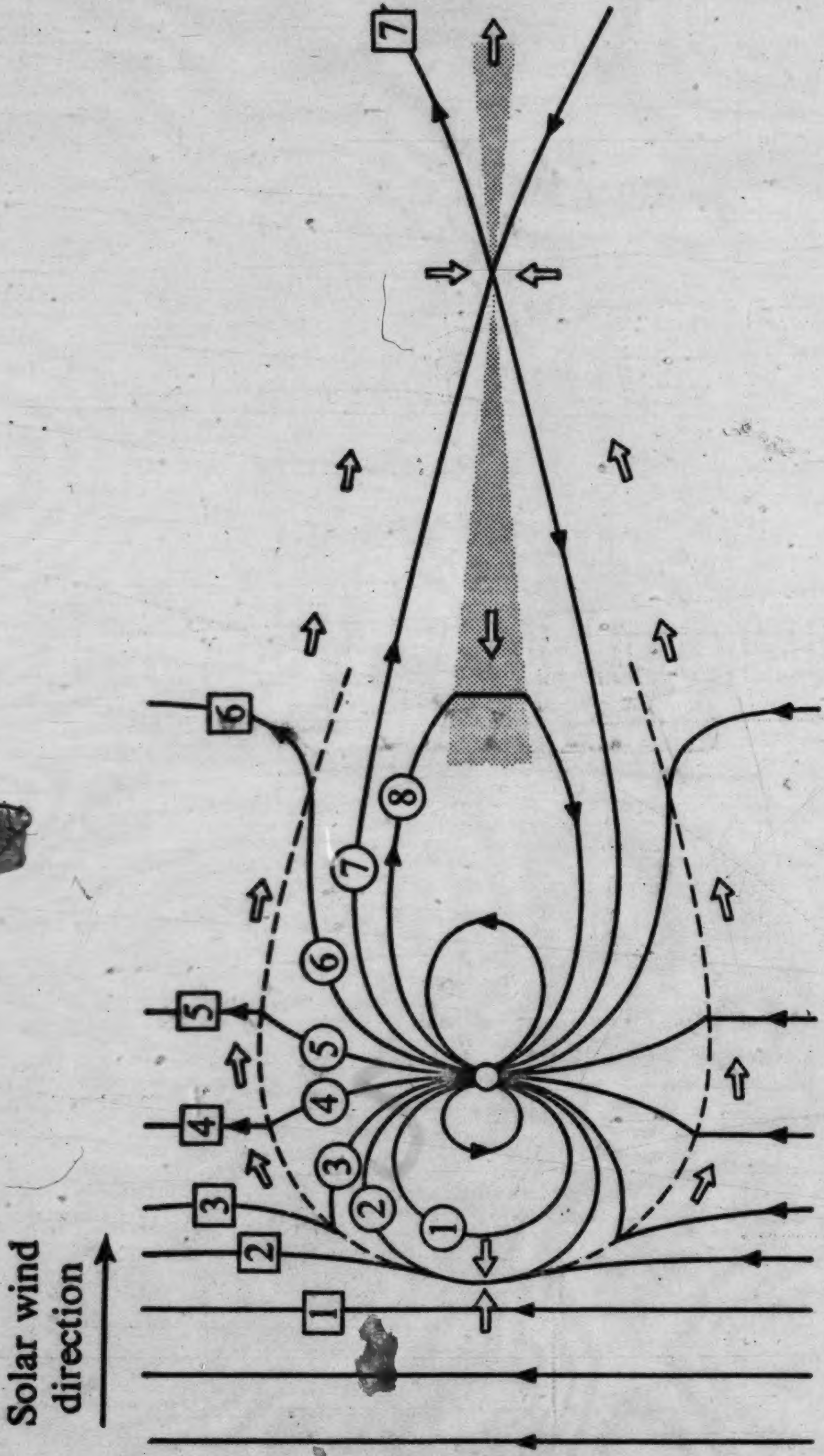
Solar wind direction
1
2
3
4
5
6
7
①
②
③
④
⑤
⑥
⑦
⑧

region that the major horizontal ionospheric currents flow. If it is assumed that the conductivity along field lines is sufficiently high to permit neglect of any potential drops along field lines, and further, that the field lines are vertical, then the equation

$$\underline{I} = \Sigma_P \underline{E}_\perp + \Sigma_H \frac{\underline{B} \times \underline{E}}{B} \qquad 1.1$$

states a generalized Ohm's Law for the ionosphere. Here, Σ_P and Σ_H are height-integrated Pedersen and Hall conductivities (see below), $\underline{E}_\perp$ is the electric field perpendicular to the magnetic field, $\underline{B}$, and $\underline{I}$ is the height-integrated current density. The height-integrated conductivities are derived from the height dependent conductivities, which, for the ionosphere, and assuming a single ion type of mass M, are given by

$$\sigma_P = \frac{ne^2\tau_e/m_e}{1+\omega^2\tau_e^2} + \frac{ne^2\tau_i/M}{1+\Omega^2\tau_i^2} \qquad 1.2$$

and

$$\sigma_H = \frac{ne^2\tau_e\omega/m_e}{1+\omega^2\tau_e^2} - \frac{ne^2\tau_i\Omega/M}{1+\Omega^2\tau_i^2} \qquad 1.3$$

where τ_e and τ_i are the electron and ion collision periods with neutral atoms, Ω is the ion gyrofrequency, and ω the electron gyrofrequency. Figure 1.4 shows the variation of σ_P and σ_H with altitude. It is clear that the Pedersen conductivity predominates at high altitudes, and this fact

Figure 1.4(a) Variation of Pedersen conductivity with altitude. (After Hanson, 1965).

Figure 1.4(b) Variation of Hall conductivity with altitude. (After Hanson, 1965).

A

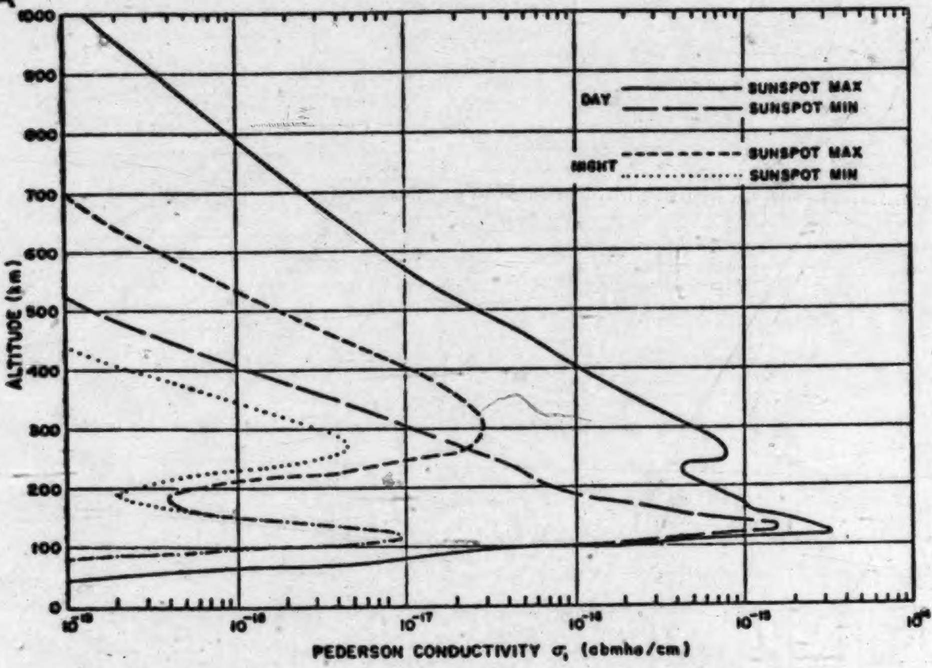
DAY SUNSPOT MAX
SUNSPOT MIN
NIGHT SUNSPOT MAX
SUNSPOT MIN
ALTITUDE (km)
0
100
200
300
400
500
600
700
800
900
1000
10^{-19}
10^{-18}
10^{-17}
10^{-16}
10^{-15}
10^{-14}
PEDERSON CONDUCTIVITY σ_1 (abmho/cm)

B

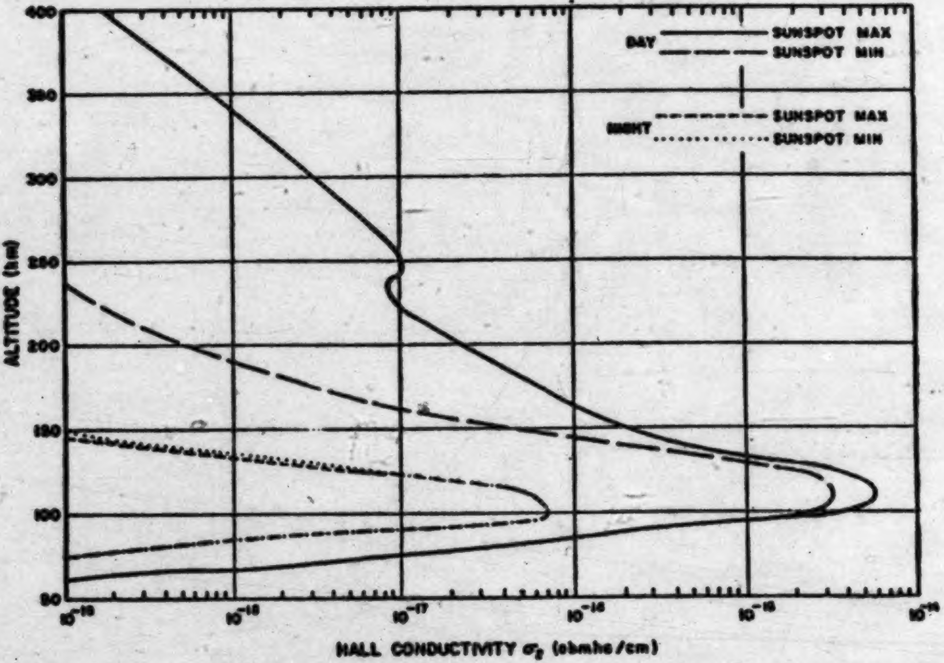
DAY SUNSPOT MAX
SUNSPOT MIN
NIGHT SUNSPOT MAX
SUNSPOT MIN
ALTITUDE (km)
50
100
150
200
250
300
350
400
10^{-19}
10^{-18}
10^{-17}
10^{-16}
10^{-15}
10^{-14}
HALL CONDUCTIVITY σ_2 (abmho/cm)

will be employed in Chapter 4. In the ionospheric E region (altitude range 85 to 140 km), electrons may gyrate freely, ($\omega\tau_e > 1$), but ions are impeded due to collisions, so that $\Omega\tau_i < 1$. From equations 1.2 and 1.3, the Pedersen current is carried mainly by ions, the Hall current by electrons. At higher altitudes, around 160 km (the F region), both ions and electrons gyrate and drift essentially freely, so that the two terms in σ_H (equation 1.2) almost cancel. However, there remains a significant Pedersen conductivity.

As well as the horizontal currents which flow by virtue of the horizontal electric fields and Hall and Pedersen conductivities, field-aligned currents also flow. Birkeland (1908,1913) first introduced the concept of field-aligned currents, but this work did not gain immediate acceptance. Fejer (1961) and Kern (1962) reintroduced the concept, and Boström (1964) made extensive use of field-aligned currents in his magnetospheric substorm models.

That, in reality, field-aligned currents must flow, has been shown by Vasyliunas (1968). Consider the non-height-integrated form of equation 1.1, including field-aligned current flow, i.e.,

$$\underset{\sim}{J} = \sigma_{\parallel}\underset{\sim}{E}_{\parallel} + \sigma_P \underset{\sim}{E}_{\perp} + \sigma_H \frac{\underset{\sim}{B} \times \underset{\sim}{E}}{B} \qquad 1.4$$

Then

$$\underset{\sim}{E} \cdot \underset{\sim}{J} = \sigma_{\parallel} E_{\parallel}^2 + \sigma_P E_{\perp}^2 > 0 \qquad 1.5$$

For the steady state, $\nabla \cdot \underset{\sim}{J} = 0$, and assuming that $\underset{\sim}{E}$ is electrostatic, $\underset{\sim}{E} = -\nabla\phi$, where ϕ is the electrostatic potential. Therefore,

$$\underset{\sim}{E}\cdot\underset{\sim}{J} = -\nabla\cdot(\phi\underset{\sim}{J}) \qquad 1.6$$

Integration of this over the volume of the ionosphere under consideration, and noting from equation 1.5 that $\underset{\sim}{E}\cdot\underset{\sim}{J} > 0$, gives,

$$\int\underset{\sim}{E}\cdot\underset{\sim}{J}\,dV = -\int\nabla\cdot(\phi\underset{\sim}{J})\,dV = -\int\phi\underset{\sim}{J}\cdot d\underset{\sim}{A} > 0 \qquad 1.7$$

The final integral is over the surface of the system, and since it is non-zero, indicates that currents are flowing into and out of the system.

Field-aligned currents were accepted before direct experimental evidence through in situ measurements was forthcoming. Zmuda et al (1967) and Armstrong and Zmuda (1970) presented evidence from polar orbiting satellites which indicated that field-aligned current sheets flowed into and out of the auroral regions. These results were based on the existence of level shifts in the east-west component of the measured magnetic field. Many similar studies of data from polar-orbiting satellites now exist (Zmuda and Armstrong, 1974; Sugiura and Potemra, 1976; Iijima and Potemra, 1976), and have confirmed that indeed, large scale field-aligned currents connect the outer magnetosphere to the ionosphere. Anderson and Vondrak (1975) have reviewed the data concerning field-aligned currents.

1.3 Large-scale Current Systems

1.3.1 The Sq and L current Systems

Observations of geomagnetic disturbances have led to the description of a number of large-scale ionospheric current systems. As global magnetic variations became available, it became possible to map the quiet-day variations in detail, and a solar variation (Sq) was isolated. Basically, this variation is caused by ionospheric currents which are driven by an atmospheric dynamo. E-region plasma is wind-driven with a horizontal velocity $\underset{\sim}{V}$, across the magnetic field, $\underset{\sim}{B}$, resulting in the production of an electric field, $\underset{\sim}{V} \times \underset{\sim}{B}$. This field drives a height-integrated current, $\underset{\sim}{I}$. As well, a space charge electric field, $\underset{\sim}{E}$, develops to give a total electric field, $\underset{\sim}{E} + \underset{\sim}{V} \times \underset{\sim}{B}$. The form of the Sq current system can be found from the solution of

$$\nabla \cdot \underset{\sim}{I} = 0$$

$$\underset{\sim}{I} = \underset{\approx}{\Sigma}\,(\underset{\sim}{E} + \underset{\sim}{V} \times \underset{\sim}{B})$$

where $\underset{\approx}{\Sigma}$ is the height-integrated conductivity tensor. (See for example, Akasofu and Chapman, 1972). Figure 1.5 is a plot of the Sq current systems for December solstitial, equinoctial, and June solstitial seasons, as well as the yearly average during IGY (1958) (Matsushita, 1969). The current direction is counter-clockwise in the northern hemisphere, in these figures.

Figure 1.5 Plots of the Sq current systems for December solstitial, equinoctial, and June solstitial seasons, and the yearly average during the IGY (1958). Current intensity between two consecutive contours is 2.5×10^4 A. (After Matsushita, 1968).

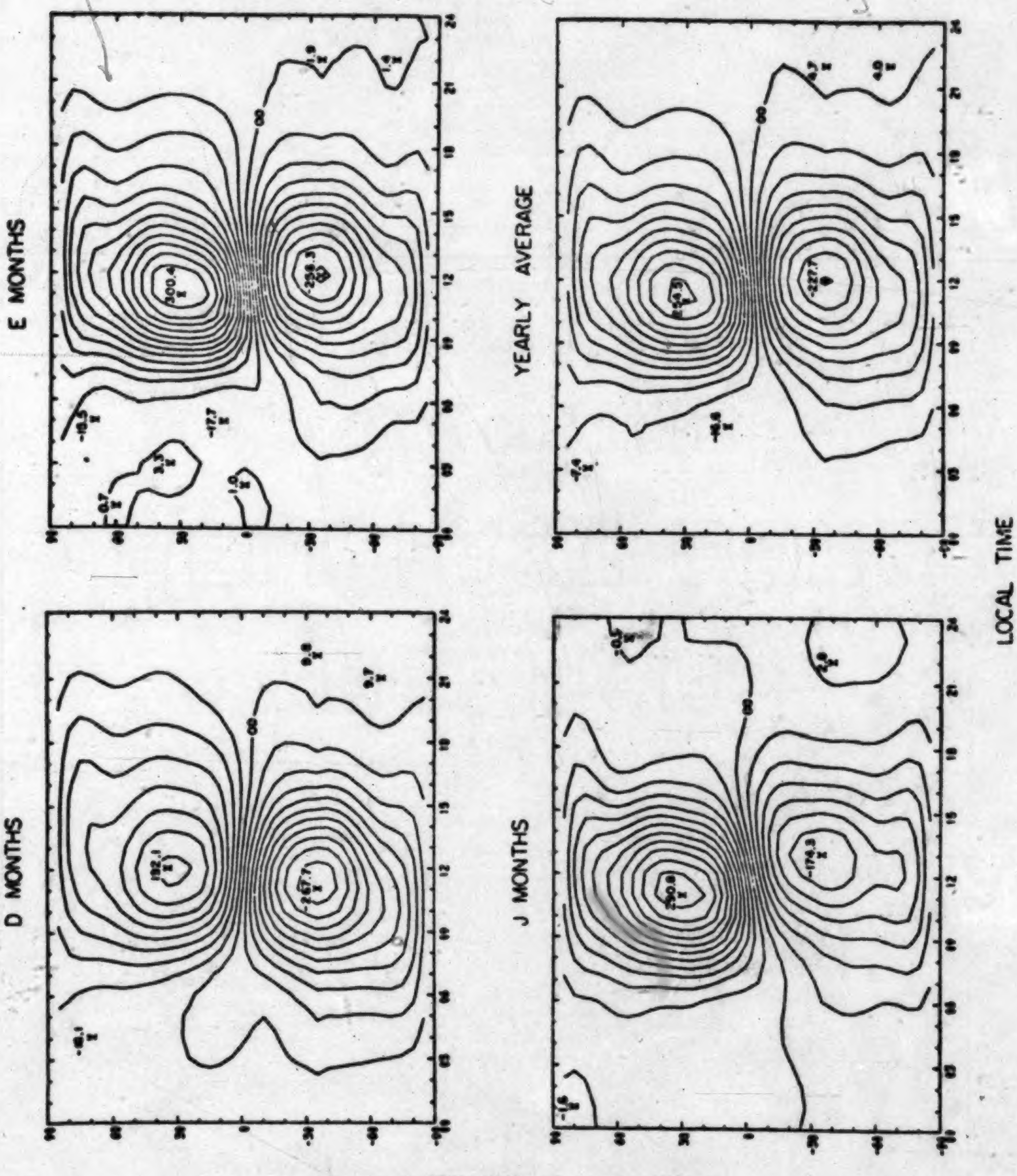
D MONTHS
E MONTHS
J MONTHS
YEARLY AVERAGE
DIP LATITUDE
LOCAL TIME
300.4
-258.3
192.1
-257.7
-174.3
-227.7
0.0

Another geomagnetic fluctuation present at all times is that found to be associated with atmospheric tidal motions, driven by the moon's gravity field. The perturbations due to this so-called L current system are approximately one order of magnitude less than the Sq variations.

1.3.2 The Dst and DP1 Current Systems

When the Sq and L magnetic variations are removed from the data, the so-called disturbance field (D) remains. This field can be represented as the sum of two components, Dst and DS. The Dst component is independent of longitude, and DS is the difference between D and Dst. The Dst component is believed to be due to a westward flowing ring current in the equatorial plane and several earth radii (Re) from the earth. Many equivalent current systems consistent with the DS component have been put forth in the literature. The DP1 system (Obayashi, 1967) is the one associated with magnetic substorms. Figure 1.6 is a polar plot of this classical system. Note that relatively intense current flows both eastward and westward near 70°N latitude, corresponding to the location of the auroral oval.

1.3.3 The S_q^p and DP-2 Current Systems

During times of very low magnetic activity, there is a polar cap magnetic variation which has been called S_q^p by Nagata and Kokubun (1962). Subsequent authors (Kawasaki and Akasofu, 1967; Feldstein and Zaitsev, 1967) revised this

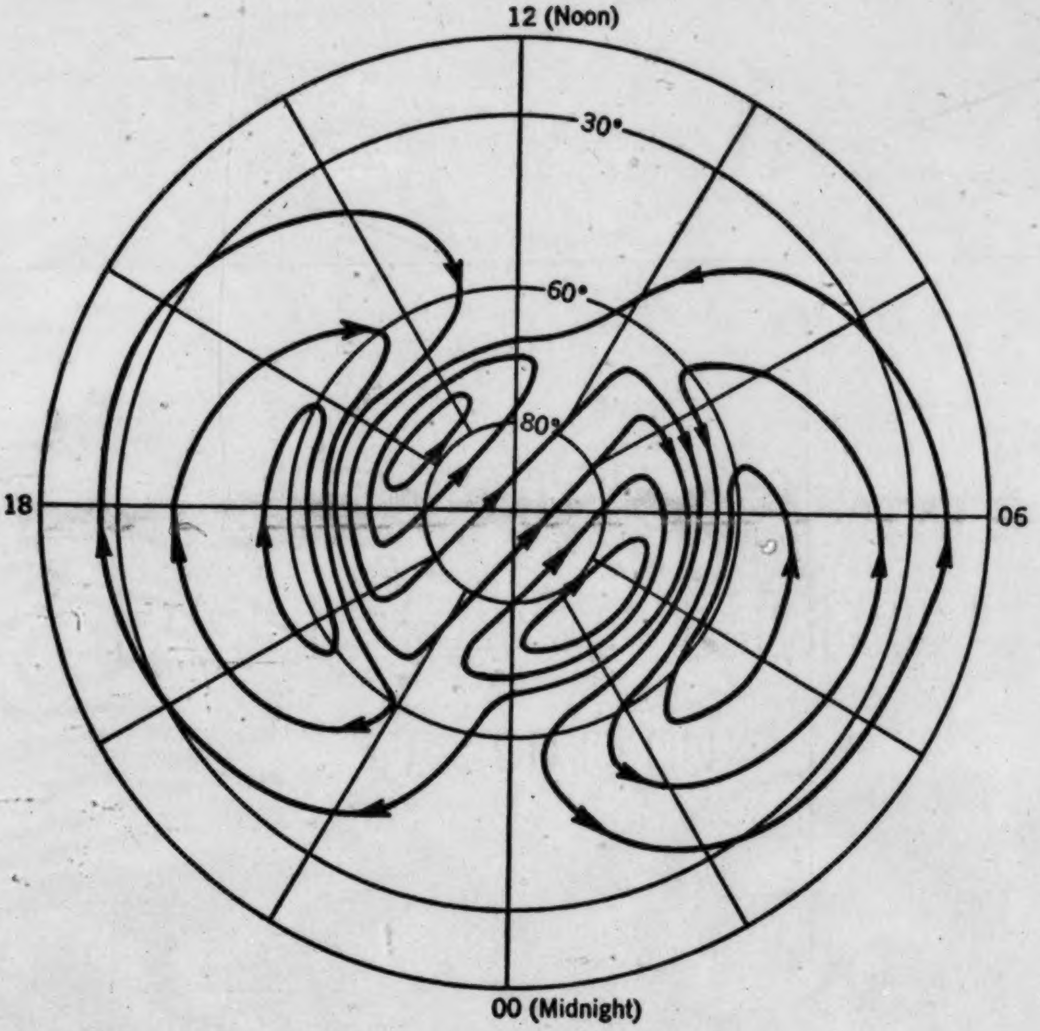
12 (Noon)
30°
60°
80°
18
06
00 (Midnight)

Figure 1.6 An equivalent ionospheric current system. If the current between contours is 10^5 A, this system would reproduce the geomagnetic disturbance of the DP1 type. (After Piddington, 1969).

system to exclude any possibility of magnetic disturbance. Figure 1.7, from Kawasaki and Akasofu (1967), shows the horizontal magnetic disturbance vectors for the S_q^p system for May 8,1964. In the same paper, these authors verified Nagata and Kokubun's observation that S_q^p was much stronger in the summer months, and concluded that the S_q^p magnetic variation was due to an ionospheric current system. Subsequent work (Kawasaki and Akasofu, 1973) has shown that the data of Figure 1.7 may be reasonably modelled by a combination of field-aligned and ionospheric currents.

Nishida (1968) proposed an additional current system, DP-2 (Figure 1.8), but Akasofu *et al* (1973) have expressed the belief that the DP-2 current system is in fact due to a combined effect of expansion of the auroral oval and an enhancement the S_q^p system.

1.3.4 The Electrojets and the Interplanetary Magnetic Field

Harang (1946) published observations of the diurnal variation of magnetic disturbance vectors at high latitudes (53.8°N to 74.2°N geomagnetic latitude). It is clear from his work and all subsequent work that there are two main ionospheric equivalent currents, the eastward and westward electrojets, which can account for the majority of magnetic observations at high latitudes. The eastward current produces a positive (i.e., northward) north-south component of magnetic field, the westward current a negative north-south component, and these signatures are apparent in

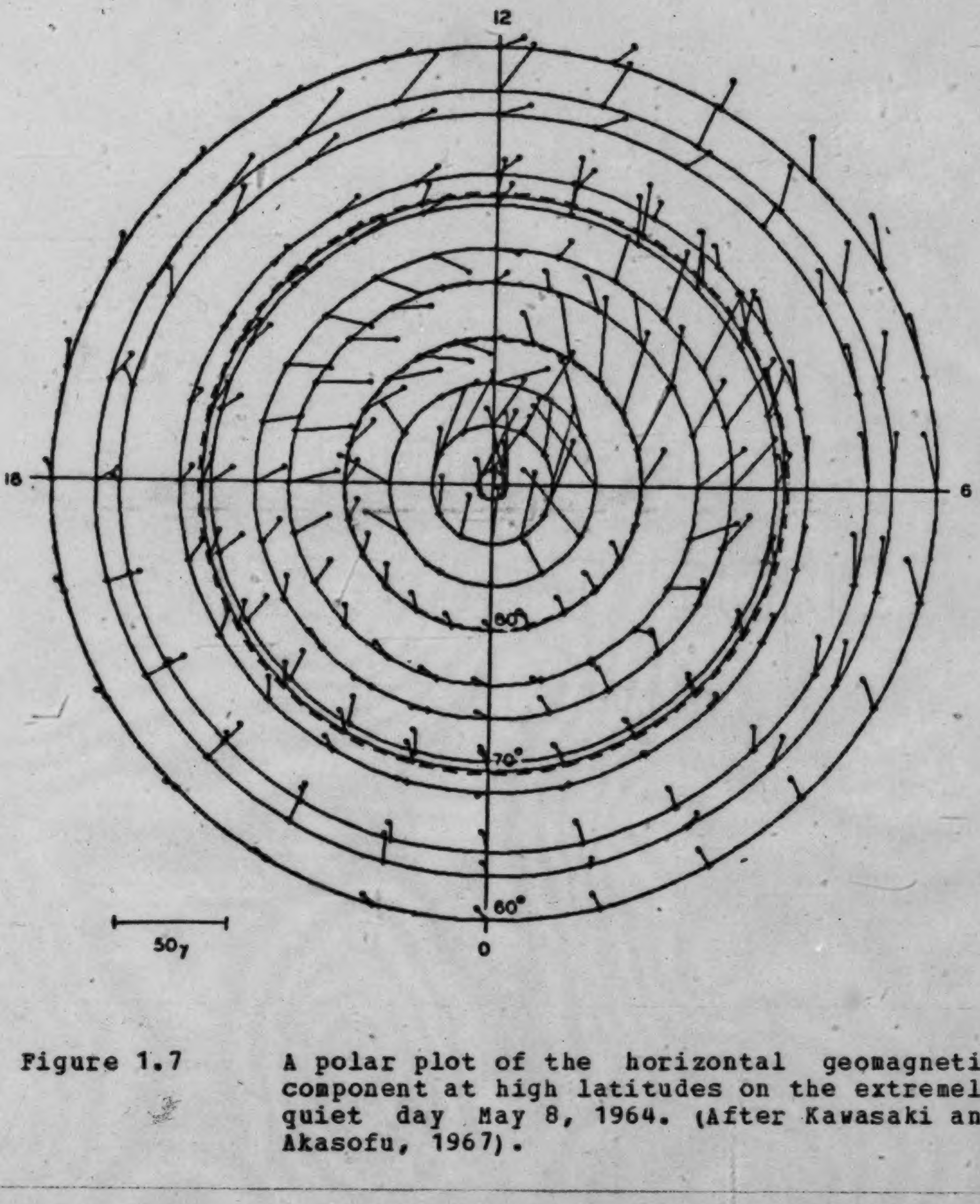

Figure 1.7 A polar plot of the horizontal geomagnetic component at high latitudes on the extremely quiet day May 8, 1964. (After Kawasaki and Akasofu, 1967).

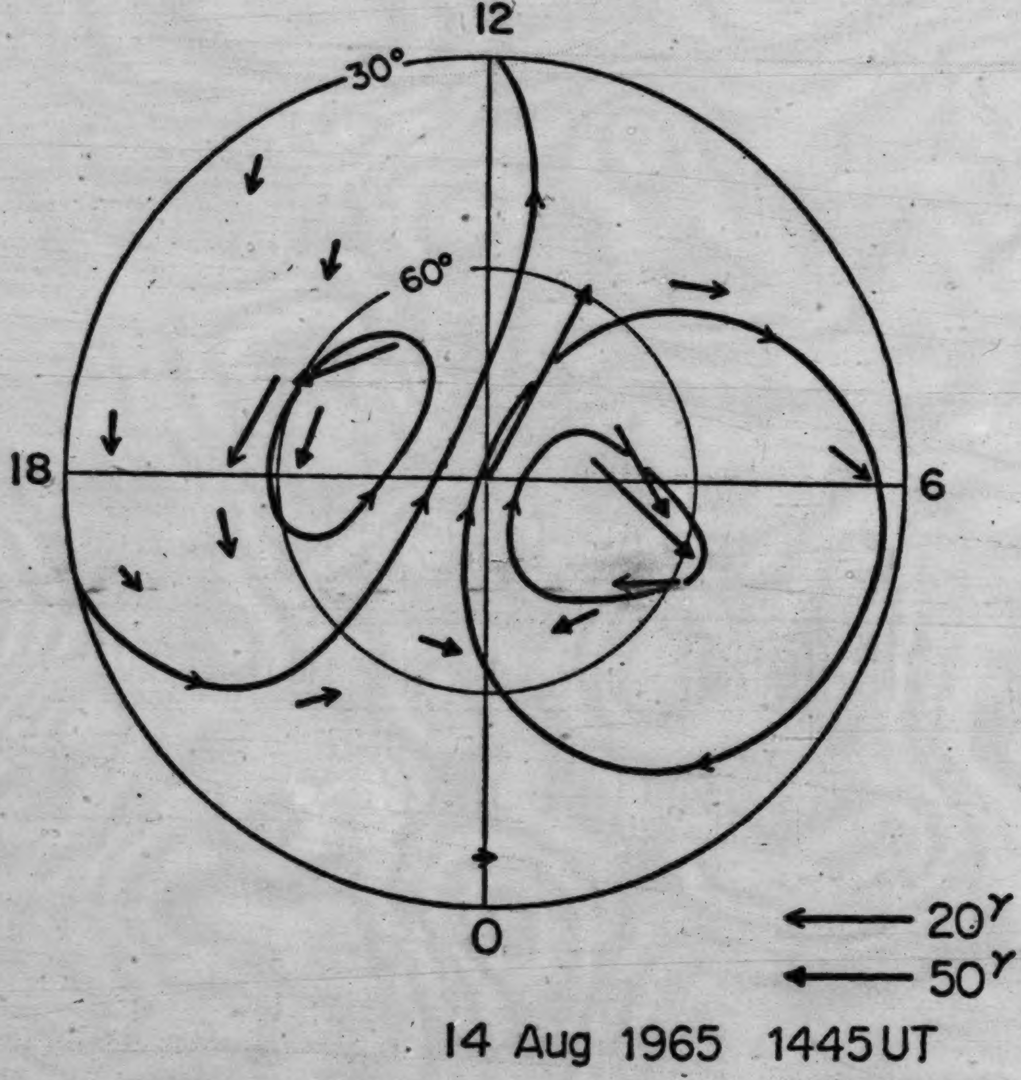
12
30°
60°
18
6
0
20^γ
50^γ
14 Aug 1965 1445 UT

Figure 1.8 The DP-2 current system. (After Nishida, 1971).

Harang's published data, with eastward current flowing from near noon to approximately midnight, and westward current flowing from noon into the pre-midnight sector. The region of current reversal, in the pre-midnight sector, has become known as the Harang discontinuity.

It has become clear in the past few years that the magnitude of auroral zone magnetic perturbations is governed by the interplanetary magnetic field (IMF) and in particular, by the sign of the vertical (B_Z) and azimuthal (B_Y) components of the IMF. As well, the average magnitude of the westward and eastward electrojets decreases from summer to winter (Meng and Akasofu, 1968; Langel and Brown, 1974, Friis-Christensen and Wilhjelm, 1975). This seasonal effect is not the same for both electrojets when examined in terms of the role of the IMF, as will be seen below.

In terms of field line merging, it is not surprising that the IMF vertical component has a marked effect on ionospheric currents, since the merging rate is enhanced when $B_Z<0$. Akasofu (1977) has given an excellent review of the relationships between B_Z and various ionospheric phenomena. He also points out that great care must be exercised in interpreting some of the relationships which have been claimed to exist. For example, the AE index, which is a measure of world-wide auroral activity, has been correlated with B_Z. The AE index is computed from magnetic records from a number of auroral zone magnetic observatories which are approximately uniformly distributed in longitude (Davis and Sugiura 1966; Allen and Kroehl, 1975). The horizontal component records are superposed, and the curves defining the upper and lower envelopes of these superposed records are defined as AU and AL respectively. Then the AE index is simply the distance between AU and AL. i.e.,

$$AE = |AU| + |AL|$$

The AE index presupposes that at least one observatory can monitor the westward electrojet to give AL, and at least one observatory can monitor the eastward electrojet, to give AU. It is assumed that these electrojets are most intense in the auroral zone, where these observatories are located. However, Holzworth and Meng (1975) have shown that B_z affects the size of the auroral oval, so that when B_z is northward, the radius of the auroral oval is reduced. Thus, Akasofu points out, a strong correlation between B_z and AE may be, at least in part, only due to the correlation between B_z and the size of the auroral oval. Hirshberg and Colburn (1969) have done a similar analysis between Kp and B_z. Kp is a 3-hour index of the level of worldwide geomagnetic activity introduced by Bartels (1949) (see review by Rostoker, 1972). This index is computed in a complicated manner from data from sub-auroral zone observatories, and Akasofu's criticism may also apply. However, Hirshberg and Colburn (1969) showed that there was a good correlation between Kp and the magnitude of B_z, when $B_z<0$. In any case, negative B_z causes an enhanced merging of field lines with a resulting increase in convection rate and thus enhanced electrojet current strengths.

The east-west component of the IMF (B_y) also plays a regulatory role in ionospheric current dynamics. Solar magnetic field lines are carried away from the sun by the solar wind, and due to the rotation of the sun, take on an Archimedes spiral configuration. Wilcox and Ness (1965) detected the interplanetary sector structure in which, on average, four sectors of alternating magnetic field direction (away from the sun, and towards the sun), were found for every solar rotation. When the IMF is directed away from the sun, it corresponds to a positive B_y. Svalgaard (1968,1973), Mansurov (1969), and Friis-Christensen _et al_ (1972) have shown that the B_y-component affects the polar cap magnetic field. In particular, when $B_y>0$, the inferred polar cap equivalent current is counterclockwise (looking down on the north pole) and the reverse direction when $B_y<0$. However, during winter months, the magnitude of the polar cap magnetic variations are extremely small, approximately two orders of magnitude less than during summer months (Svalgaard, 1973).

Returning to the seasonal differences in the eastward and westward electrojets and the role of B_y, Langel and Brown (1974) have found that, during the summer, $|\Delta H|$ and $|\Delta Z|$ in the westward jet region are larger than in winter when $B_y<0$. During away sectors ($B_y>0$), $|\Delta H|$ is less in summer than in winter, while $|\Delta Z|$ is approximately the same in winter and in summer. In the eastward electrojet region, $|\Delta H|$ and $|\Delta Z|$ are both greater in the summer.

The observations concerning the role of the IMF upon ionospheric current systems are presented here for completeness. In this thesis, data have not been ordered according to the polarity of the IMF. However, an argument is developed in Chapter 4 which depends, in part, on the above considerations.

1.4 Ionospheric Current Models

The ultimate test of any interpretation of data is the construction of a model consistent with that interpretation, and the comparison of computed results with the data. A large number of current models have been devised to describe specific current systems, although many of these have consisted of only ionospheric currents. Kawasaki and Akasofu (1973) had reasonable success in modelling the S_q^p current system, using a model consisting of field-aligned current (along dipole field lines) and a flat earth approximation for the ionospheric currents. Maeda and Maekawa (1973) undertook a numerical study of modelling global polar ionospheric currents. They considered that current would be driven by i) an atmospheric dynamo electric field; ii) a polarization electric field, arising from conductivity gradients; and iii) an externally applied electric field, induced by the solar wind. They did not include the effect of field-aligned currents, although the existence of such currents as sources and sinks was pointed out. Three different models of conductivity were employed, as described by Fejer (1953). Maeda and Maekawa found that the geomagnetic variations produced by one type of polarization electric field, in which a positive point charge was placed near dawn, and a negative point charge near dusk, are very similar to S_q^p. This charge distribution is similar to that used by Kawasaki and Akasofu (1973), although these authors used charge sheets. However, Maeda and Maekawa do not give a detailed comparison between their calculations and real data.

Several global current models have been developed by Yasuhara et al (1975). In their investigation, it was assumed that field-aligned current sheets flowed into and out of the auroral oval at its borders, such that current was downwards on the poleward side, from midnight to noon, and upwards on the poleward side of the oval from noon to midnight. The field-aligned current at the equatorward borders was of the opposite sense, and of reduced intensity by a factor of approximately 2. For the model developed for relatively quiet periods, the auroral oval was assumed to be an annulus with an enhanced conductivity structure with respect to the region outside the annulus. The ratio of Pedersen to Hall height-integrated conductivities was two everywhere. To determine the ionospheric current flow, the equation

$$\nabla \cdot \underset{\sim}{I} = J_{\parallel} \sin \chi$$

was solved, assuming that the field-aligned current, $J_{\parallel}$, was vertical, (i.e., χ =90°), and where $\underline{I}$ is the height-integrated ionospheric current density. This model yields both eastward and westward electrojets confined to the auroral oval, as shown in Figure 1.9 . As well, some current flows across the polar cap, from about midnight to noon, and there is weak current at sub-auroral latitudes. However, the choice of field-aligned current distribution was somewhat arbitrary in that the exact distribution was not known at that time. As a result, the currents derived from this model do not appear too realistic, inasmuch as eastward current is shown just past dawn, and magnetometer evidence does not verify this (see Chapter 3 of this thesis for example). Although this model was not tested against ground-based magnetic data, it does demonstrate an approach that could be quite fruitful in approaching ionospheric current flow. As well, these authors demonstrated for the first time that east-west aligned field-aligned current sheet pairs, if unbalanced along a meridian, can produce ionospheric current flows that resemble those which are believed to exist.

Nothing has been said concerning the mapping of these various current systems to the outer magnetosphere. As this mapping is required to understand the possible driving mechanisms for the currents, it will be included in Chapter 5 of this thesis, where some possible current generators are described.

Figure 1.9 A model ionospheric current pattern. The current strength between two adjacent current contours is 2×10^4 A. (After Yasuhara *et al* 1975.)

Ionospheric Current Pattern

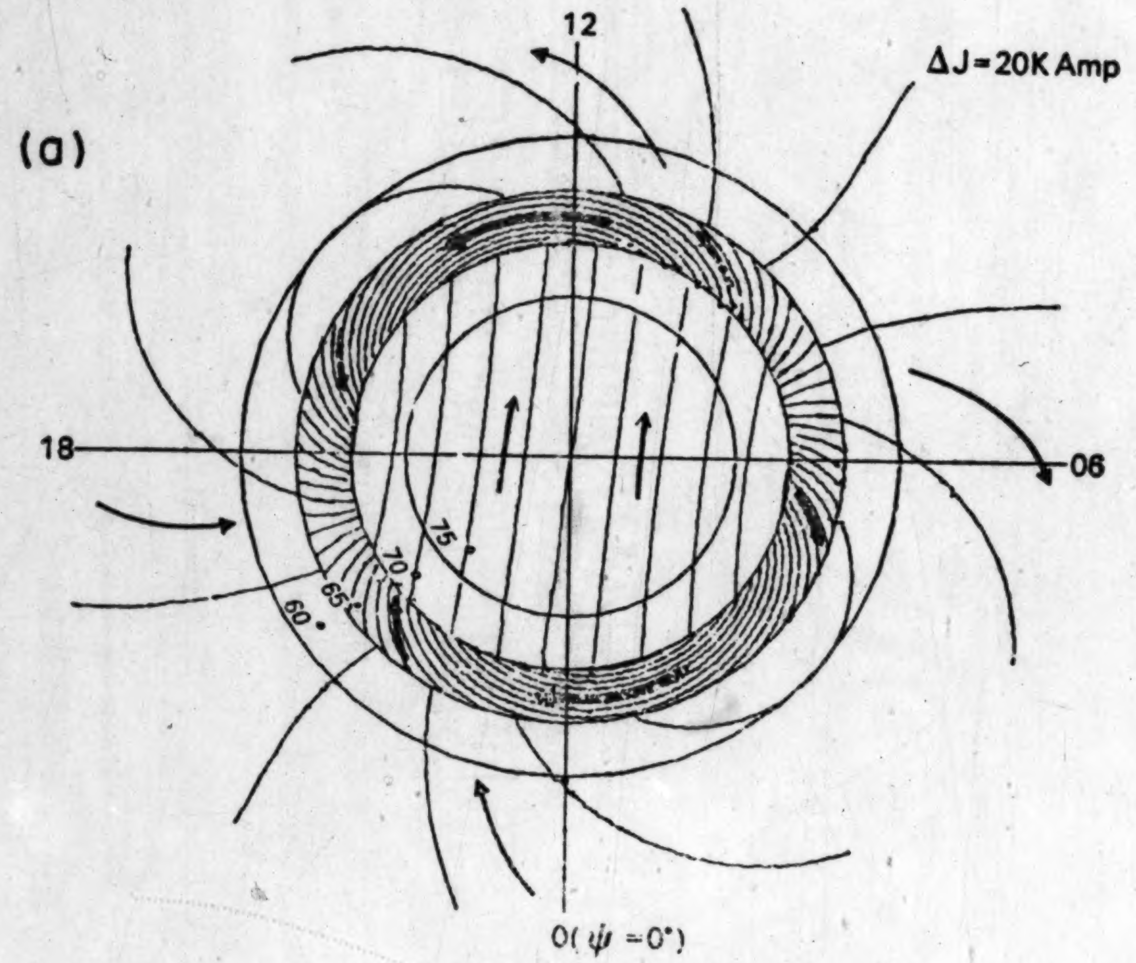
(a)
12
ΔJ = 20K Amp
18
06
75°
70°
65°
60°
0(ψ =0°)

1.5 The Objectives of this Thesis

The data analysis presented in the thesis was undertaken in the hope that it would lead to a model of ionospheric and magnetospheric currents which would be consistent with all known observations in the high latitude regions of the earth. This goal was, in retrospect, perhaps too ambitious. However, working from ground-based magnetic data, and using average characteristics of the ionospheric electric field and ionospheric conductivities, a current model has been developed, which, although it does not reproduce the observations exactly, does reproduce in a statistically significant way, many features of the data. This is the first time that a current model has been so rigidly tested against real data, and the prime value of this thesis lies in that test.

CHAPTER 2 DATA PROCESSING AND ANALYSIS

2.1 Data Handling

From late in 1969 to early in 1972, the University of Alberta intermittently operated a number of 3-component magnetic observatories. In the centered dipole system of coordinates, these observatories all lie along approximately the 300°E meridian. Table 2.1 gives the positions of these observatories, as well as the observatory or station mnemonic, and Figure 2.1 shows a map of the location of these stations. As well as these observatories, data from Resolute Bay (RESO;83.0°N, 290.5°E) and Newport (NEWP;55.1°N,300.0°E) were available to extend the coverage of the line of stations both northward and southward. At each of the sites shown in Figure 2.1, data were recorded digitally on 7-track magnetic tape, with a sample rate of one data point in each of 3 channels every 1.92 seconds, timing of the data being considered accurate to ±1s (Kisabeth,1972). The system has a dynamic range of ±1000nT with a ±1nT sensitivity. As well as recording the magnetic data, a timing signal from radio station WWVB was recorded for 2 minutes every 7.5 hours. Kisabeth (1972) has described the instrumentation in some detail.

For computer compatibility, the field tapes were converted to 9-track station master tapes, containing data for one station only. As this was being done, the WWVB timing data were interpreted by a special computer code, and

TABLE 2.1

COORDINATES OF MAGNETOMETER LINE SITES

SITE	CODE NAME	GEOGRAPHIC LATITUDE (°N)	GEOGRAPHIC LONGITUDE (°E)	GEOMAGNETIC LATITUDE (°N)	GEOMAGNETIC LONGITUDE (°E)
Cambridge Bay	CAMB	69.1	255.0	76.8	296.6
Contwoyto Lake	CONT	65.5	249.7	72.6	295.8
Fort Reliance	RELI	62.7	251.0	70.3	300.1
Fort Smith	SMIT	60.0	248.0	67.3	300.0
Fort Chipewyan	CHIP	58.8	248.0	66.3	303.1
Fort McMurray	MCMU	56.7	248.8	64.2	303.5
Meanook	MENK	54.6	246.7	61.9	300.8
Leduc	LEDU	53.3	246.5	60.6	302.9

Figure 2.1 A map showing the location of the University of Alberta magnetic observatory sites. Data were also available from Newport, U.S.A., and Resolute Bay, Canada (not shown) along the same meridian as the University of Alberta observatories.

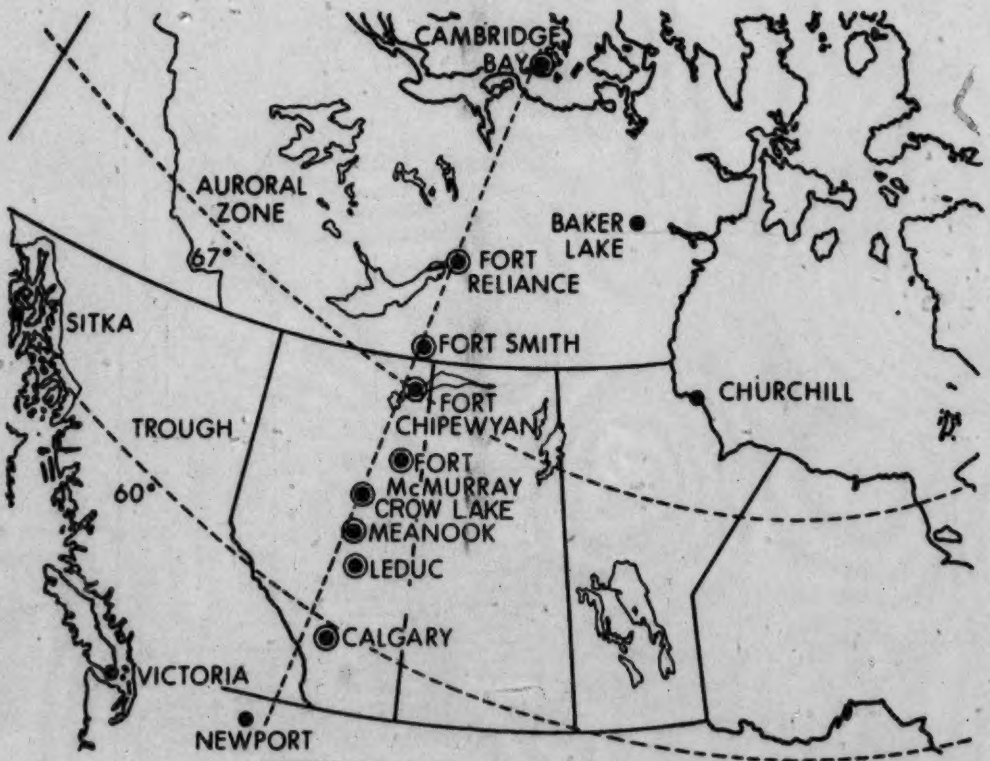
CAMBRIDGE BAY
AURORAL ZONE
BAKER LAKE
67°
FORT RELIANCE
SITKA
FORT SMITH
CHURCHILL
FORT CHIPEWYAN
TROUGH
FORT McMURRAY
60°
CROW LAKE
MEANOOK
LEDUC
CALGARY
VICTORIA
NEWPORT

timing information, along with the station mnemonic was written as a label for each block of data (1 hour, 5 minutes, 32 seconds of data). In some instances, the WWVB timing information was not machine decodeable. Then, a Cal Comp plot was made of the WWVB signal, and it was interpreted by hand.

When all data had been transferred to 9-track magnetic tapes, a so-called event tape was created for specific intervals of time. Each event tape contains a series of files, with each file containing all data for the time interval for one station. Thus, each event tape contains the data for all the stations for a given interval of time. The availability of event tapes minimizes the number of tapes which must be manipulated to study a specific period of time, or event.

At the beginning of this thesis study, the data were available on 9-track master tapes; data acquisition did not play a significant role in this thesis.

The magnetometer sensors at each of the observatories were aligned in the direction of local magnetic north, local magnetic east, and the vertical (H,D, and Z respectively, where H is positive northward, D is positive eastward, and Z is positive downward). To facilitate the interpretation of the data and the modelling of the magnetic field sources, the centered dipole coordinate system (an orthogonal system) was used, and all data in this thesis will be presented in this system. This required that the measured horizontal components (H, D) of the magnetic field be rotated into the centered dipole system through the transformation

$$\begin{pmatrix} X' \\ Y' \end{pmatrix} = \begin{pmatrix} \cos\theta & -\sin\theta \\ \sin\theta & \cos\theta \end{pmatrix} \begin{pmatrix} H \\ D \end{pmatrix}$$

where the primed coordinates represent the centered dipole system and the unprimed coordinates the local magnetic system. Here, θ is defined as the difference between the magnetic declination of the station and the dipole declination. Table 2.2 lists θ for the observatories used in this thesis.

2.2 Data Processing

2.2.1 Latitude Profiles

The primary suite of data that was used in this study was from the time period from Day 332,1971, (November 28, 1971) to Day 24, 1972, (January 24, 1972). The data will be presented in the form of latitude profiles. A latitude profile is constructed from data points acquired at all stations at a given time, plotted as a function of the latitude of the station. This method of presentation has been chosen for several reasons. A latitude profile depicts a large amount of information in a single frame; that is, the latitudinal behaviour of the three components of the magnetic field at a given time is shown on one plot. Also, in many cases, a latitude profile can be interpreted readily in terms of overhead ionospheric currents (see below). These

TABLE 2.2

The Angle θ for the Observatories used in this thesis

OBSERVATORY	θ(°E)
RESO	-45.5
CAMB	2.5
CONT	8.2
BELI	7.6
SMIT	7.5
FTCH	7.7
MCMU	7.2
MENK	7.2
LEDU	7.1
NEWP	6.3

two features greatly facilitate the interpretation of large amounts of magnetic data. An example of a latitude profile is shown in Figure 2.2(a). This is a model profile (i.e., it is the result of calculating the magnetic field due to a hypothetical current system), for an ionospheric current of 5° in latitudinal extent, and 20° in longitudinal extent, and with uniform current density. Figure 2.2(b) shows a similar profile, but for a case where the current density is distributed in latitude according to the expression $J(x) = \exp(-3x^2)$ where x is the latitudinal distance from the centre of the current. Both of these current systems are connected to the magnetosphere by field-aligned currents with closure in the equatorial plane as shown in Figure 2.2(c). Note that the north-south or X'-component peaks directly under the centre of the electrojet, and that the positions of the poleward and equatorward edges of the current system are provided by the Z-component extrema. The profiles shown in Figure 2.2(a) and 2.2(b) are calculated for ionospheric current flowing in a westward direction. For current flowing eastward, the signs of all the perturbation components are reversed.

As well as such an east-west current system, current may flow in a north-south direction in the ionosphere, linking the two anti-parallel field-aligned Birkeland current sheets. An idealized picture of such a current system is shown in Figure 2.3. Kisabeth (1972) has computed latitude profiles for short (i.e., limited in longitudinal

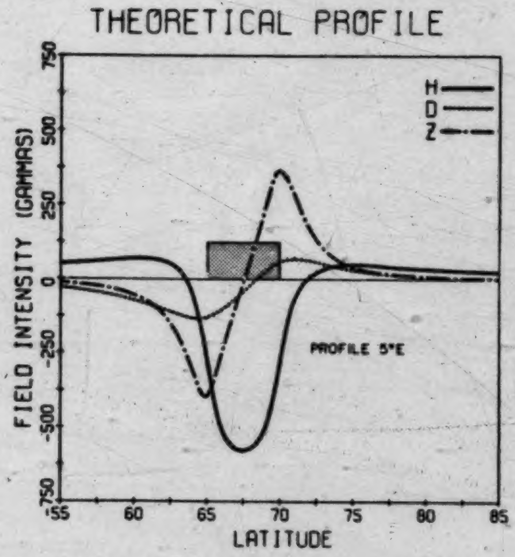

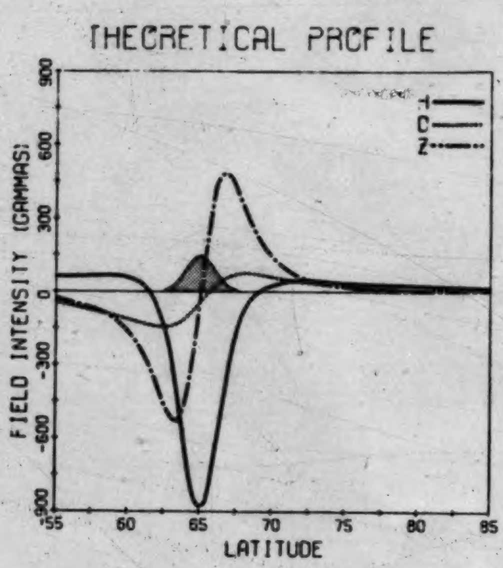

Figure 2.2(a) A model latitude profile for a current of 5° latitudinal extent and 20° longitudinal extent, and of uniform density. The total current is 10^6 A and the profile is taken along a line 5° east of the central meridian. (After Kisabeth, 1972).

Figure 2.2(b) Similar to Figure 2.2(a), but for a current density distributed according to $J(x) = \exp(-3x^2)$, where x is the distance from the latitudinal center of the system. (After Kisabeth, 1972).

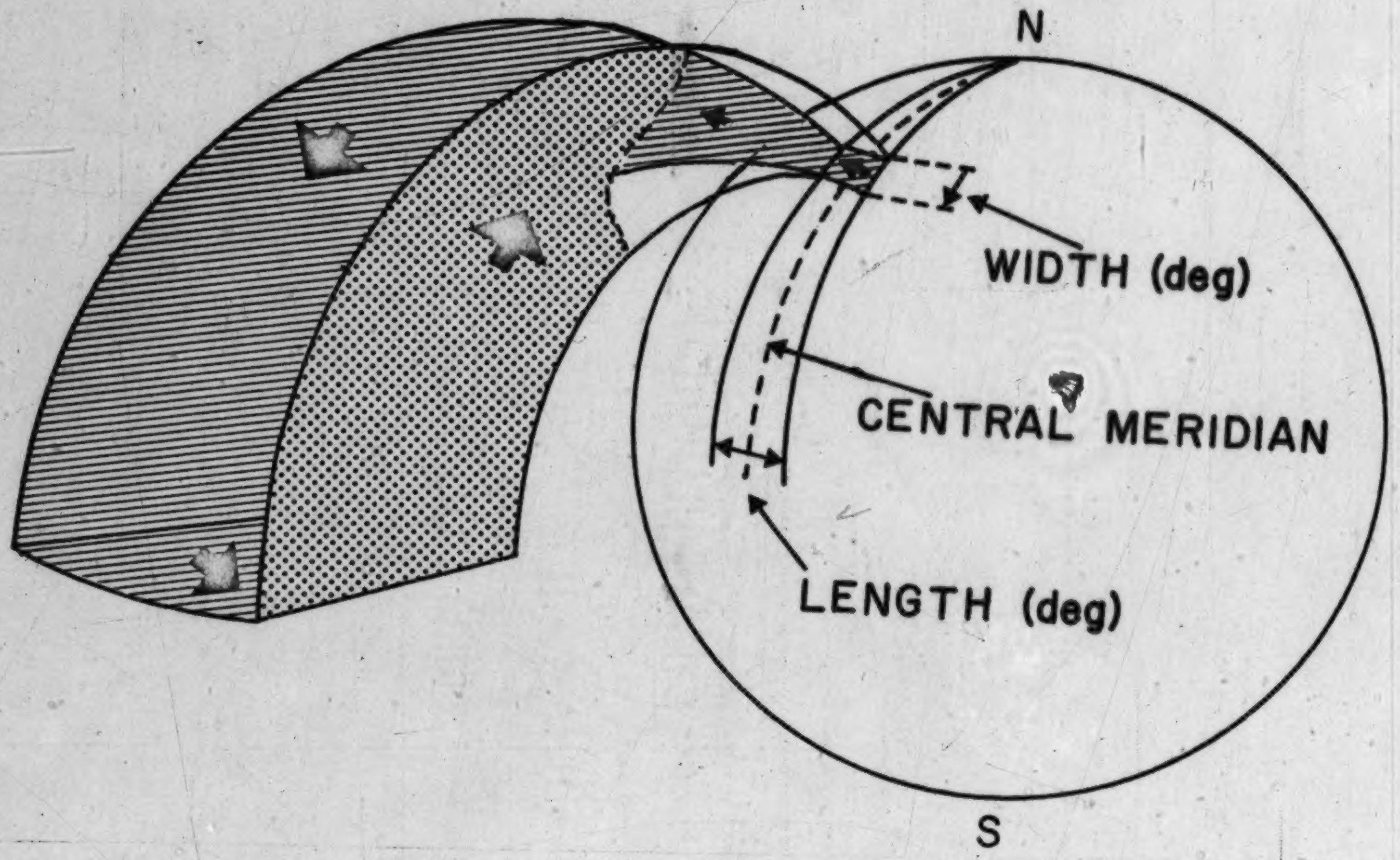
N
WIDTH (deg)
CENTRAL MERIDIAN
LENGTH (deg)
S

Figure 2.2(c) Complete three-dimensional current system involving an ionospheric current flowing in the east-west direction. (After Kisabeth, 1972)

Figure 2.3 Complete three-dimensional current system involving an ionospheric current system flowing in the north-south direction. (After Kisabeth, 1972).

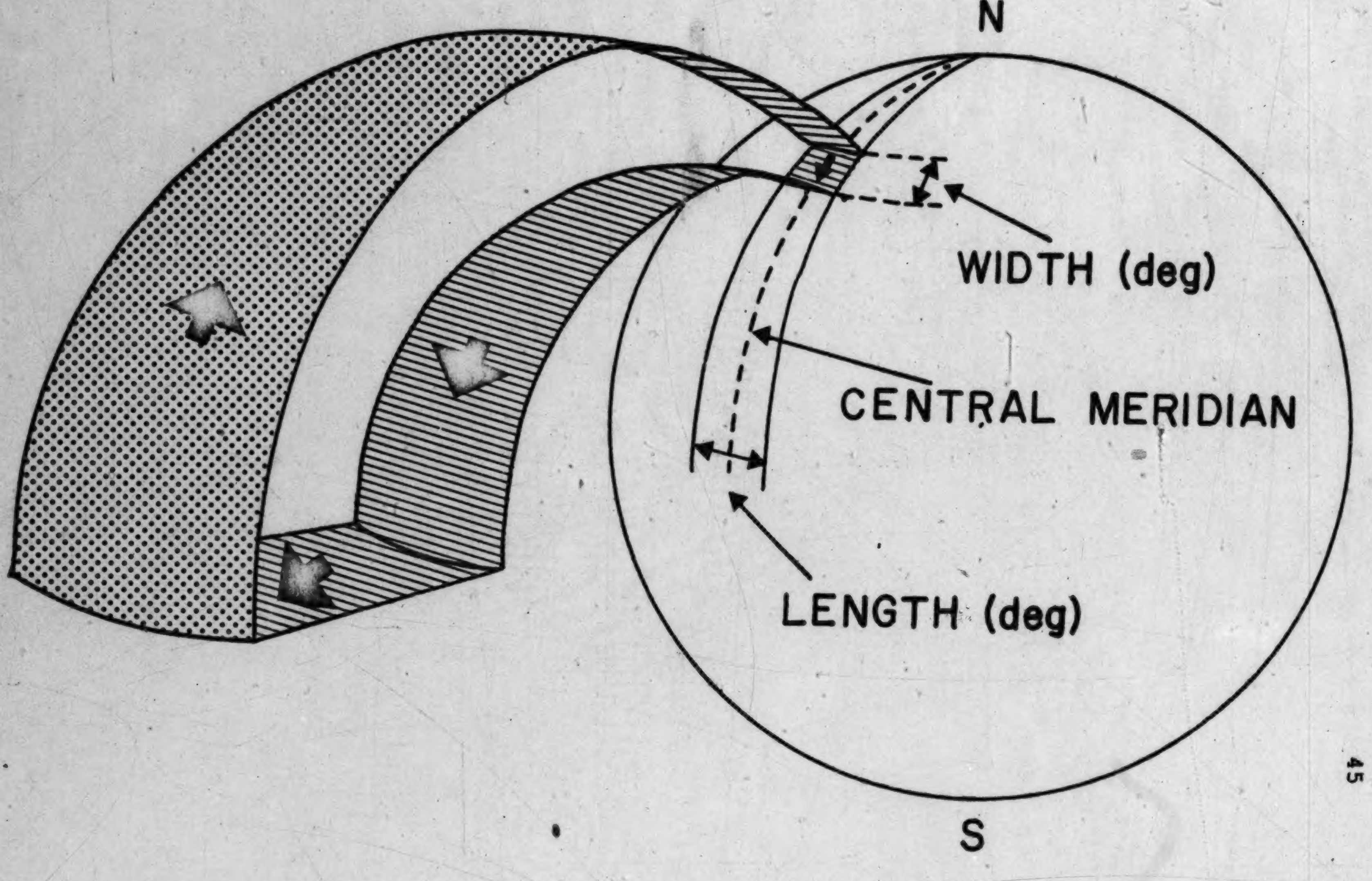
N
WIDTH (deg)
CENTRAL MERIDIAN
LENGTH (deg)
S

extent) north-south systems; such a profile is shown in Figure 2.4, along with the perturbations due to the contributing systems. As well, Figure 2.5 shows the magnetic perturbations for a very long (180° in longitudinal extent) north-south current system. It will be observed that the general features are similar to those shown in Figure 2.4.

It is instructive at this point to consider the magnetic perturbations due to certain other hypothetical currents as well.

For a current system which, unlike that shown in Figure 2.2(c) does not flow along lines of equal latitude, the latitude profile produced along a meridian line differs from that shown in Figure 2.2(a). For such a "tilted" current system, the perturbation in the X'-component is decreased while the perturbation in the Y'-component is increased in such a way that $X'^2 + Y'^2$ is a constant. Figure 2.6 shows the effect of constraining the ionospheric current to flow along the path described by $\theta = \theta_1 + \frac{1}{2}(\theta_2 - \theta_1)(1 + \cos\varphi)$ where θ is the colatitude, φ the longitude (measured counterclockwise from midnight), and θ_1 and θ_2 correspond to the colatitude at φ =180° and 0° respectively. For the profile shown, the poleward boundary has values of $(\theta_1, \theta_2) = (15°, 20°)$ while for the equatorward boundary, $(\theta_1, \theta_2) = (20°, 25°)$. It is apparent that $\Delta Y'$ follows $\Delta X'$.

Later in this thesis, reference will be made to "net field-aligned currents"; that is, currents flowing into the

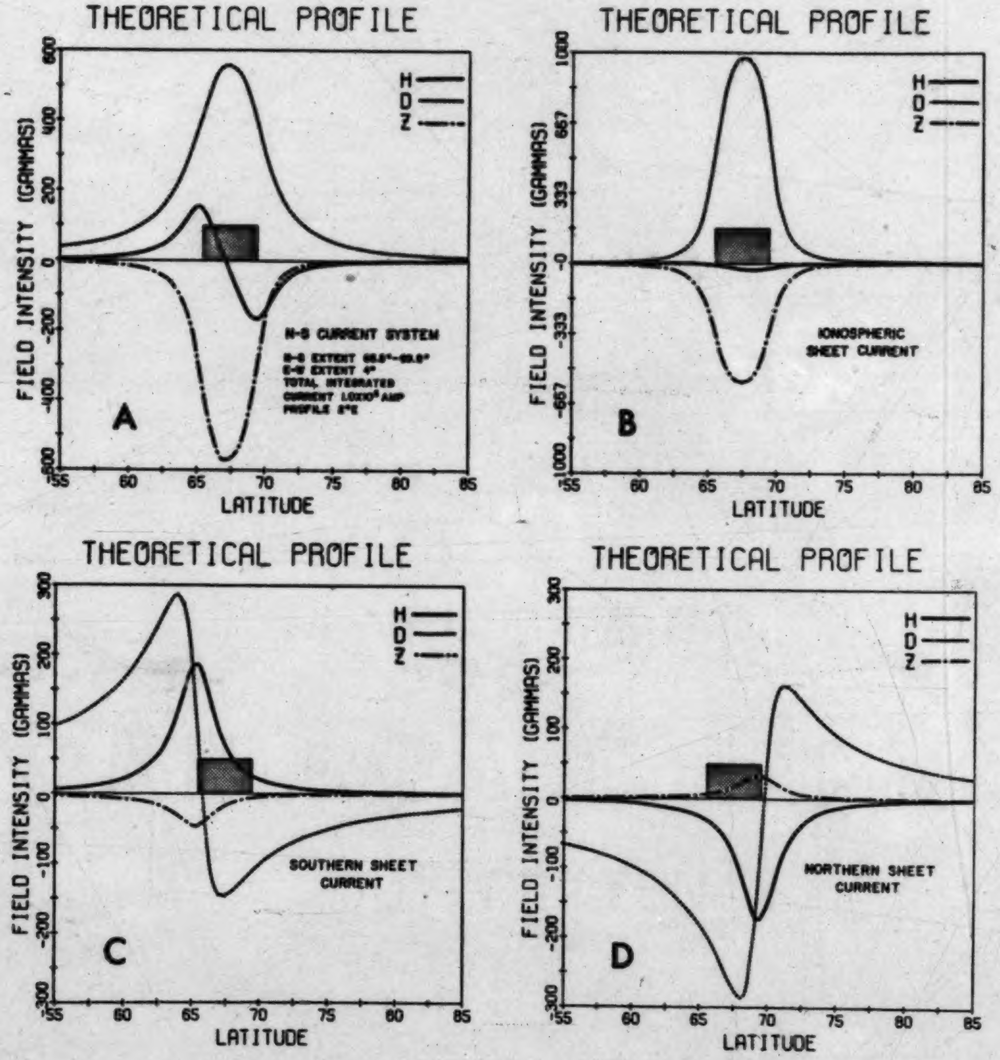

Figure 2.4 Model latitude profile for a three-dimensional north-south current system, as shown in Figure 2.2. This system lies between latitudes 65.5°N to 69.5°N, and between longitudes 0° to 4°. The profile is taken 2° east of the central meridian, and there is a total of 10^6 A flowing. The contributions of the component current systems are shown as well.

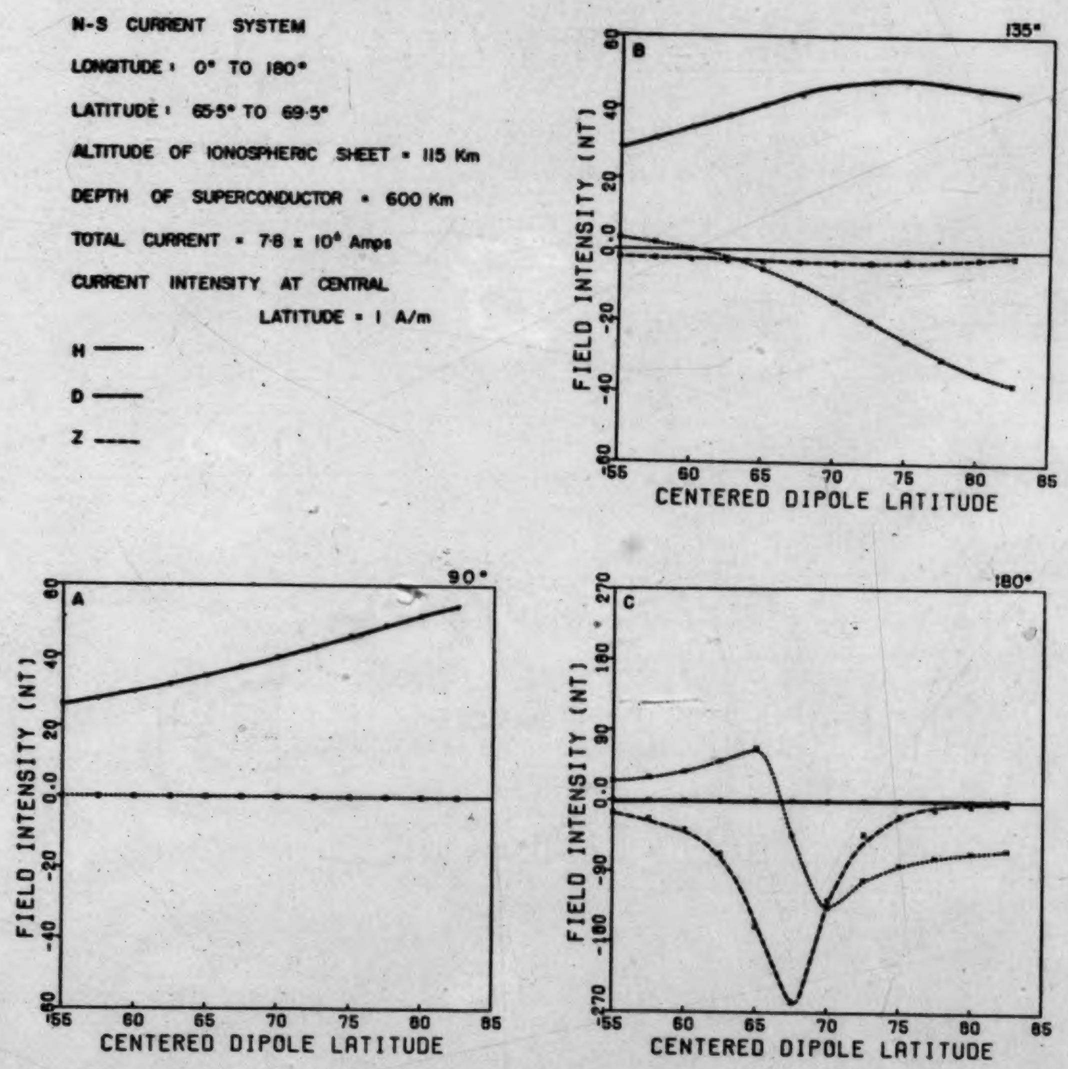

Figure 2.5 Model latitude profile of a very long north-south current system. The system lies between latitudes 65.5°N and 69.5°N, and is 180° in longitudinal extent. At latitude 67.5°, the height-integrated ionospheric current density is 1.0 Am^{-1}, and the total current in the system is 7.8 x 10^{6} A. The profiles are located at:

a) the central meridian (90°);
b) 45° east of the central meridian;
c) 90° east of the central meridian.

Figure 2.6 A model latitude profile for current constrained to flow along the path described by $\theta = \theta_1 + \frac{1}{2}(\theta_2 - \theta_1)(1 + \cos\varphi)$, where θ is the colatitude, φ the longitude, and θ_1 and θ_2 correspond to the colatitudes at $\varphi = 180°$ and 0° respectively. For this profile, the poleward boundary has $(\theta_1, \theta_2) = (15°, 20°)$ and the equatorward boundary has $(\theta_1, \theta_2) = (20°, 25°)$. A total of 10^6 A is flowing between longitudes 0° to 20°. The profile is calculated at $\varphi = 10°$.

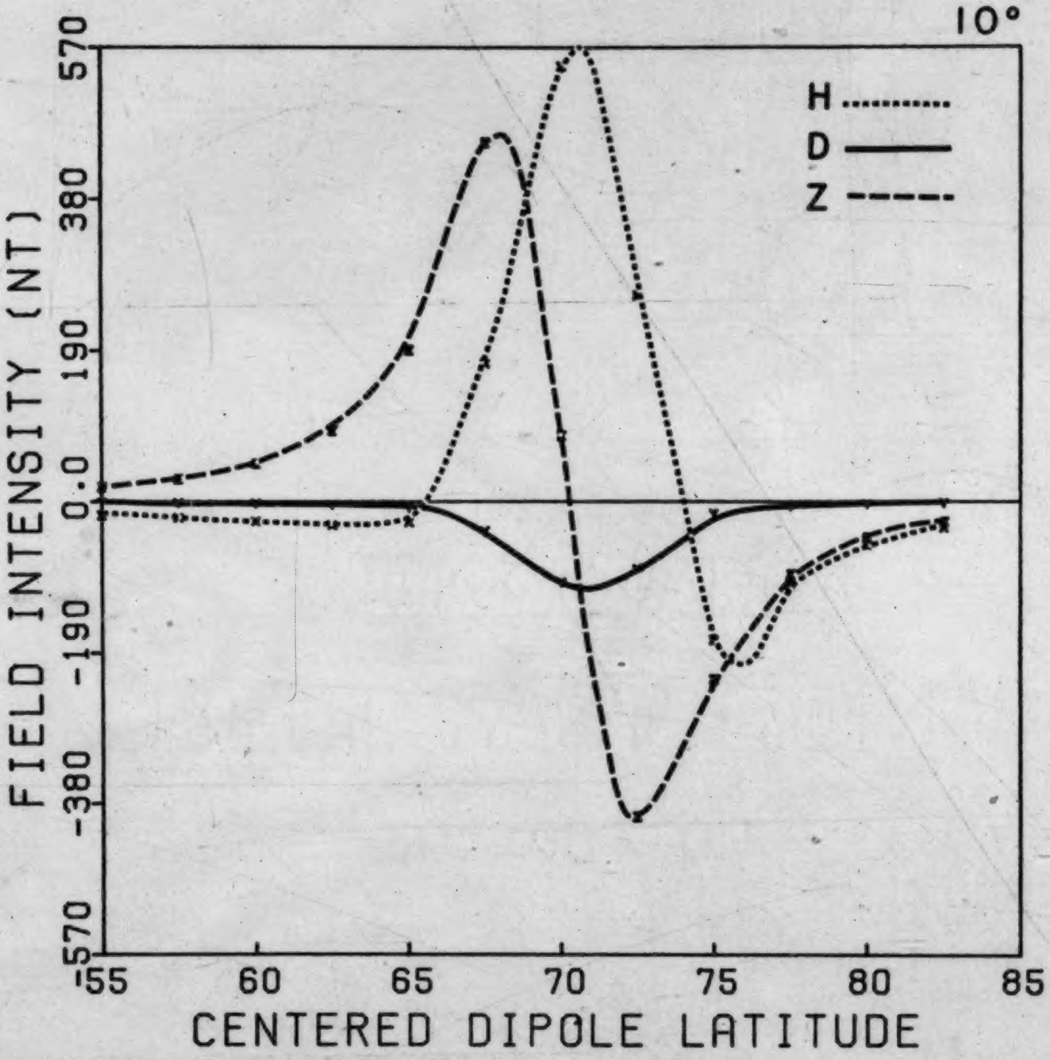
10°
H
D
Z
FIELD INTENSITY (NT)
570
380
190
0.0
-190
-380
-570
55
60
65
70
75
80
85
CENTERED DIPOLE LATITUDE

ionosphere along a magnetic field line at one longitude which flow up the field line into the magnetosphere at some other longitude. The magnetic perturbations which are produced by such currents are characterized by a level shift in the east-west component of the magnetic field across the latitudinal extent of the net current flow. Figure 2.7 is the latitude profile for net downward field-aligned current, distributed uniformly over 5° of latitude and 20° of longitude.

When recording magnetic data, one cannot easily separate the field perturbations due to ionospheric currents from those induced in the conducting earth. It has been useful in the past to attempt to compensate for this effect by modelling the earth by a sphere which is perfectly conducting up to some depth below the surface of the earth, and is an insulator above that depth (Boström,1969; Kisabeth,1972). This is only an approximation to the real situation, but has the advantage that the model is time independent, i.e., the nature of the induced field is not dependent upon the time variation of the external field. If an earth of finite conductivity is used, then one must be concerned with the skin depth which is frequency dependent, as well as the phase difference between the magnetic induction field and the induced electric field (which is also frequency dependent). For an infinitely conducting material, the skin depth and phase difference are constants. Kisabeth (1972) has presented results of this approach for

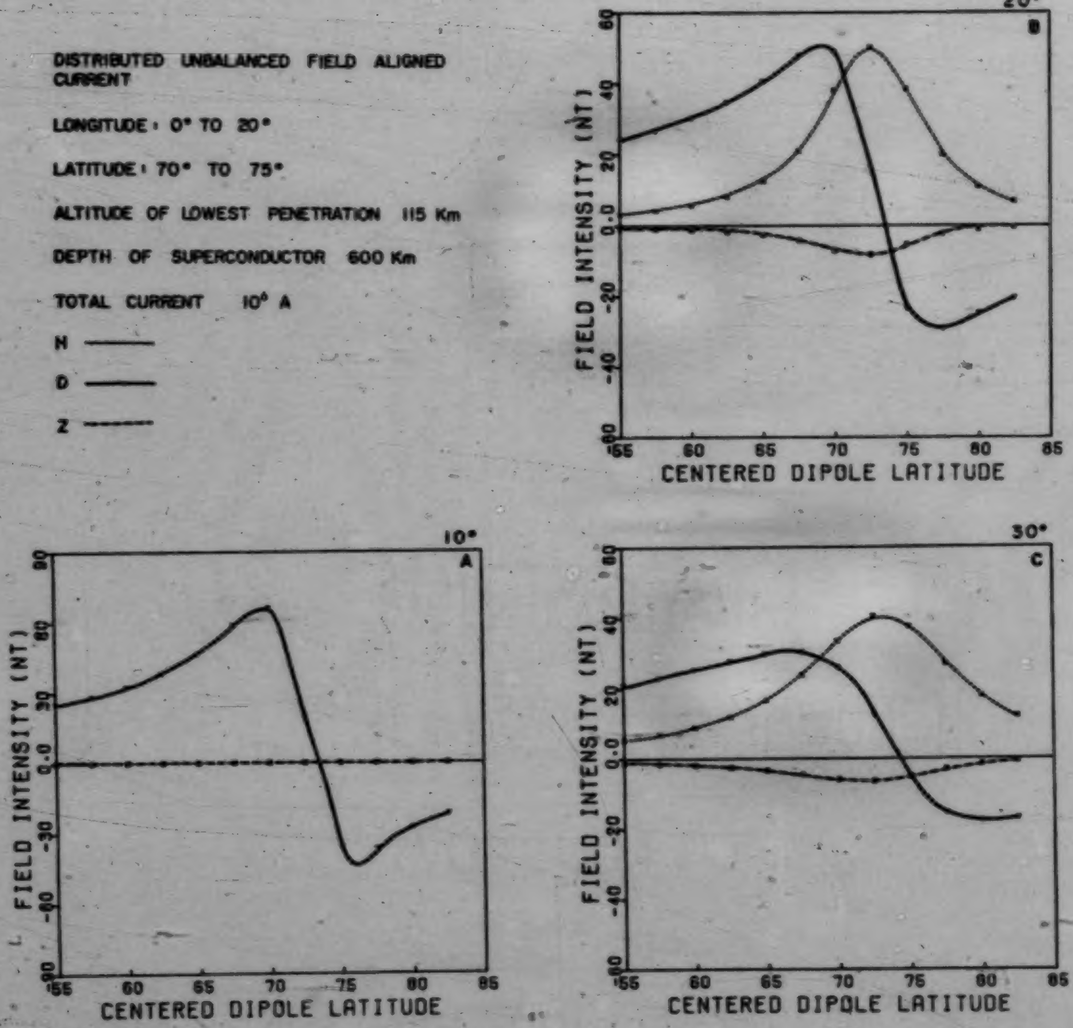

Figure 2.7 Model latitude profile for a downward field-aligned current distributed uniformly over 5° of latitude and 20° of longitude. A total of 10^6 A is flowing, and the profiles are taken at:

a) 10° east of the central meridian;
b) 20° east of the central meridian;
c) 30° east of the central meridian.

different depths of an infinite conductor, and these are reproduced in Figure 2.8 . It will be noted that the X'- and Y'-components are enhanced by the induction and the Z-component is reduced. Although this approach involves a rather risky approximation to the earth's conductivity structure, insufficient detail about the conductivity structure under the University of Alberta magnetometer line is known to warrant the use of techniques to separate the external and internal components of the perturbation field. However, it is believed that the techniques used by Kisabeth provide at least a first order correction to the data making any inferences drawn more reliable than they would have been were not some correction for induction taken into account.

The latitude profiles of real data presented in this thesis are smooth curves drawn through the data points. These curves are meant to serve as an aid to the eye and do not necessarily represent real data between the labelled points. However, the curves are drawn based on experience with a very large number of such profiles. Since the discussion of the data will be directed more towards the statistics of the samples rather than the individual events, it is believed that it is reasonable to discuss the profiles as drawn.

2.2.2 Polar plots

Although for analysis of the data it has been found that latitide profiles represent the preferred method of

Figure 2.8 Model latitude profiles showing the effect on the computed components of the perturbation magnetic field of placing a superconducting sphere at different depths. The panels on the left show the total field and those on the right the field due to the induction only. These profiles are for an east-west current loop, spanning the latitude range 65°N to 75°N. A total of 10^6 A is flowing over 20° of longitude. The profiles are taken 5° east of the central meridian. (After Kisabeth, 1972).

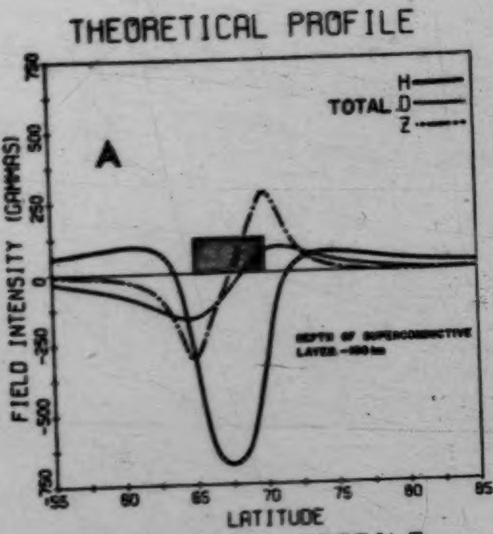
THEORETICAL PROFILE
A
H
TOTAL D
Z
FIELD INTENSITY (GAMMAS)
750
500
250
0
-250
-500
-750
DEPTH OF SUPERCONDUCTIVE LAYER - 100 km
55
60
65
70
75
80
85
LATITUDE

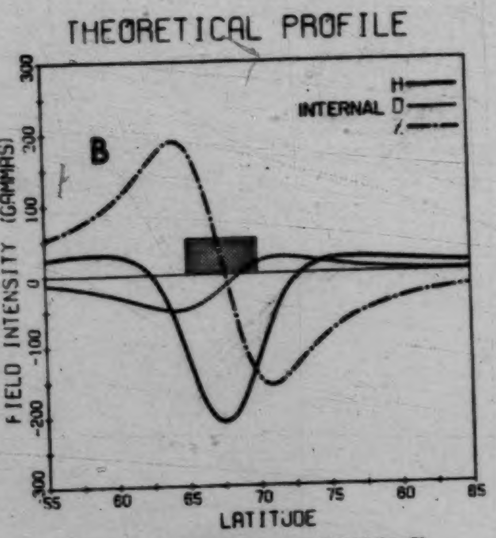
THEORETICAL PROFILE
B
H
INTERNAL D
Z
FIELD INTENSITY (GAMMAS)
300
200
100
0
-100
-200
-300
55
60
65
70
75
80
85
LATITUDE

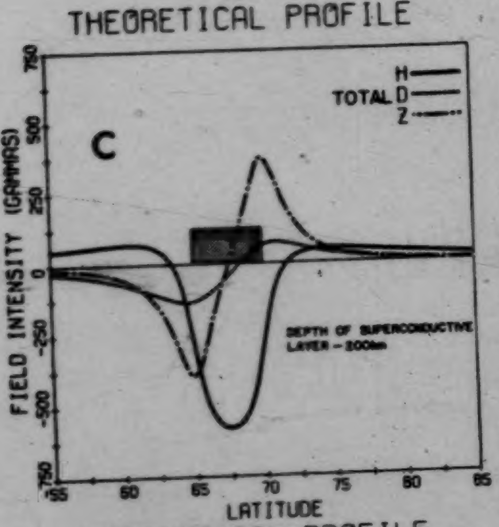
THEORETICAL PROFILE
C
H
TOTAL D
Z
FIELD INTENSITY (GAMMAS)
750
500
250
0
-250
-500
-750
DEPTH OF SUPERCONDUCTIVE LAYER - 200km
55
60
65
70
75
80
85
LATITUDE

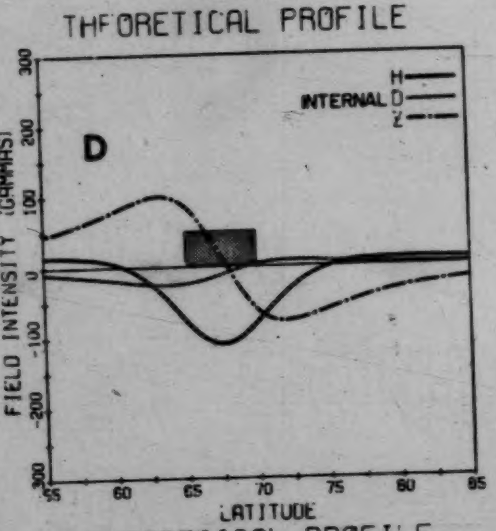
THEORETICAL PROFILE
D
H
INTERNAL D
Z
FIELD INTENSITY (GAMMAS)
300
200
100
0
-100
-200
-300
55
60
65
70
75
80
85
LATITUDE

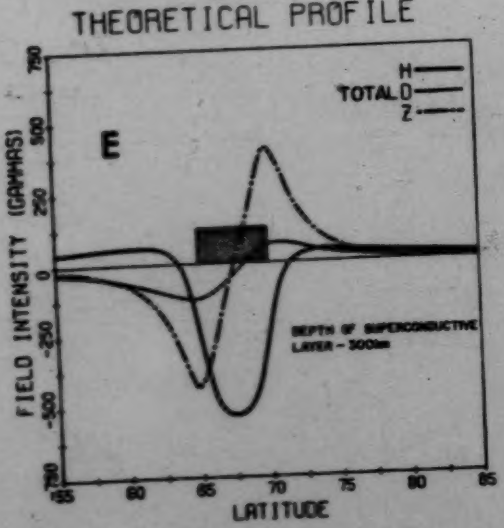
THEORETICAL PROFILE
E
H
TOTAL D
Z
FIELD INTENSITY (GAMMAS)
750
500
250
0
-250
-500
-750
DEPTH OF SUPERCONDUCTIVE LAYER - 300km
55
60
65
70
75
80
85
LATITUDE

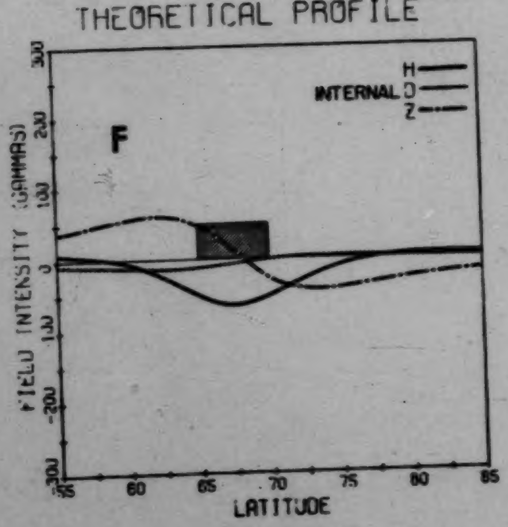
THEORETICAL PROFILE
F
H
INTERNAL D
Z
FIELD INTENSITY (GAMMAS)
300
200
100
0
-100
-200
-300
55
60
65
70
75
80
85
LATITUDE

data presentation, frequently in auroral physics, current systems are displayed in polar plots. In this thesis, this method of displaying the data and model results will be used on occasion. In these plots, the horizontal magnetic field vector has been rotated through 90° so as to represent an equivalent horizontal current, and the equivalent current vectors have magnitudes proportional to the strength of the magnetic perturbation. Note that the equivalent currents do not necessarily represent real currents; some portion of the observed magnetic perturbations arises due to field-aligned currents which link the ionosphere to the outer magnetosphere. However, this presentation permits easy comparison of the results of this study with some earlier work in which equivalent ionospheric current systems have been used.

2.3 Discussion of Inversion Theory

Appendix II describes briefly Backus-Gilbert linear inversion theory, and more detail may be obtained from the published papers on this topic (Backus and Gilbert, 1967, 1970), and a recent review by Parker (1977). However, it should be emphasized that considerable care must be exercised when interpreting the results of an inversion and in particular when using the results of a "model that fits the data". As pointed out in the Appendix, one must be able to forward model the data before it can be successfully inverted. In the case of inverting magnetic latitude profiles, one must have a current model which will reproduce the observations of the magnetic field, subject only to finding the correct latitudinal current distribution.

To demonstate this, a latitude profile was generated for a hypothetical eastward flowing current with a 4° latitudinal extent (colatitude 20° to 24°) and a 20° longitudinal extent. (Figure 2.9). The current was uniform in latitude and closed along field lines via an equatorial ring current. The profile thus obtained was inverted for the current density, subject to different model parameters.

In the ideal case, the geometry of the current system is exactly known, as are all the currents whose fields contribute to the profile. If the data of Figure 2.9 are inverted, and the correct parameters (i.e., the correct current boundaries) are supplied to the computer code, then the result is as shown in Figure 2.10. The solid line is the average $\langle J(\theta) \rangle$, and the broken line is the so-called flattest model (see Appendix II). In this example, the average agrees exactly with the known current distribution, as there are errors neither in the data nor in the supplied parameters. The flattest model, which is only one of an infinite set of models which may fit the data has been constrained to have zero current intensity at the latitudinal extrema, and in order to fit the observations, this constraint introduces spatial oscillations into the model.

The results of a second inversion of the data is shown

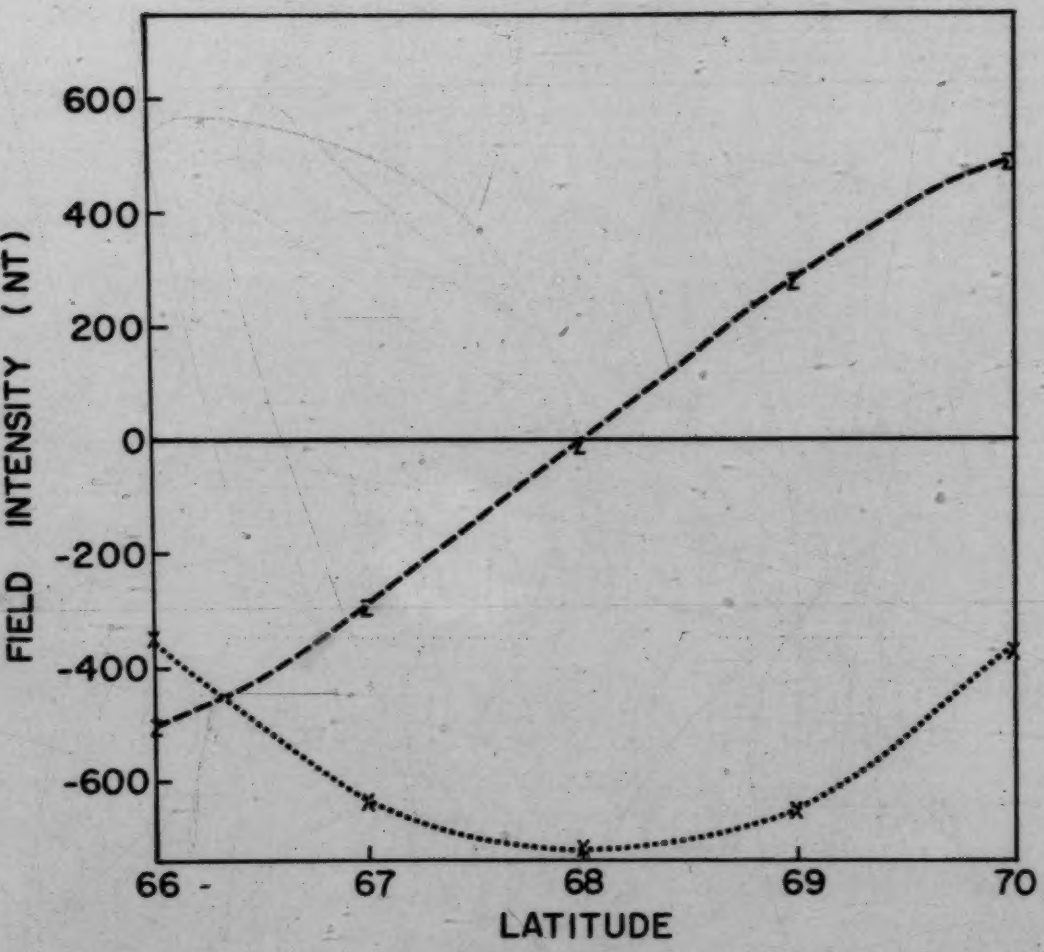

Figure 2.9 A model latitude profile demonstrating the inversion of magnetic data to obtain height-integrated current density (current intensity) as a function of latitude. A total current of 10^6 A was distributed uniformly over 4° (66°N to 70°N) of latitude for a current intensity of 2.22 Am^{-1}.

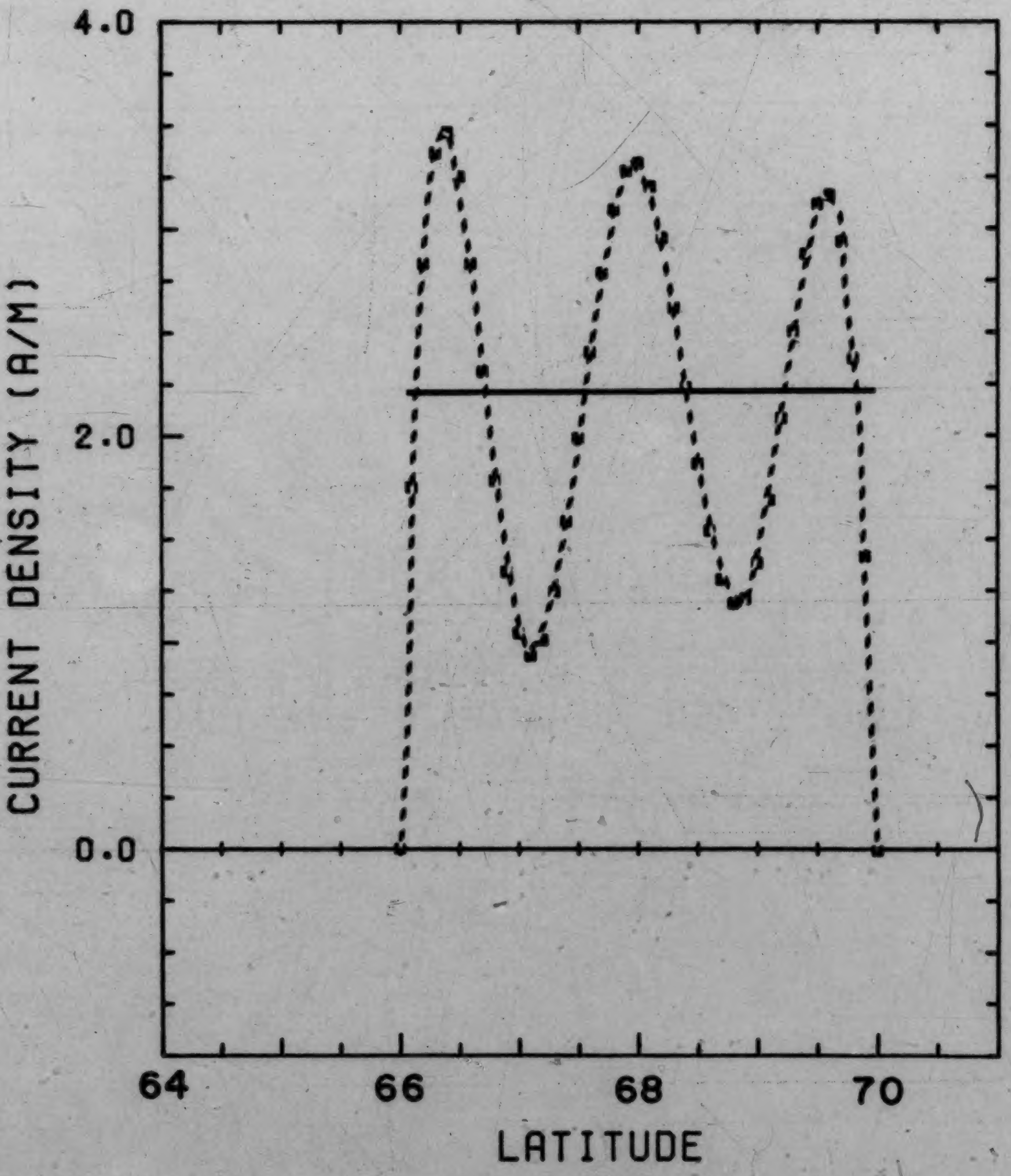

Figure 2.10 Result of inverting the data shown in Figure 2.9. The solid line is the curve of <J(θ)>, the average current intensity. The dashed line is the current intensity for the flattest model. In this example, the current limits were set to 66°N and 70°N.

in Figure 2.11. In this case the constraints on the latitudinal extent have been relaxed, and this allows the flattest model to fit the data while still permitting zero current at the poleward and equatorward borders. In this case the model approximates the known current distribution. However, the current estimate no longer yields an exact current density, because by supplying the computer code with a latitudinal extent that is wider than that used to generate the data, the inversion puts current into a region where in reality there is no current, thus causing an overall degradation of the result.

Finally, the data of Figure 2.9 were inverted assuming that no field-aligned current or ring current contributed to the profile. Although this is not physically realistic, it serves to demonstrate the effect of using an incorrect model, or, alternatively, of errors in the data. For these results (Figure 2.12), $<J(\theta)>$ is reduced because less current is required to produce the magnetic field perturbations if the field-aligned and ring current contributions are ignored. The flattest model in this example consists of large amplitude spatial oscillations, and bears little resemblence to the known current intensity distribution.

These examples serve to demonstrate several features of the inverse problem. In the first place, each of the flattest models of current distribution, if used in the forward problem, will generate $\Delta X'$ and ΔZ profiles in good

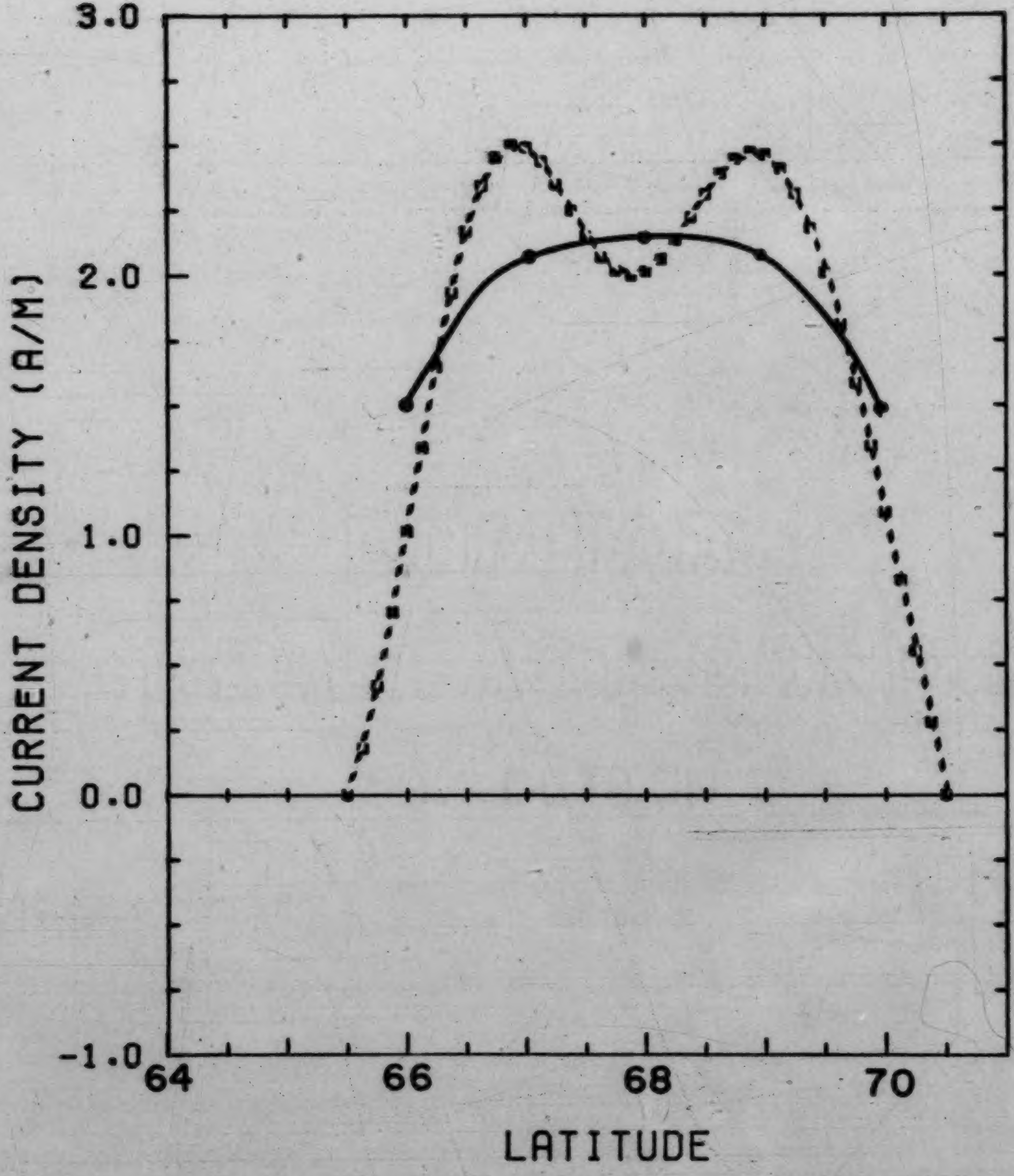

Figure 2.11 Similar to Figure 2.10. The constraint on the current limits has been relaxed to the latitude range 65.5°N to 70.5°N.

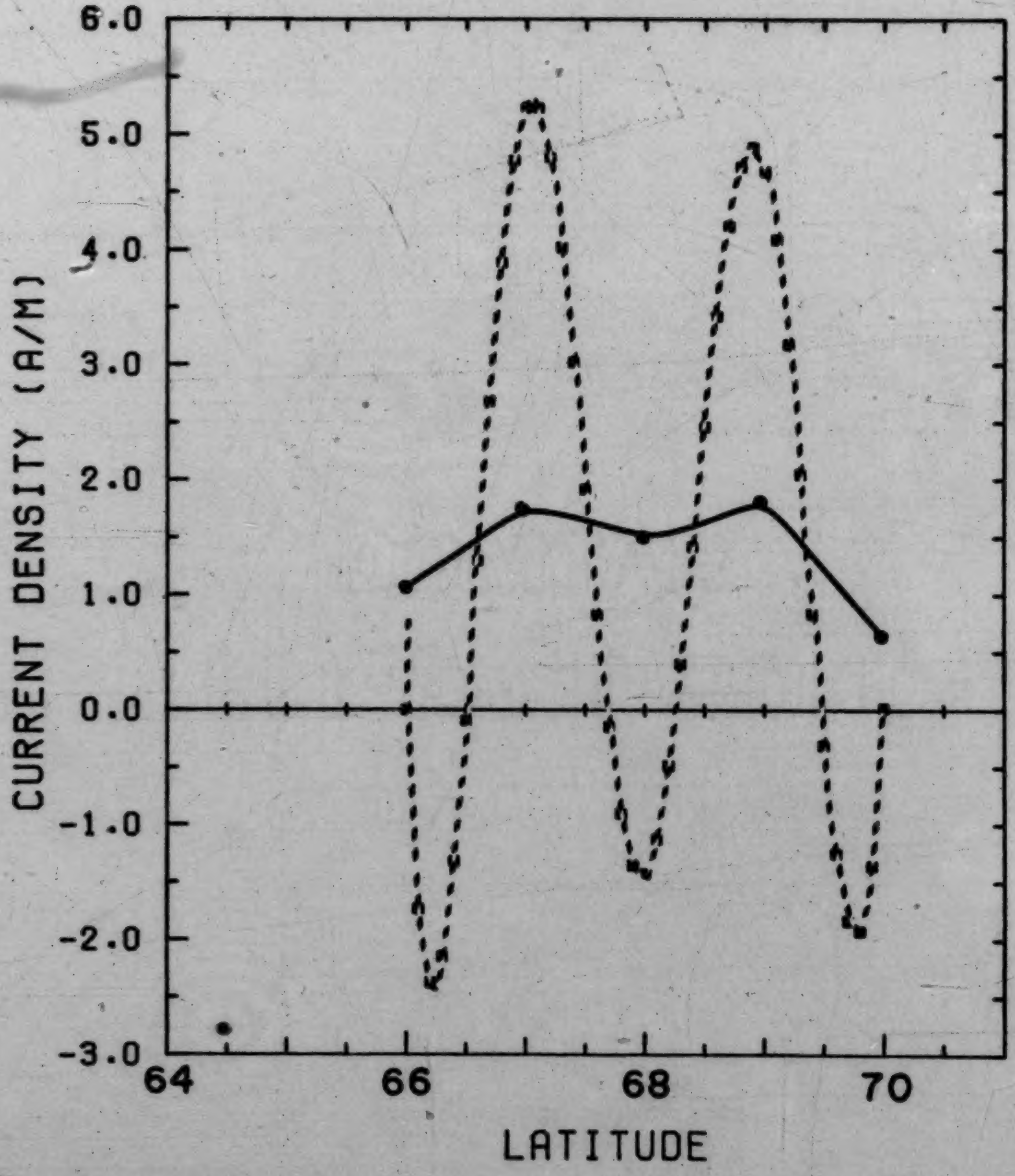

Figure 2.12 Similar to Figure 2.11. In this example, it was assumed that there was no field-aligned or ring current contributing to the magnetic field.

agreement with the hypothetical observations (Figure 2.13). However, each of these models differ in character demonstrating the non-uniqueness of the problem. Choice of an incorrect forward model can lead to grossly incorrect models that fit the data, although the unique average, $<J(\theta)>$ (i.e., unique for a given set of parameters) in all cases gives a not unreasonable current distribution. Errors in the data do not grossly affect the result of the inversion of the latitude profiles. Errors in the data may arise from statistical considerations or systematic data collection errors. However, if an incorrect forward model is chosen, or the parameters are incorrectly specified, then, relative to that model, the data are in error as well. If the data of Figure 2.9 had been real data, and had been inverted using incorrect model parameters, then the result of Figure 2.12 could have been obtained. The fit to the data is very good (the root mean square relative error is less than 0.1%). Given no a priori knowledge of the nature of the current distribution, this model might be acceptable. During periods of strong magnetospheric activity, ionospheric conductivity and electric fields may become quite intense in spatially localized regions, and in such cases, one might not expect a smooth current distribution. However, the data suite used in this thesis consists of hourly averaged data, and the averaging process will tend to smooth out intense latitudinally localized auroral variations. This assumption together with the knowledge of how spatially oscillatory

Figure 2.13 Comparison of the model data from Figure 2.9 with that calculated from the flattest model current distribution.

a) Results from the flattest model of Figure 2.10.

b) Results from the flattest model of Figure 2.11.

c) Results from the flattest model of Figure 2.12.

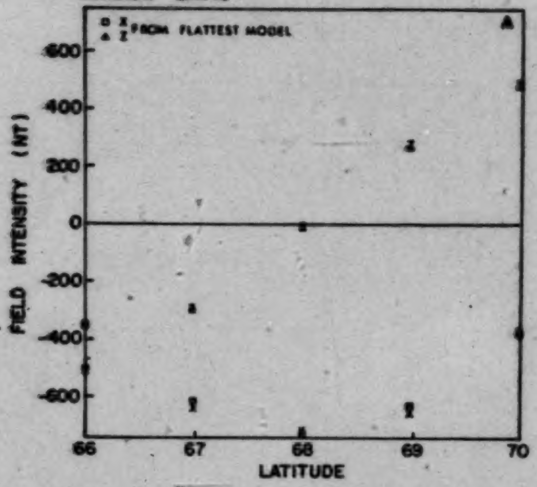

NARROW LIMITS

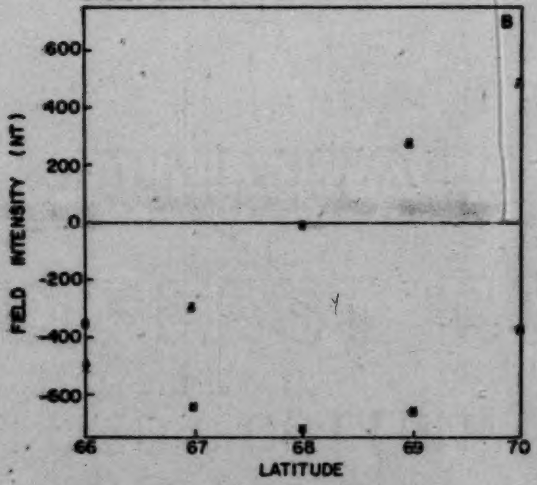

BROAD LIMITS

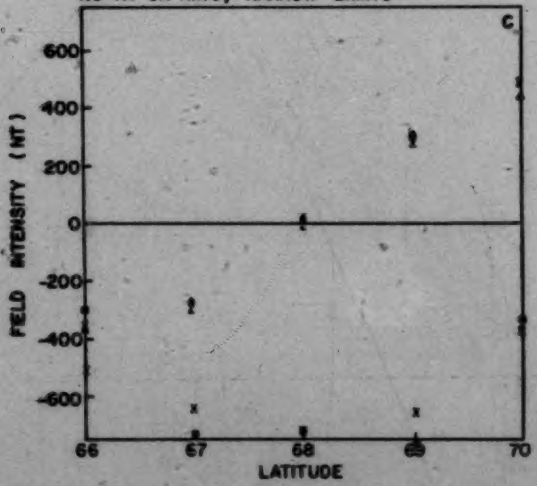

NO FA OR RING, NARROW LIMITS

models may arise justifies the search for smooth current distributions, and this criterion was applied to the inversion results to test the correctness of the forward model.

2.4 Superposed Epoch Analysis

Although the latitude profiles used in this study consist of data points which are averages, and although profiles from a given hour have very similar qualitative characteristics from day to day, there is still an unavoidable variability which is difficult to quantify. In order to obtain what might be called a set of generalized latitude profiles which would facilitate modelling of the source current systems, the method of superposed epoch analysis(SPEA) was used (Chree,1912,1913). That is, latitude profiles for the same hourly interval on each day were examined for a common feature, the latitudinal reference point. Values of each curve on each profile were then obtained at angular distances of ±5, ±10, ±15 degrees from the reference point. In this study, the reference point was the peak value of the negative X'-component in the pre-noon sector and the peak value of the positive X'-component in the post-noon sector. In the noon sector, the X'-component was not well defined, and the reference point was chosen as the base of the Y'-component ramp that was always observed in this sector. Averages were then computed for each component at each relative latitude. The resulting profiles, one for each hour of the day, are what will be called the SPEA latitude profiles. Note that the SPEA profiles involve a fair degree of subjectivity. That is, curves were drawn through the data points of the original averaged latitude profiles, and as pointed out earlier, these curves are drawn subject to a certain degree of subjectivity, although the curves do pass through each data point, and are constructed with the characteristic behaviour of typically observed profiles studied over several years in mind.

There is obviously a severe problem in presenting large data suites in which subsets of the data demonstrate qualitatively similar features. The actual number of data points used in this thesis is of the order of 5.4×10^7, and it would be unreasonable to present each of these. The superposed epoch technique allows one to show a large amount of data concisely, although it must be borne in mind that the method is designed to enhance certain features of the data. In addition, the SPEA may mask other features of the data. For example, consider the latitude profile shown in Figure 2.6. When it is digitized as described above, in 5° steps away from the $\Delta X'$ peak as reference point, the ΔZ extrema do not fall at digitization points. In fact, the resulting profile has Z-component extrema 10° apart (Figure 2.14), giving the impression of an electrojet that is 10° in latitudinal extent. In other words, a 5° digitization increment is insufficient to resolve features less than or equal to 5° apart. However, the SPEA profiles will be used

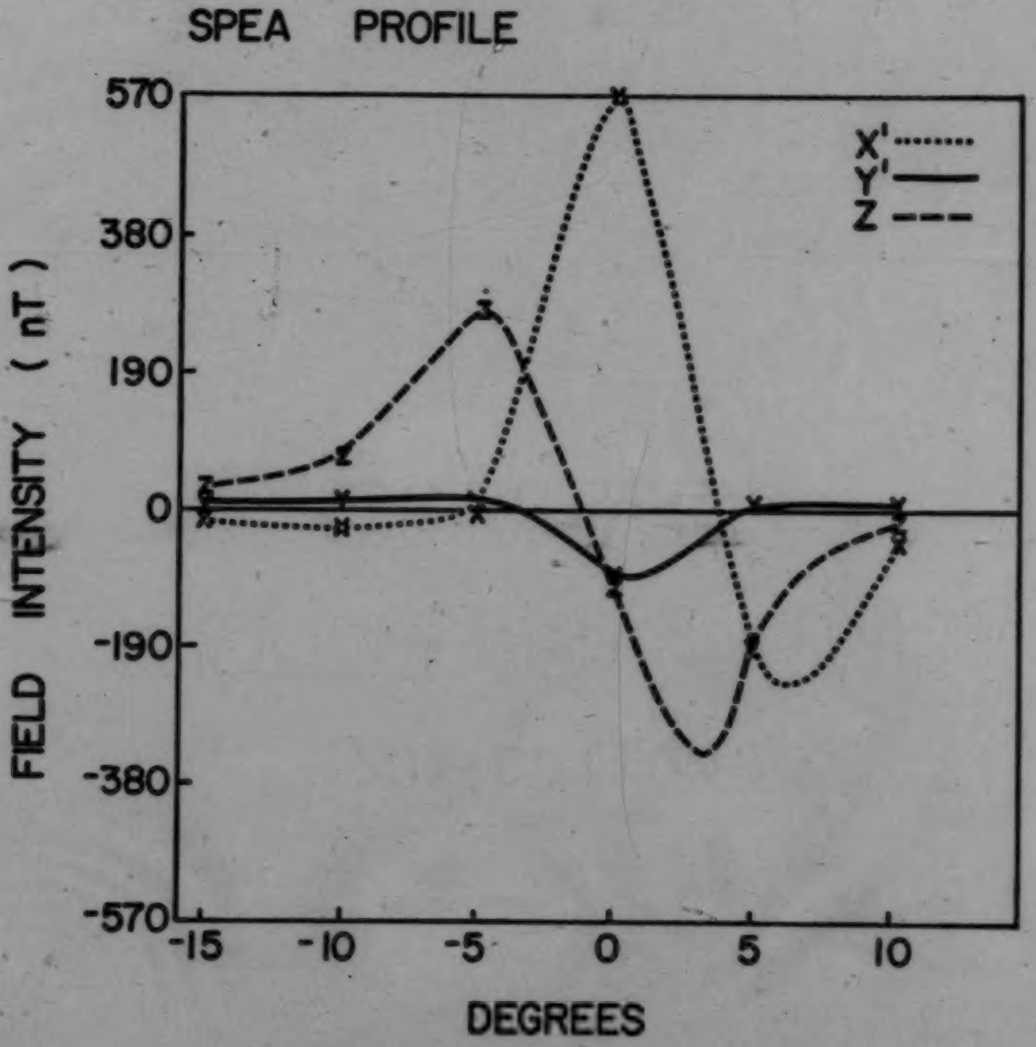

Figure 2.14 The latitude profile that results from digitizing Figure 2.6 at 5° intervals away from the peak in the X'-component. Note that the ΔZ extrema appear more widely separated than in Figure 2.6, although the character of ΔX' and ΔY' remain essentially the same.

primarily to provide estimates of the magnitude of the X'-component peak value, and the size of the level shift in the Y'-component. Neither one nor the other of these are affected by the 5° digitization step.

CHAPTER 3 RESULTS OF DATA ANALYSIS

3.1 Description of the Data

For this study, latitude profiles from hourly averaged values (centered on the half hour) of X', Y', and Z, were generated for the period from Day 332, 1971, to Day 24, 1972. Since the absolute field is not measured, baseline values were required from which to measure the magnetic field perturbations. To this end, values of the three components at each station were determined over the hourly interval 0500-0600 universal time (UT) (i.e., approximately 2100-2200 magnetic local time (MLT)) on days during which the observed magnetic field exhibited only small perturbations during the day (a so-called "quiet" day). For the data suite in this study, baseline values were chosen on Day 345, 1971 ($\sum$ Kp=10+) and Day 7, 1972 ($\sum$ Kp=7-) and these baselines were used over an interval of ±2 weeks.

Single station magnetograms for the entire period of this study were examined for obvious drifts in the baseline values. When they were detected, a straight line was fitted through the data for the period during which drift occurred, and the data were then referenced to this line before removing the quiet day baselines. For example, from Day 357, 1971 to Day 15, 1972 at Fort Smith, the X'-component showed an approximately linear drift of 425 nT, the Y'-component a drift of 150 nT, and the Z-component a drift of -60 nT. Similarly, the data from Leduc exhibited drifts of 670 nT in the X'-component, 150 nT in the Y'-component, and -150 nT in the Z-component over the time period from Day 341, 1971 to Day 350, 1971. All the other stations had stable baselines during the observation period.

In this chapter, a description of typical latitude profiles as a function of time will be presented, and a phenomenological model of the currents as inferred from this data will be developed.

3.2 Statistical Characterization of the Data Suite

Examination of the entire data suite led to a decomposition of each day into several sectors, each characterized by its own type of latitude profile.

3.2.1 The 2200 - 0200 MLT Regime

The first such sector or regime spans the period from about 2200 MLT to about 0200 MLT, across the region of the Harang discontinuity. Representative profiles from each of the 4 hourly intervals are shown in Figures 3.1(a,b,c,d). It is evident from these profiles that there is a great variability in the magnitudes of the average perturbations. In spite of this, in general, $\Delta X'$ and ΔZ in this regime are indicative of either westward flowing current, or both eastward and westward flowing current. It is probable that the magnetometer line senses end effects of electrojets which are not directly overhead, so that a signature such as that shown in Figure 3.1(a), where $\Delta X'$ undergoes a sign

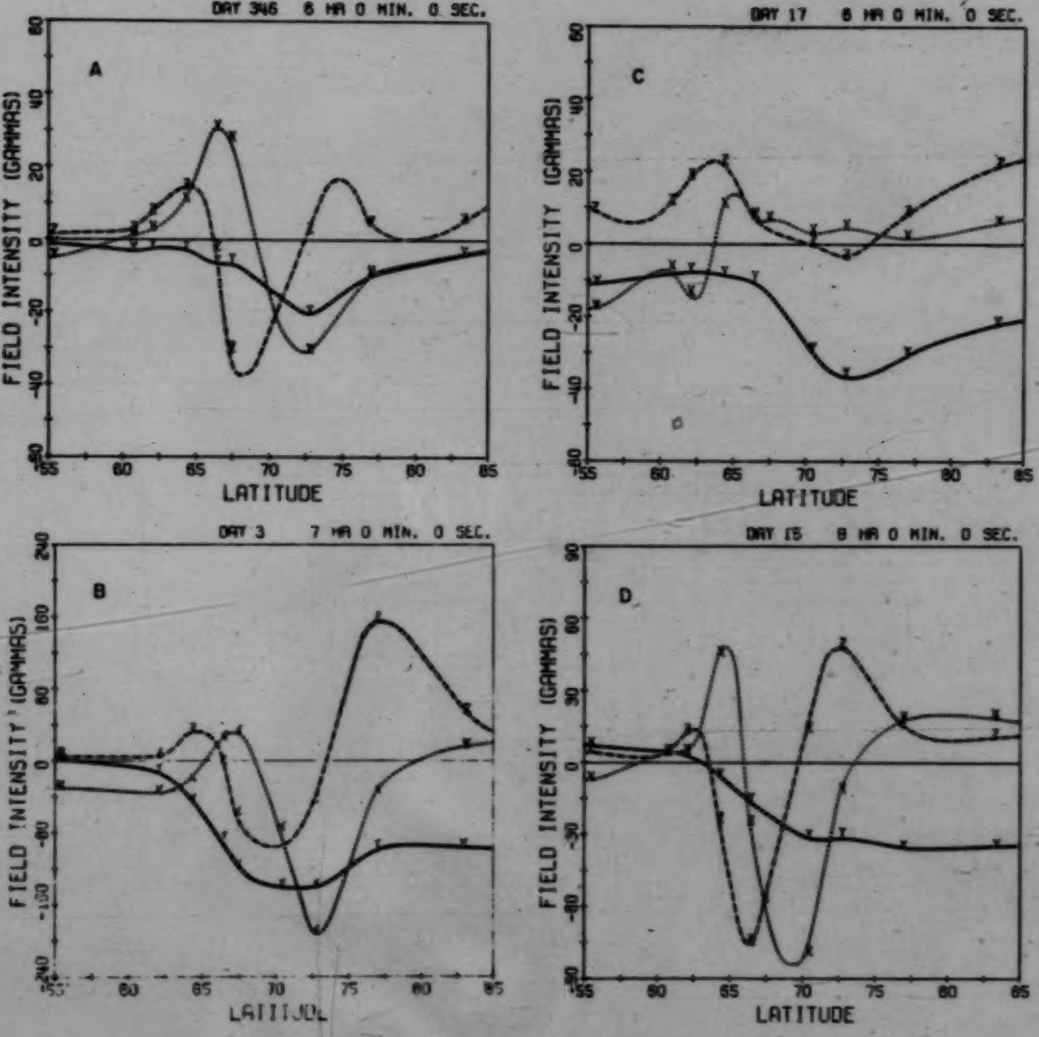

Figure 3.1 Representative hourly average latitude profiles for the hours:

(a) 2200-2300 MLT (0600-0700 UT)
(b) 2300-2400 MLT (0700-0800 UT)
(c) 0000-0100 MLT (0800-0900 UT)
(d) 0100-0200 MLT (0900-1000 UT)

change does not necessarily mean that both eastward and westward currents are flowing directly over the magnetometer line. Rather, for example, eastward flowing current may exist to the west of the line while westward flowing current flows directly overhead. However, regardless of the nature of the X'- and Z-component profiles in this time sector, the $\Delta Y'$ signature is distinctive in that it is negative across the entire auroral oval. Also, there is usually a step-like character to $\Delta Y'$ at the equatorward border of the oval, as is shown in each panel of Figure 3.1.

The SPEA of all the data for this regime (Figure 3.2) demonstrates the above characteristics as well. As will be discussed later, negative $\Delta Y'$ signature is interpreted as the result of poleward flowing Hall current diverging poleward within the eastward and westward electrojets.

3.2.2 The 0200 - 1000 MLT Regime

The second distinctive regime spans the dawn meridian, lying between approximately 0200 MLT and 1000 MLT (about 1000 to 1800 UT). This time period is dominated by the westward electrojet, although frequently there is an indication of a weak eastward flowing current equatorward of the westward electrojet particularly during recovery from periods of enhanced magnetospheric activity (Rostoker and Hron, 1975). Figures 3.3(a) through 3.3(h) are typical examples of latitude profiles from each hour of this regime. The interval from 0200 to 0300 MLT (Figure 3.3(a)) is

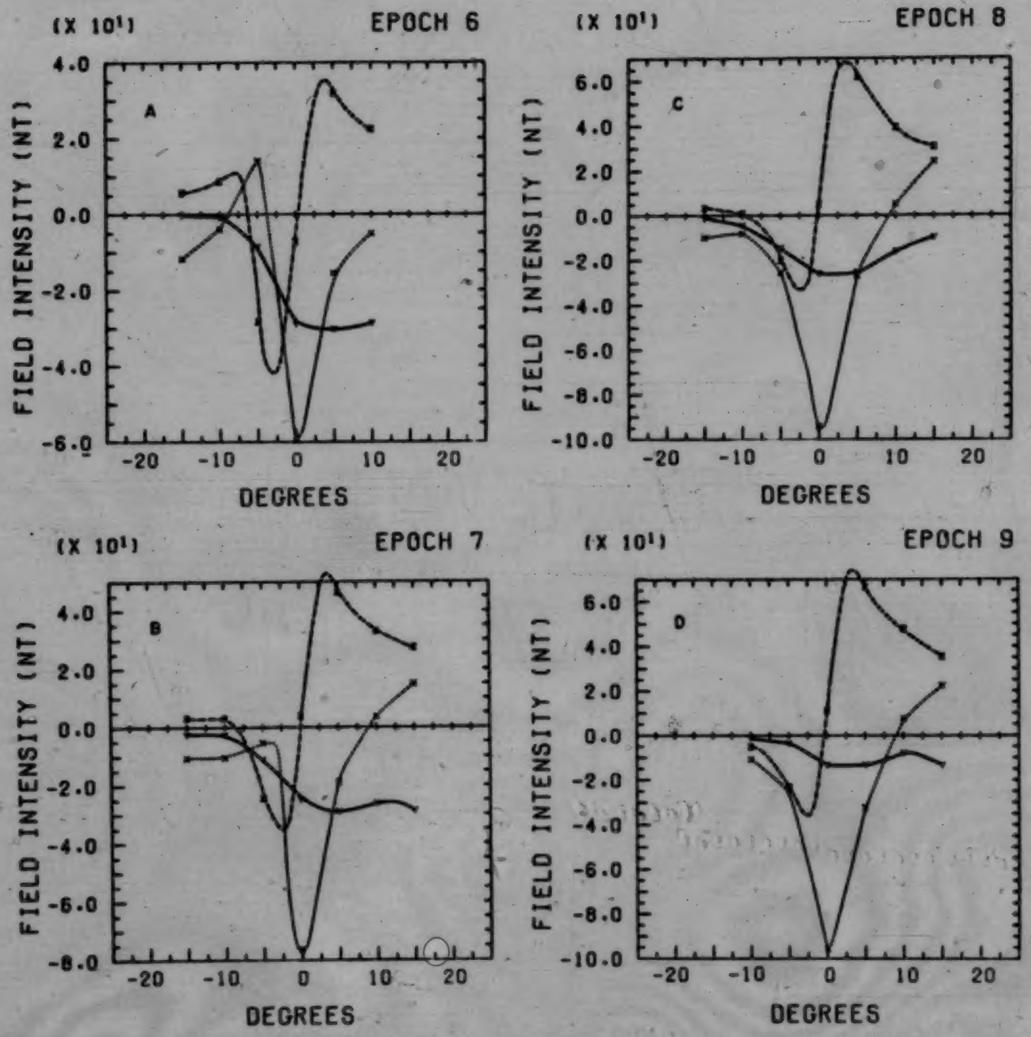

Figure 3.2 Superposed epoch analysis of the hourly averaged latitude profiles for the hours:
(a) 2200-2300 MLT (0600-0700 UT)
(b) 2300-2400 MLT (0700-0800 UT)
(c) 0000-0100 MLT (0800-0900 UT)
(d) 0100-0200 MLT (0900-1000 UT)

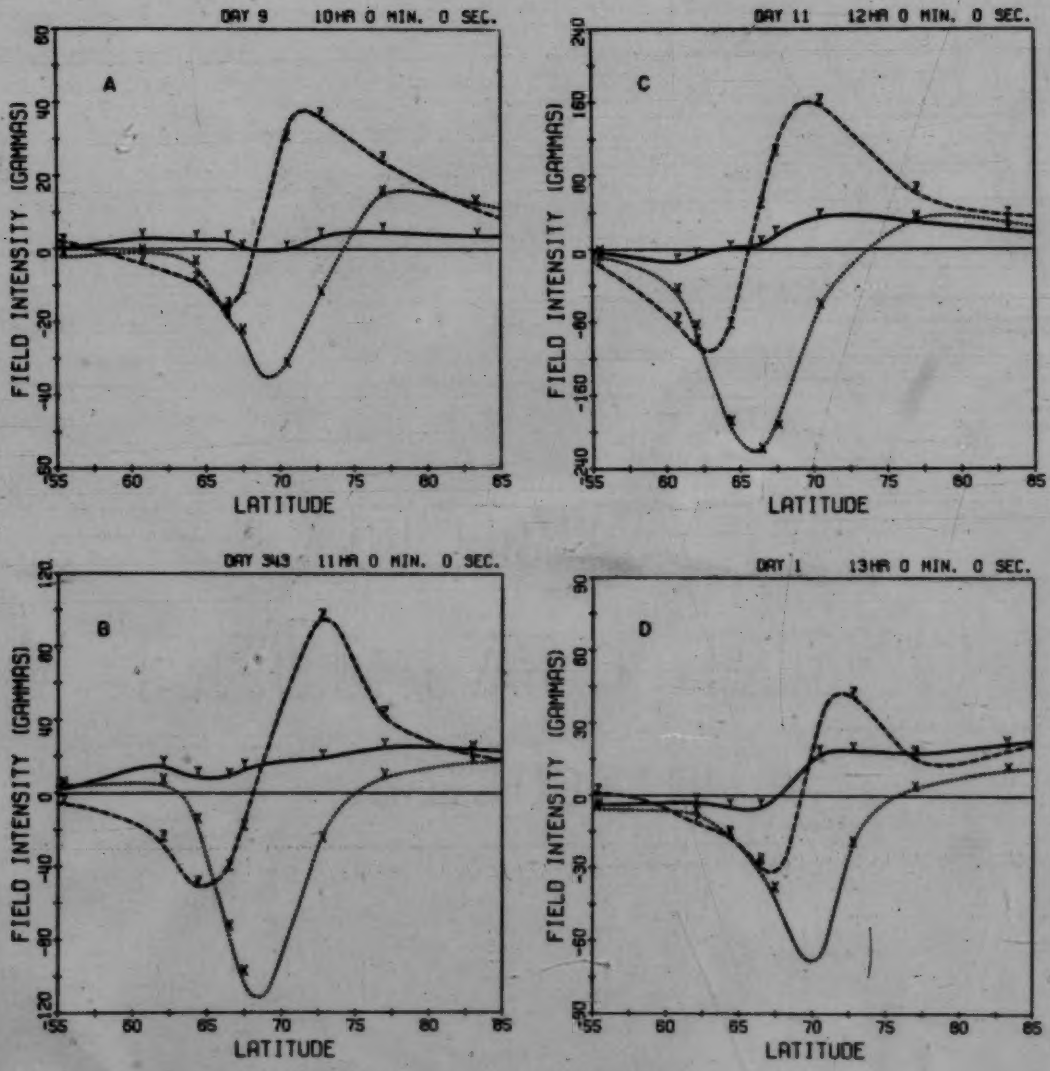

Figure 3.3 Representative hourly average latitude profiles for the hours:

(a) 0200-0300 MLT (1000-1100 UT)
(b) 0300-0400 MLT (1100-1200 UT)
(c) 0400-0500 MLT (1200-1300 UT)
(d) 0500-0600 MLT (1300-1400 UT)

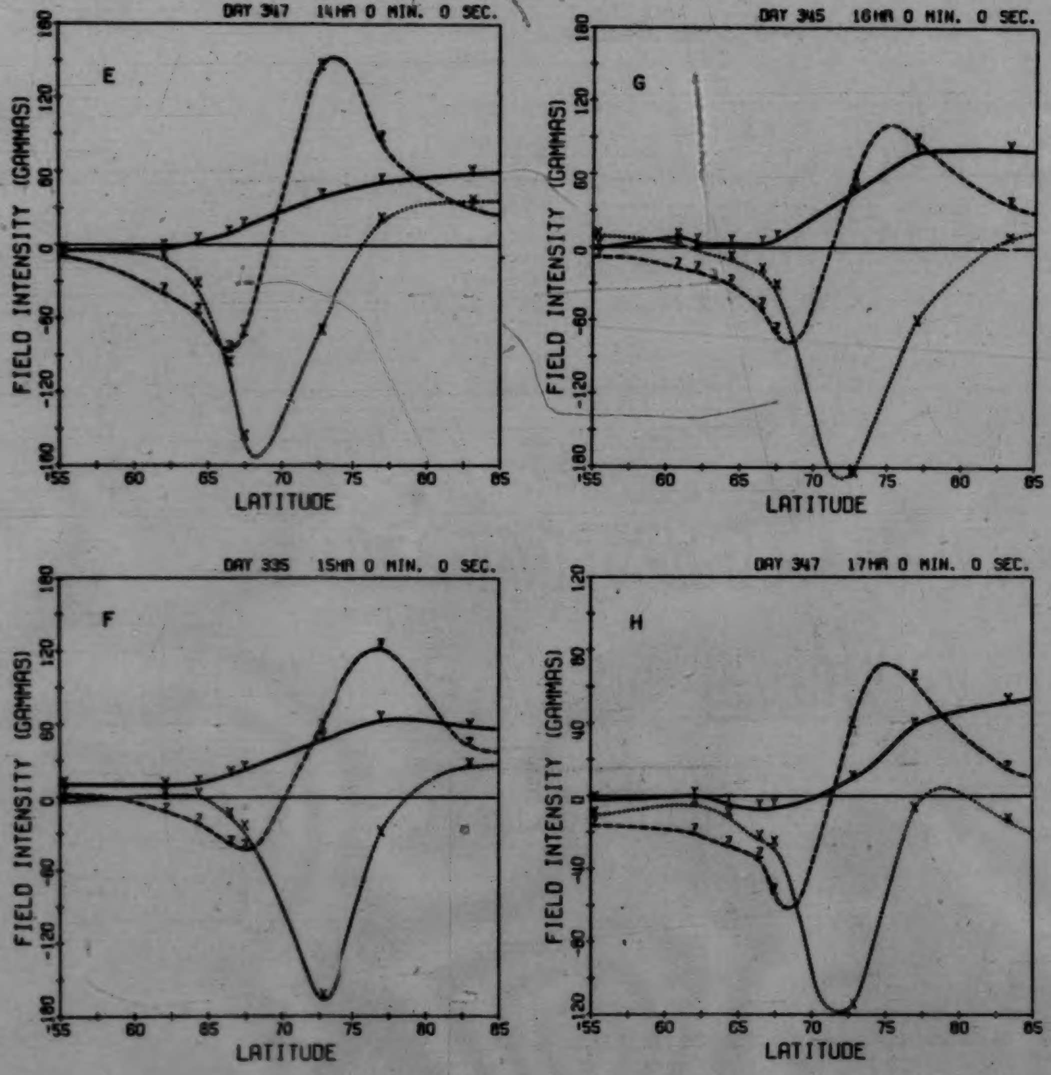

Figure 3.3 Representative hourly average latitude profiles for the hours:
(e) 0600-0700 MLT (1400-1500 UT)
(f) 0700-0800 MLT (1500-1600 UT)
(g) 0800-0900 MLT (1600-1700 UT)
(h) 0900-1000 MLT (1700-1800 UT)

characterized by a predominately positive $\Delta Y'$ profile and a weak or non-existent level shift across the electrojet region in this same component. The SPEA profile (Figure 3.4(a)) demonstrates that, on average, there is a level shift in the Y'-component, although Figure 3.3(a) does not show this. The $\Delta X'$ profile is consistent with a westward electrojet combined with an equatorward flowing north-south current system. This latter is suggested by the positive $\Delta X'$ in the poleward part of the profile. Note that the Z-component is asymmetric about the horizontal axis in that the positive extremum is greater than the negative extremum. This feature is characteristic of this time sector, and is consistent with observations reported by Langel (1974a, 1974b) of the perturbation magnetic field observed at high latitudes by the polar orbiting satellites Ogo 2, Ogo 4, and Ogo 6.

Figure 3.3(b) is a profile for the interval 1100 to 1200 UT (approximately 0300 to 0400 MLT). Qualitatively, it does not differ significantly from the previous latitude profile. The SPEA profile for this interval (Figure 3.4(b)) is also similar to that for the previous hour although there is a more distinct level shift in the Y'-component.

The next hourly interval (1200-1300 UT; 0400-0500 MLT; Figure 3.3(c)) shows a clear level shift in the Y'-component although it is small relative to the maximum $\Delta X'$ perturbation. This level shift, and its relative magnitude is preserved in the SPEA profile shown in Figure 3.4(c)

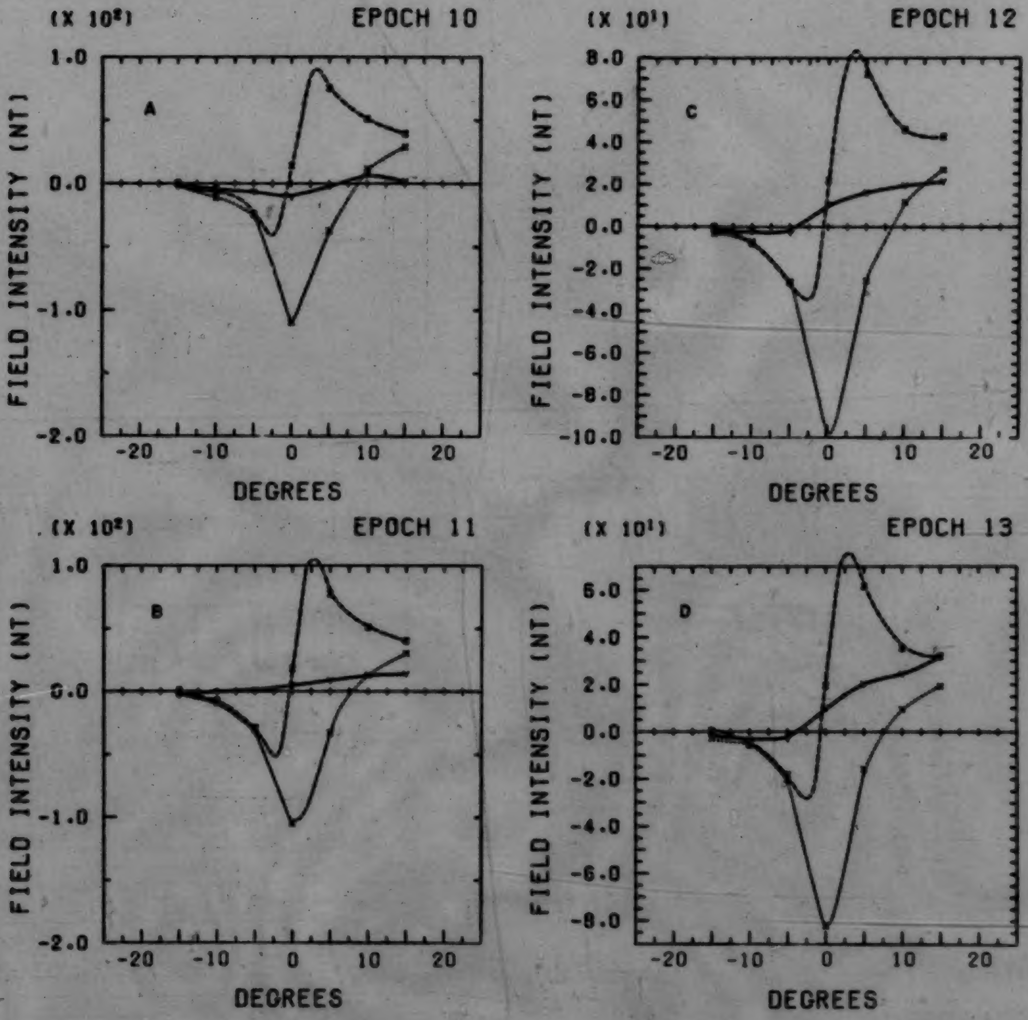

Figure 3.4 Superposed epoch analysis of the hourly averaged latitude profiles for the hours:

(a) 0200-0300 MLT (1000-1100 UT)
(b) 0300-0400 MLT (1100-1200 UT)
(c) 0400-0500 MLT (1200-1300 UT)
(d) 0500-0600 MLT (1300-1400 UT)

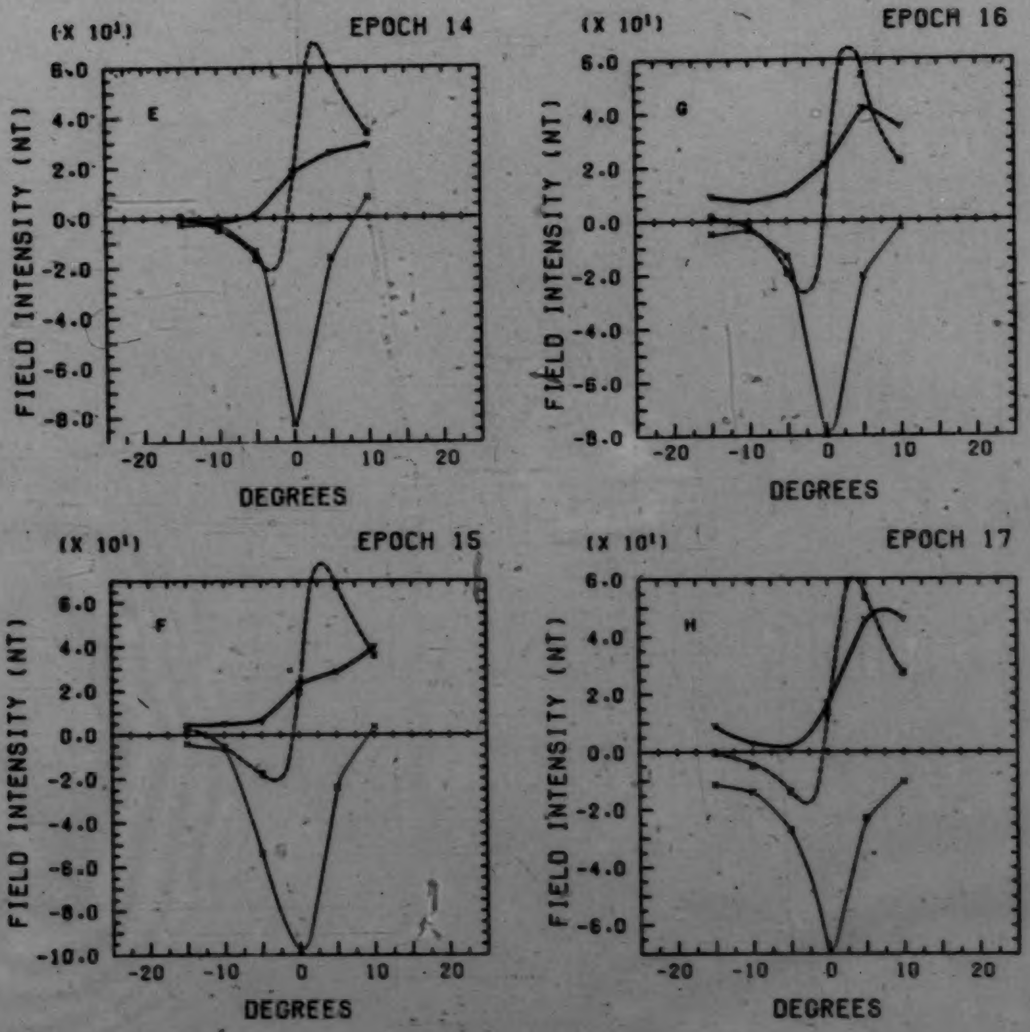

Figure 3.4 Superposed epoch analysis of the hourly averaged latitude profiles for the hours:
(e) 0600-0700 MLT (1400-1500 UT)
(f) 0700-0800 MLT (1500-1600 UT)
(g) 0800-0900 MLT (1600-1700 UT)
(h) 0900-1000 MLT (1700-1800 UT)

In fact, the remainder of the panels in Figure 3.3 are not unlike Figure 3.3(c) insofar as they all indicate an indisputable level shift in the Y'-component. As well, this shift increases in magnitude relative to the X'-component negative extremum as the local time of the profiles approaches noon. Also, the asymmetry in the Z-component that was described above persists as a general feature. The remainder of the SPEA latitude profiles in Figure 3.4 bear out this description as a general feature of this entire magnetic local time sector.

3.2.3 The 1000 - 1400 MLT Regime

The third distinctive region which has been delineated spans local magnetic noon from about 1000 MLT to 1400 MLT (1800 UT to 2200 UT). This region corresponds to the "zone of confusion" identified by Harang (1946). An examination of latitude profiles from this sector bears out this description. Figure 3.5 shows a series of latitude profiles for the same day from 1000 MLT to 1400 MLT. The Z-component in Figure 3.5(a) is consistent with a weak eastward flowing current centered at about 67.5° N, and a stronger westward flowing current centered at about 73° N. However, the X'-component profile is not consistent with this. Similarly, the Z- and X'-components in Figure 3.5(b) are not consistent with any simple eastward/westward electrojet interpretation. Indeed, none of the profiles in Figure 3.5 can be interpreted in any simple way, and this difficulty exists on

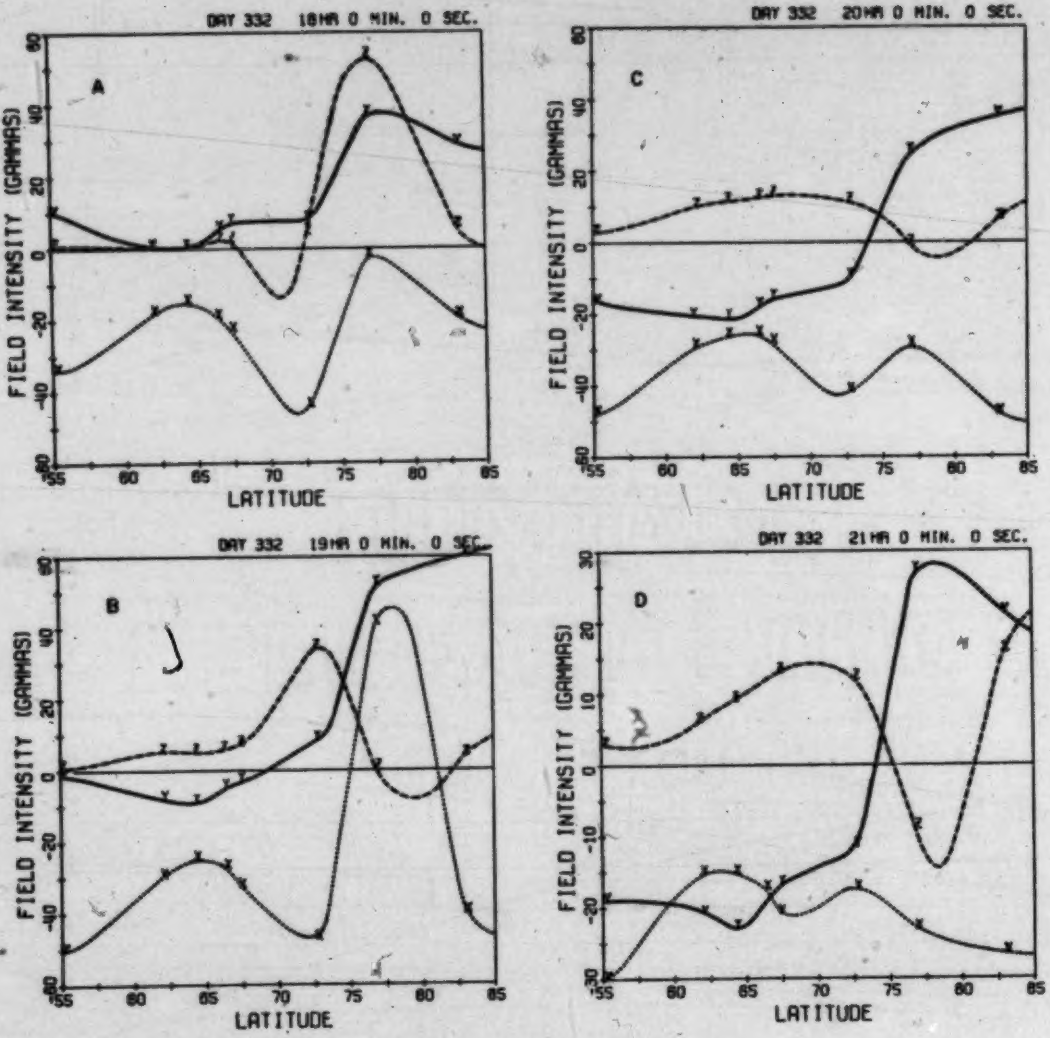

Figure 3.5 Representative hourly average latitude profiles for the hours:
(a) 1000-1100 MLT (1800-1900 UT)
(b) 1100-1200 MLT (1900-2000 UT)
(c) 1200-1300 MLT (2000-2100 UT)
(d) 1300-1400 MLT (2100-2200 UT)

all days examined in this sector. The one feature that appears consistently in the latitude profiles from this region is the clear, relatively large positive-going level shift in the Y'-component.

The SPEA of the profiles from 1000 to 1400 MLT (Figure 3.6(a,b,c,d)) is very difficult to explain in terms of any simple east-west current flows. However, again the level shift in $\Delta Y'$ is brought out clearly, as is the overall negative bias in the X'-component. The level shift in the Y'-component actually appears more as a ramp but this is more an artefact of the SPEA than a feature of the real data. That is, in this time sector, there is a real level shift in $\Delta Y'$, but the latitude range over which this occurs varies considerably from day to day so that the Heaviside-like Y'-component becomes smeared out.

3.2.4 The 1400 - 1900 MLT Regime

The fourth regime which has been identified is the post-noon quadrant, lying between approximately 1400 to 1900 MLT (2200-0300 UT). This regime presents latitude profiles in which $\Delta X'$ and ΔZ can be interpreted in terms of a simple eastward electrojet. For example, Figure 3.7(b), the latitude profile for 2300 to 2400 UT (1500 to 1600 MLT) on Day 10, 1972, may be interpreted as an eastward current centered about 67.5° N, combined with a poleward flowing current to give the negative $\Delta X'$ poleward of 70° N. Further similar examples are shown in the remainder of

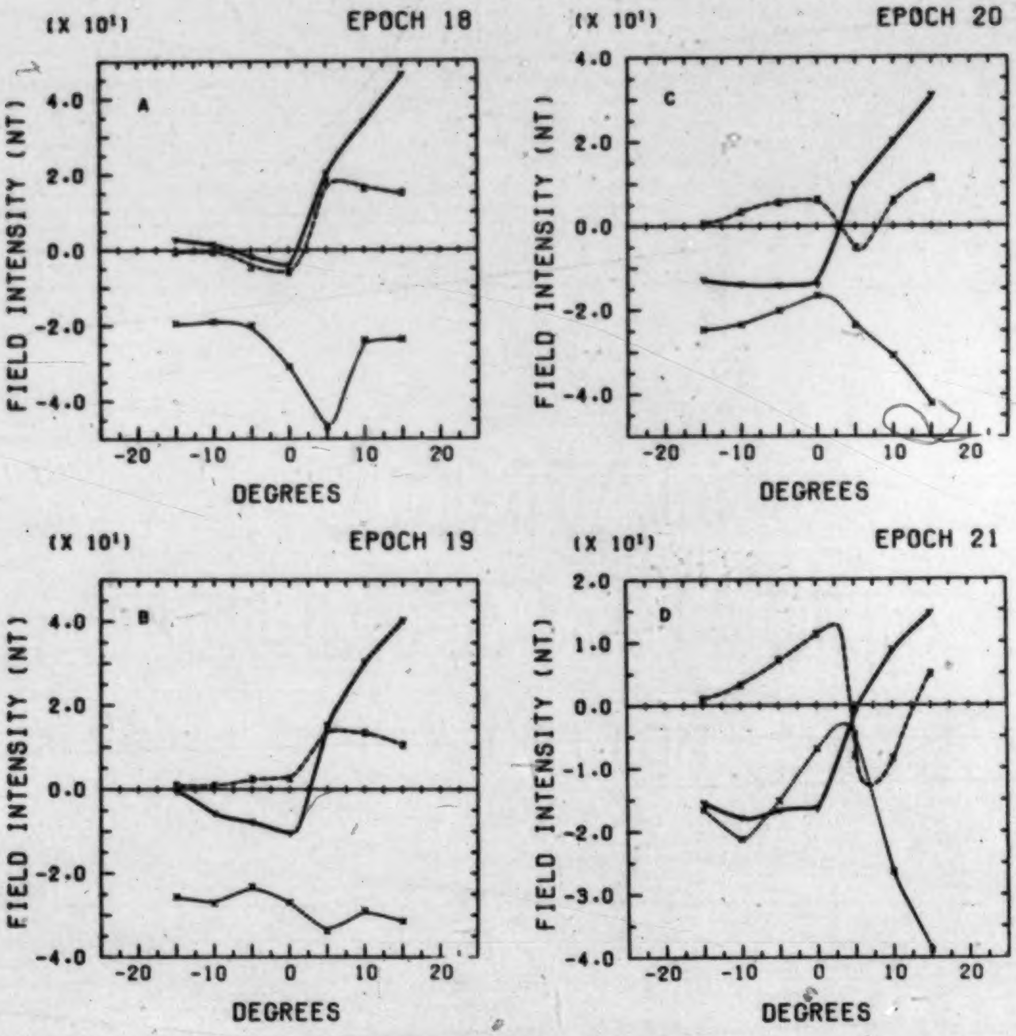

Figure 3.6 Superposed epoch analysis of the hourly averaged latitude profiles for the hours:

(a) 1000-1100 MLT (1800-1900 UT)
(b) 1100-1200 MLT (1900-2000 UT)
(c) 1200-1300 MLT (2000-2100 UT)
(d) 1300-1400 MLT (2100-2200 UT)

Figure 3.7 Representative hourly average latitude profiles for the hours:

(a) 1400-1500 MLT (2200-2300 UT)
(b) 1500-1600 MLT (2300-2400 UT)
(c) 1600-1700 MLT (0000-0100 UT)
(d) 1700-1800 MLT (0100-0200 UT)
(e) 1800-1900 MLT (0200-0300 UT)

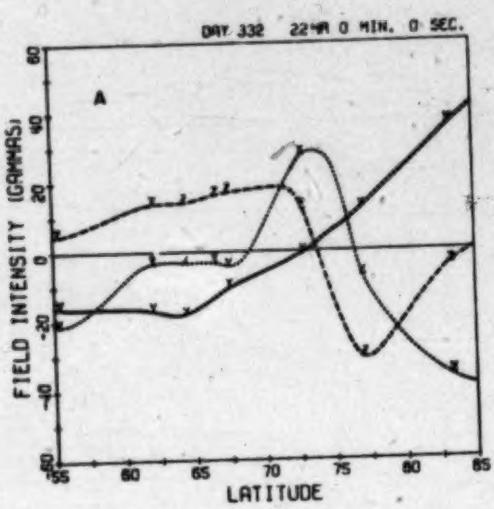
DAY 332 22 HR 0 MIN. 0 SEC.
A
FIELD INTENSITY (GAMMAS)
60
40
20
0
-20
-40
-60
55
60
65
70
75
80
85
LATITUDE

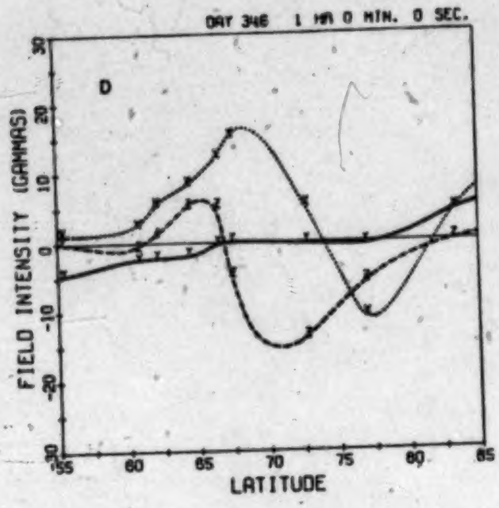
DAY 346 1 HR 0 MIN. 0 SEC.
D
FIELD INTENSITY (GAMMAS)
30
20
10
0
-10
-20
-30
55
60
65
70
75
80
85
LATITUDE

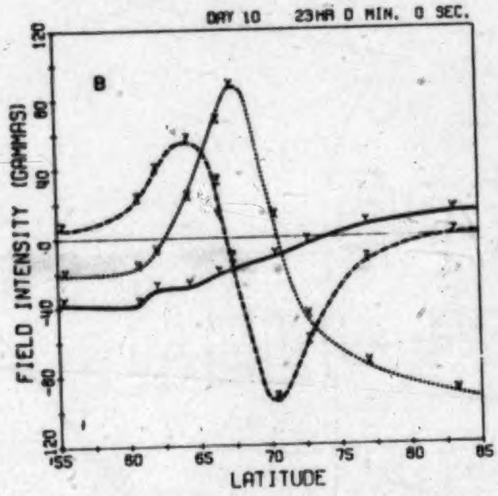
DAY 10 23 HR 0 MIN. 0 SEC.
B
FIELD INTENSITY (GAMMAS)
120
80
40
0
-40
-80
-120
55
60
65
70
75
80
85
LATITUDE

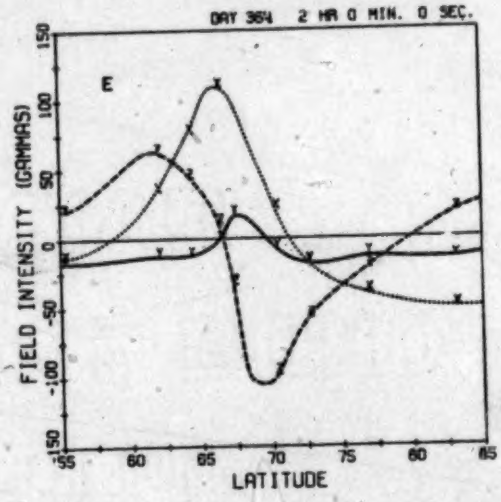
DAY 364 2 HR 0 MIN. 0 SEC.
E
FIELD INTENSITY (GAMMAS)
150
100
50
0
-50
-100
-150
55
60
65
70
75
80
85
LATITUDE

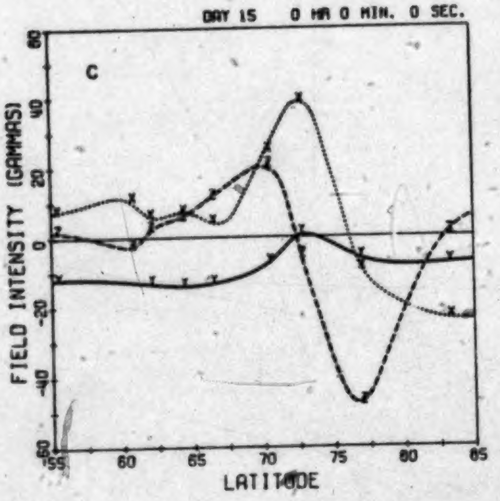
DAY 15 0 HR 0 MIN. 0 SEC.
C
FIELD INTENSITY (GAMMAS)
60
40
20
0
-20
-40
-60
55
60
65
70
75
80
85
LATITUDE

Figure 3.7. The Y'-component in this time regime is variable in that, part of the time, there is a positive-going level shift (e.g., Figure 3.7(b) and (c)), and other times there is no level shift (e.g Figure 3.7(d)). The SPEA of the data in this sector indicates prior to approximately dusk a positive-going level shift in ΔY' (Figure 3.8). Near dusk (Figure 3.8(e)), the Y'-component tends to follow the X'-component, indicating that the ionospheric current likely does not flow in a direction orthogonal to the magnetometer chain. Beyond this time in this regime, the SPEA gives profiles in which the Y'-component shows a negative-going level shift although it is is not as clear a shift as observed in the pre-noon sector. However, some of the examples of the original data shown in Figure 3.7 show that indeed a negative-going level shift does occur in many instances although the majority of profiles up to 1900 MLT show no distinct level shift in ΔY'.

3.2.5 The 1900 - 2200 MLT Regime

The fifth and final region that has been identified from this study occurs in the evening sector from about 1900 to 2200 MLT (0300 to 0600 UT). This regime is dominated by the positive ΔX' signature of the eastward electrojet. However, this time period is distinctive in that there exists a negative-going level shift in the Y'-component, and a region of negative ΔX' poleward of the positive ΔX' regime. Although in the previous sector there also existed a

Figure 3.8 Superposed epoch analysis of the hourly averaged latitude profiles for the hours:

(a) 1400-1500 MLT (2200-2300 UT)
(b) 1500-1600 MLT (2300-2400 UT)
(c) 1600-1700 MLT (0000-0100 UT)
(d) 1700-1800 MLT (0100-0200 UT)
(e) 1800-1900 MLT (0200-0300 UT)

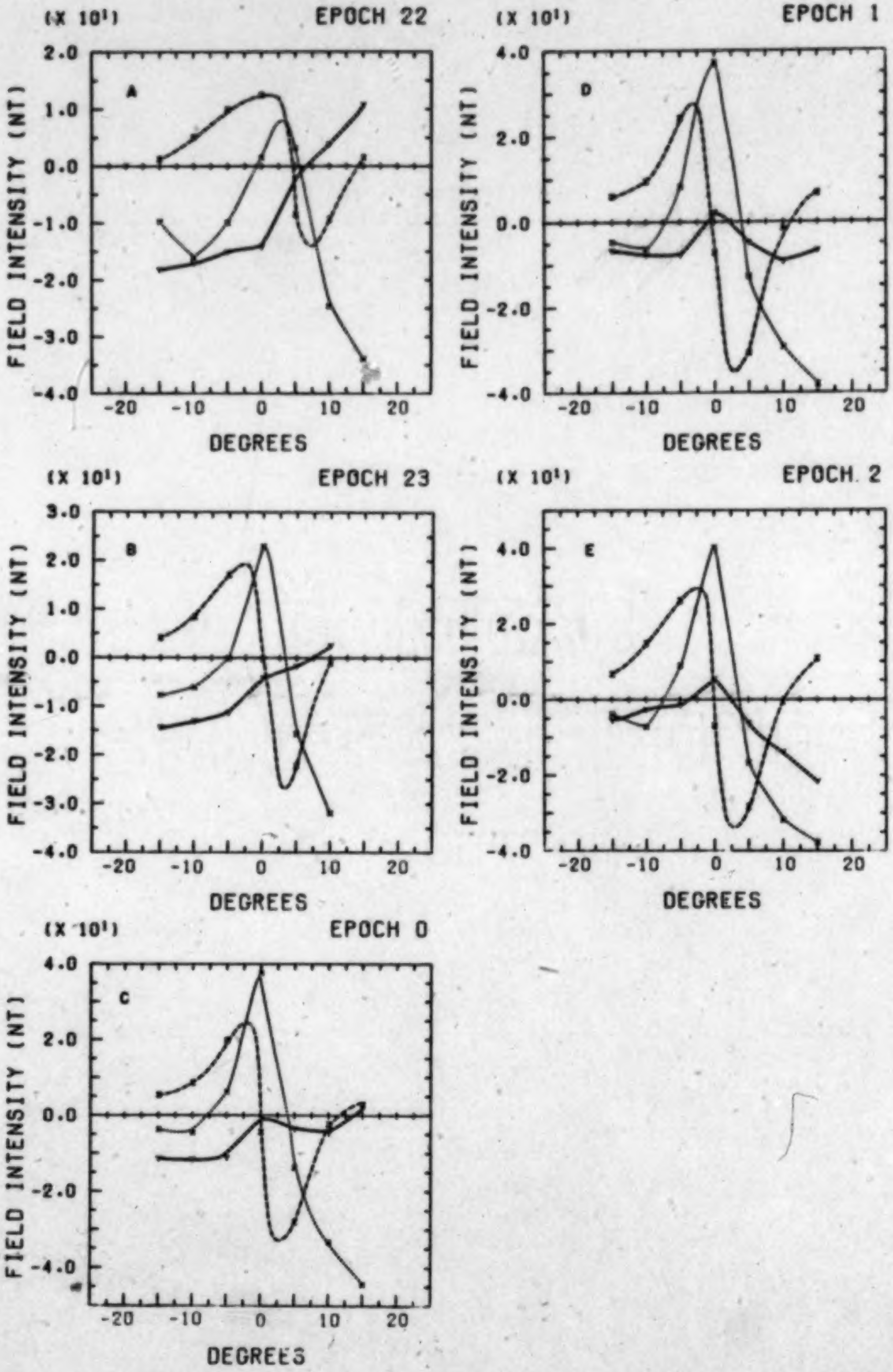
(X 10¹)
EPOCH 22
A
FIELD INTENSITY (NT)
2.0
1.0
0.0
-1.0
-2.0
-3.0
-4.0
-20
-10
0
10
20
DEGREES
(X 10¹)
EPOCH 1
D
FIELD INTENSITY (NT)
4.0
2.0
0.0
-2.0
-4.0
-20
-10
0
10
20
DEGREES
(X 10¹)
EPOCH 23
B
FIELD INTENSITY (NT)
3.0
2.0
1.0
0.0
-1.0
-2.0
-3.0
-4.0
-20
-10
0
10
20
DEGREES
(X 10¹)
EPOCH 2
E
FIELD INTENSITY (NT)
4.0
2.0
0.0
-2.0
-4.0
-20
-10
0
10
20
DEGREES
(X 10¹)
EPOCH 0
C
FIELD INTENSITY (NT)
4.0
2.0
0.0
-2.0
-4.0
-20
-10
0
10
20
DEGREES

region of negative $\Delta X'$ in the poleward part of the profile, the X'-component did not peak in ths region, and the Z-component was consistent with only an eastward current. The $\Delta Y'$ level shift in the 1900-2200 MLT regime occurs over a narrow latitudinal width across and poleward of the eastward electrojet positive X'-bay signature. Figures 3.9(a,b,c) are typical of each hourly interval in this time sector. The corresponding SPEA profiles (Figure 3.10(a,b,c)) again serve to emphasize the general nature of the observations in this regime.

3.2.6 Summary of the Five Regimes

To summarize so far, hourly averaged latitude profiles of the perturbation magnetic field may be divided into 5 distinct regions, characterized primarily by the behaviour of the east-west or Y'-component of the field. Around midnight, including the region of the so-called Harang discontinuity, the Y'- component is negative over the width of the profile, and the X'-component shows the signature of a westward electrojet and, at times, of an eastward electrojet as well. From 0200 MLT to near noon, there is a distinct level shift in $\Delta Y'$, positive-going with increasing latitude. This level shift is confined primarily to the region of the westward electrojet and increases in magnitude (with respect to the maximum $\Delta X'$) as noon is approached. The third region spans noon and is characterized by great variability in the X'- and Z-components. However

Figure 3.9 Representative hourly average latitude profiles for the hours:

(a) 1900-2000 MLT (0300-0400 UT)
(b) 2000-2100 MLT (0400-0500 UT)
(c) 2100-2200 MLT (0500-0600 UT)

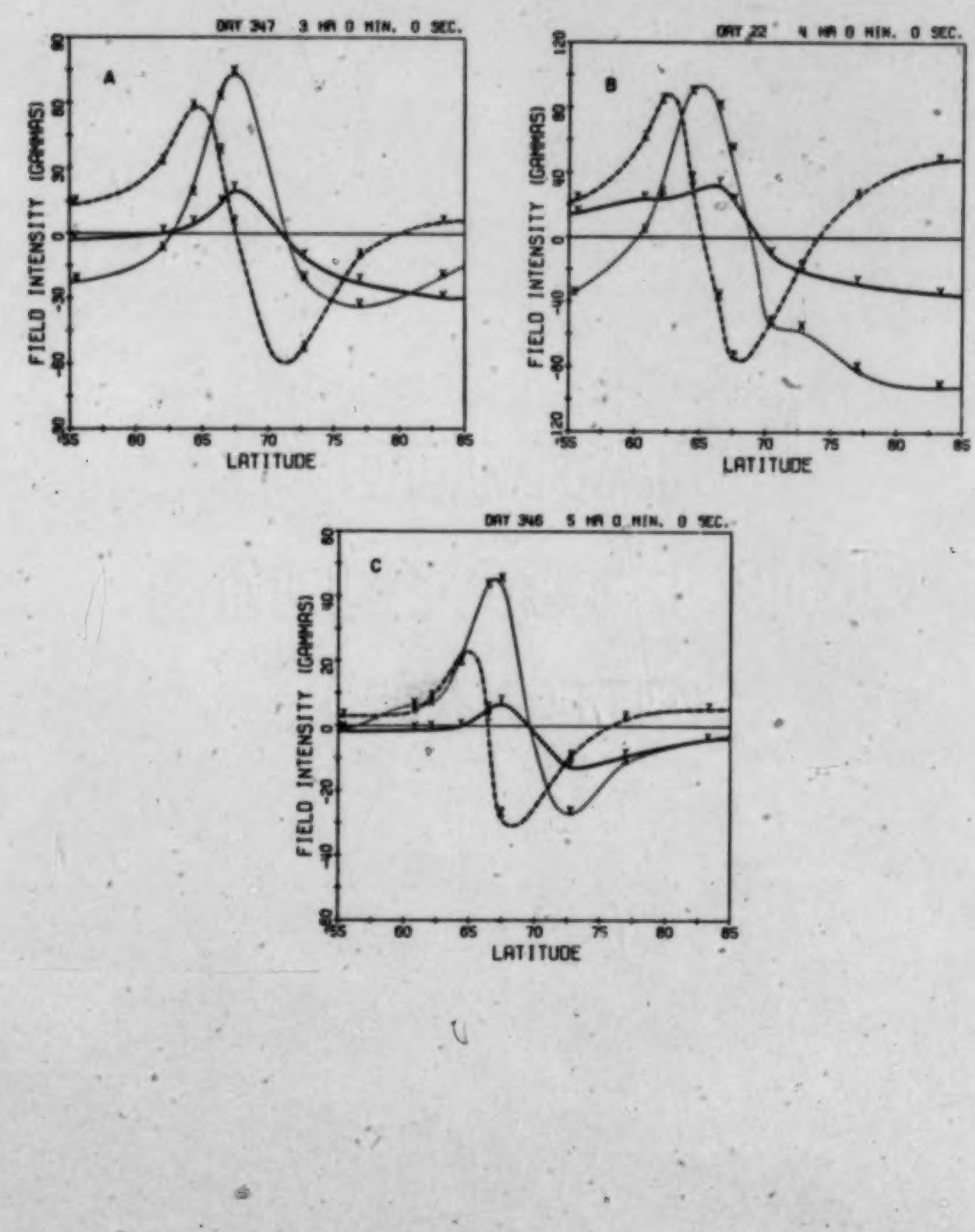
DAY 347 3 HR 0 MIN. 0 SEC.
A
FIELD INTENSITY (GAMMAS)
90
60
30
0
-30
-60
-90
55
60
65
70
75
80
85
LATITUDE
DAY 22 4 HR 0 MIN. 0 SEC.
B
FIELD INTENSITY (GAMMAS)
120
80
40
0
-40
-80
-120
55
60
65
70
75
80
85
LATITUDE
DAY 346 5 HR 0 MIN. 0 SEC.
C
FIELD INTENSITY (GAMMAS)
60
40
20
0
-20
-40
-60
55
60
65
70
75
80
85
LATITUDE

Figure 3.10 Superposed epoch analysis of the hourly averaged latitude profiles for the hours:

(a) 1900-2000 MLT (0300-0400 UT)
(b) 2000-2100 MLT (0400-0500 UT)
(c) 2100-2200 MLT (0500-0600 UT)

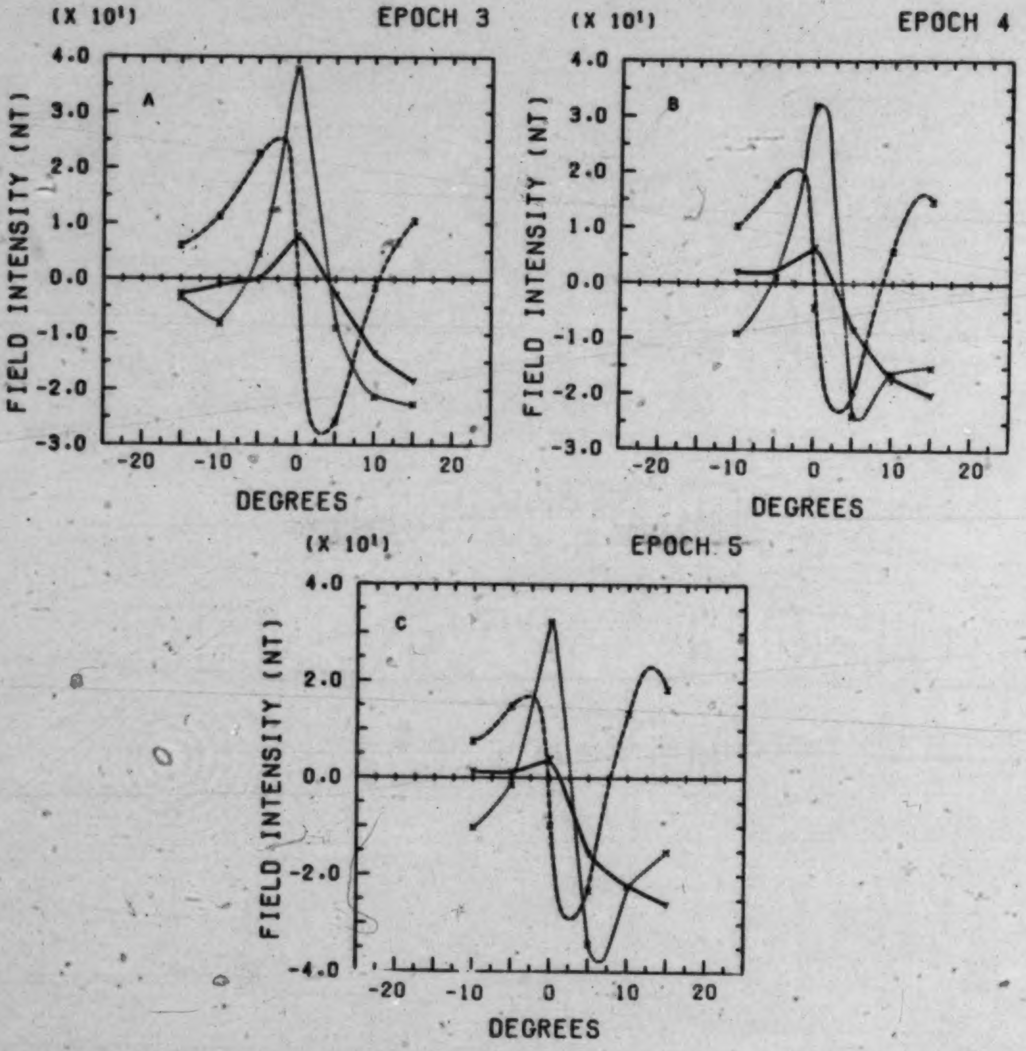
(X 10¹)
EPOCH 3
A
FIELD INTENSITY (NT)
4.0
3.0
2.0
1.0
0.0
-1.0
-2.0
-3.0
-20
-10
0
10
20
DEGREES
(X 10¹)
EPOCH 4
B
FIELD INTENSITY (NT)
4.0
3.0
2.0
1.0
0.0
-1.0
-2.0
-3.0
-20
-10
0
10
20
DEGREES
(X 10¹)
EPOCH 5
C
FIELD INTENSITY (NT)
4.0
2.0
0.0
-2.0
-4.0
-20
-10
0
10
20
DEGREES

ΔY' consistently shows a large positive-going step or level shift. From about 1400 to 1900 MLT, the profiles are characterized by the signature of an eastward flowing current and either a small positive-going step in ΔY' or no step at all. From 1900 to 2200 MLT, the profiles provide evidence of both eastward and westward currents (the latter being the most poleward current) and with these, a negative-going level shift in the Y'- component.

The remainder of this chapter will deal with the interpretation of these profiles in terms of a worldwide three dimensional current system, as well as presenting some other information derived from these profiles and other sources.

3.3 Interpretation of the Data Suite

The most distinctive feature of the data is the level shift which occurs in the Y'-component. As described in Chapter 3, a net field-aligned current produces as a ground magnetic signature, a step in ΔY'. Field-aligned currents were first proposed by Birkeland (1908,1913) and subsequently were reintroduced by Fejer (1961), Kern (1962) and Boström (1964) in three-dimensional current models for auroral regions. It was not until recently (Zmuda *et al*, 1967; Armstrong and Zmuda,1970) that such currents were identified from *in situ* measurements by magnetometers on board polar orbiting satellites. Several more recent studies (Yasuhara *et al*, 1975; Sugiura and Potemra,1976;Iijima and

Potemra,1976) show that there is a tendency for there to be net downward current flow in the morning sector of the auroral oval, and net upward flow in the evening sector. If this is indeed the case, and the net field-aligned currents are uniformly diverging in the ionosphere, then no ground based signature would be observed (Vasyliunas,1972). Fukushima (1969) has given a simple description of this phenomenon by considering a line current flowing into the ionosphere (Figure 3.11). If the total inflow is I amps, then at a radial distance r from the current, on the ground, the magnetic field is given by I/r, and is directed clockwise (looking along the current). If this current diverges uniformly radially outward (in the horizontal plane), then the overhead ionospheric current density at the same observation point is $I/2\pi r$, and the magnetic effect on the ground is given by I/r, but in the counter-clockwise direction. The net effect is thus zero magnetic perturbation below the ionosphere. However, the ionosphere provides a highly conducting channel in the form of the auroral oval, so that one would expect to see distinctive magnetic signatures at ground based observatories. These will have the basic characteristic of a level shift in the east-west component of the magnetic field across the region of net field-aligned current flow. This fact together with satellite observations of field-aligned currents has been used to aid in the interpretation of the latitude profiles. In fact, if a positive-going $\Delta Y'$ step is taken to be the

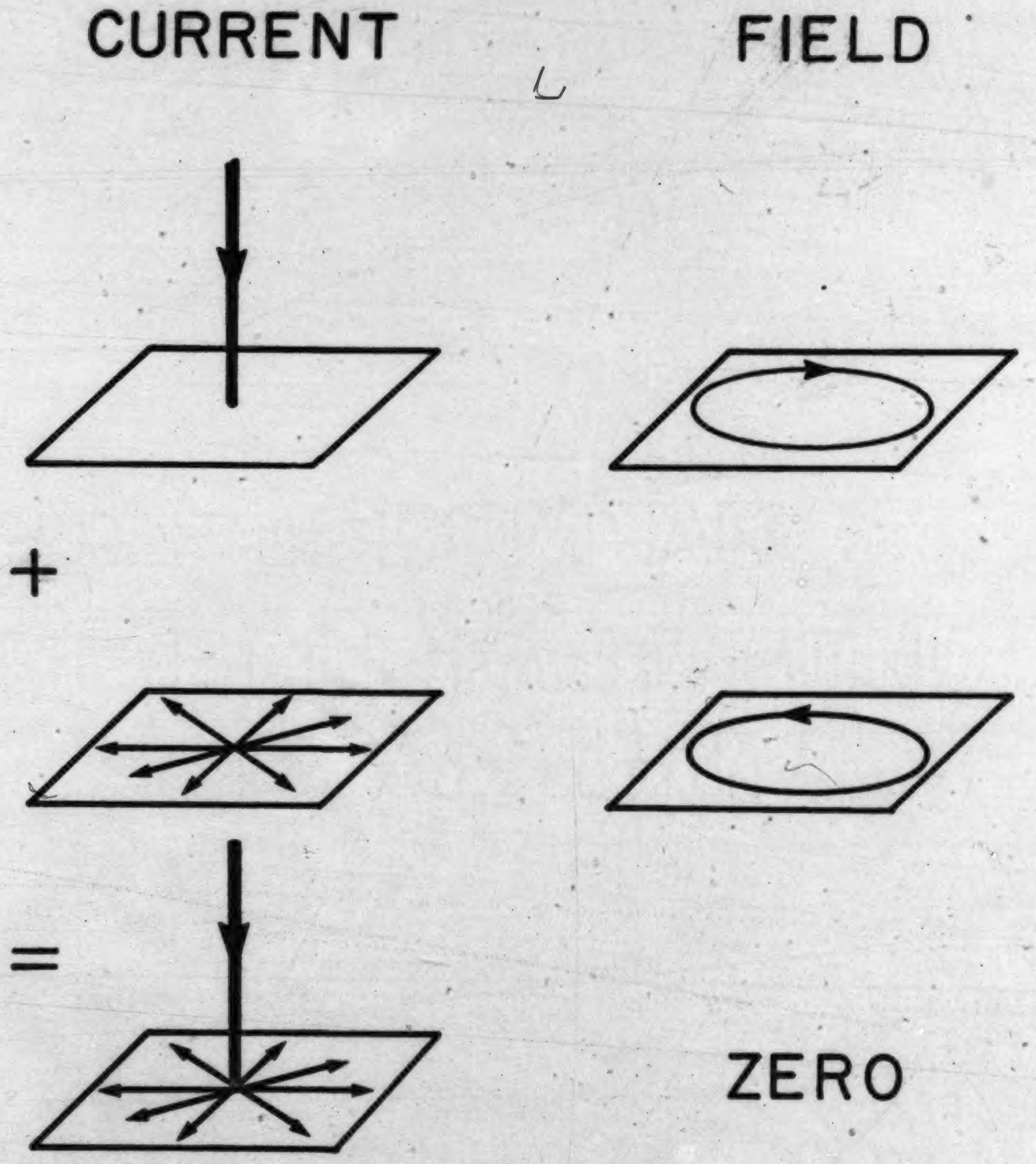

Figure 3.11 Schematic drawing to demonstrate how a vertical current which diverges uniformly into the horizontal plane produces no net magnetic perturbation. See text for details.

signature of a net downward field-aligned current, and a negative-going $\Delta Y'$ step to be the signature of upward flowing current, then a picture of the diurnal variation of the disturbance component of the magnetic field associated with the field-aligned current flow may be obtained. Such a picture is shown in Figure 3.12. This is a histogram of the frequency of occurrence of inward and outward net field-aligned current, as well as the number of cases when no such cases were observed in the ground data. The cross-hatched region delineates that region of the auroral oval known as the Harang discontinuity.

There is a remarkable similarity between the behaviour of the net field-aligned current as inferred from the latitude profiles, and the diurnal variation of the average electric field observed at auroral latitudes (Mozer and Lucht, 1974; Iversen and Madsen, 1977). Figure 3.13(a) is a plot of the east-west and north-south components of the average auroral zone electric field as a function of local time obtained by Mozer and Lucht (1974). Most of the data used in compiling this plot was collected at Thompson, Manitoba, and Churchill, Manitoba, where local time is approximately the same as magnetic local time. Figure 3.13(b) is similar data in a polar plot, obtained by Iversen and Madsen (1977).

The first region discussed above (2200 to 0200 MLT) features an electric field which is westward and poleward (towards dusk), and westward and equatorward (towards dawn).

Figure 3.12 Histogram showing the distribution of net field-aligned current as a function of Universal Time, as inferred from the ground-based magnetic measurements. Approximate magnetic local time is shown across the top of the figure.

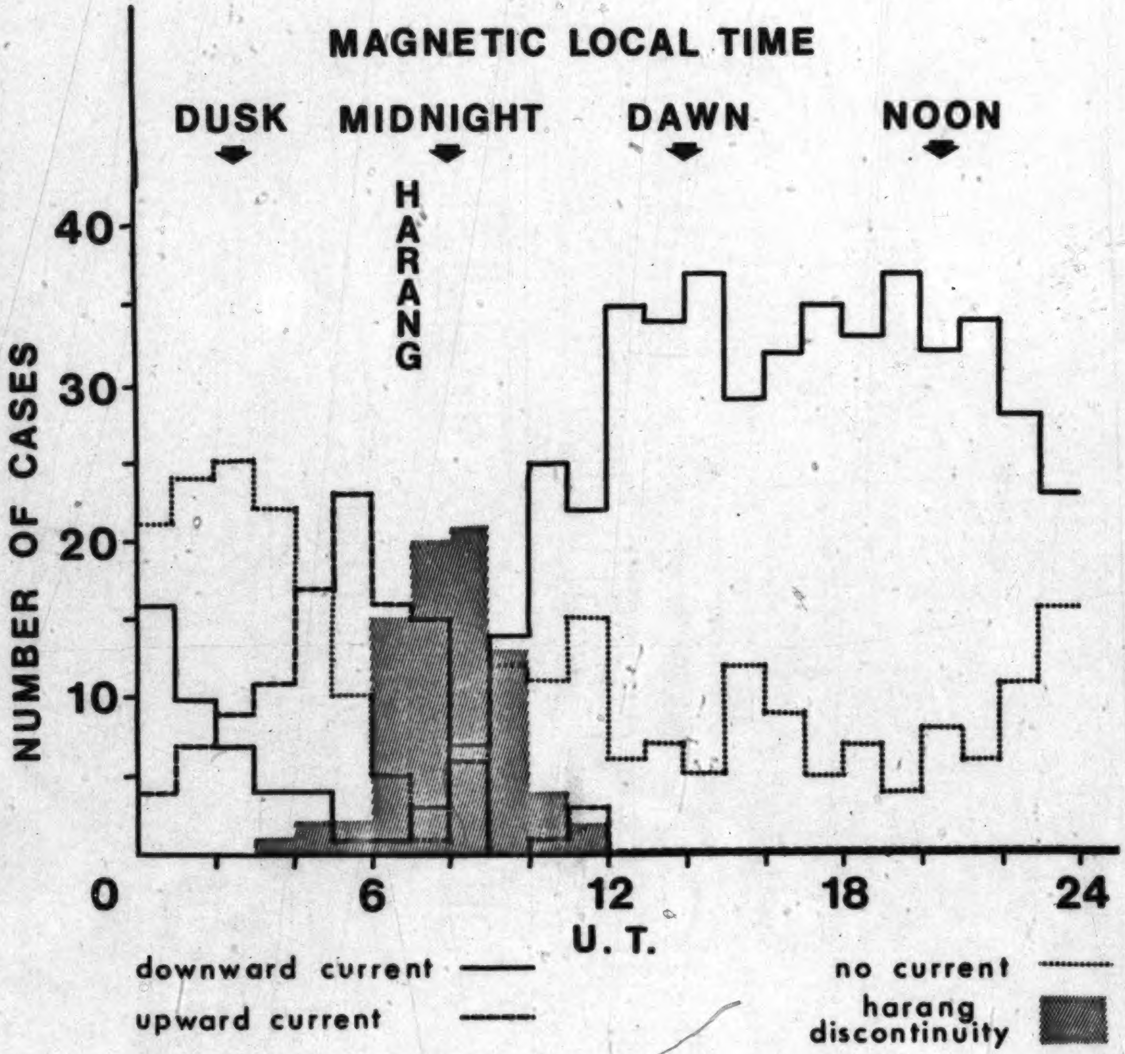

MAGNETIC LOCAL TIME
DUSK
MIDNIGHT
DAWN
NOON
HARANG
NUMBER OF CASES
40
30
20
10
0
6
12
18
24
U. T.
downward current
upward current
no current
harang discontinuity

Figure 3.13(a) The diurnal variation in the ionospheric electric field in the region of the auroral oval. The time scale is local time, which, for these data, is approximately equal to magnetic local time (see text). (After Mozer and Lucht, 1974).

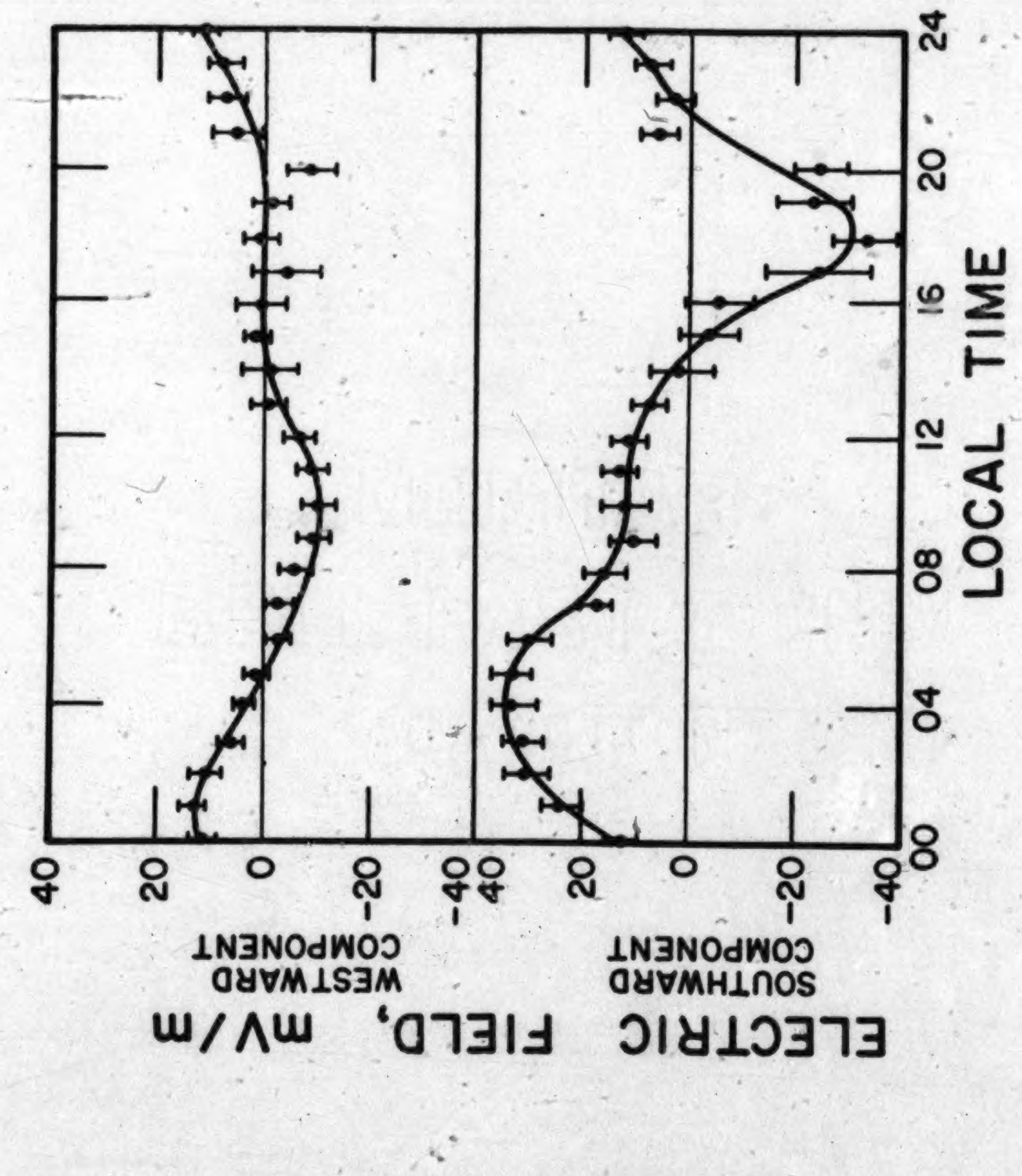
ELECTRIC FIELD, mV/m
WESTWARD COMPONENT
SOUTHWARD COMPONENT
40
20
0
-20
-40
40
20
0
-20
-40
00
04
08
12
16
20
24
LOCAL TIME

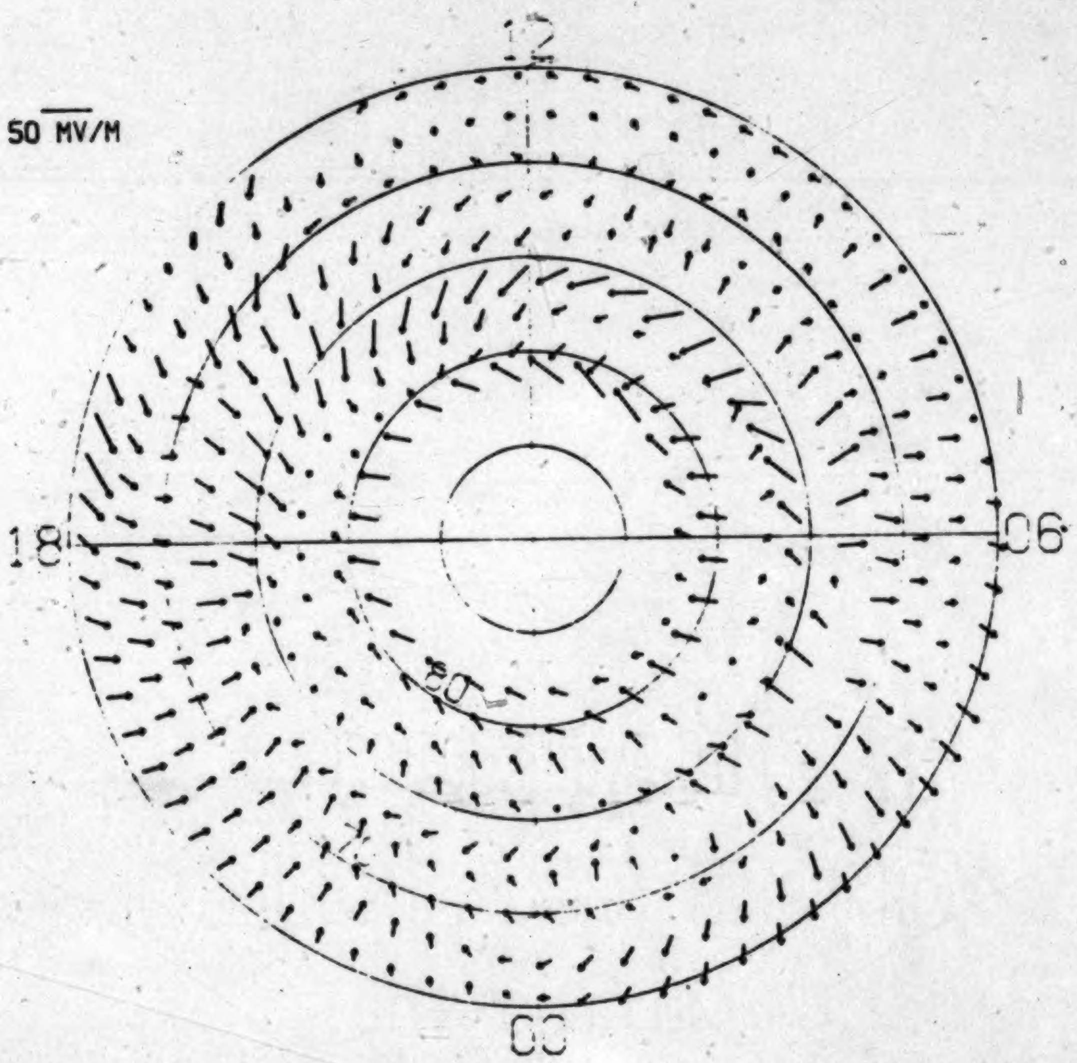

Figure 3.13(b) Average ionospheric electric field vectors in the region of the auroral zone, plotted in a geomagnetic latitude, magnetic local time frame. (After Iversen and Madsen, 1977).

This field can drive a poleward Hall current and a westward Pedersen current. In this region, the latitude profiles show a Y'-component which is negative across the profile, and this signature can be produced by poleward flowing current. The second region, or dawn regime has a dominantly equatorward component of electric field and the east-west component, although small, is primarily eastward. This equatorward electric field can drive a westward flowing Hall current, consistent with the magnetic signatures observed in this sector. The noon sector (1000 to 1400 MLT) is characterized by a weak or zero east-west electric field, and a transitional north-south electric field. In this region, the ground based magnetic observations are confused with respect to electrojet flow, although the Y'-component signature is that of a strong inward net field-aligned current flow. In the post-noon quadrant, the data of Mozer and Lucht indicate an essentially zero east-west component to the electric field, but a strong poleward component. This, too, is consistent with the latitude profiles which show in this sector an eastward electrojet that would be a Hall current driven by a poleward electric field. The data of Iversen and Madsen (1977) show a small eastward component in the electric field. However, the near absence of an east-west component in the electric field is consistent with essentially no north-south component of Hall current. Thus one would not expect the electrojet Hall current to diverge significantly along field lines in this region. Finally, from 1900 to 2200 MLT the electric field has a westward component increasing toward midnight and a poleward component increasing toward dusk. These fields are also consistent with the observed eastward electrojet flow that is observed in this sector. Table 3.1 is a summary of these comparisons.

As pointed out above, the level shift in the Y'-component ($\Delta Y'_{step}$) is believed to be related to net field-aligned current flow into and out of the ionosphere. The positive-going $\Delta Y'_{step}$ in the dawn and noon sectors is then interpreted as the signature of net inward field-aligned current flow. To maintain current continuity, it was hypothesized that this net inward current feeds the westward ionospheric electrojet. Similarly, the net inward flow in the immediate post-noon sector could feed the eastward electrojet. In the dusk sector, where $\Delta Y'_{step}$ is negative-going and apparently related in position to the negative X' latitudinal regime, the inferred upward field-aligned current has been hypothesized to be the result of the electrojets bleeding upward along the field lines into the magnetosphere.

To test this hypothesis, it was assumed that the peak values of the X'-component ($\Delta X'_{peak}$) were related to the magnitude of the electrojet current strength, and further that $\Delta Y'_{step}$ was an indicator of the magnitude of the unbalanced field-aligned current. Subject to these assumptions, one would then predict that the norm of the

TABLE 3.1

Correspondence Between Net Field-Aligned Current Flow and Auroral Zone Electric Field

LMT SPAN	REGIME	ELECTRIC FIELD	FIELD-ALIGNED CURRENT AND IONOSPHERIC CURRENT FLOW
2200-0200	Harang Discontinuity (Midnight Sector)	Primarily westward Equatorward toward dawn equatorward toward dawn	Poleward Hall current flow Westward Pedersen current flow
0200-1000	Dawn Sector	Pronounced eastward component Consistent equatorward component	Dominated by westward Hall current flow; net downward field-aligned current regime
1000-1400	Noon Sector	Weak westward component or zero eastward component Confused north-south component	No pronounced consistent electrojet flow Continued downward net field-aligned current flow
1400-1900	Post-noon Quadrant	Zero east-west component	Eastward electrojet flow High probability of no net field-aligned current flow
1900-2200	Pre-midnight Quadrant	Westward component toward midnight edge of regime Consistent poleward component	Eastward electrojet flow Net upward field-aligned current flow

ratio of $\Delta Y'_{\mathrm{step}}$ to $\Delta X'_{\mathrm{peak}}$ from 0200 MLT to noon would increase and from noon to dusk, the same ratio would decrease. In the dusk quadrant, $|\Delta Y'_{\mathrm{step}} / \Delta X'_{\mathrm{peak}}|$ would increase for negative $\Delta X'$, and decrease for positive $\Delta X'$. Figure 3.14 shows this ratio obtained through the SPEA, plotted as a function of magnetic local time. It is apparent that qualitatively, the above expectations are realized. Near noon, it was difficult to establish a value for $\Delta X'$, so no values are plotted for this regime.

This analysis is important in that the results form a basis for a world-wide current system model which will be discussed in detail in Chapter 4. That is, it is believed that the distinctive positive level shift in $\Delta Y'$ of the hourly averaged latitude profiles across local noon and in the pre-noon sector is a signature, at least in part, of unbalanced field-aligned current flow into the ionosphere, which feeds the ionospheric Hall current electrojets. The negative level shift in $\Delta Y'$ in the pre-midnight quadrant reflects field-aligned current flow out of the ionosphere.

An alternative way to examine these data is to consider $\Delta Y'_{\mathrm{step}}$ and $\Delta X'_{\mathrm{peak}}$ separately as functions of magnetic local time. Figure 3.15 is the plot of the average, for a given hour, of $\Delta Y'_{\mathrm{step}}$ and $\Delta X'_{\mathrm{peak}}$ versus MLT. Note that for the dawn regime, $\Delta X'_{\mathrm{peak}}$ increases from 0200 -1000 MLT (i.e.,it becomes less negative),by about a factor of three, while $\Delta Y'_{\mathrm{step}}$ increases by a factor of 2 to 3.

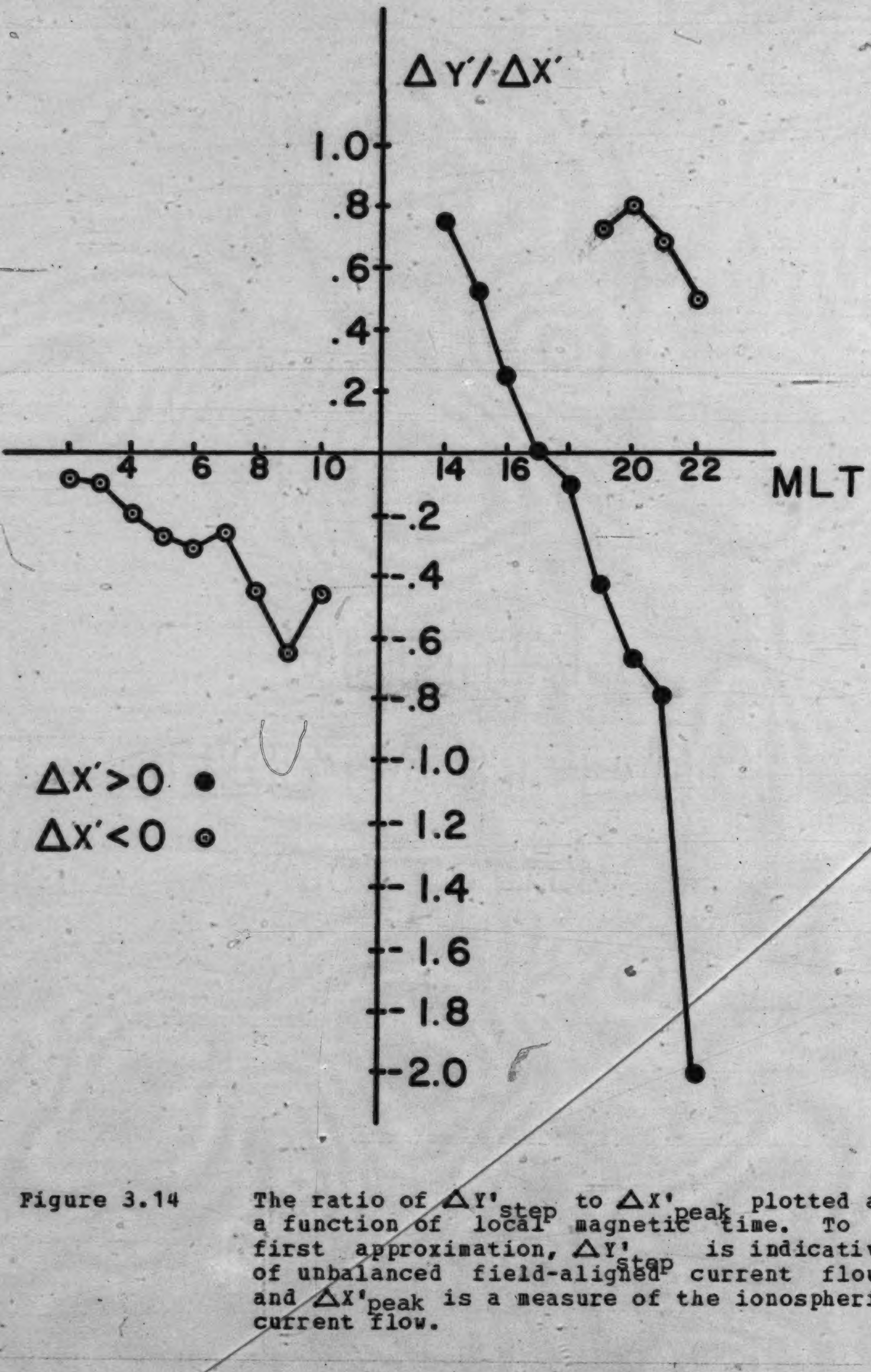

Figure 3.14 The ratio of $\Delta Y'_{step}$ to $\Delta X'_{peak}$ plotted as a function of local magnetic time. To a first approximation, $\Delta Y'_{step}$ is indicative of unbalanced field-aligned current flow, and $\Delta X'_{peak}$ is a measure of the ionospheric current flow.

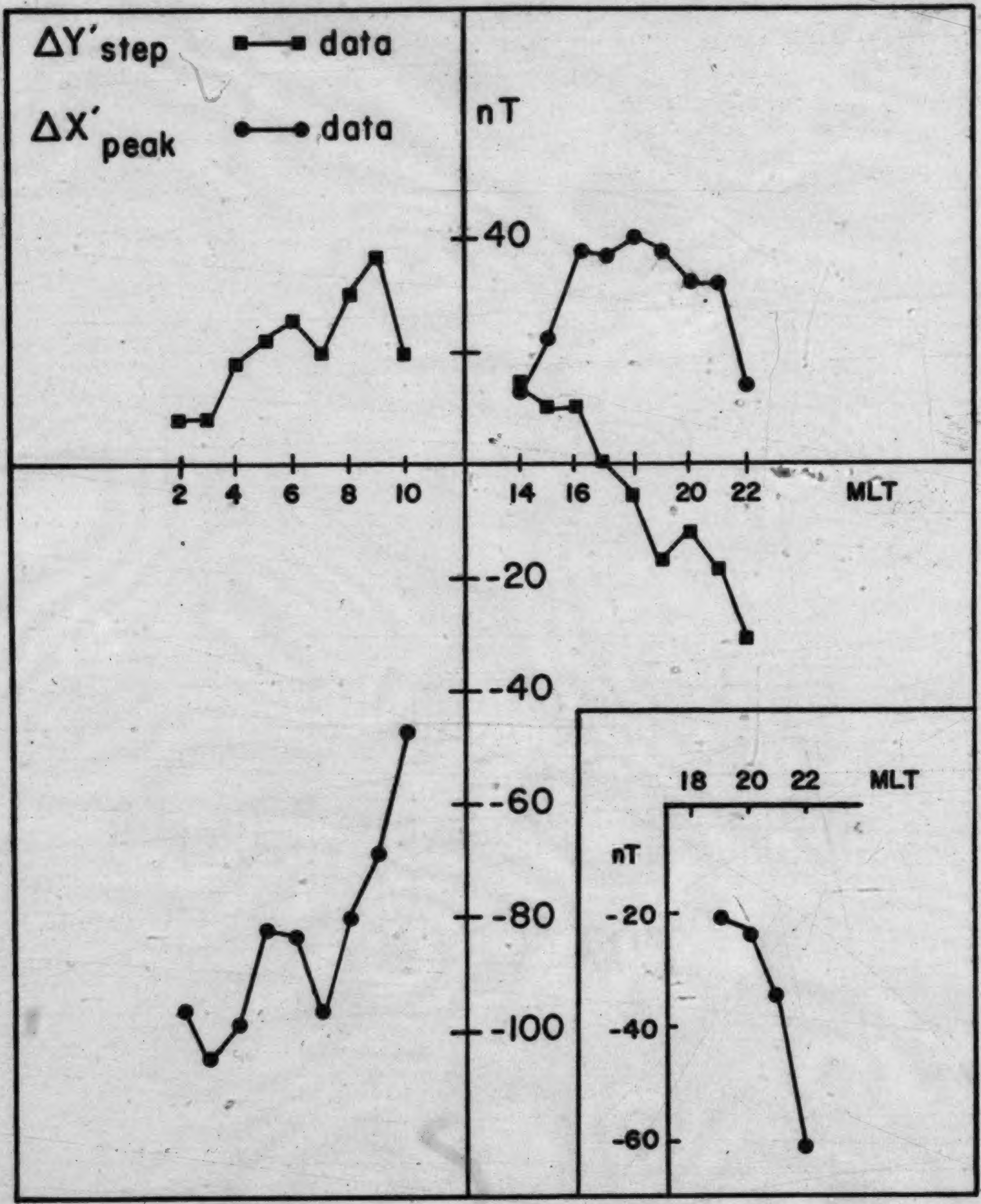

Figure 3.15 Plot of $\Delta Y'_{step}$ and $\Delta X'_{peak}$ as a function of magnetic local time. Positive $\Delta Y'_{step}$ means a positive-going level shift from south to north; negative $\Delta Y'_{step}$ means a negative-going level shift from south to north. Positive $\Delta X'_{peak}$ is the signature of eastward flowing current, negative $\Delta X'_{peak}$ is the signature of westward flowing current.

Similarly, in the region of the eastward electrojet, $\Delta X'_{peak}$ increases until about dusk while $\Delta Y'_{step}$ decreases. Beyond this time, $\Delta Y'_{step}$ becomes increasingly negative in coincidence with a decreasing $\Delta X'_{peak}$. All these observations are consistent with the interpretation given in the previous paragraph.

In the diurnal variation of $\Delta X'_{peak}$ for the interval 0200 to 1000 MLT, there is a distinct inflection on the curve near local magnetic dawn. This inflection is thought to be due to a decrease in the total westward flowing current near dawn. Some of the current flows up field lines near dawn due to a conductivity gradient between the sunlit and dark hemispheres, This observation will be discussed in some detail in Chapter 4. Finally it is noted that $\Delta X'_{peak}$ has a negative extremum during the hour 0200-0300MLT. This is in agreement with Allen and Kroehl (1975) who found that AL (indicative of the strength of the westward electrojet) tended to reach peak values approximately three hours after local magnetic midnight.

The time sectors in which upward and downward net field-aligned current are found from ground based data are in good agreement with those described by Sugiura and Potemra (1976) (Figure 3.16) except in the 1200-1400 MLT sector. These authors find net upward field-aligned current in this sector, whereas in the present study, the reverse current flow was observed, and this latter is consistent with a growing eastward electrojet. Most of the published

Figure 3.16 Percentage occurrence of level shifts in the east-west component of the magnetic field observed by the Triad satellite, as a function of MLT. The dotted regions represent net upward field-aligned current, the clear regions net downward field-aligned current. (After Sugiura and Potemra, 1976).

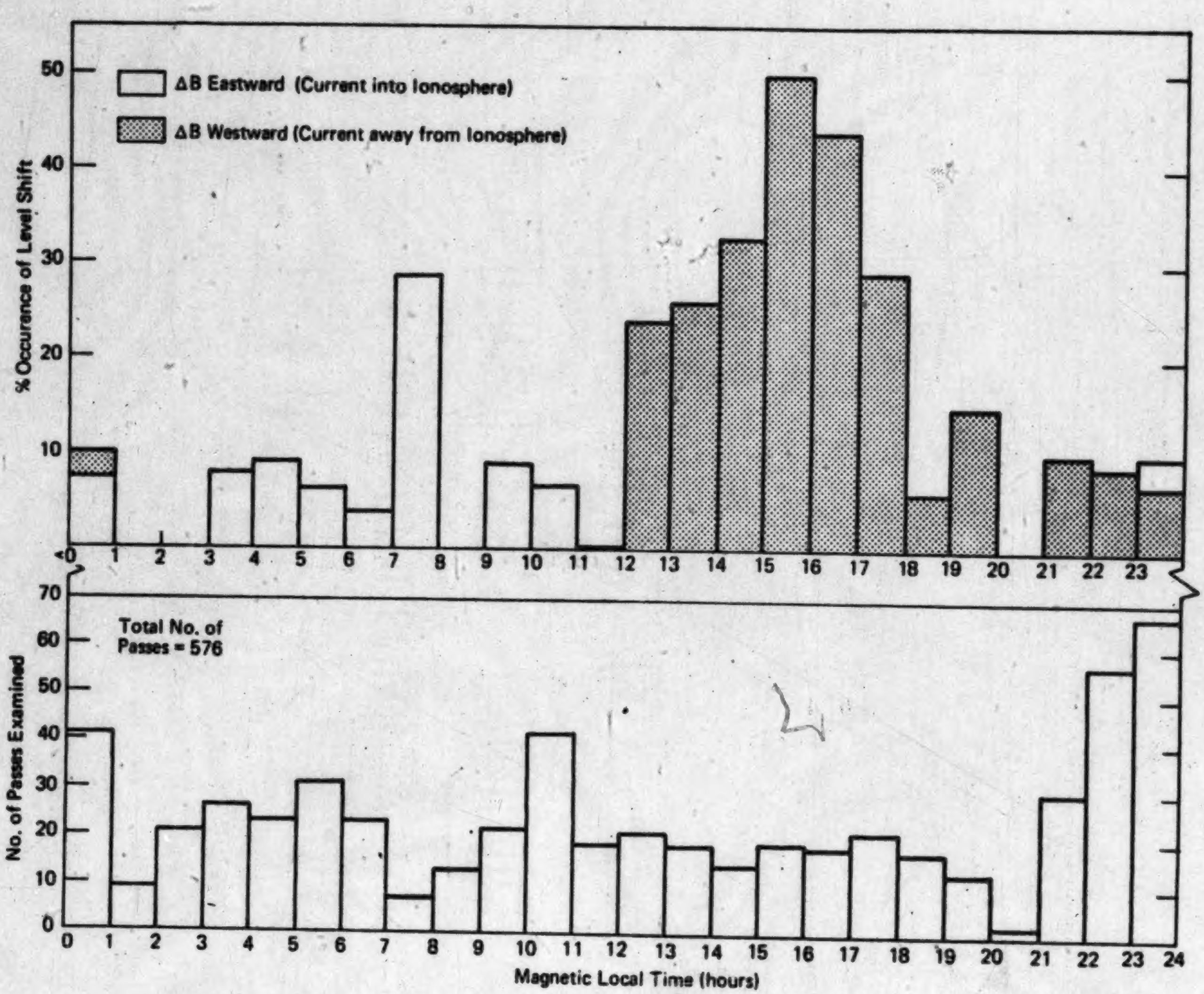
ΔB Eastward (Current into Ionosphere)
ΔB Westward (Current away from Ionosphere)
% Occurence of Level Shift
50
40
30
20
10
<0
0
1
2
3
4
5
6
7
8
9
10
11
12
13
14
15
16
17
18
19
20
21
22
23
24
70
60
Total No. of
Passes = 576
No. of Passes Examined
Magnetic Local Time (hours)

data from the Triad satellite have been from the summer months, whereas all the ground- based data in the present study come from winter months. An explanation of the discrepancy between the Triad satellite and ground magnetometer data will be offered in Chapter 4.

Because of the role that the interplanetary magnetic field (IMF) plays in magnetospheric and auroral physics (see Chapter 2), it was useful to examine the correlation between the IMF and the presence of the $\Delta Y'$ level shift observed in the latitude profiles. To this end, data were selected from two regions showing pronounced level shifts in the Y'-component. The hours 1600-1700 UT and 1700-1800 UT (approximately 0800-0900 MLT and 0900-1000 MLT) were chosen as representative of positive-going level shifts in the Y'-component, and the hours 0400-0500 UT and 0500-0600 UT (2000-2100 MLT and 2100-2200 MLT) were chosen to represent the negative-going $\Delta Y'$ level shifts. Figure 3.17 (a,b,c,and d) are plots of $\Delta Y'_{step}$ vs B_z, (i.e., the component of the IMF normal to the ecliptic plane). Although in some cases there were no data for the IMF for thoses cases where data did exist, there is a clear linear relationship between $\Delta Y'_{step}$ and B_z for the pre-noon sector. That is when $B_z > 0$ (i.e., the IMF points northwards, or is parallel to the earth's field in the ecliptic plane) there is a weak $\Delta Y'_{step}$; however, if $B_z < 0$, then $\Delta Y'_{step}$ increases linearly with increasing negative B_z. If as suggested above, the level shift in $\Delta Y'$ is related to a net

Figure 3.17 Plots of $\Delta Y'_{step}$ as a function of the component of the IMF normal to the ecliptic plane (B), for the hours

(a) 0400-0500 UT

(b) 0500-0600 UT

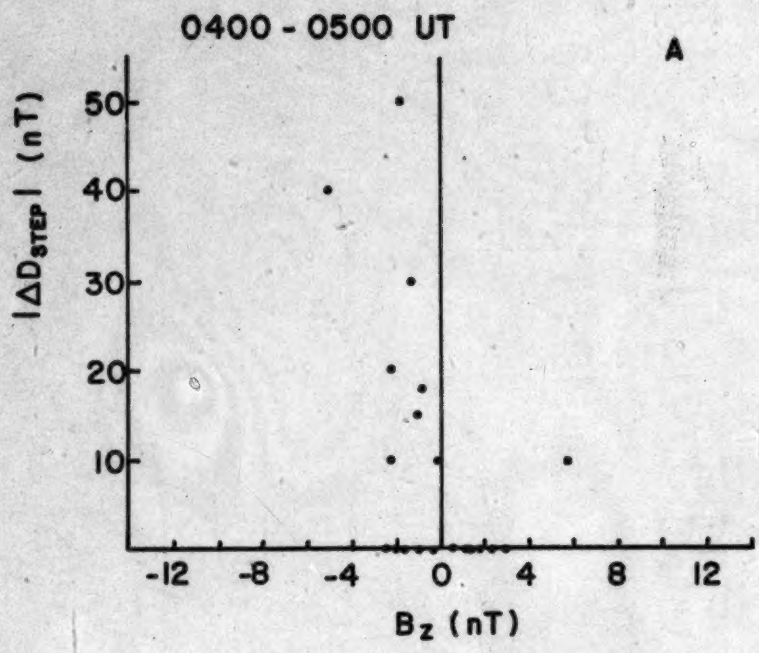
0400 - 0500 UT
A
|ΔD_STEP| (nT)
50
40
30
20
10
-12
-8
-4
0
4
8
12
Bz (nT)

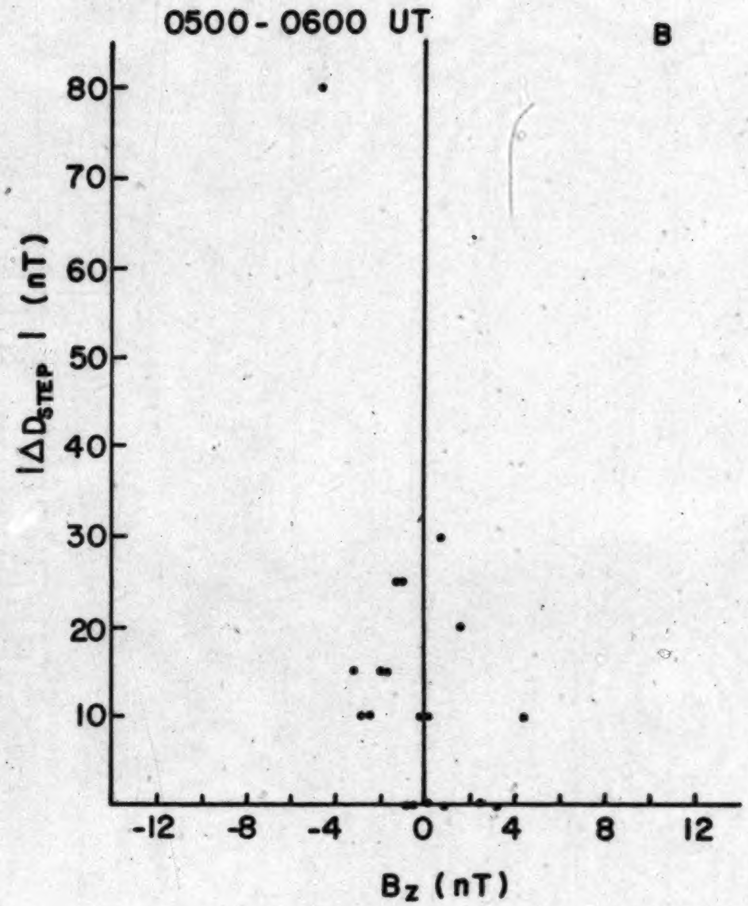
0500 - 0600 UT
B
|ΔD_STEP| (nT)
80
70
60
50
40
30
20
10
-12
-8
-4
0
4
8
12
Bz (nT)

Figure 3.17 Plots of $\Delta Y'_{step}$ as a function of the component of the IMF normal to the ecliptic plane (B), for the hours

(c) 1600-1700 UT
(d) 1700-1800 UT

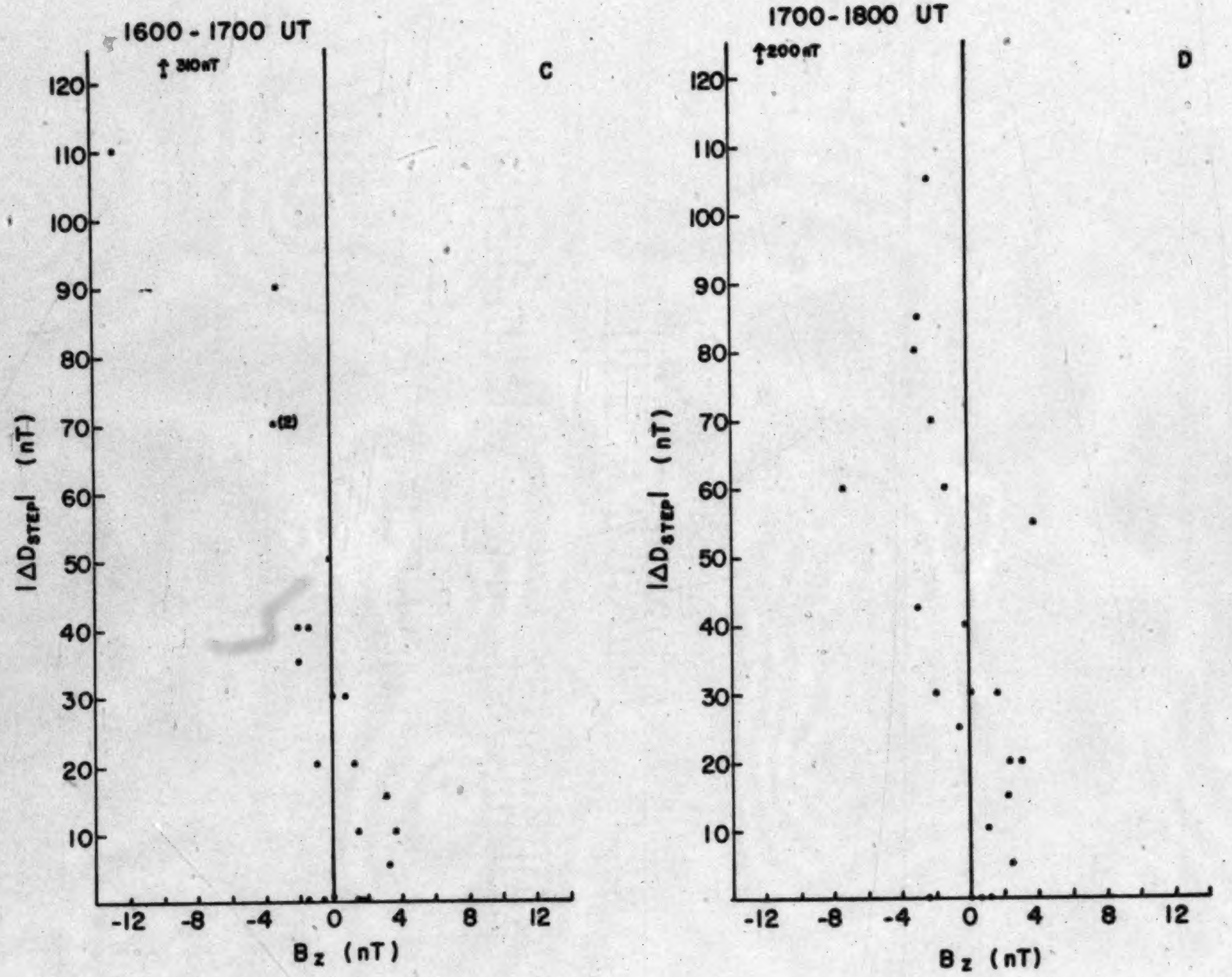
1600 - 1700 UT
↑ 310nT
C
(2)
|ΔD_STEP| (nT)
120
110
100
90
80
70
60
50
40
30
20
10
-12
-8
-4
0
4
8
12
B_z (nT)
1700-1800 UT
↑ 200nT
D
|ΔD_STEP| (nT)
120
110
100
90
80
70
60
50
40
30
20
10
-12
-8
-4
0
4
8
12
B_z (nT)

component of field-aligned current which in turn is related to the strength of the westward current, such a relationship between $\Delta Y'_{step}$ and B_z would be expected. In fact, Hirshberg and Colburn (1969) have shown a good correlation between Kp, a measure of auroral activity, and B_z, when B_z is directed southward.

In the evening sector, the relationship between $\Delta Y'_{step}$ and B_z is not as clear, although a pattern similar to that observed in the pre-noon sector is observed here. It would be of considerable help in determining unequivocably the relationship between $\Delta Y'_{step}$ and B_z if there were more cases of large $\Delta Y'_{step}$ in this local time interval. However, for the period of this study, there was IMF data for about only 50% of the days in each hourly interval, and of this 50%, only about half of the cases provided large level shifts in $\Delta Y'$. The result of this unfortunate circumstance is a paucity of data involving large level shifts in the Y'-component. However, the results are consistent with the observations of others (Hirshberg and Colburn, 1969) in view of the interpretation of the Y'-component level shift presented in this thesis.

3.4 Inversion of Latitude Profile Data near Dusk

It was pointed out earlier in this chapter that there was evidence for penetration of the westward electrojet poleward of the eastward electrojet as far westward as 1800 MLT. Rostoker and Kisabeth (1973) have shown that eastward and westward electrojets exist simultaneously in this time sector during polar magnetic substorms. More recently, Kamide and Akasofu (1976) have published a similar result. As the existence of a westward flowing current in this time sector during quiet to moderately disturbed times is important to the understanding of magnetospheric processes, a detailed study of the current flow in this regime was undertaken using the linear inversion theory of Backus and Gilbert (1970). In particular, the formulation developed by Oldenburg (1976) was used to determine the latitudinal distribution of current in this time sector. Appendix II gives a brief outline of the theory involved in this technique.

Besides carrying out the inversion, which leads to the only unique solution to the problem, a model of current intensity that "fits the data" was generated. That is, out of the infinite set of particular models, one which satisfied the relation $\int J'(\theta)\, d\theta$ = minimum, and which was constrained to fit the observations that fit the data as closely as possible, was developed as an aid in interpreting the results of the inversion. There is not necessarily any physical reason for choosing such a model. However, such a choice is analytically and numerically easy to handle, and does satisfy the intuitive belief that the current density of auroral current systems, on average, will vary latitudinally in a smooth manner when averaged over the time span of one hour.

To demonstrate the results of the inversion, one example from each hour from the sector 2300 to 0600 UT (1500 to 2200 MLT) is presented. For each latitude profile, there are three accompanying figures. The first is a plot of standard deviation vs colatitude, contoured for constant values of averaging function width. These plots are in effect a graph of the trade-off between error in the calculation of the current density, and the resolution for the same calculation. This figure is required to interpret the second plot which shows average current density as a function of colatitude contoured for a constant standard deviation. Finally, the "flattest" model of height-integrated current density that fits the data is plotted to assist in the evaluation of the current density estimates. As discussed in Appendix II, the forward model used in this study employs both east-west current flows and north-south current flows. Furthermore, in this regime, the electric field is approximately northward, so that the simplified relationship between the Hall current and the Pedersen current, as developed in the Appendix, has been used. In all cases, the ratio of height-integrated Hall conductivity to height-integrated Pedersen conductivity was set to two in accordance with the results of Brekke et al, (1974). The results of the inversion are shown in Figures 3.18 through 3.26. It is evident that prior to 1800 MLT, only eastward current is detected, as shown by the curves of $\langle J(\theta) \rangle$. It is interesting to compare the profiles in Figure 3.20 to those

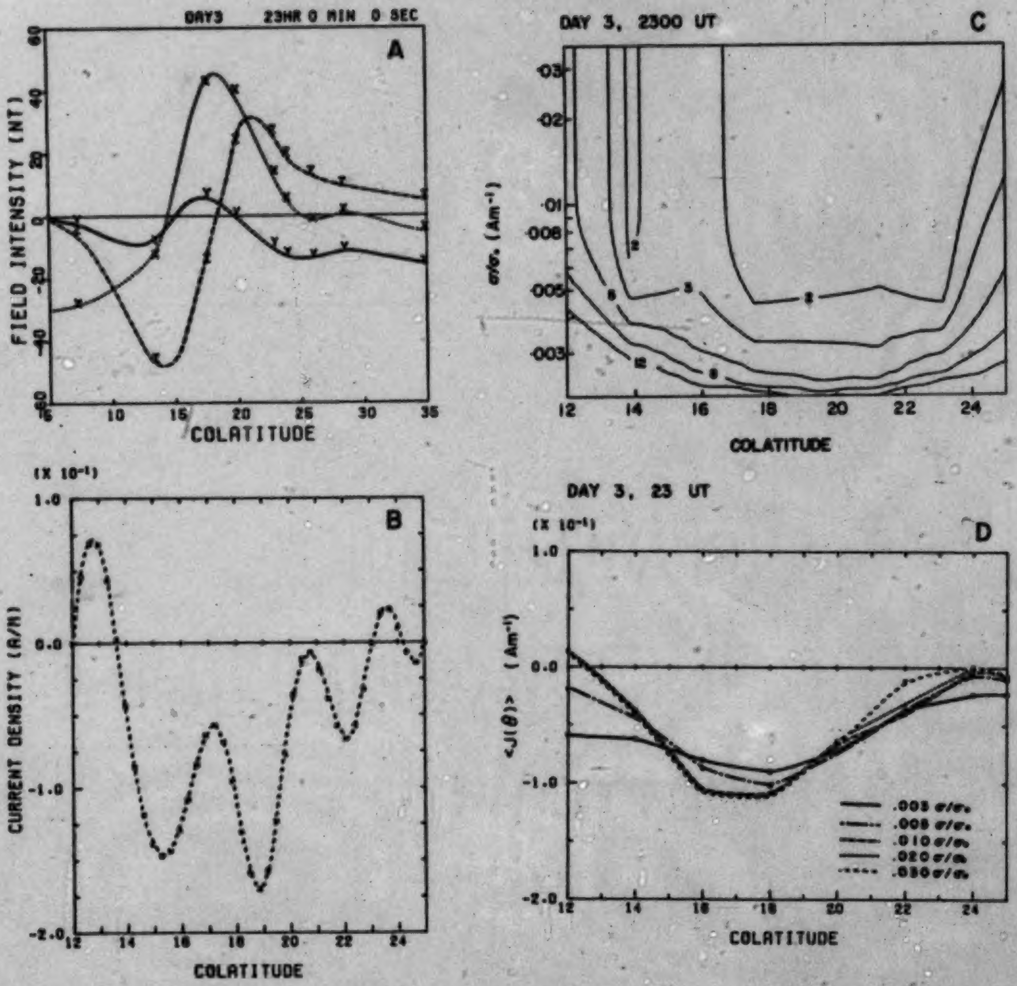

Figure 3.18 Results of inverting the hourly averaged latitude profile for 1500-1600 MLT (2300-2400 UT), Day 3, 1972.
(a) The latitude profile as a function of colatitude.
(b) The flattest height-integrated current density model.
(c) The standard deviation of the current estimates as a function of colatitude
(d) Estimates of height-integrated current density as a function of colatitude, contoured for constant standard deviation.

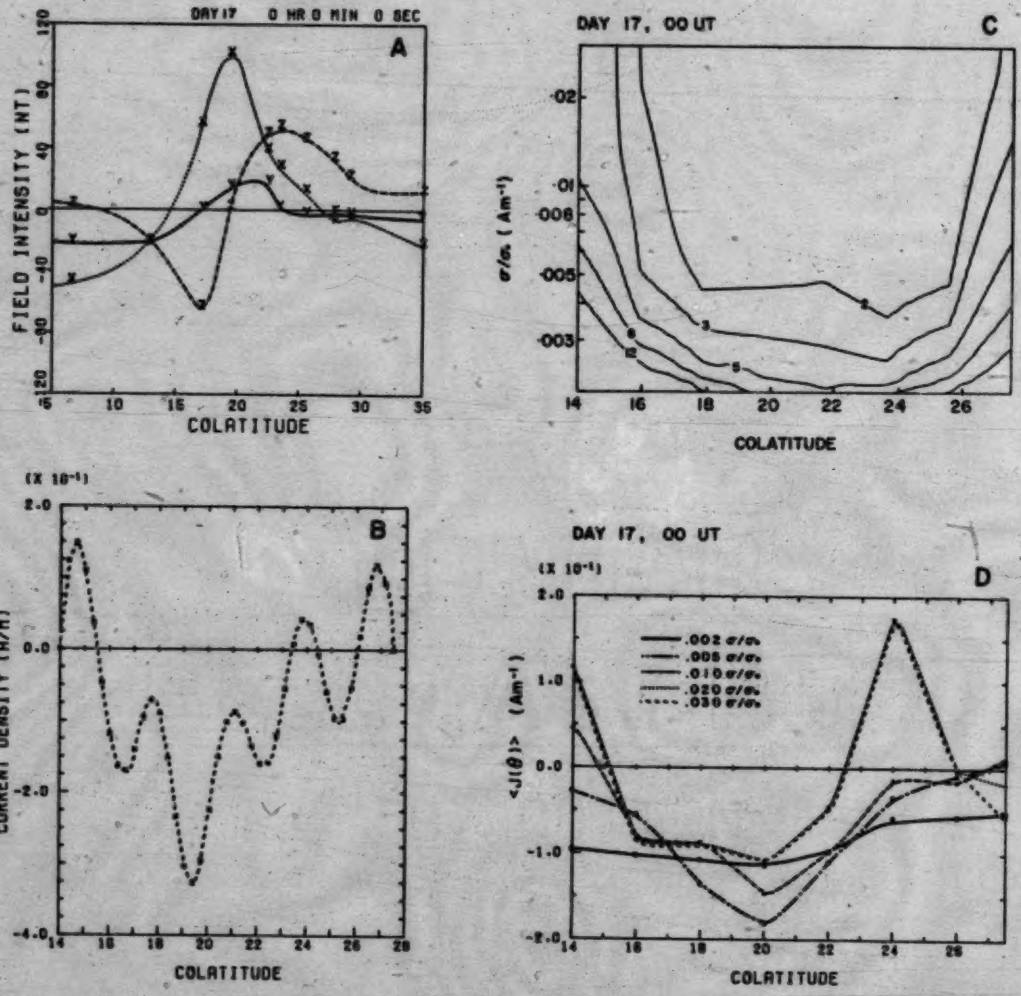

Figure 3.19 Results of inverting the hourly averaged latitude profile for 1600-1700 MLT (0000-0100 UT), Day 17, 1972.
(a) The latitude profile as a function of colatitude.
(b) The flattest height-integrated current density model.
(c) The standard deviation of the current estimates as a function of colatitude
(d) Estimates of height-integrated current density as a function of colatitude, contoured for constant standard deviation.

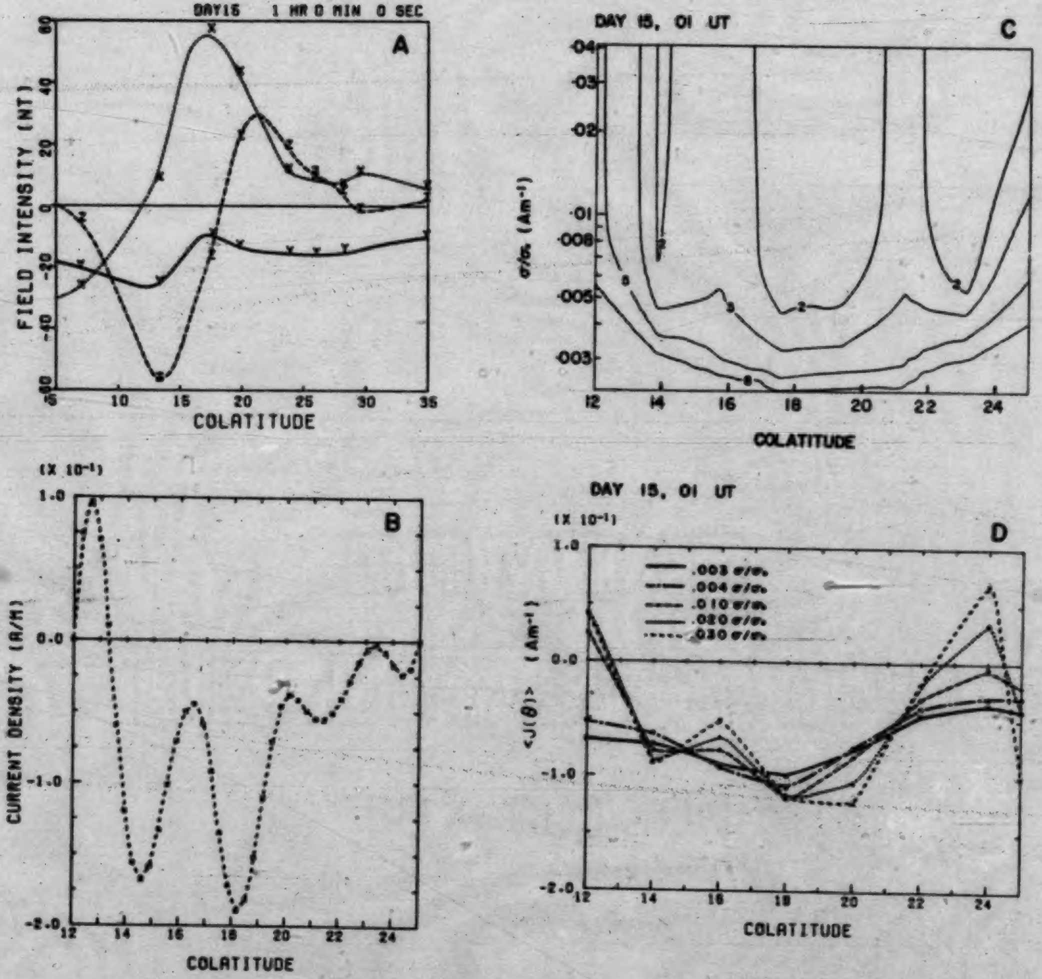

Figure 3.20 Results of inverting the hourly averaged latitude profile for 1700-1800 MLT (0100-0200 UT), Day 15, 1972.

(a) The latitude profile as a function of colatitude.

(b) The flattest height-integrated current density model.

(c) The standard deviation of the current estimates as a function of colatitude

(d) Estimates of height-integrated current density as a function of colatitude, contoured for constant standard deviation.

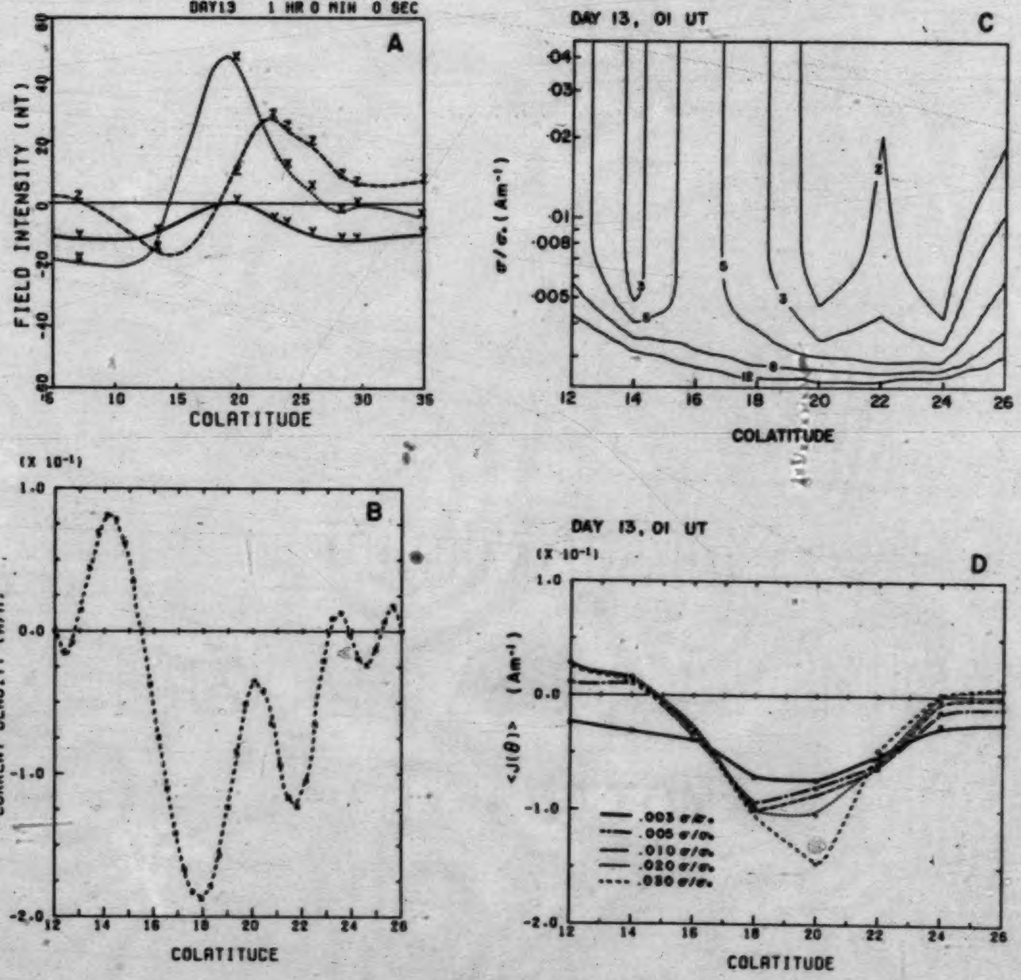

Figure 3.21 Results of inverting the hourly averaged latitude profile for 1700-1800 MLT (0100-0200 UT), Day 13, 1972.

(a) The latitude profile as a function of colatitude.

(b) The flattest height-integrated current density model.

(c) The standard deviation of the current estimates as a function of colatitude

(d) Estimates of height-integrated current density as a function of colatitude, contoured for constant standard deviation.

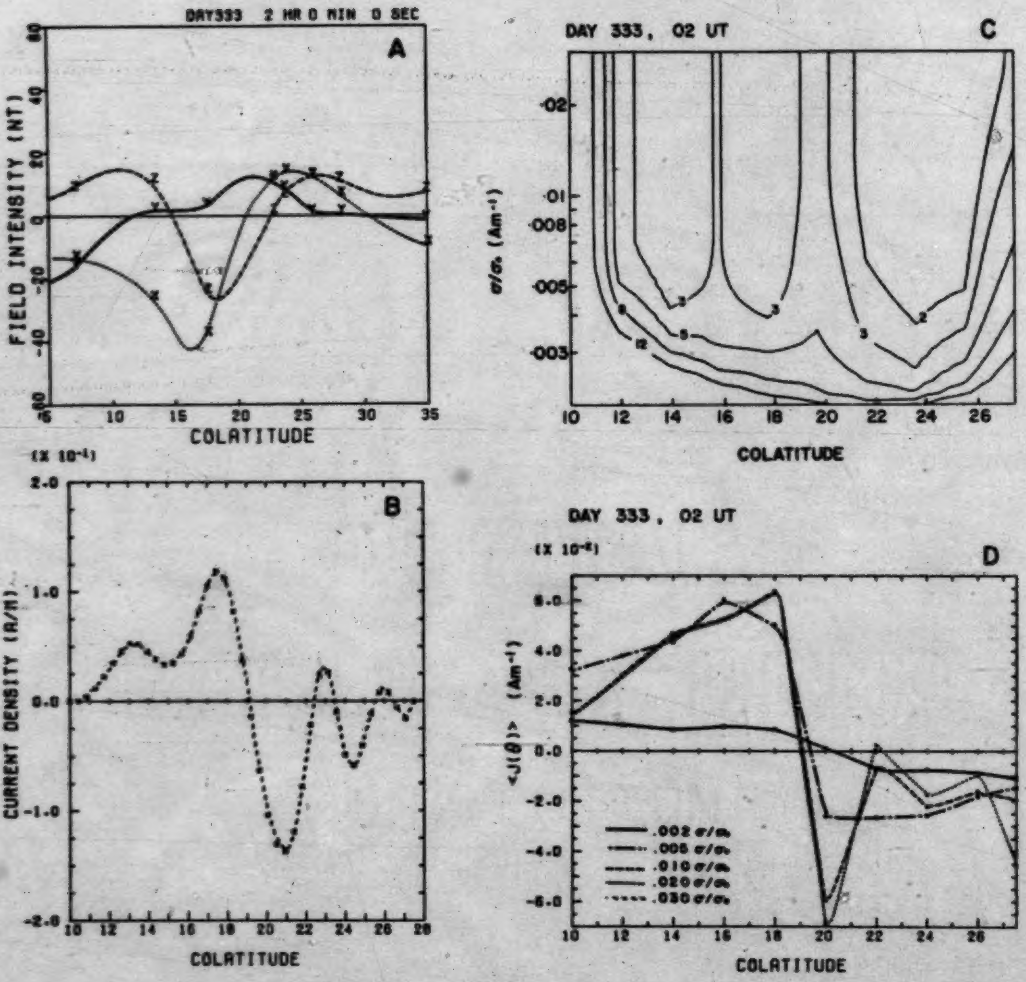

Figure 3.22 Results of inverting the hourly averaged latitude profile for 1800-1900 MLT (0200-0300 UT), Day 333, 1971.

(a) The latitude profile as a function of colatitude.

(b) The flattest height-integrated current density model.

(c) The standard deviation of the current estimates as a function of colatitude

(d) Estimates of height-integrated current density as a function of colatitude, contoured for constant standard deviation.

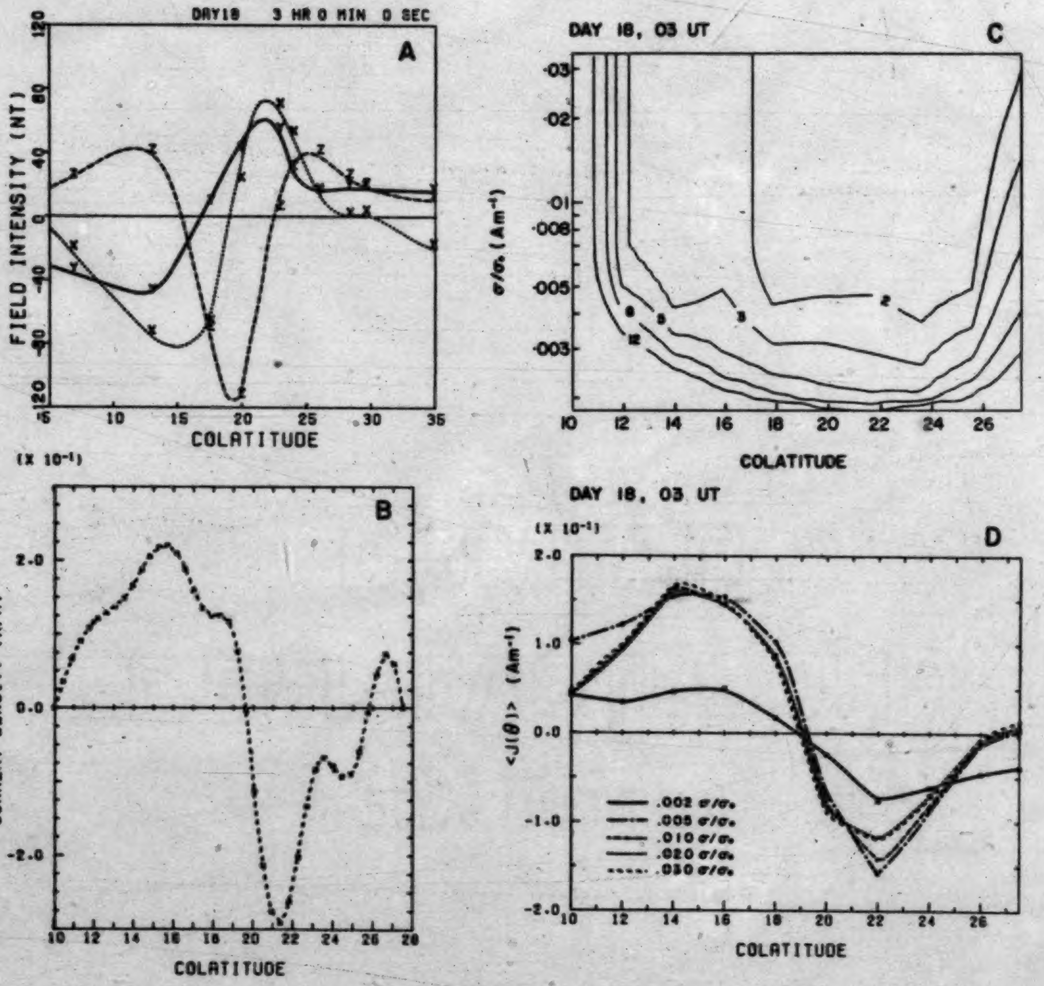

Figure 3.23 Results of inverting the hourly averaged latitude profile for 1900-2000 MLT (0300-0400 UT), Day 18, 1972.

(a) The latitude profile as a function of colatitude.

(b) The flattest height-integrated current density model.

(c) The standard deviation of the current estimates as a function of colatitude

(d) Estimates of height-integrated current density as a function of colatitude, contoured for constant standard deviation.

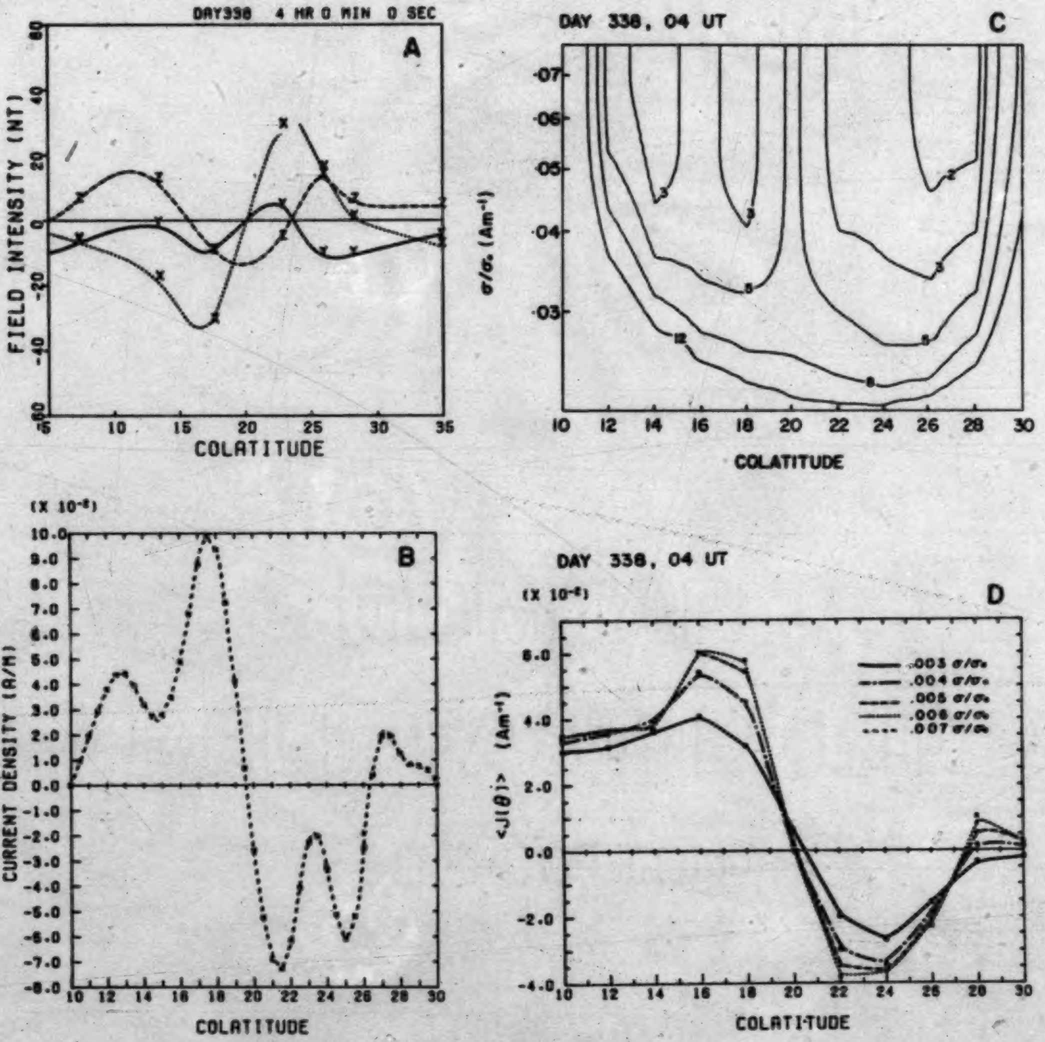

Figure 3.24 Results of inverting the hourly averaged latitude profile for 2000-2100 MLT (0400-0500 UT), Day 338, 1971.

(a) The latitude profile as a function of colatitude.

(b) The flattest height-integrated current density model.

(c) The standard deviation of the current estimates as a function of colatitude

(d) Estimates of height-integrated current density as a function of colatitude, contoured for constant standard deviation.

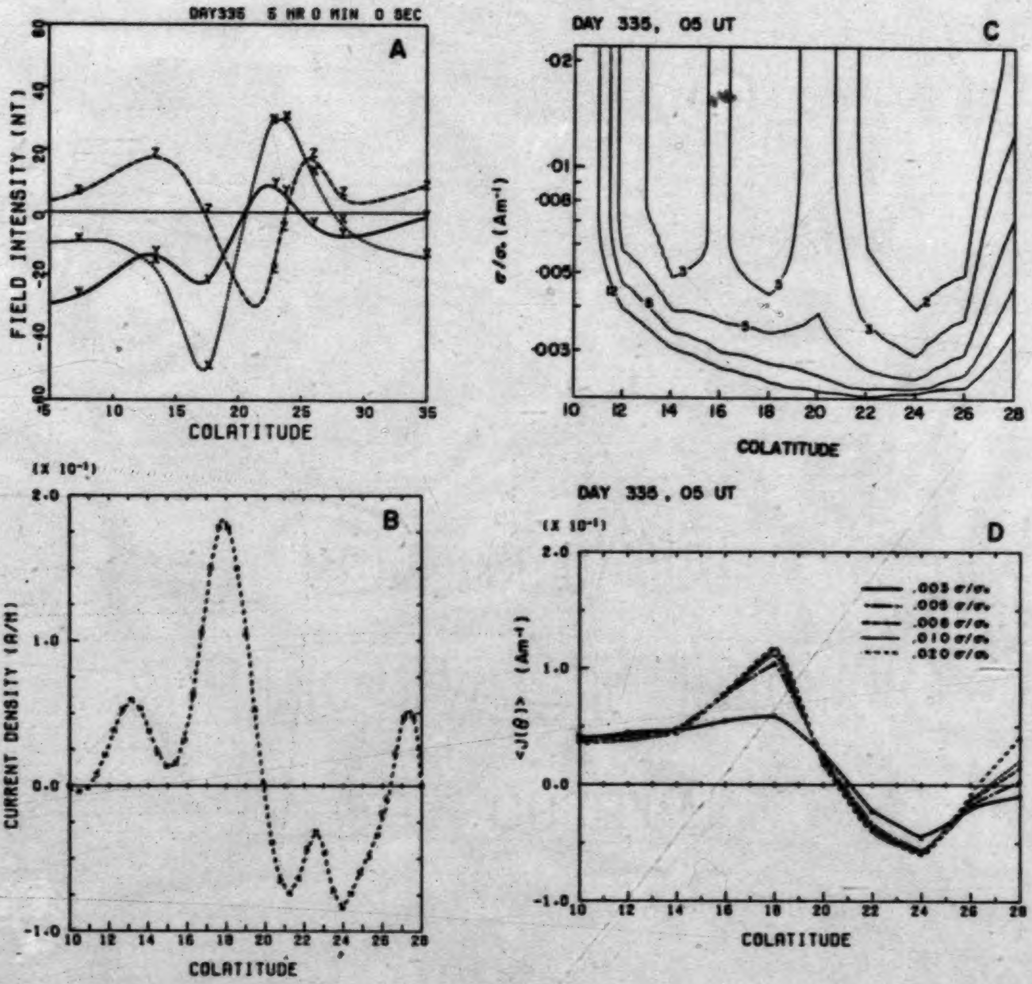

Figure 3.25 Results of inverting the hourly averaged latitude profile for 2100-2200 MLT (0500-0600 UT), Day 335, 1971.
(a) The latitude profile as a function of colatitude.
(b) The flattest height-integrated current density model.
(c) The standard deviation of the current estimates as a function of colatitude
(d) Estimates of height-integrated current density as a function of colatitude, contoured for constant standard deviation.

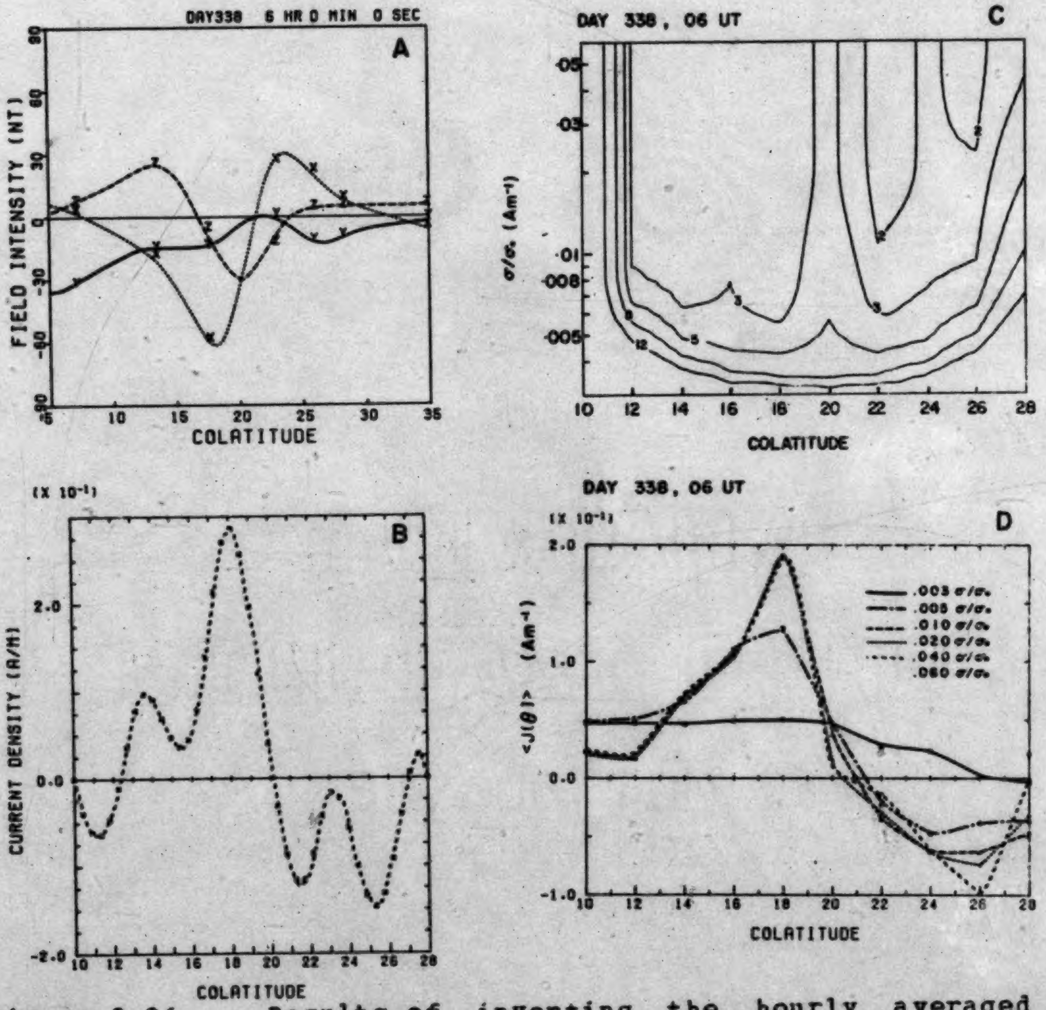

Figure 3.26 Results of inverting the hourly averaged latitude profile for 2200-2300 MLT (0600-0700 UT), Day 338, 1971.

(a) The latitude profile as a function of colatitude.

(b) The flattest height-integrated current density model.

(c) The standard deviation of the current estimates as a function of colatitude

(d) Estimates of height-integrated current density as a function of colatitude, contoured for constant standard deviation.

in Figure 3.21 for the hour 1700-1800 MLT. In Figure 3.21, there is a possibility of a westward current poleward of the main eastward electrojet, or this simply may be due to a westward current to the east of the magnetometer whose strength is large enough so that the resulting magnetic perturbations can be seen at the magnetometer line. For times later than 1800 MLT, the contours of $\langle J(\theta) \rangle$ show unambiguously that there is a westward electrojet flowing poleward of the eastward electrojet. The validity of the forward model used is somewhat open to question as evidenced by the oscillatory nature of the flattest model. However, such behaviour of the particular model does not detract in any great measure from the results of the actual inversion, as shown in Appendix II. Table 3.2 is a summary of the results of the inversions of latitude profiles in this sector. All cases included in this table are for times when no substorm activity was present in the magnetometer chain sector. The positive X'-component extremum varied from 10 nT to 100 nT, while the negative X'-component extremum varied from 10 nT to 105 nT.

Since the examples analysed in this study were for quiet or only moderately disturbed periods, as evidenced by the range of the X'-component peak values, the westward electrojet that has been detected in the dusk sector is not the substorm westward electrojet. Rather, these results show that the convection westward electrojet may penetrate as far westward as 1800 MLT. Previous workers (Kisabeth and

Table 3.2

Summary of the Results of Inverting Hourly Averaged Latitude Profiles

Interval (MLT)	Number of Cases	Current Direction (Eastward: E Westward: W)
1500 - 1600	4	E
1600 - 1700	4	E
1700 - 1800	3 1	E E+W
1800 - 1900	3	E+W
1900 - 2000	4	E+W
2000 - 2100	3	E+W
2100 - 2200	3	E+W
2200 - 2300	5	E+W

Rostoker,1973; Kamide and Akasofu,1976) have found substorm westward electrojets in this sector. The results of the inversion, together with these other results, make it imperative to include the westward current poleward of the eastward electrojet in the pre-midnight sector up to local dusk in any world-wide current model.

Chapter 4 A WORLDWIDE CURRENT MODEL

4.1 Introduction

In this chapter, the data and its interpretation outlined in the previous chapter, are synthesized to provide the input parameters for a world-wide three dimensional current model. The model is tested against the data inasmuch as the gross features of the data are reproduced. That is, no attempt is made to, say, least squares fit a model latitude profile to an observed profile. Rather, the comparison that has been made is one of comparing the magnitudes of the $\Delta X'$ extrema and the level-shift in $\Delta Y'$. This is justified in that the model is designed to reproduce only the gross features of current flow in the ionosphere. However, it is believed that suitable variation of the model parameters will lead to current models that will reproduce specific latitude profiles. Several examples of such current models are described to demonstrate this.

4.2 Elementary Considerations

4.2.1 The Auroral Oval

In order to develop a model of worldwide current flow, one must determine the direction of current flow and the geometry of the current systems. Chapter 3 has outlined the longitudinal distribution of eastward and westward current flow. However, it is also necessary to define the latitudinal extent of the current systems. From the superposed epoch analysis, and using the ΔZ extrema as indicators of the latitudinal boundaries of current (Kisabeth 1972), it is found that in general the east-west current systems are confined to a region about 5° wide in latitudinal extent. Furthermore, there is evidence that the eastward and westward ionospheric currents do not flow in a direction normal to the magnetometer line. That is, the Y'-component in the latitude profiles cannot be attributed solely to field-aligned current, but is in part due to a tilt of the main electrojet with respect to lines of constant latitude (see section 2.2 and Figure 2.6). Indeed, the electrojets are observed to flow along the auroral oval (Feldstein, 1963, Akasofu et al, 1965). Kisabeth (1972) modelled substorm current systems flowing along the auroral oval by representing the current path by a parabola given by

$$\theta = \frac{ab}{(b^2\cos^2\varphi + a^2\sin^2\varphi)^{1/2}} \qquad 4.1$$

Where θ is the colatitude of the boundary, φ is the longitude (measured counter-clockwise from midnight), a is the midnight colatitude (φ=0) and b is the dawn or dusk colatitude (φ=90° or φ=270° respectively). However, he was interested in currents of relatively short longitudinal extent (up to 20°), whereas the work presented here deals with currents of global longitudinal extent. Kamide and Fukushima (1970) have examined current flow along a path given by

$$\theta = \theta_1 + \tfrac{1}{2}(\theta_2 - \theta_1)(1 + \cos\varphi) \qquad 4.2$$

where θ and φ are as given above, and θ_1 is the colatitude of the path at noon (φ=180°) and θ_2 is the colatitude at midnight (φ=0°). Since small scale current structures are of little concern in this thesis, equation 4.2 is ideally suited for describing the auroral oval since a single specification of θ_1 and θ_2 suffices to describe an entire oval boundary.

In the midnight sector, it is believed that there is a component of poleward flow and that both eastward and westward electrojets coexist. To accommodate such currents, a separate specification of boundaries is required, but equation 4.2 may also be used to describe the path. Figure 4.1 is a polar plot of the auroral oval boundaries used in this thesis and table 4.1 gives the parameters that describe these boundaries (Since the polar plot is in terms of latitude, the table lists latitudes (λ) instead of colatitude (θ)).

4.2.2. Location of Currents

The nature of the ionospheric current flow is based on the interpretation of the latitude profiles given in the previous chapter. Westward current flows from noon around to midnight where it flows poleward and westward across the midnight sector to 2200 MLT. This flow then continues westward to 1800 MLT. Eastward current flows from noon

Table 4.1

Boundaries of the Model Auroral Oval

LONGITUDE (MLT) (degrees)	(hours)	DESCRIPTION	POLAR BOUNDARY (° latitude)		EQUATORWARD BOUNDARY (° latitude)	
			λ_1	λ_2	λ_1	λ_2
0-180	(00-12)	Main westward current	75.0	70.0	70.0	65.0
180-315	(12-21)	main eastward current	75.0	70.0	70.0	65.0
270-315	(18-21)	Pre-midnight westward current	73.0	73.0	75.0	70.0
315-360	(21-24)	Harang region westward current	90.5	70.0	104.1*	65.0
315-360	(21-24)	Continuation of eastward current	104.1*	65.0	70.0	65.0

*This value is not truly a latitude, but is the value that λ must have in this longitude regime to correctly define the boundary.

Figure 4.1 Polar plot of the auroral oval used for modelling purposes. The boundaries follow the locus $\theta = \theta_1 + 1/2(\theta_2 - \theta_1)(1 + \cos\varphi)$ where θ is colatitude and φ longitude, measured counterclockwise from midnight. θ_1 and θ_2 are the colatitudes at noon and midnight respectively. The values of θ_1 and θ_2 are given in Table 4.1.

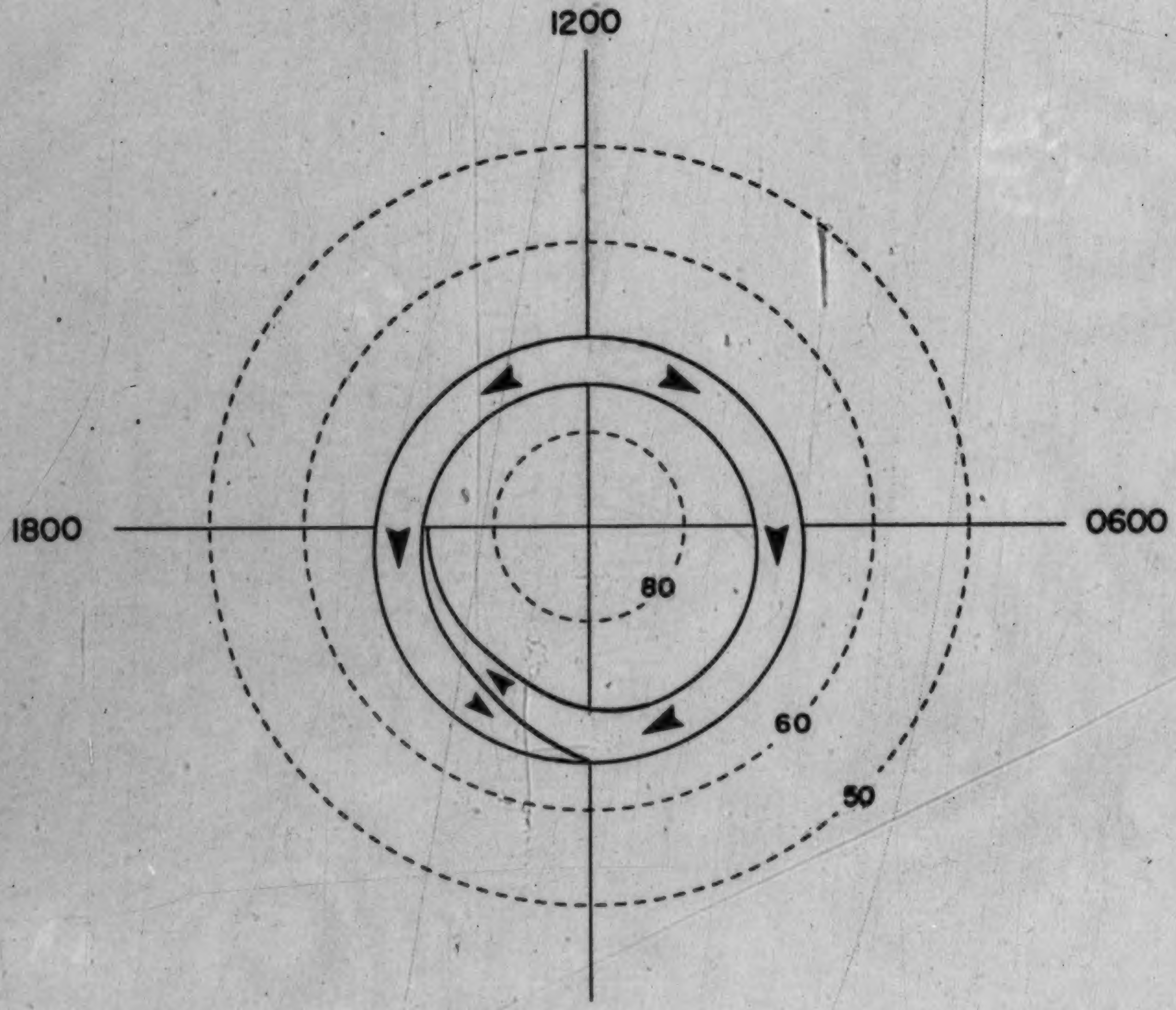
1800

around through dusk to 2200 MLT and then northward and eastward to the equatorward boundary of the midnight sector westward electrojet, terminating at 2400 MLT. Both the eastward and westward electrojets are one segment of a three dimensional current loop similar to that used by Kisabeth (1972). However, the field-aligned currents connecting the ionospheric electrojets to the magnetosphere are not confined to sheets at the ends of the ionospheric currents but are in general distributed over the length of these currents. Thus in this model, the electrojets are assumed to grow and decay over a finite longitudinal extent, as described in Chapter 3.

From the nature of the electric field configuration in the auroral zone (see figures 3.12 and 3.13), it is apparent that the eastward and westward electrojets are essentially Hall currents, so that for a complete current model, one must also account for the currents in the direction of the electric field, the so-called Pedersen currents. Indeed, recent observations by the Triad satellite (Iijima and Potemra, 1976) indicate that the auroral oval is bounded by regions of field-aligned current (Figure 4.2). These currents close in the ionosphere through north-south currents. In the model which has been developed for this thesis, all east-west ionospheric currents are bounded by infinitesimally thin sheets of field-aligned current which are in turn connected by north-south ionospheric current. In regions of westward current flow, there is downward field-

Figure 4.2 The location of field-aligned current sheets as deduced from magnetometer data from the polar-orbiting Triad satellite (From Iijima and Potemra, 1978) The panel on the left is for low level activity (AL<100), and that on the right for higher activity (AL>100).

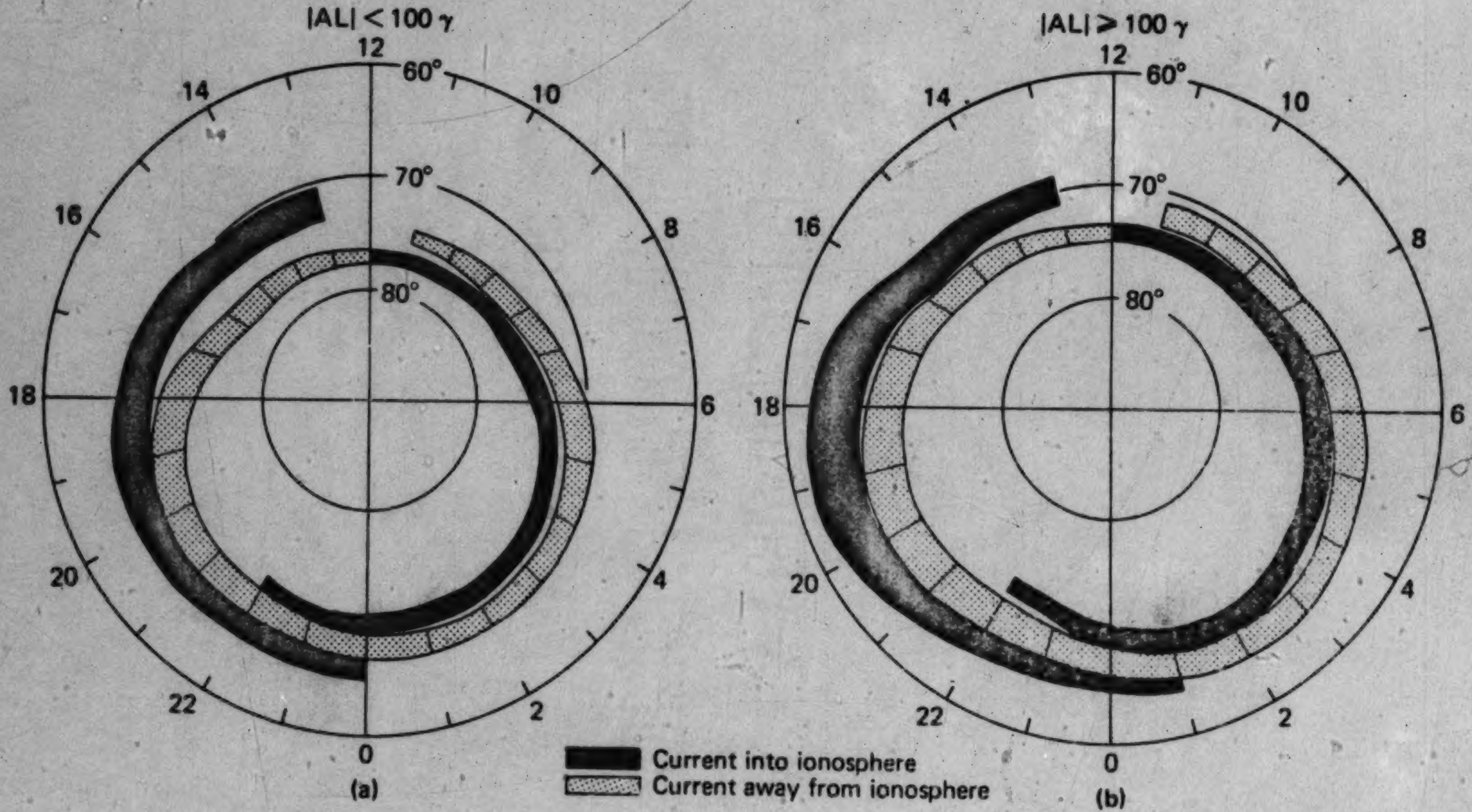
|AL| < 100 γ
|AL| ≥ 100 γ
12
60°
70°
80°
10
8
6
4
2
0
22
20
18
16
14
(a)
(b)
Current into ionosphere
Current away from ionosphere

aligned current along the poleward boundary and this diverges equatorward in the ionosphere, across the electrojet, and up field lines at the equatorward boundary of the electrojet. In regions of eastward ionospheric current, the north-south current system is reversed.

As well as these large scale currents, two other current systems are involved in this global model. Rostoker and Hron (1975) have shown that there is a weak eastward current equatorward of the main westward electrojet in the dawn sector. This current system is believed to be a signature of electron precipitation associated with a reconfiguration of the magnetosphere after a period of strong activity. On a statistical basis then, the strength of this current system would average out to be relatively weak, and it has been included in the model only as a very weak current system. An additional current system which may be similar to S_q^p or DP-2 has also been added to the model and the reasons for including this system will be discussed at length later in this chapter.

Current in the polar cap (the region from the north pole to the poleward boundary of the auroral oval) has not been included in this model. All the magnetic data which has been used in formulating the current model is winter data, and during this period, the polar cap is essentially dark throughout the day. Figure 4.3 shows the sunlit-dark terminator for 1900 UT at its extreme positions during the period of Day 332 1971 to Day 23 1972. Thus, there is little

Figure 4.3 The extreme positions of the sunlit-dark terminator for the period from Day 332, 1971 to Day 24, 1972, at an altitude of 115 km. The solid lines oriented from left to right indicate the terminator, and the dotted line is the position of the poleward border of the model auroral oval. The approximate location of the magnetometer line is shown for 1700 UT, and the location of the Greenwich Meridian is shown at 0° longitude.

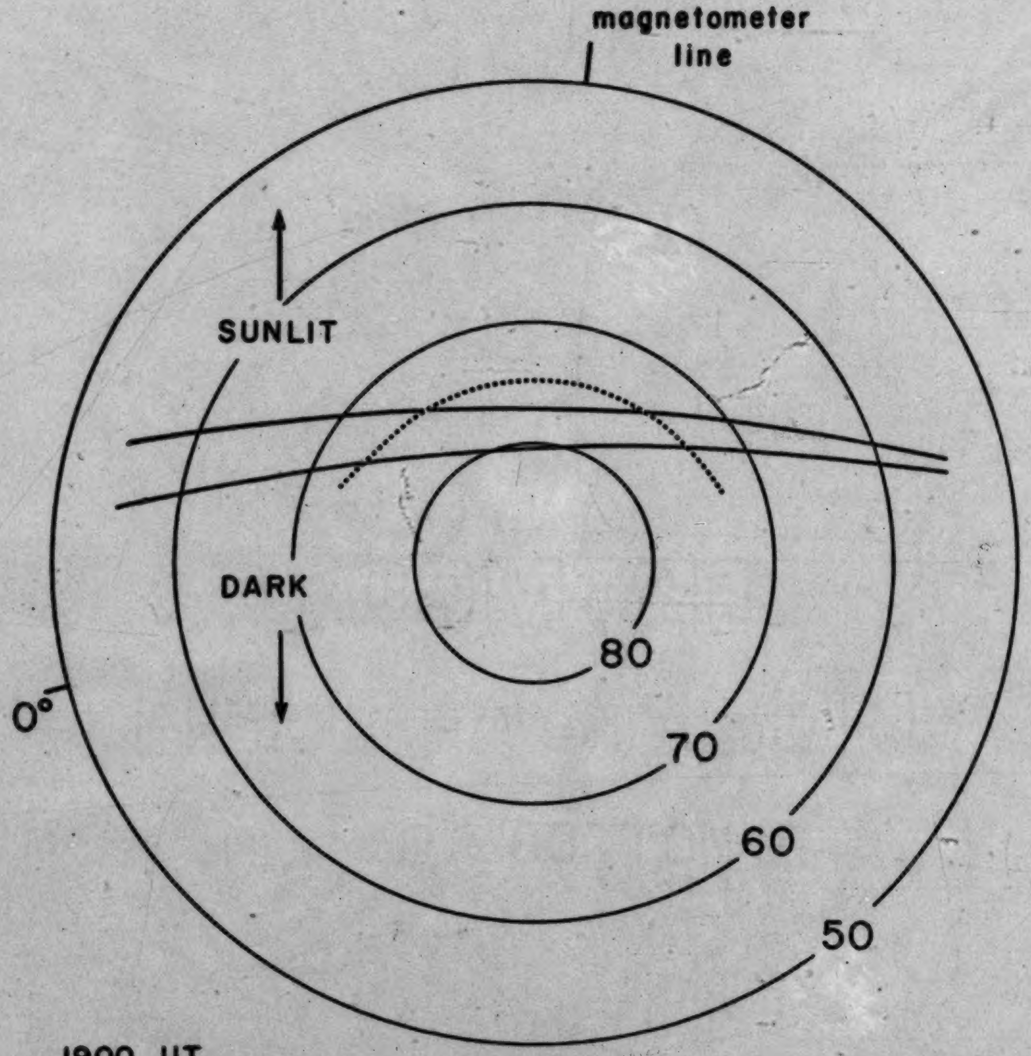
magnetometer line
SUNLIT
DARK
0°
80
70
60
50

1900 UT
extreme positions of the terminator

if any solar ultra-violet radiation reaching the polar cap upper atmosphere and therefore there is little if any photo-ionization. This in turn means that there is little if any polar cap conductivity, and therefore no significant polar cap current.

4.2.3 The Electric Field and Conductivity Model

Mozer and Lucht (1974) and Iversen and Madsen (1977) have published data on the auroral zone electric field. When the research for this thesis was initiated only the former data were available and these data were used as the electric field model required in modelling the currents. The electric field consistent with the global current model is shown in figure 4.4. This polar plot shows only the unit vectors of the electric field because to define the electric field explicity, one requires an explicit model of the conductivity. This will be dealt with in detail in section 4.3.

Figure 4.4 is most easily compared with the data of Iversen and Madsen (1977) (Figure 3.13). In the region of the auroral zone the model electric field is in reasonable agreement with the real data. Note that the model electric field immediately equatorward of the auroral zone in the dawn sector is essentially eastward. This is in keeping with the work of Rostoker and Hron (1975) in which it is shown that the dawn eastward electrojet is a Pedersen current. The east-west component of the low latitude electric field is

Figure 4.4 Polar plot of the unit vectors of the electric field used in the auroral current flow model.

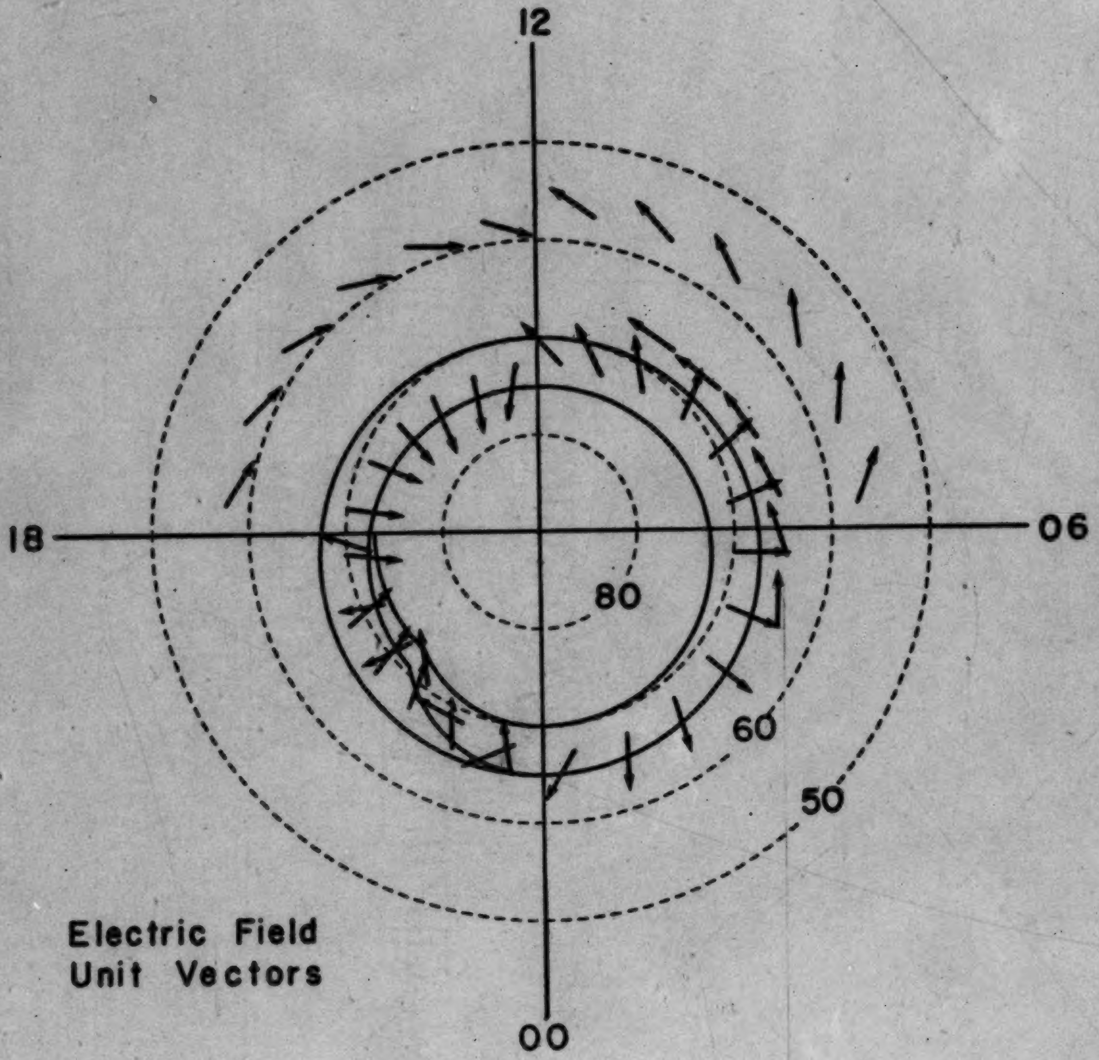

Electric Field
Unit Vectors

directed towards noon in all instances, and the north-south component is equatorward in the morning and poleward in the afternoon. This is qualitatively in agreement with the ion drift velocity measurements of Heelis et al (1976). As well, an electric field of this configuration, for a ratio of height-integrated conductivities (Hall to Pedersen) of 2, drives currents which are similar to the S_q^p system.

The conductivity was not absolutely defined in this model. However, the ratio of the height-integrated Hall conductivity to Pedersen conductivity was taken to be 2 everywhere. Brekke et al (1974) have shown that for low magnetic activity, this ratio holds in the auroral zone. Yasuhara et al, (1975) similarly have used this same height-integrated conductivity ratio in the auroral zone and sub-auroral latitudes. Since the current model developed for this thesis is a model for average conditions, the ratio of 2 is well justified.

4.3 The Approach to Current Modeling

As described in the previous chapter, a basic concept of what east-west and field-aligned currents were flowing had been established and it was also pointed out that there exist north-south currents which significantly influence the magnetic perturbation pattern. The approach taken in developing this model was to generate magnetic perturbations from all currents believed to be present in the ionosphere and magnetosphere and combine these to produce a total perturbation field. The currents could not all be chosen independently of one another; that is, current continuity had to be maintained. This approach is similar to that used by Kisabeth (1972) to model substorms, but it is unlike that used by Yasuhara _et al_ (1975) in which a global model of height-integrated Hall and Pedersen conductivities was assumed, along with a field-aligned current model, to solve the equation

$$\nabla \cdot \underset{\sim}{I} = J_{\parallel}$$

where $\underset{\sim}{I}$ is the ionospheric height-integrated current density and $J_{\parallel}$ the field-aligned current density.

In this thesis, $\underset{\sim}{I}$ in the east-west direction has been assumed, and $J_{\parallel}$ has been derived to afford current continuity. To determine the north-south component of $\underset{\sim}{I}$, the electric field model and ratio of height-integrated conductivities has been invoked. Consider a coordinate system in which x is directed northward, y eastward and z down. The horizontal height-integrated current density is given by

$$\underset{\sim}{I} = \Sigma_P \underset{\sim}{E} + \Sigma_H \frac{\underset{\sim}{B} \times \underset{\sim}{E}}{B} \qquad 4.3$$

where Σ_H and Σ_P are the height-integrated Hall and Pedersen conductivities respectively, $\underset{\sim}{E}$ is the horizontal electric field vector, and $\underset{\sim}{B}$ the magnetic induction field vector. If $\underset{\sim}{B}$ is chosen as $\underset{\sim}{B} = B\hat{z}$, then

$$I_x = \Sigma_P E_x - \Sigma_H E_y \qquad 4.4$$

$$I_y = \Sigma_H E_x + \Sigma_P E_y \qquad 4.5$$

Dividing equation 4.5 by 4.4

$$\frac{I_y}{I_x} = \frac{\Sigma_H/\Sigma_P + E_y/E_x}{1 - (\Sigma_H/\Sigma_P)(E_y/E_x)} \qquad 4.6$$

Thus, if one component of the horizontal current is assumed known, then one need only specify the ratio of the electric field components and the ratio of the height-integrated conductivities. The value of E_y/E_x is the tangent of the angle that $\underline{E}$ makes with the x-axis, and because of this, only unit vectors have been shown in figure 4.4.

It should be pointed out that since the locus of east-west current flow is not along parallels of latitude (see equation 4.1), before equation 4.6 may be used, a correction must be applied to the east-west height-integrated current density. That is, the auroral oval has an azimuthal deflection angle (α) from a latitude circle given by

$$\alpha = \tan^{-1}\left(\frac{\theta_2 - \theta_1}{2}\sin\varphi\right) \qquad 4.7$$

and care must therefore be taken in specifying the true east-west current density.

When, from the ground based data, it was determined that the east-west current was varying in longitude, this variation has been assumed to be linear. There is no evidence available concerning the exact nature of the longitudinal variation of the convection electrojets, and so the simplest variation possible, but one still able to reproduce the observations, has been chosen.

In the model developed for this thesis, ionospheric current is assumed to flow in a sheet of infinitesimal vertical extent; that is, the current is height-integrated. One must therefore decide at what altitude this ionospheric current sheet must be placed. Kamide and Brekke (1977) have examined radar data and found that on average, the westward electrojet is situated at 120 km, and the eastward jet at 100 km. For both electrojets, Kisabeth (1972) has used the value of 115 km. In this thesis, it has been assumed that the ionospheric sheet currents flow at an altitude of 115 km. Any error in the results due to an incorrect value of the current altitude will be less than 10% (Kamide and Brekke 1977).

To produce the most reliable quantitative current model, it is desirable to include the effects of currents induced in the earth. As discussed in the previous chapter, induction effects have been included by placing an infinitely conducting sphere at depth. For calculation of model substorm fields, Kisabeth (1972, 1975) and Kisabeth and Rostoker (1977) used a depth of 250 km, based on the fact that this depth gives the best fit between model calculations and real data. In the modelling for this thesis, a depth of 600 km has been used throughout. This too is an empirical result, giving the best qualitative fit of the model to the data, when cases dominated by pure overhead electrojet flow are considered. Indeed, since this work is concerned with only slowly varying pertubations inasmuch as all the data is hourly averaged, one might expect that the induction effect would be less than for the case of substorm modelling.

4.4 The Basic Current Systems

In this section, the main current systems employed in the model will be described at some length. Basically there are 5 main currents; i) the westward flowing current, which flows from noon through midnight to dusk; ii) the eastward flowing current, which flows from noon to midnight; iii) the north-south current associated with each of the above east-west currents; iv) the current which flows equatorward in the morning sector and poleward in the afternoon sector, and v) an eastward current in the dawn sector.

4.4.1 The Westward Current System.

It will be recalled from Chapter 3 that the ground based data for the time period noon through dawn to approximately midnight had been interpreted basically as a growing westward current. However, near dawn (approximately 0800 MLT for winter) there was a marked decrease in the magnitude of the peak of the superposed epoch $\Delta X'$ profile. It is not perfectly clear what causes this decrease, but the following is offered as a possible explanation.

Currents flow in the auroral oval because this region of the atmosphere has an enhanced electrical conductivity relative to the rest of the atmosphere. This conductivity is brought about by the precipitation of charged particles from the magnetosphere which, through collisional processes, produce charge carriers in the ionosphere. As well as this, where the upper atmosphere is sunlit, solar ultra-violet (UV) radiation may produce charge carriers in the atmosphere through photo-ionization processes. Thus, up to dawn (and symmetrically, up to dusk), there are two sources of conductivity, solar UV and particle precipitation. Away from dawn (and dusk), towards midnight, only particle precipitation is available to produce electrical conductivity so that near the dawn and dusk terminators there is a gradient in conductivity (probably over a narrow region). As well, there is a gradient in the electric field near dawn and dusk, (see Figure 3.13(a)). In order to accommodate these gradients in the conductivities and the electric field, current flows up field lines. Thus there is a reduction in the magnitude of the ionospheric current, and a corresponding reduction in the peak of the X'-component, as observed.

In the global current model, it has been assumed that both the Hall and Pedersen conductivities vary in such a manner that their ratio remains constant. In section 4.6.1 of this chapter, the effect of this reduction in electrojet strength will be examined in more detail. Figure 4.5 is a plot of current intensity as a function of time for both the eastward and westward electrojets. It is seen that the westward jet (the curve with values everywhere less than

Figure 4.5 The model height-integrated current density for the east-west currents, as a function of MLT. The current densities for both the eastward current (values > 0) and the westward current (values < 0) are shown.

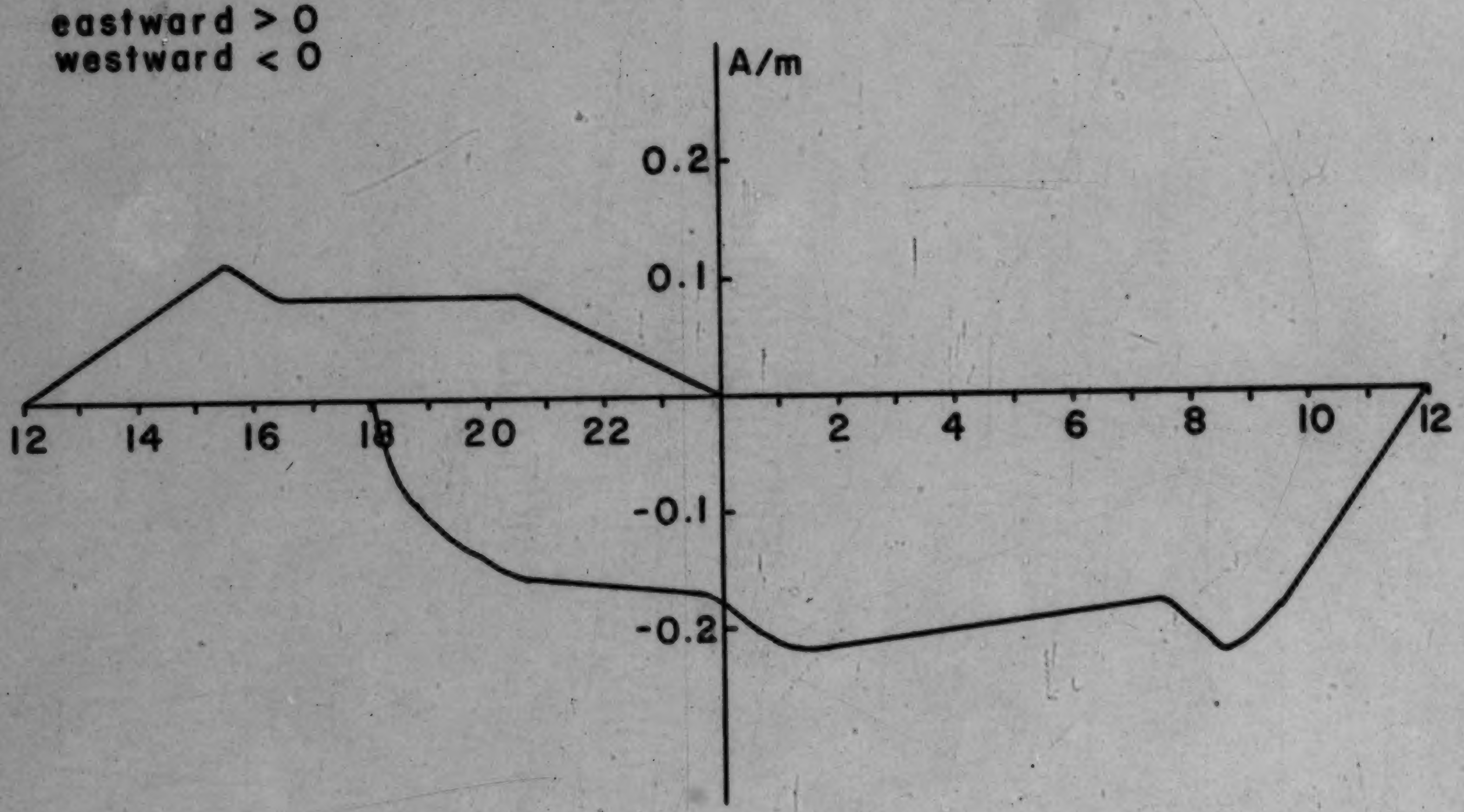

IONOSPHERIC CURRENT INTENSITY vs MLT

zero) exhibits variations over its entire length. From noon to about 0800 MLT, the current density increases linearly from 0.0 to 0.221 Am^{-1}. In this sector, the width is constant at 5° of latitude, so the current here ranges from 0.0 A to $1.25x10^{5}$A. Near 0800 MLT, there is a 20% reduction in the total current, with a concomitant reduction in the height-integrated current density. As a result, $2.5x10^{4}$A is fed out of the ionosphere in a field-aligned current sheet. This field-aligned current is most likely distributed over a finite longitudinal range, but this range cannot be determined from the available data. In lieu of this, the upward flowing current is replaced by an equivalent upward flowing current sheet.

From 0800 MLT to 0100 MLT, the westward current continues to grow back to its peak value in the sunlit sector. That is, the total current increases from $1.00x10^{5}$A at 0800 MLT to $1.25x10^{5}$A at 0100 MLT.

Over the entire region discussed so far, since the westward current is growing, there must be a downward field-aligned current feeding the westward jet, (apart from the upward current sheet at 0800 MLT). Since the ionospheric current grows most rapidly in the sector from noon to 0800 MLT, this is obviously where the greatest inward field-aligned current flows. Figure 4.6 is a plot of field-aligned current density as a function of magnetic local time. It is clear that between midnight and 0800 MLT, very little field-aligned current flows into the ionosphere. This field-

Figure 4.6 The model unbalanced field-aligned current densities that connect with the east-west current systems, as a function of MLT. ⊗ denotes downward field-aligned current, and ⊙ upward field-aligned current.

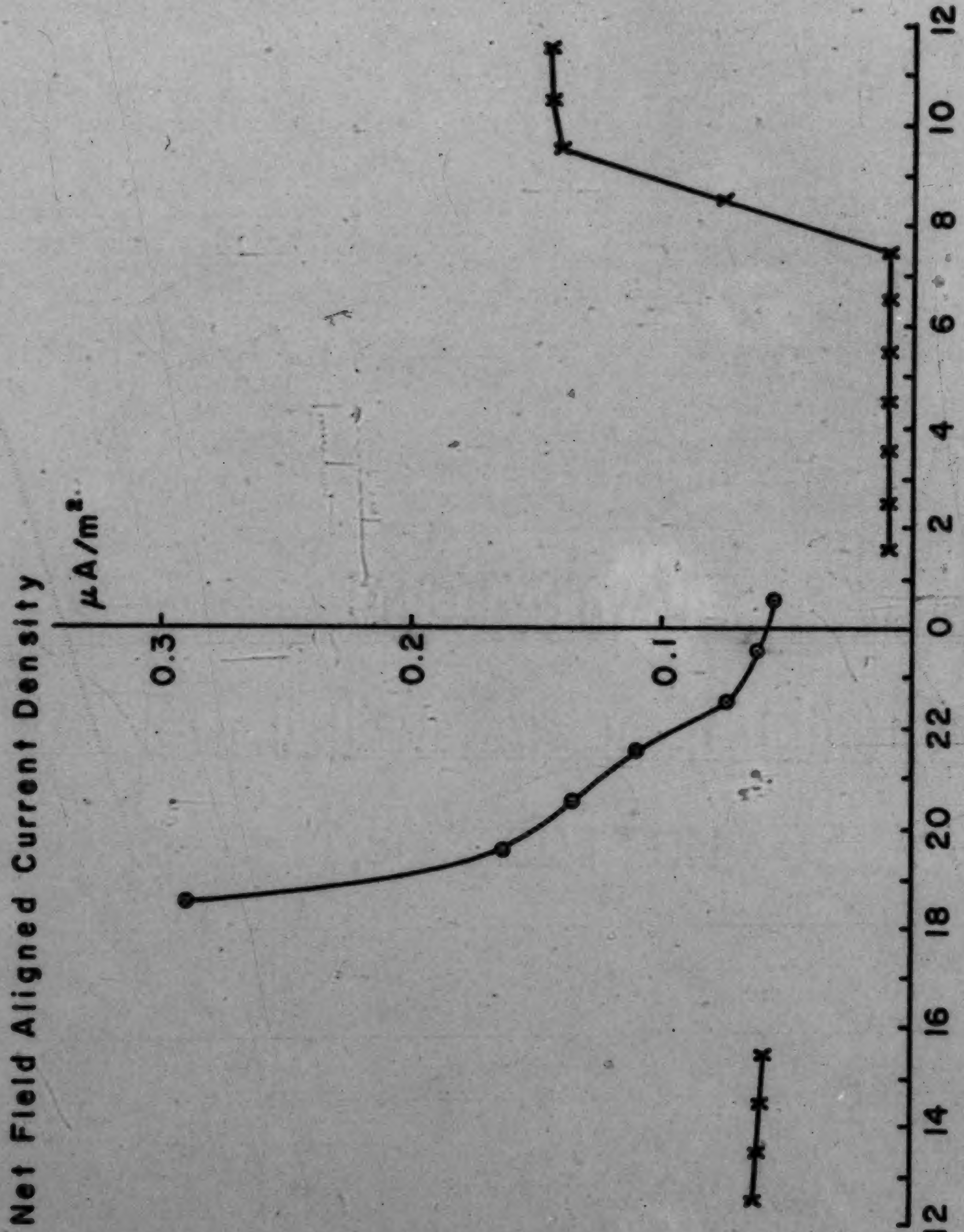
Net Field Aligned Current Density
μA/m²
0.3
0.2
0.1
12
14
16
18
20
22
0
2
4
6
8
10
12
MLT

aligned current which feeds the electrojet is a local net field-aligned current inasmuch as if one were to integrate along a meridian, there is an imbalance in the field-aligned current flow.

Referring to figure 4.5 again, it is seen that the westward current intensity generally decreases from 0100 MLT to 1800 MLT. In fact, the total current flowing across a meridian in this sector decreases linearly from $1.25\text{x}10^5$A at 0100 MLT, to 0.0 A at 1800 MLT. The non-linear variations in the current intensity come about from variations in the width of the westward current in this regime. In this sector, field-aligned current must flow out of the ionosphere, and the outward field-aligned current density is shown by the open circles in figure 4.6. The variations in this curve are again due to the varying width of the current. In fact, the upward flowing current as a function of longitude is constant. The high current density at 1800 MLT is due solely to the extremely narrow (0.5°) latitudinal extent of the electrojet at this point.

Superimposed on this entire westward electrojet system is a north-south current system. In accordance with the procedure outlined earlier, the current flowing in the north-south system was obtained directly from the electric field and conductivity models. Figure 4.7 is a plot of the global north-south current system plotted in terms of the field-aligned current contribution. The curves of immediate interest are the upper two curves in the pre-midnight hours

Figure 4.7 The field-aligned current strength for the north-south current systems as a function of MLT. ⊙ denotes upward field-aligned current, and ⊗ indicates downward field-aligned current. The dashed line represents current flow at the equatorward border of the auroral oval, and the solid line indicates current flow at the poleward border of the auroral oval.

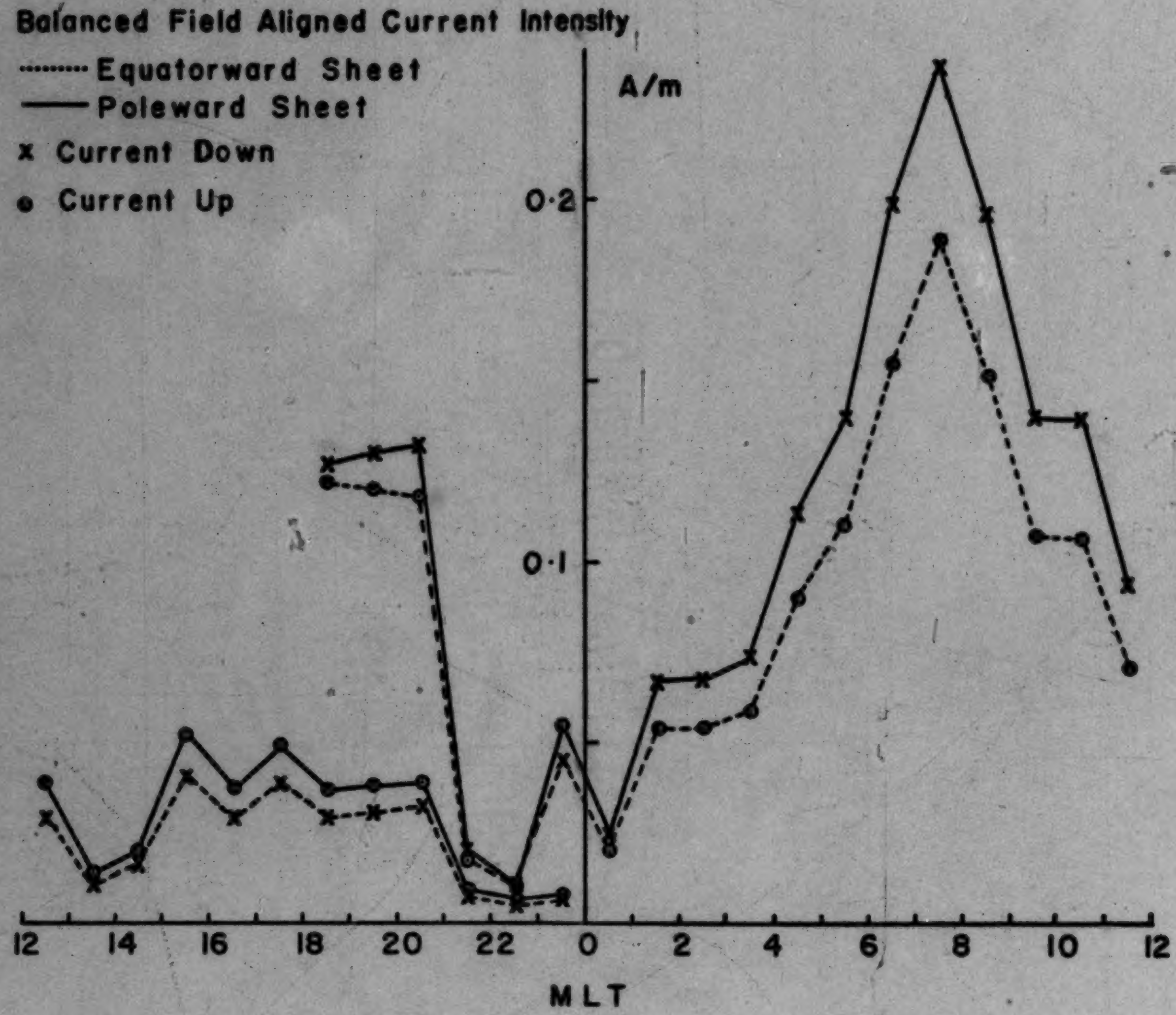
Balanced Field Aligned Current Intensity
Equatorward Sheet
Poleward Sheet
x Current Down
● Current Up
A/m
0·2
0·1
12
14
16
18
20
22
0
2
4
6
8
10
12
MLT

and their continuation into the post-midnight hours. Note that the downward current density is greater than the upward. This is due to the fact the southward flowing current flows along meridians and therefore diverges, so that for a constant current, the current density varies as the sine of the colatitude.

The 24 panels of Figure 4.8 are the model latitude profiles for the westward flowing currents, including the associated "net" field-aligned currents, but excluding the north-south currents. The features that one might expect from knowledge of the current distribution are evident in these profiles. There is a decrease in the X'-component extrema from 0900 MLT to 0800 MLT (Figure 4.8(j) and Figure 4.8(i) respectively). Because of the presence of unbalanced, downward field-aligned current from 0100 to noon MLT, one would expect a positive going level shift (north-to-south) in the east-west component. This in fact is seen only up to 0300 MLT; the model profiles for 0100 and 0200 MLT show either a weak negative going shift in $\Delta Y'$, or no shift at all. This is due to the strong upward field-aligned current in the midnight sector, completely masking the weak downward current in the post-midnight sector. Indeed, the positive-going level-shift is seen beyond noon, spilling over as an end-effect into the 1300 MLT and perhaps 1400 MLT sector. However, the magnitude of all these level-shifts appears small relative to those suggested by the real data. This could be due to one or both of two possibilities: (1) there

Figure 4.8 Model latitude profiles due to the complete westward current system (including the ionospheric and field-aligned currents).

a) 0000 to 0100 MLT
b) 0100 to 0200 MLT
c) 0200 to 0300 MLT
d) 0300 to 0400 MLT
e) 0400 to 0500 MLT
f) 0500 to 0600 MLT

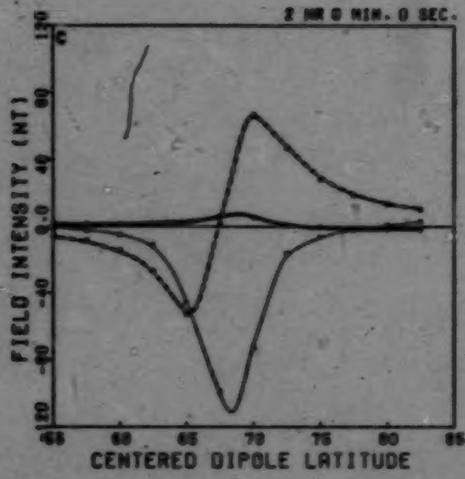
C
2 HR 0 MIN. 0 SEC.
FIELD INTENSITY (NT)
120
80
40
0.0
-40
-80
-120
55
60
65
70
75
80
85
CENTERED DIPOLE LATITUDE

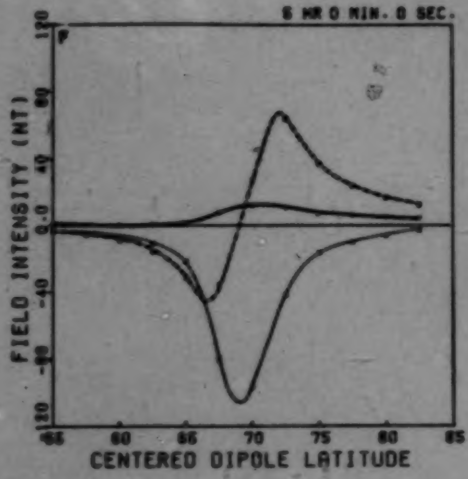
F
5 HR 0 MIN. 0 SEC.
FIELD INTENSITY (NT)
120
80
40
0.0
-40
-80
-120
55
60
65
70
75
80
85
CENTERED DIPOLE LATITUDE

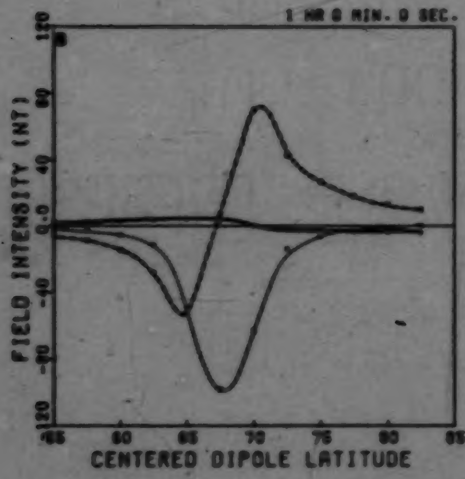
B
1 HR 0 MIN. 0 SEC.
FIELD INTENSITY (NT)
120
80
40
0.0
-40
-80
-120
55
60
65
70
75
80
85
CENTERED DIPOLE LATITUDE

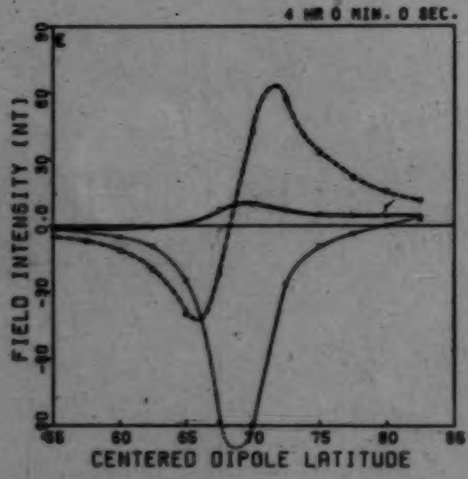
E
4 HR 0 MIN. 0 SEC.
FIELD INTENSITY (NT)
90
60
30
0.0
-30
-60
-90
55
60
65
70
75
80
85
CENTERED DIPOLE LATITUDE

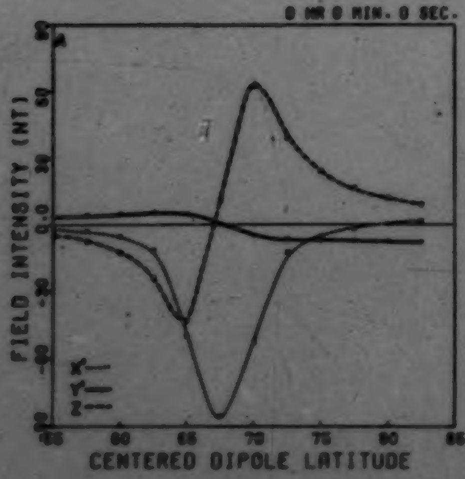
A
0 HR 0 MIN. 0 SEC.
FIELD INTENSITY (NT)
90
60
30
0.0
-30
-60
-90
X
Y
Z
55
60
65
70
75
80
85
CENTERED DIPOLE LATITUDE

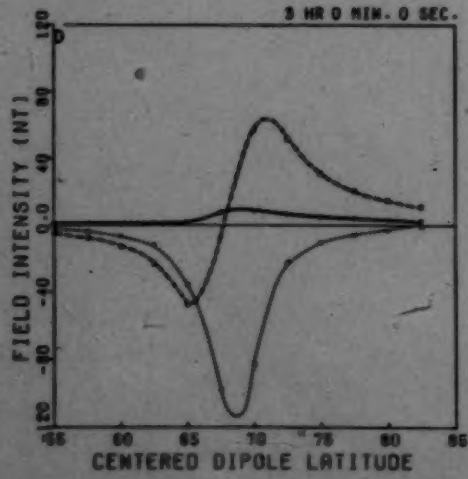
D
3 HR 0 MIN. 0 SEC.
FIELD INTENSITY (NT)
120
80
40
0.0
-40
-80
-120
55
60
65
70
75
80
85
CENTERED DIPOLE LATITUDE

Figure 4.8 Model latitude profiles due to the complete westward current system (including the ionospheric and field-aligned currents).

g) 0600 to 0700 MLT
h) 0700 to 0800 MLT
i) 0800 to 0900 MLT
j) 0900 to 1000 MLT
k) 1000 to 1100 MLT
l) 1100 to 1200 MLT

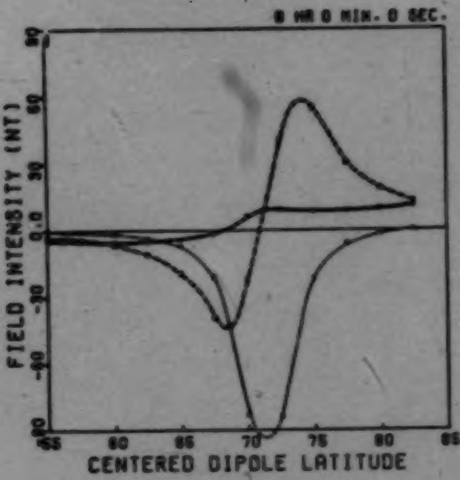
8 HR 0 MIN. 0 SEC.
FIELD INTENSITY (NT)
90
60
30
0.0
-30
-60
-90
55
60
65
70
75
80
85
CENTERED DIPOLE LATITUDE

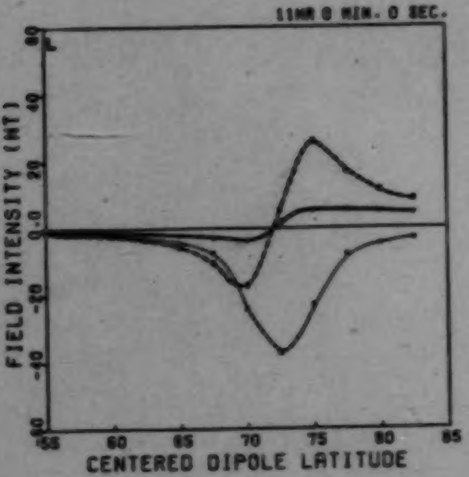
11HR 0 MIN. 0 SEC.
L
FIELD INTENSITY (NT)
60
40
20
0.0
-20
-40
-60
55
60
65
70
75
80
85
CENTERED DIPOLE LATITUDE

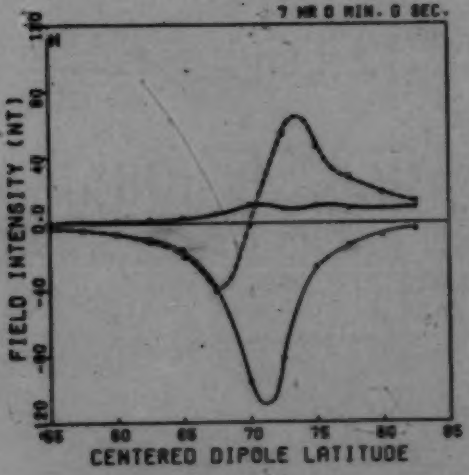
7 HR 0 MIN. 0 SEC.
H
FIELD INTENSITY (NT)
120
80
40
0.0
-40
-80
-120
55
60
65
70
75
80
85
CENTERED DIPOLE LATITUDE

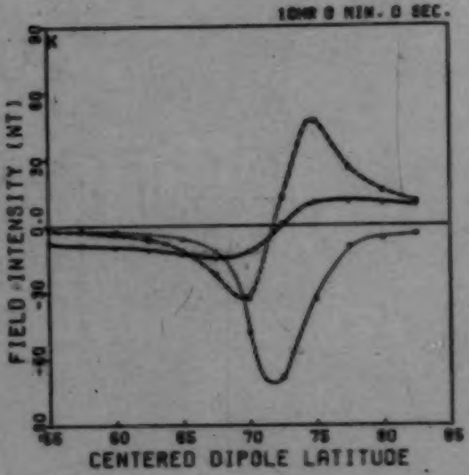
10HR 0 MIN. 0 SEC.
K
FIELD INTENSITY (NT)
90
60
30
0.0
-30
-60
-90
55
60
65
70
75
80
85
CENTERED DIPOLE LATITUDE

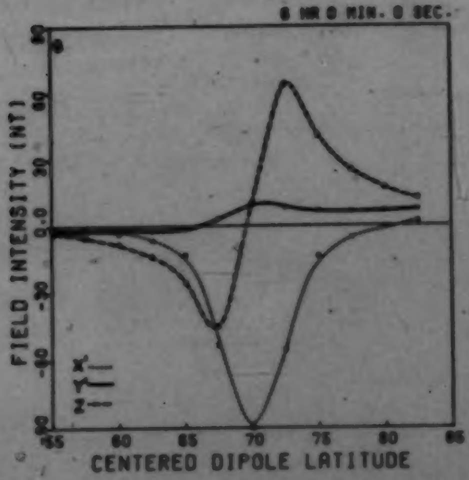
6 HR 0 MIN. 0 SEC.
G
FIELD INTENSITY (NT)
90
60
30
0.0
-30
-60
-90
X
Y
Z
55
60
65
70
75
80
85
CENTERED DIPOLE LATITUDE

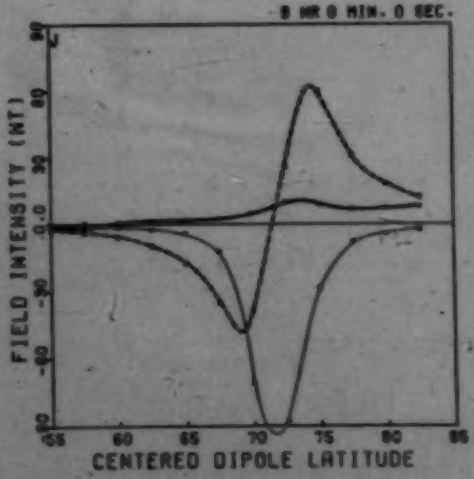
9 HR 0 MIN. 0 SEC.
J
FIELD INTENSITY (NT)
90
60
30
0.0
-30
-60
-90
55
60
65
70
75
80
85
CENTERED DIPOLE LATITUDE

Figure 4.8 Model latitude profiles due to the complete westward current system (including the ionospheric and field-aligned currents).

m) 1200 to 1300 MLT
n) 1300 to 1400 MLT
o) 1400 to 1500 MLT
p) 1500 to 1600 MLT
q) 1600 to 1700 MLT
r) 1700 to 1800 MLT

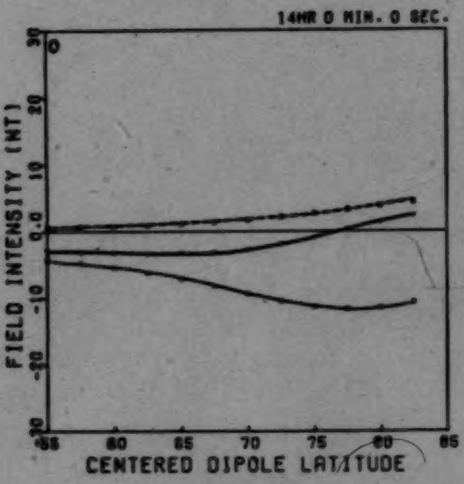
14HR 0 MIN. 0 SEC.
O
FIELD INTENSITY (NT)
30
20
10
0.0
-10
-20
-30
55
60
65
70
75
80
85
CENTERED DIPOLE LATITUDE

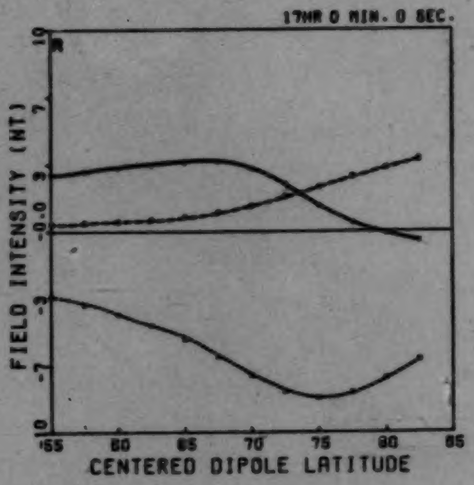
17HR 0 MIN. 0 SEC.
R
FIELD INTENSITY (NT)
10
7
3
-0.0
-3
-7
-10
55
60
65
70
75
80
85
CENTERED DIPOLE LATITUDE

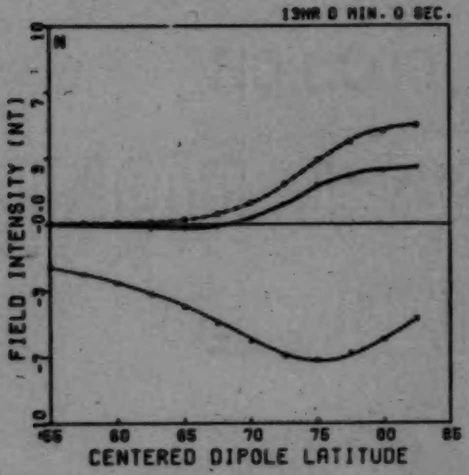
13HR 0 MIN. 0 SEC.
N
FIELD INTENSITY (NT)
10
7
3
-0.0
-3
-7
-10
55
60
65
70
75
80
85
CENTERED DIPOLE LATITUDE

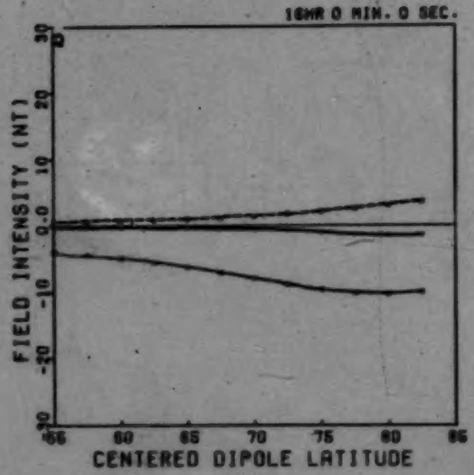
16HR 0 MIN. 0 SEC.
Q
FIELD INTENSITY (NT)
30
20
10
0.0
-10
-20
-30
55
60
65
70
75
80
85
CENTERED DIPOLE LATITUDE

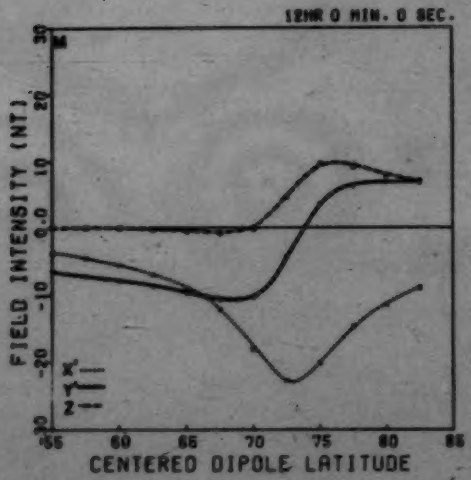
12HR 0 MIN. 0 SEC.
M
FIELD INTENSITY (NT)
30
20
10
0.0
-10
-20
-30
X
Y
Z
55
60
65
70
75
80
85
CENTERED DIPOLE LATITUDE

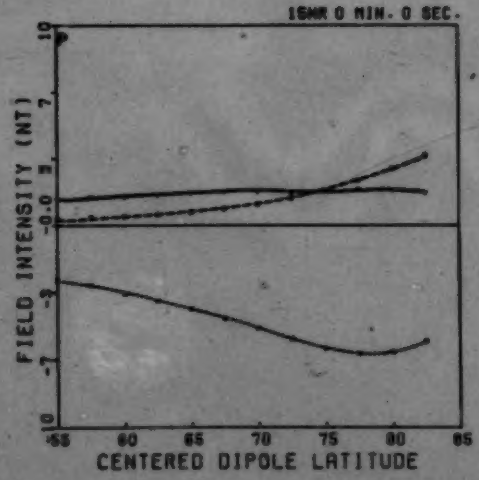
15HR 0 MIN. 0 SEC.
P
FIELD INTENSITY (NT)
10
7
3
-0.0
-3
-7
-10
55
60
65
70
75
80
85
CENTERED DIPOLE LATITUDE

Figure 4.8 Model latitude profiles due to the complete westward current system (including the ionospheric and field-aligned currents).

s) 1800 to 1900 MLT
t) 1900 to 2000 MLT
u) 2000 to 2100 MLT
v) 2100 to 2200 MLT
w) 2200 to 2300 MLT
x) 2300 to 2400 MLT

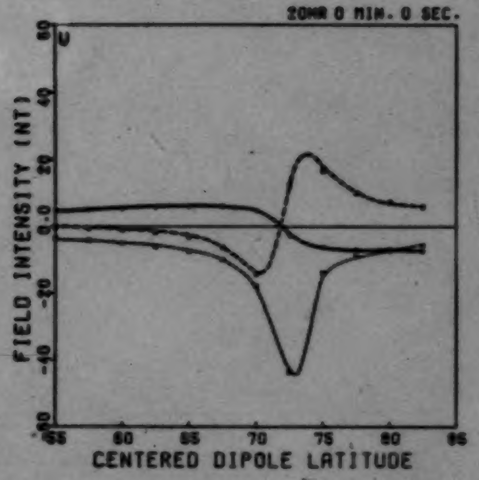
20HR 0 MIN. 0 SEC.
U
FIELD INTENSITY (NT)
60
40
20
0.0
-20
-40
-60
55
60
65
70
75
80
85
CENTERED DIPOLE LATITUDE

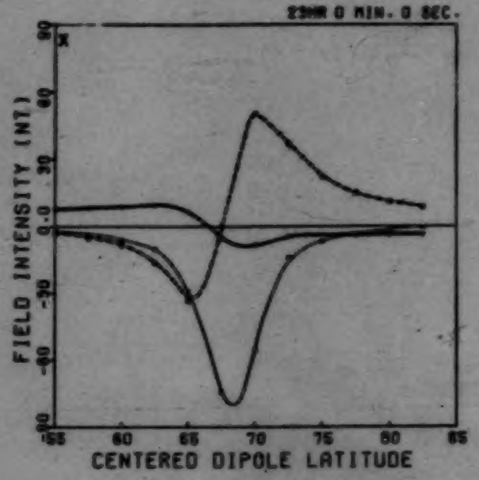
23HR 0 MIN. 0 SEC.
X
FIELD INTENSITY (NT)
90
60
30
0.0
-30
-60
-90
55
60
65
70
75
80
85
CENTERED DIPOLE LATITUDE

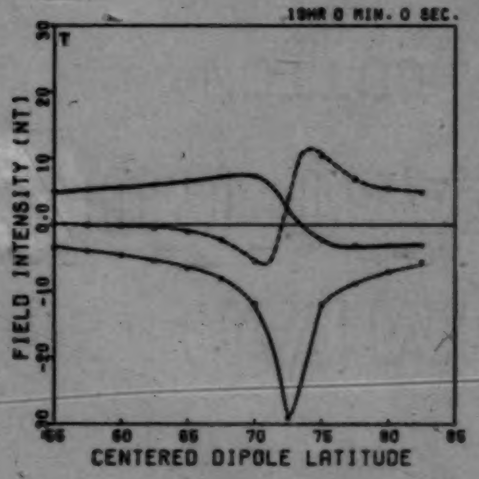
19HR 0 MIN. 0 SEC.
T
FIELD INTENSITY (NT)
30
20
10
0.0
-10
-20
-30
55
60
65
70
75
80
85
CENTERED DIPOLE LATITUDE

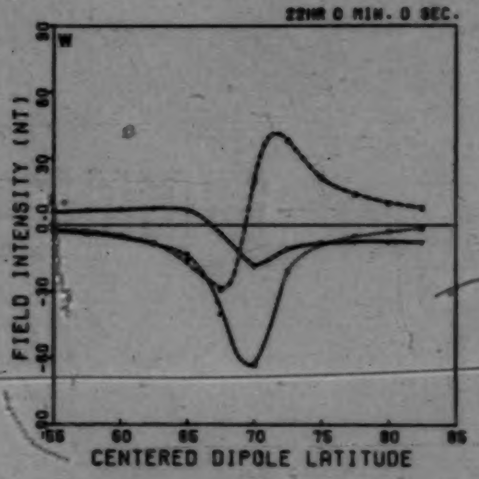
22HR 0 MIN. 0 SEC.
W
FIELD INTENSITY (NT)
90
60
30
0.0
-30
-60
-90
55
60
65
70
75
80
85
CENTERED DIPOLE LATITUDE

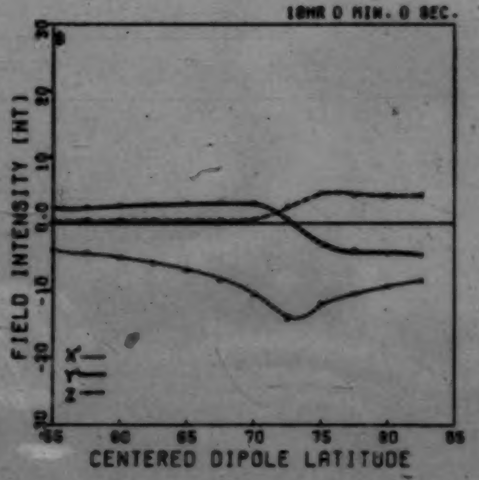
18HR 0 MIN. 0 SEC.
S
FIELD INTENSITY (NT)
30
20
10
0.0
-10
-20
-30
X
Y
Z
55
60
65
70
75
80
85
CENTERED DIPOLE LATITUDE

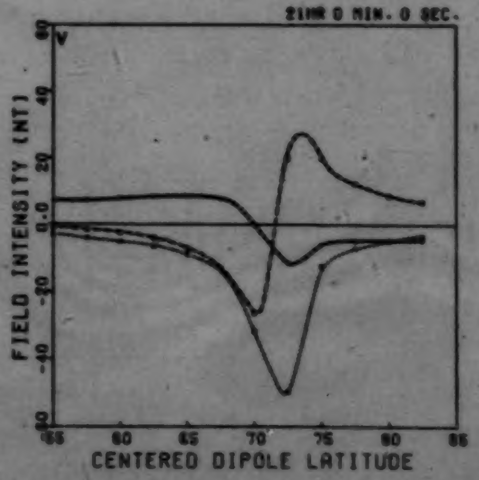
21HR 0 MIN. 0 SEC.
V
FIELD INTENSITY (NT)
60
40
20
0.0
-20
-40
-60
55
60
65
70
75
80
85
CENTERED DIPOLE LATITUDE

is more unbalanced field-aligned current than has been used in the model, or (2) there are other current systems which will produce a $\Delta Y'$ level-shift. The first of these requires an ionospheric current system other than a westward current, since increasing this latter will not change the size of the Y'-component level-shift relative to the X'-component extremum. Since, as pointed out earlier, it is not believed that significant currents flow in the winter polar cap, this first possibility suggests the presence of currents flowing equatorward. Such a current system has been included in the global model, and will be returned to later in this chapter (section 4.4.3). The second possibility is also a viable one, insofar as the north-south current system has not yet been considered.

First, however, the remaining features of the westward system alone should be considered. Note that the Z-component exhibits an asymmetry not unlike that in the data, in the post-midnight hours. Also, the east-west component is not negative across the entire profile, as it is in the data, in the midnight sector. Finally, the east-west component does show a negative-going step, in the pre-midnight hours, similar to that observed in the data.

When the appropriate north-south currents are added to this westward current system, the model profiles are improved considerably when compared with the real data. Figure 4.9 (24 panels) are plots of model profiles in which the profiles of figure 4.8 have been added to the southward

Figure 4.9 Model latitude profiles due to the complete westward current system, to which has been added the corresponding north-south current system.

s) 1800 to 1900 MLT
t) 1900 to 2000 MLT
u) 2000 to 2100 MLT
v) 2100 to 2200 MLT
w) 2200 to 2300 MLT
x) 2300 to 2400 MLT

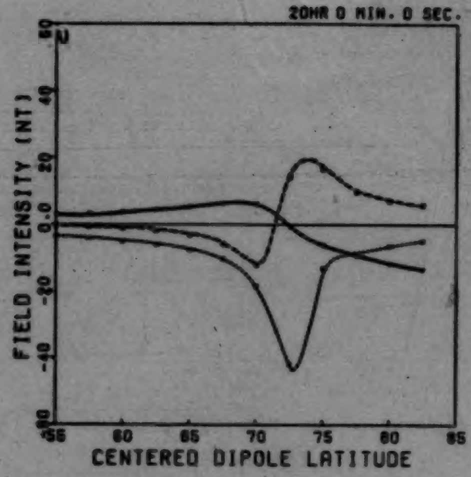
20HR 0 MIN. 0 SEC.
U
FIELD INTENSITY (NT)
60
40
20
0.0
-20
-40
-60
55
60
65
70
75
80
85
CENTERED DIPOLE LATITUDE

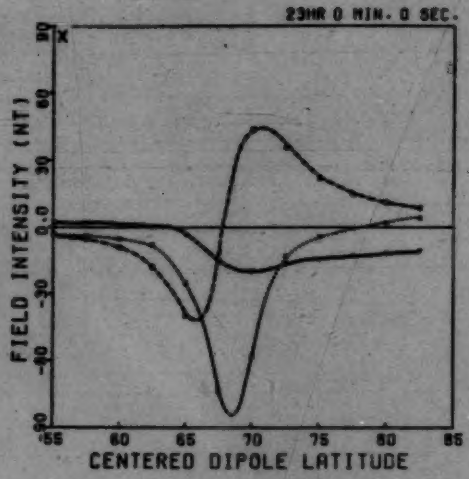
23HR 0 MIN. 0 SEC.
X
FIELD INTENSITY (NT)
90
60
30
0.0
-30
-60
-90
55
60
65
70
75
80
85
CENTERED DIPOLE LATITUDE

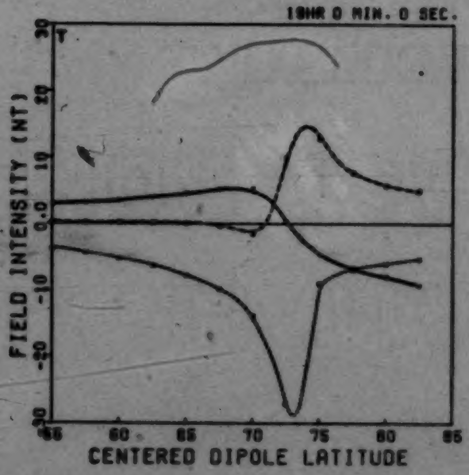
19HR 0 MIN. 0 SEC.
T
FIELD INTENSITY (NT)
30
20
10
0.0
-10
-20
-30
55
60
65
70
75
80
85
CENTERED DIPOLE LATITUDE

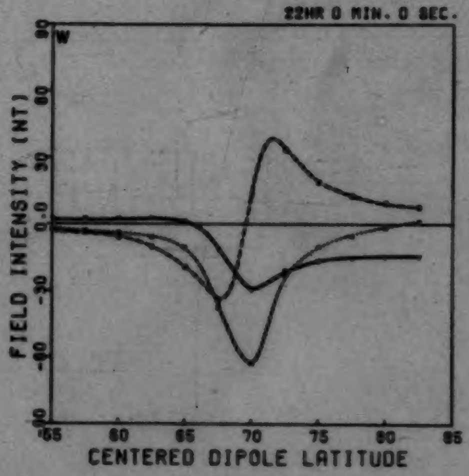
22HR 0 MIN. 0 SEC.
W
FIELD INTENSITY (NT)
90
60
30
0.0
-30
-60
-90
55
60
65
70
75
80
85
CENTERED DIPOLE LATITUDE

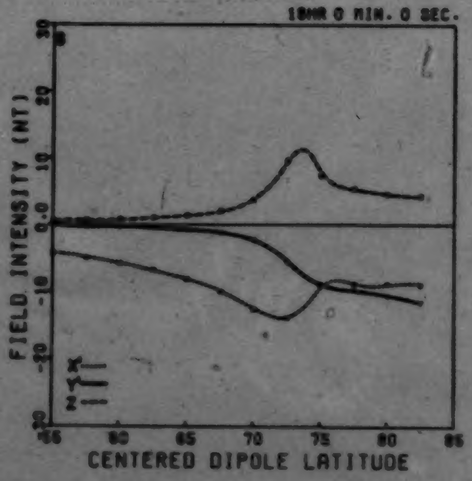
18HR 0 MIN. 0 SEC.
S
FIELD INTENSITY (NT)
30
20
10
0.0
-10
-20
-30
X
Y
Z
55
60
65
70
75
80
85
CENTERED DIPOLE LATITUDE

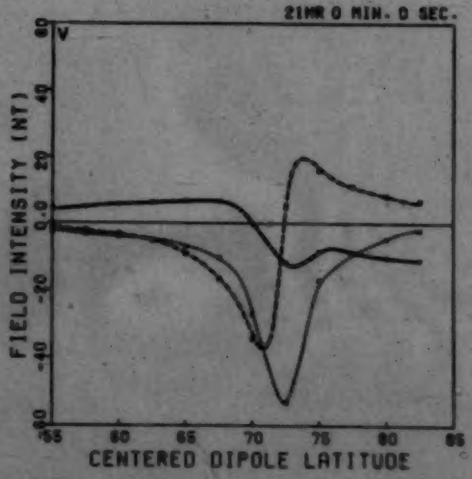
21HR 0 MIN. 0 SEC.
V
FIELD INTENSITY (NT)
60
40
20
0.0
-20
-40
-60
55
60
65
70
75
80
85
CENTERED DIPOLE LATITUDE

Figure 4.9 Model latitude profiles due to the complete westward current system, to which has been added the corresponding north-south current system.

m) 1200 to 1300 MLT
n) 1300 to 1400 MLT
o) 1400 to 1500 MLT
p) 1500 to 1600 MLT
q) 1600 to 1700 MLT
r) 1700 to 1800 MLT

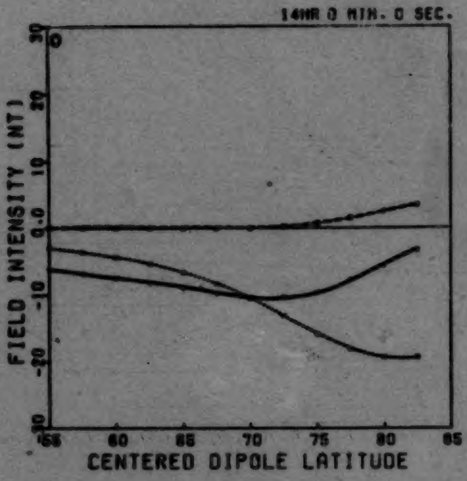
14HR 0 MIN. 0 SEC.
O
FIELD INTENSITY (NT)
30
20
10
0.0
-10
-20
-30
55
60
65
70
75
80
85
CENTERED DIPOLE LATITUDE

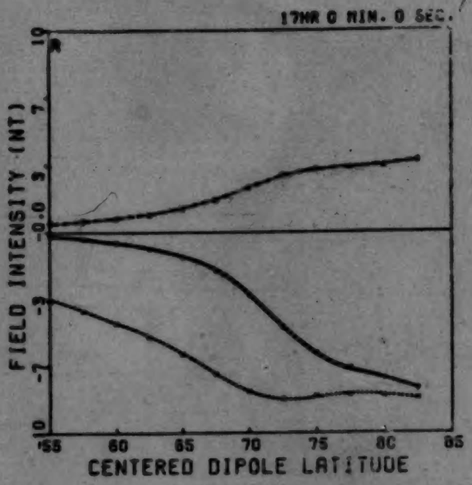
17HR 0 MIN. 0 SEC.
R
FIELD INTENSITY (NT)
10
7
3
0.0
-3
-7
-10
55
60
65
70
75
80
85
CENTERED DIPOLE LATITUDE

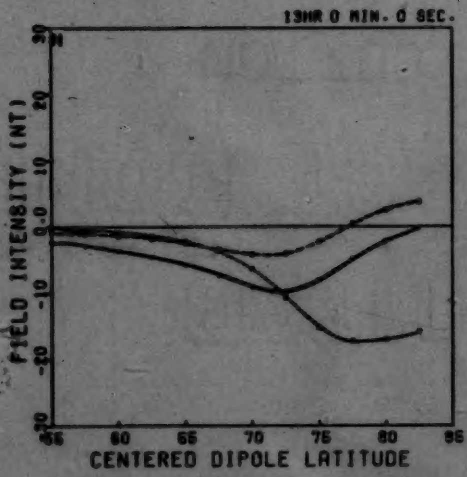
13HR 0 MIN. 0 SEC.
N
FIELD INTENSITY (NT)
30
20
10
0.0
-10
-20
-30
55
60
65
70
75
80
85
CENTERED DIPOLE LATITUDE

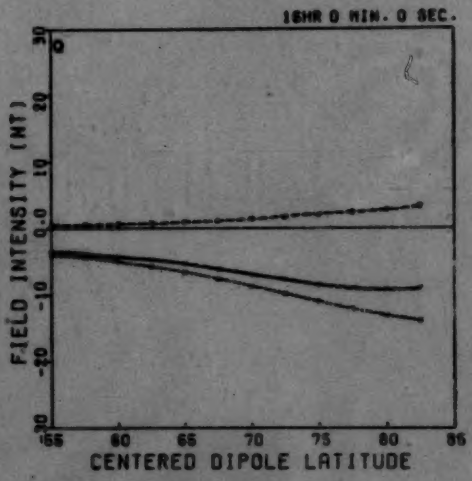
16HR 0 MIN. 0 SEC.
Q
FIELD INTENSITY (NT)
30
20
10
0.0
-10
-20
-30
55
60
65
70
75
80
85
CENTERED DIPOLE LATITUDE

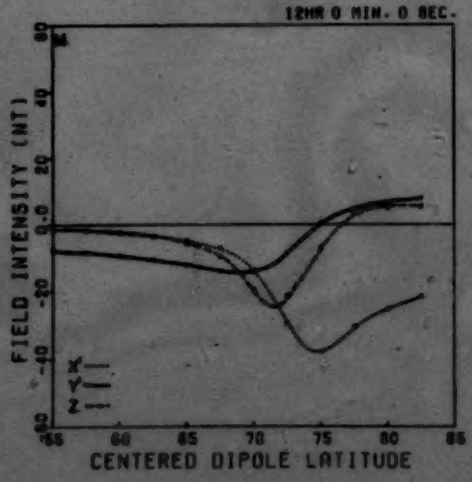
12HR 0 MIN. 0 SEC.
M
FIELD INTENSITY (NT)
60
40
20
0.0
-20
-40
-60
X
Y
Z
55
60
65
70
75
80
85
CENTERED DIPOLE LATITUDE

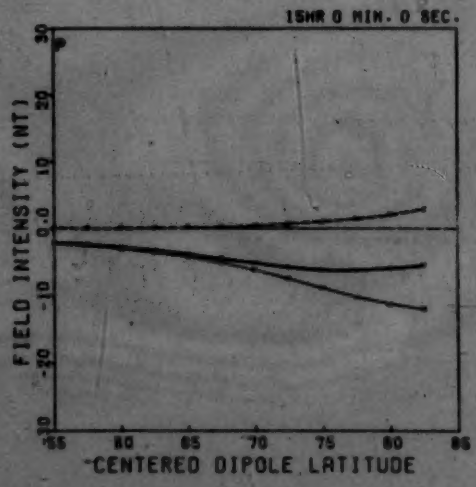
15HR 0 MIN. 0 SEC.
P
FIELD INTENSITY (NT)
30
20
10
0.0
-10
-20
-30
55
60
65
70
75
80
85
CENTERED DIPOLE LATITUDE

Figure 4.9 Model latitude profiles due to the complete westward current system, to which has been added the corresponding north-south current system.

g) 0600 to 0700 MLT
h) 0700 to 0800 MLT
i) 0800 to 0900 MLT
j) 0900 to 1000 MLT
k) 1000 to 1100 MLT
l) 1100 to 1200 MLT

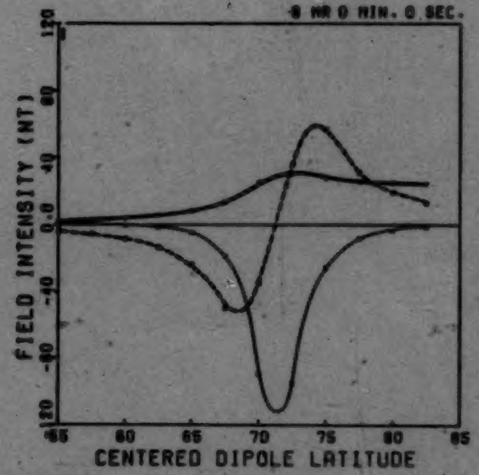
8 HR 0 MIN. 0 SEC.
I
FIELD INTENSITY (NT)
120
80
40
0.0
-40
-80
-120
55
60
65
70
75
80
85
CENTERED DIPOLE LATITUDE

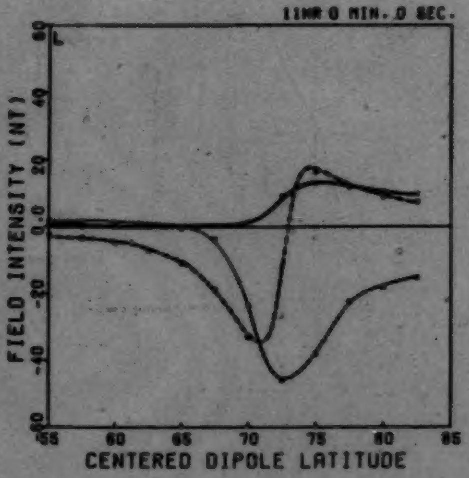
11HR 0 MIN. 0 SEC.
L
FIELD INTENSITY (NT)
60
40
20
0.0
-20
-40
-60
55
60
65
70
75
80
85
CENTERED DIPOLE LATITUDE

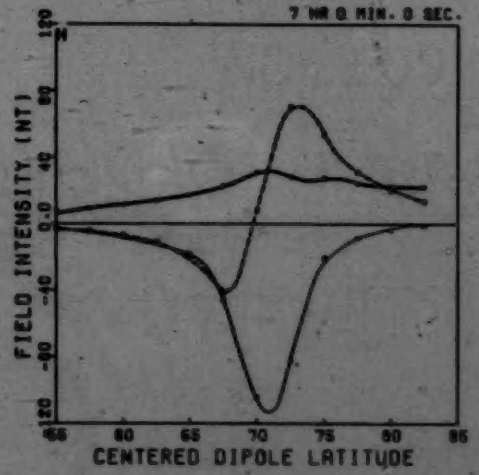
7 HR 0 MIN. 0 SEC.
H
FIELD INTENSITY (NT)
120
80
40
0.0
-40
-80
-120
55
60
65
70
75
80
85
CENTERED DIPOLE LATITUDE

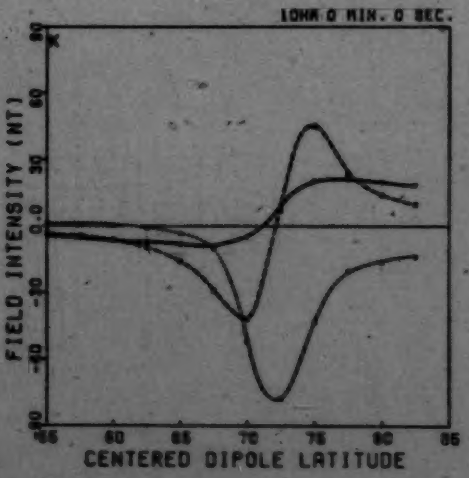
10HR 0 MIN. 0 SEC.
K
FIELD INTENSITY (NT)
90
60
30
0.0
-30
-60
-90
55
60
65
70
75
80
85
CENTERED DIPOLE LATITUDE

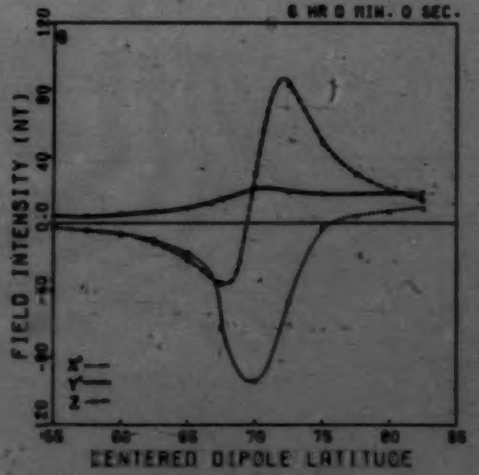
6 HR 0 MIN. 0 SEC.
G
FIELD INTENSITY (NT)
120
80
40
0.0
-40
-80
-120
X
Y
Z
55
60
65
70
75
80
85
CENTERED DIPOLE LATITUDE

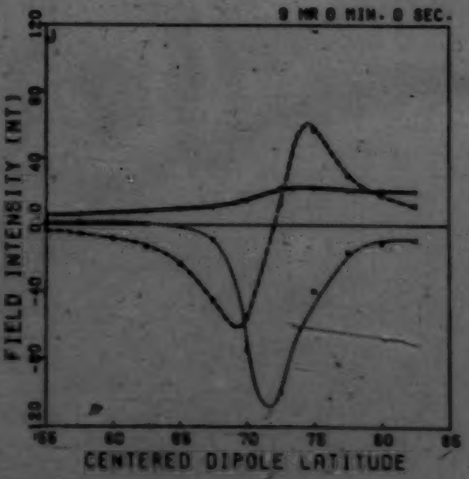
9 HR 0 MIN. 0 SEC.
J
FIELD INTENSITY (NT)
120
80
40
0.0
-40
-80
-120
55
60
65
70
75
80
85
CENTERED DIPOLE LATITUDE

Figure 4.9 Model latitude profiles due to the complete westward current system, to which has been added the corresponding north-south current system.

a) 0000 to 0100 MLT
b) 0100 to 0200 MLT
c) 0200 to 0300 MLT
d) 0300 to 0400 MLT
e) 0400 to 0500 MLT
f) 0500 to 0600 MLT

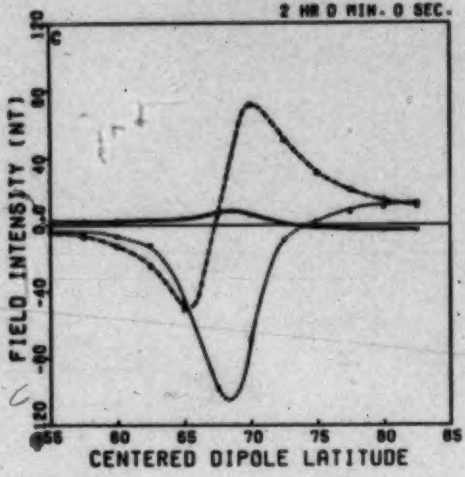
2 HR 0 MIN. 0 SEC.

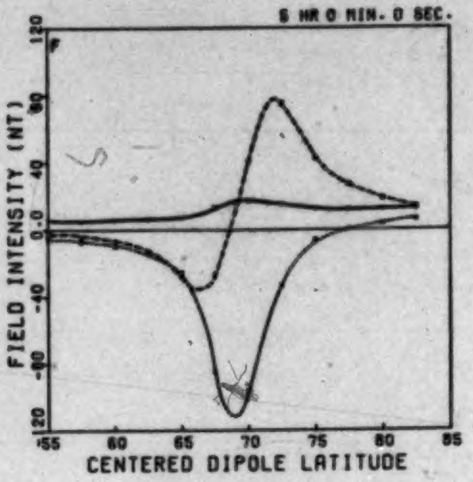
5 HR 0 MIN. 0 SEC.

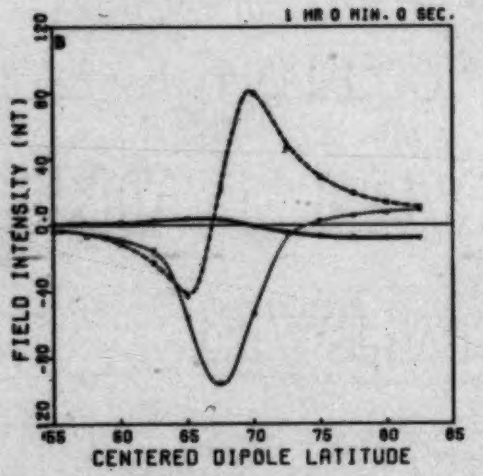
1 HR 0 MIN. 0 SEC.

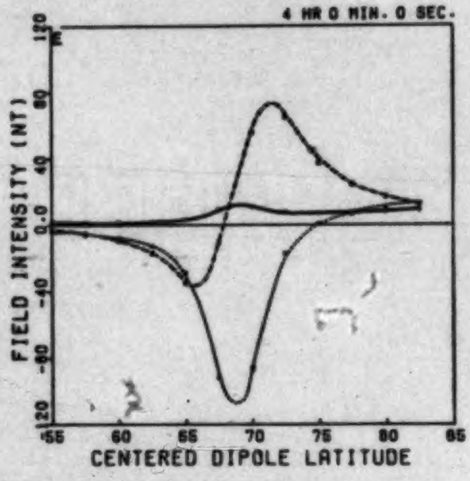
4 HR 0 MIN. 0 SEC.

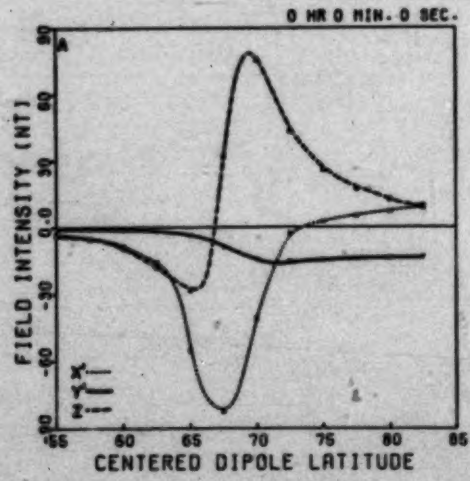
0 HR 0 MIN. 0 SEC.

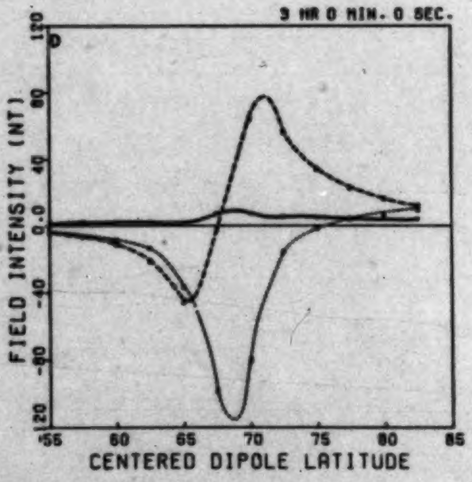
3 HR 0 MIN. 0 SEC.

flowing meridional current system consistent with the electric field and conductivity model. In the post-midnight sector, to noon, the size of the Y'-component level-shift is enhanced. As will be demonstrated later in this chapter, this level-shift is now in close agreement with the data. Thus, as suggested in the penultimate paragraph, the possibility of additional currents producing a $\Delta Y'$ level-shift is a reasonable one. Although level-shifts in the east-west component may be due in part to unbalanced field-aligned current, they cannot be explained totally on this basis; a north-south current system of great longitudinal extent will also produce a similar Y'-component. However, it is not possible to model the Y'-component level-shift solely by north-south current flow, and still produce the observed variation in the X'-component. As already discussed, it is evident that the westward electrojet grows over a region of some longitudinal extent, and this demands the presence of unbalanced field-aligned current into the ionosphere.

Significant end effects of the north-south system associated with the westward electrojet are evident in the model profiles for times immediately after noon (Figure 4.9) when they are compared with the corresponding panels of Figure 4.8. This effect is seen mainly in the Z-component, and is due primarily to the ionospheric portion of the north-south three-dimensional system. A similar effect may be seen in the 1800 MLT model profiles, (Figures 4.8(s) and 4.9(s)) and is due to the north-south current system associated with the pre-midnight westward electrojet.

4.4.2 The Eastward Current System

In Chapter 3, it was shown that the ground based magnetic data in the post-noon sector were indicative of an eastward flowing electrojet. In fact, based on the magnitude of the X'-component positive extremum this eastward current was found to grow from noon to near dusk, where there is a small decrease in the apparent current magnitude. This is similar to the behaviour of the westward current flow, although this decrease in current strength is not as pronounced. However, the same argument as developed for the westward current has been applied to the eastward current in the post-noon sector. As well, there is a marked decrease in the magnitude of the positive $\Delta X'$ extrema from about 2000 MLT to 2200 MLT. Figure 4.5 is a plot of the height-integrated current density for the eastward electrojet (the curve with positive values in this figure). The current grows linearly from 0.0 Am^{-1} at noon to a maximum of 0.116 Am^{-1} ($6.57x10^{4}$A total) at 1600 MLT. At this time, there is a reduction in current, with 20% of the current flowing out of the ionosphere in a field-aligned current sheet. The current remains constant until 2100 MLT, at which time it begins to flow poleward. As can be seen in figure 4.1, in this regime (2100 to 2400 MLT) the eastward current is constrained to a wedge-like region of the auroral oval. As the eastward flowing current diverges poleward, it encounters the equatorward border of the westward current, where the eastward current diverges up the field lines. Thus, in the model, the eastward electrojet flows out of the ionosphere in a field-aligned current sheet, the locus of which separates the eastward and westward electrojets in the region of the Harang discontinuity. Figure 4.6 shows the current density of the field-aligned current which feeds the eastward electrojet (1200 to 1600 MLT). It is considerably less then the main feed to the westward electrojet (0900 to 1200 MLT), in keeping with the relatively smaller total current that flows in the eastward electrojet. As in the case of the westward flowing current, there is a north-south current system associated with the eastward electrojet. In the post-noon sector, this current is directed poleward in keeping with the electric field observations. Figure 4.7 includes a plot of the field-aligned current density associated with this north-south current. Although this current density is considerably less than that used for the westward current, it is consistent with the electric field model and conductivity ratio described earlier. Figure 4.10 (24 panels) are plots of the model latitude profiles for the eastward current together with its associated field-aligned currents. The growth of the eastward electrojet is apparent in the post-noon profiles up to 1600 MLT (Figures 4.10 (m) through 4.10(q)). The slight decrease in the peak value of $\Delta X'$ is visible at 1600 MLT, and from 1600 MLT to about 2100 MLT (Figures 4.10(q) to 4.10(v)) the magnitude of the X'-

Figure 4.10 Model latitude profiles due to the complete eastward current system (including the ionospheric and field-aligned currents).

a) 0000 to 0100 MLT
b) 0100 to 0200 MLT
c) 0200 to 0300 MLT
d) 0300 to 0400 MLT
e) 0400 to 0500 MLT
f) 0500 to 0600 MLT

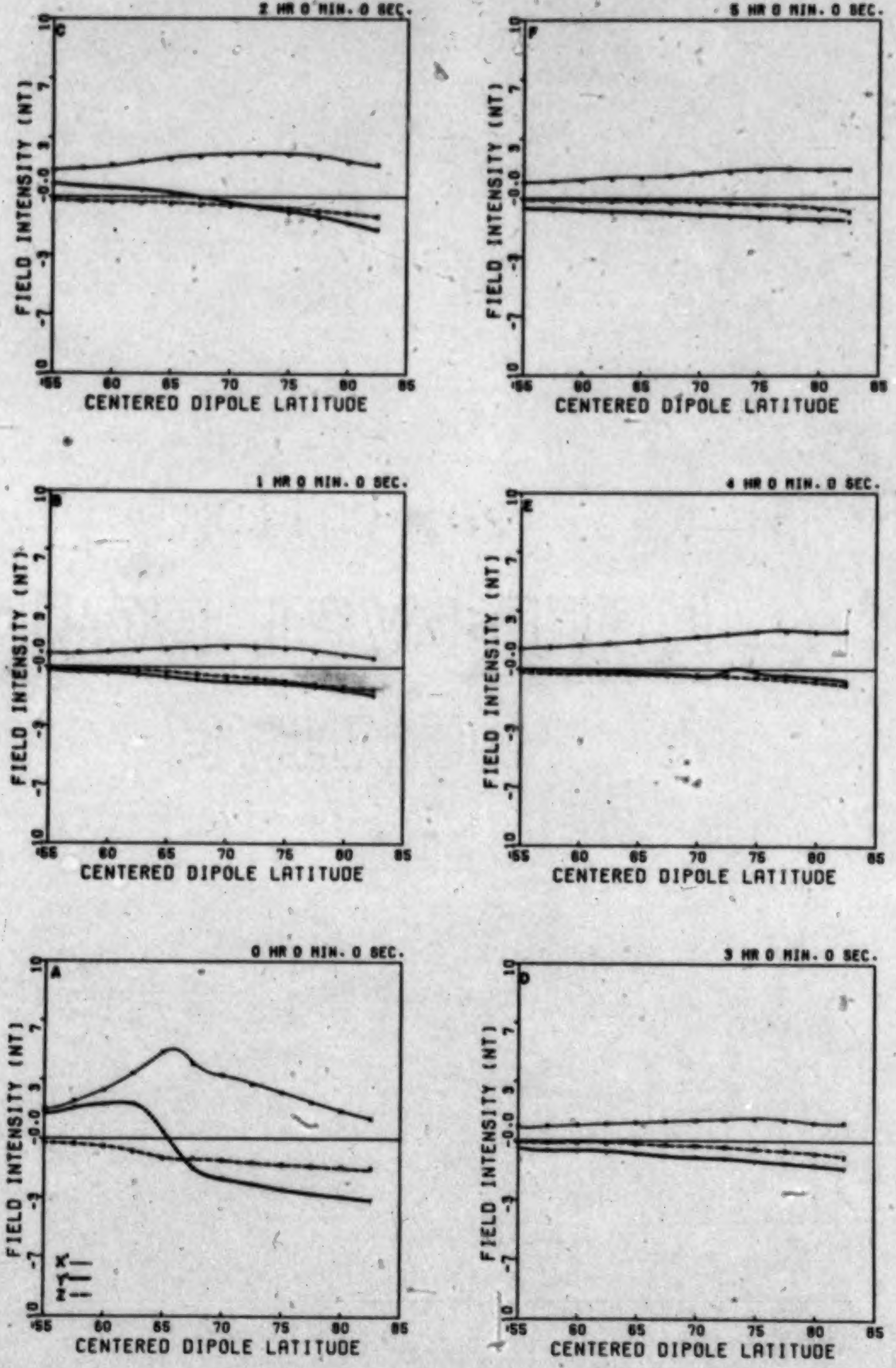
2 HR 0 MIN. 0 SEC.
C
5 HR 0 MIN. 0 SEC.
F
1 HR 0 MIN. 0 SEC.
B
4 HR 0 MIN. 0 SEC.
E
0 HR 0 MIN. 0 SEC.
A
3 HR 0 MIN. 0 SEC.
D
FIELD INTENSITY (NT)
10
7
3
0.0
-0.0
-3
-7
10
CENTERED DIPOLE LATITUDE
55
60
65
70
75
80
85
X
Y
Z

Figure 4.10 Model latitude profiles due to the complete eastward current system (including the ionospheric and field-aligned currents).

g) 0600 to 0700 MLT
h) 0700 to 0800 MLT
i) 0800 to 0900 MLT
j) 0900 to 1000 MLT
k) 1000 to 1100 MLT
l) 1100 to 1200 MLT

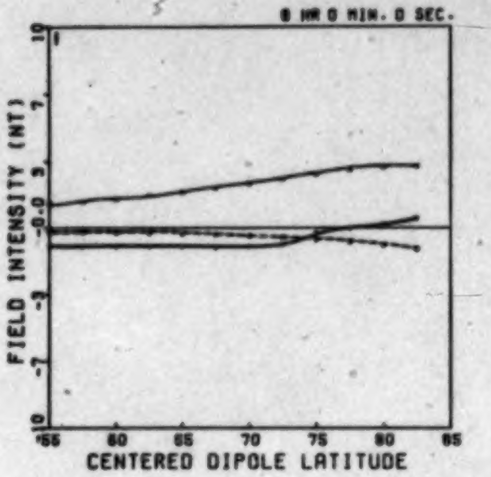
8 HR 0 MIN. 0 SEC.
I
FIELD INTENSITY (NT)
10
7
3
0.0
-0.0
-3
-7
10
55
60
65
70
75
80
85
CENTERED DIPOLE LATITUDE

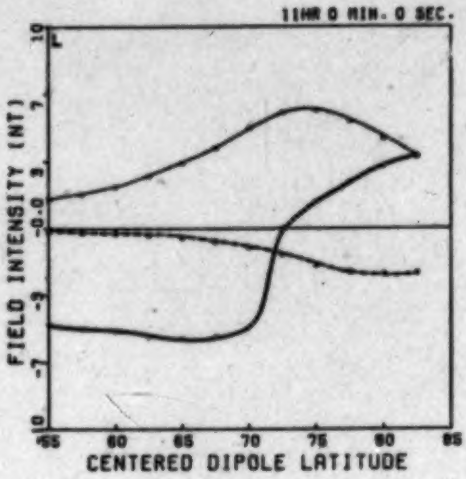
11HR 0 MIN. 0 SEC.
L
FIELD INTENSITY (NT)
10
7
3
0.0
-0.0
-3
-7
10
55
60
65
70
75
80
85
CENTERED DIPOLE LATITUDE

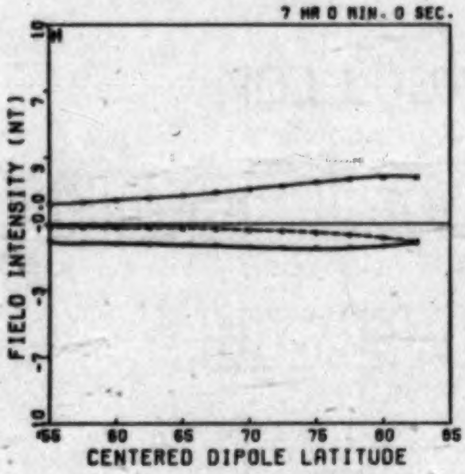
7 HR 0 MIN. 0 SEC.
H
FIELD INTENSITY (NT)
10
7
3
0.0
-0.0
-3
-7
10
55
60
65
70
75
80
85
CENTERED DIPOLE LATITUDE

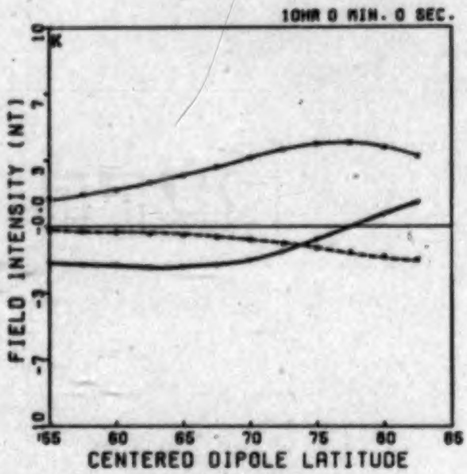
10HR 0 MIN. 0 SEC.
K
FIELD INTENSITY (NT)
10
7
3
0.0
-0.0
-3
-7
10
55
60
65
70
75
80
85
CENTERED DIPOLE LATITUDE

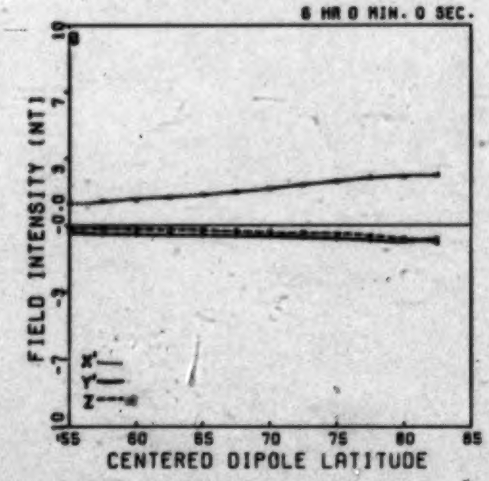
6 HR 0 MIN. 0 SEC.
G
FIELD INTENSITY (NT)
10
7
3
0.0
-0.0
-3
-7
10
X*
Y*
Z
55
60
65
70
75
80
85
CENTERED DIPOLE LATITUDE

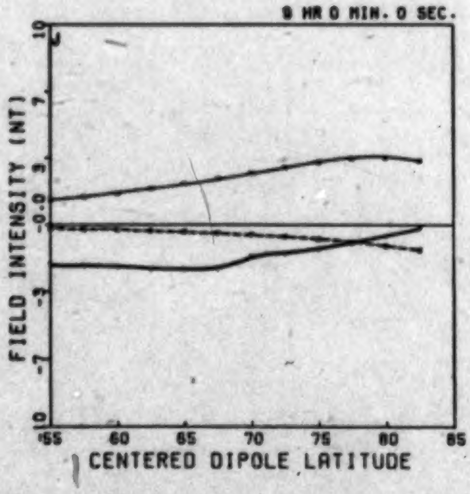
9 HR 0 MIN. 0 SEC.
J
FIELD INTENSITY (NT)
10
7
3
0.0
-0.0
-3
-7
10
55
60
65
70
75
80
85
CENTERED DIPOLE LATITUDE

Figure 4.10 Model latitude profiles due to the complete eastward current system (including the ionospheric and field-aligned currents).

m) 1200 to 1300 MLT
n) 1300 to 1400 MLT
o) 1400 to 1500 MLT
p) 1500 to 1600 MLT
q) 1600 to 1700 MLT
r) 1700 to 1800 MLT

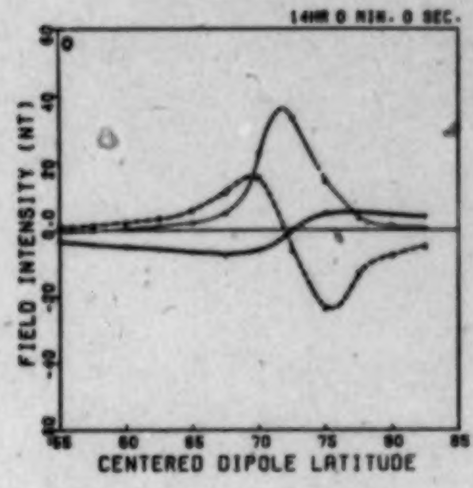
14HR 0 MIN. 0 SEC.
O
FIELD INTENSITY (NT)
60
40
20
0.0
-20
-40
-60
55
60
65
70
75
80
85
CENTERED DIPOLE LATITUDE

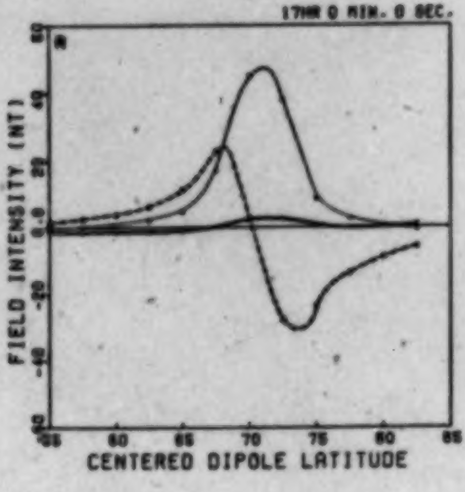
17HR 0 MIN. 0 SEC.
R
FIELD INTENSITY (NT)
60
40
20
0.0
-20
-40
-60
55
60
65
70
75
80
85
CENTERED DIPOLE LATITUDE

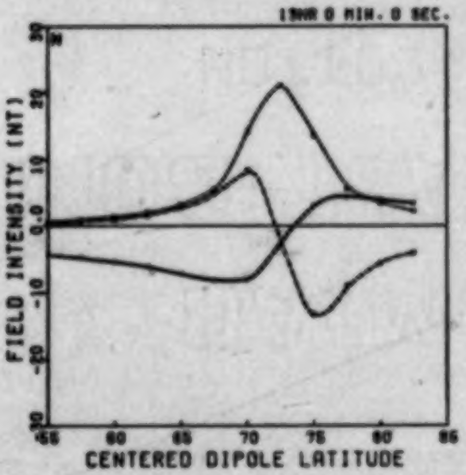
13HR 0 MIN. 0 SEC.
N
FIELD INTENSITY (NT)
30
20
10
0.0
-10
-20
-30
55
60
65
70
75
80
85
CENTERED DIPOLE LATITUDE

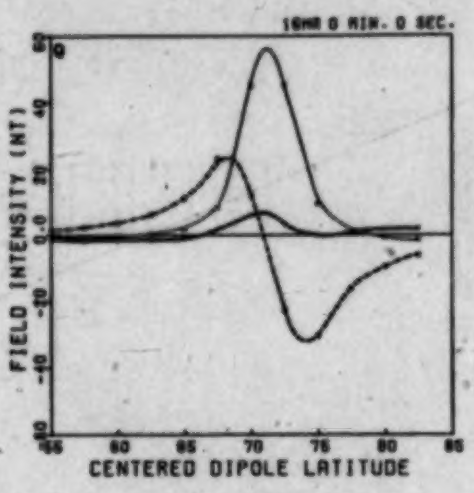
16HR 0 MIN. 0 SEC.
Q
FIELD INTENSITY (NT)
60
40
20
0.0
-20
-40
-60
55
60
65
70
75
80
85
CENTERED DIPOLE LATITUDE

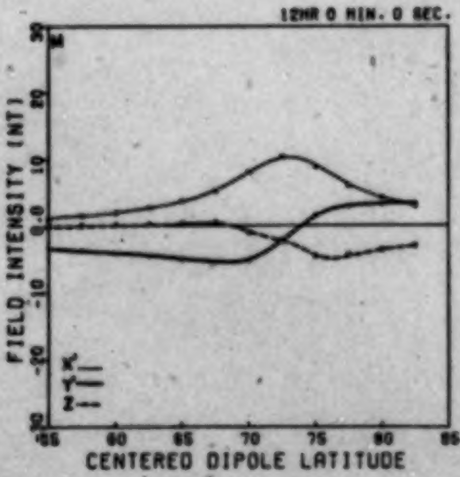
12HR 0 MIN. 0 SEC.
M
FIELD INTENSITY (NT)
30
20
10
0.0
-10
-20
-30
X
Y
Z
55
60
65
70
75
80
85
CENTERED DIPOLE LATITUDE

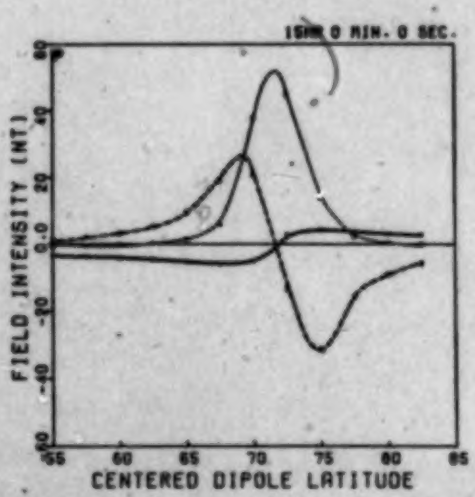
15HR 0 MIN. 0 SEC.
P
FIELD INTENSITY (NT)
60
40
20
0.0
-20
-40
-60
55
60
65
70
75
80
85
CENTERED DIPOLE LATITUDE

Figure 4.10 Model latitude profiles due to the complete eastward current system (including the ionospheric and field-aligned currents).

s) 1800 to 1900 MLT
t) 1900 to 2000 MLT
u) 2000 to 2100 MLT
v) 2100 to 2200 MLT
w) 2200 to 2300 MLT
x) 2300 to 2400 MLT

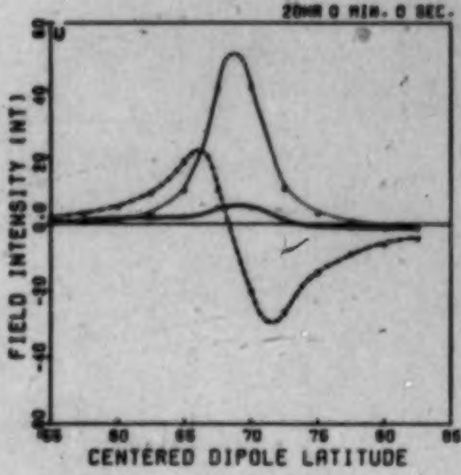
20HR 0 MIN. 0 SEC.
U
FIELD INTENSITY (NT)
60
40
20
0.0
-20
-40
-60
55
60
65
70
75
80
85
CENTERED DIPOLE LATITUDE

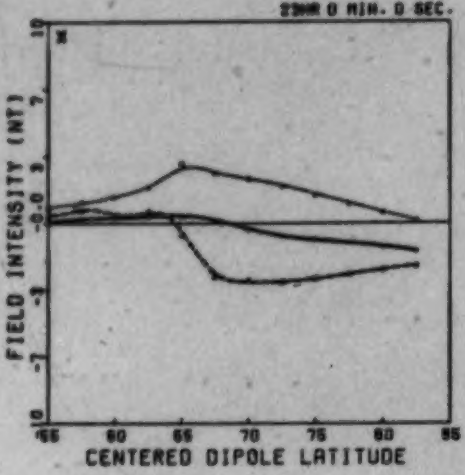
23HR 0 MIN. 0 SEC.
X
FIELD INTENSITY (NT)
10
7
3
0.0
-3
-7
-10
55
60
65
70
75
80
85
CENTERED DIPOLE LATITUDE

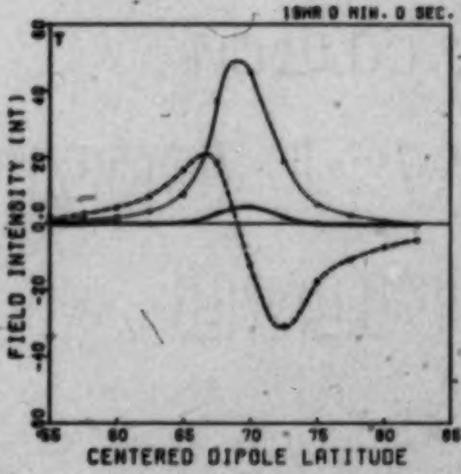
19HR 0 MIN. 0 SEC.
T
FIELD INTENSITY (NT)
60
40
20
0.0
-20
-40
-60
55
60
65
70
75
80
85
CENTERED DIPOLE LATITUDE

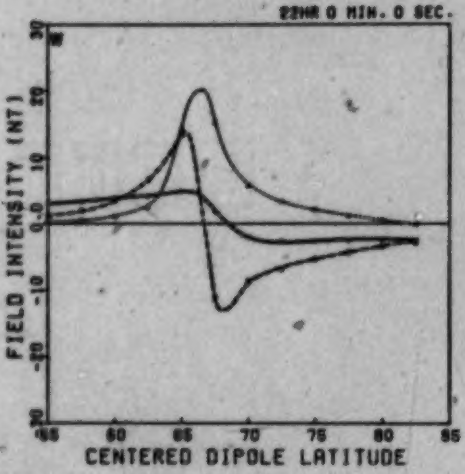
22HR 0 MIN. 0 SEC.
W
FIELD INTENSITY (NT)
30
20
10
0.0
-10
-20
-30
55
60
65
70
75
80
85
CENTERED DIPOLE LATITUDE

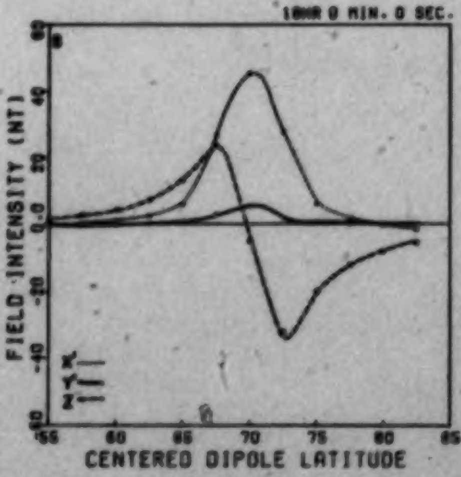
18HR 0 MIN. 0 SEC.
S
FIELD INTENSITY (NT)
60
40
20
0.0
-20
-40
-60
X
Y
Z
55
60
65
70
75
80
85
CENTERED DIPOLE LATITUDE

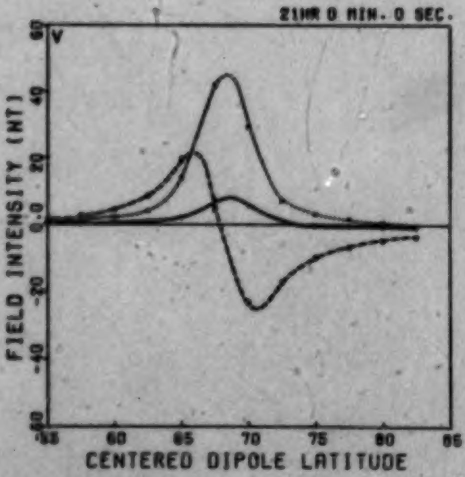
21HR 0 MIN. 0 SEC.
V
FIELD INTENSITY (NT)
60
40
20
0.0
-20
-40
-60
55
60
65
70
75
80
85
CENTERED DIPOLE LATITUDE

component peak is essentially constant. Beyond this time to midnight, the strength of the eastward electrojet decreases. The tilt of the current flow with respect to parallels of latitude that has been built into the model is evident in the model profiles for 1700 MLT to 1900 MLT. (Figures 4.10(r) to 4.10(t)). In this time period, the tilt in the oval is greatest, and in these profiles, it is clear that the east-west component follows the north-south component. The east-west component in the immediate pre-midnight sector (Figures 4.10(a), 4.10(w), 4.10(x)) shows a negative going level-shift (from south to north latitudes) consistent with the presence of the upward field-aligned current sheet in this regime.

Outside the regime of the eastward current, some effects are visible. For example, there is a small, broad, positive $\Delta X'$ signature seen in the model profile for 0000 MLT (Fig. 4.21(a)). Similarly, an end-effect is evident in the two hours preceding nocn (Figures 4.10(k) and 4.10(l)). In general however, the eastward flowing current produces little effect in regimes outside the actual location of the current.

The result of adding the north-south current system which flows in conjunction with the eastward current is shown in Figure 4.11. The effect of the system on the profiles shown in Figure 4.10 is not as large as was seen in the case of the westward electrojet. The main effect is observed in the profiles for 2100 MLT through midnight to

Figure 4.11 Model latitude profiles due to the complete eastward current system, to which has been added the corresponding north-south current system.

a) 0000 to 0100 MLT
b) 0100 to 0200 MLT
c) 0200 to 0300 MLT
d) 0300 to 0400 MLT
e) 0400 to 0500 MLT
f) 0500 to 0600 MLT

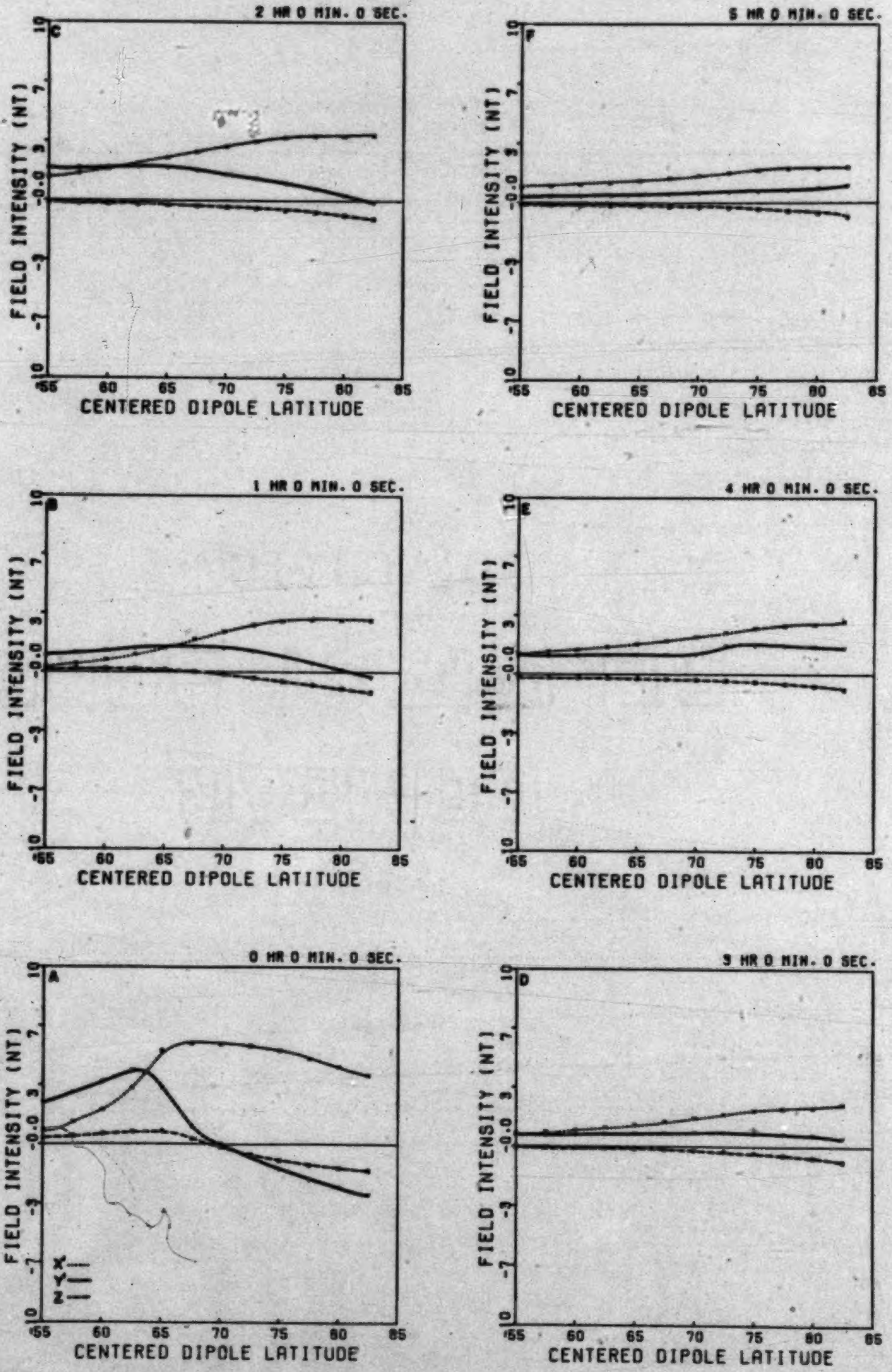
C
2 HR 0 MIN. 0 SEC.
F
5 HR 0 MIN. 0 SEC.
B
1 HR 0 MIN. 0 SEC.
E
4 HR 0 MIN. 0 SEC.
A
0 HR 0 MIN. 0 SEC.
D
3 HR 0 MIN. 0 SEC.
FIELD INTENSITY (NT)
10
7
3
0.0
-0.0
-3
-7
10
55
60
65
70
75
80
85
CENTERED DIPOLE LATITUDE
X
Y
Z

Figure 4.11 Model latitude profiles due to the complete eastward current system, to which has been added the corresponding north-south current system.

g) 0600 to 0700 MLT
h) 0700 to 0800 MLT
i) 0800 to 0900 MLT
j) 0900 to 1000 MLT
k) 1000 to 1100 MLT
l) 1100 to 1200 MLT

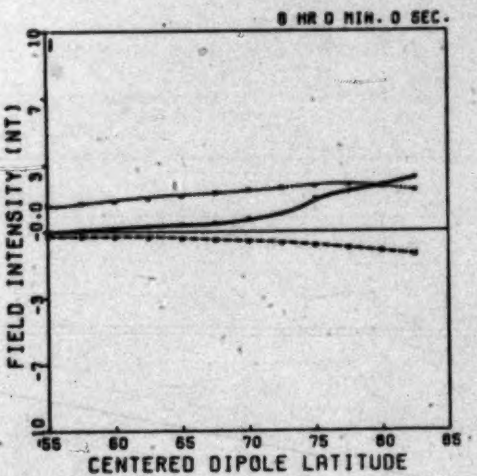
8 HR 0 MIN. 0 SEC.
I
FIELD INTENSITY (NT)
10
7
3
0.0
-0.0
-3
-7
10
55
60
65
70
75
80
85
CENTERED DIPOLE LATITUDE

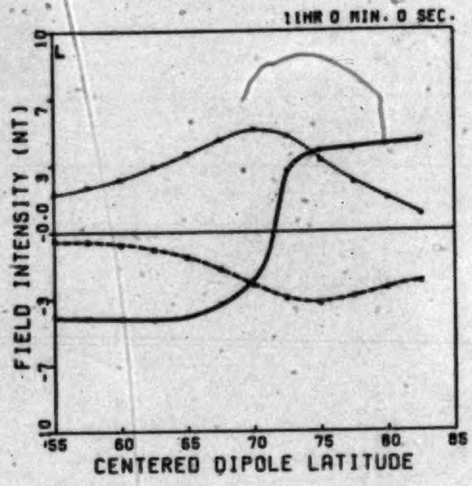
11HR 0 MIN. 0 SEC.
L
FIELD INTENSITY (NT)
10
7
3
0.0
-0.0
-3
-7
0
55
60
65
70
75
80
85
CENTERED DIPOLE LATITUDE

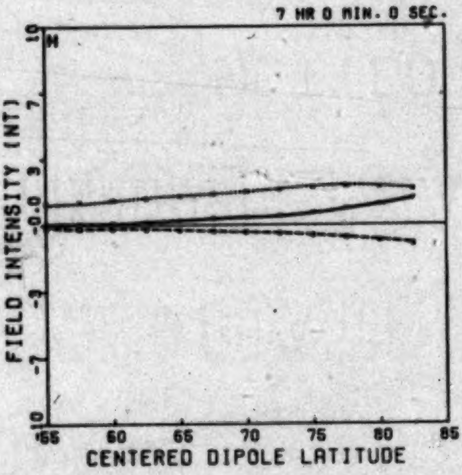
7 HR 0 MIN. 0 SEC.
H
FIELD INTENSITY (NT)
10
7
3
0.0
-0.0
-3
-7
0
55
60
65
70
75
80
85
CENTERED DIPOLE LATITUDE

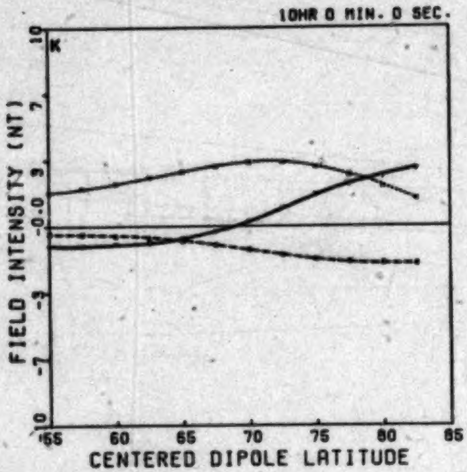
10HR 0 MIN. 0 SEC.
K
FIELD INTENSITY (NT)
10
7
3
0.0
-0.0
-3
-7
0
55
60
65
70
75
80
85
CENTERED DIPOLE LATITUDE

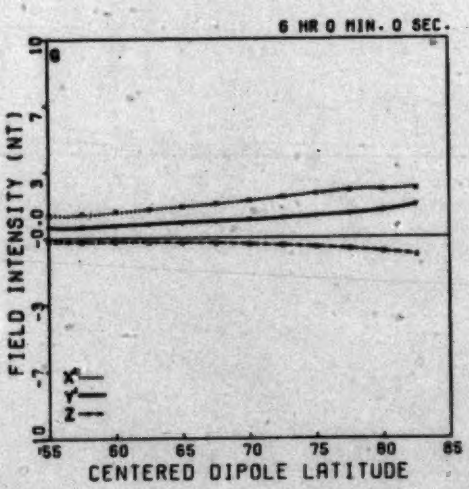
6 HR 0 MIN. 0 SEC.
G
FIELD INTENSITY (NT)
10
7
3
0.0
-0.0
-3
-7
10
X
Y
Z
55
60
65
70
75
80
85
CENTERED DIPOLE LATITUDE

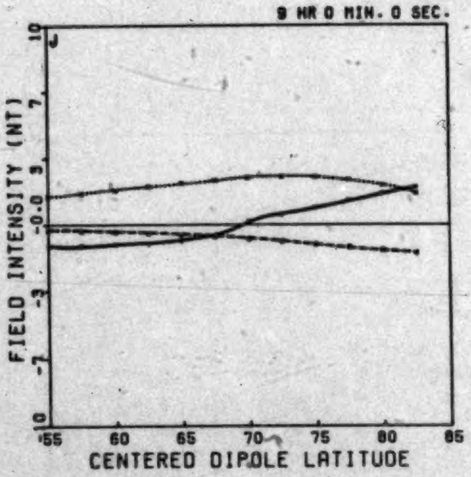
9 HR 0 MIN. 0 SEC.
J
FIELD INTENSITY (NT)
10
7
3
0.0
-0.0
-3
-7
0
55
60
65
70
75
80
85
CENTERED DIPOLE LATITUDE

Figure 4.11 Model latitude profiles due to the complete eastward current system, to which has been added the corresponding north-south current system.

m) 1200 to 1300 MLT
n) 1300 to 1400 MLT
o) 1400 to 1500 MLT
p) 1500 to 1600 MLT
q) 1600 to 1700 MLT
r) 1700 to 1800 MLT

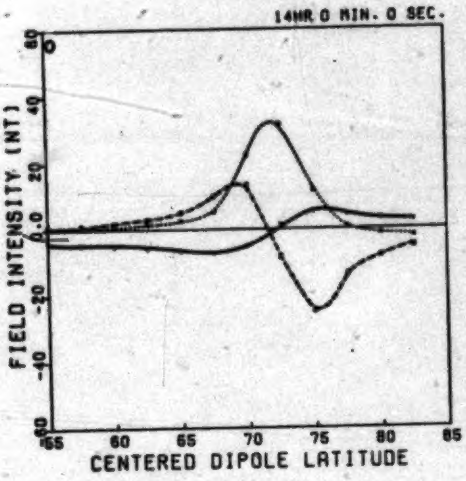
14HR 0 MIN. 0 SEC.
O
FIELD INTENSITY (NT)
60
40
20
0.0
-20
-40
-60
55
60
65
70
75
80
85
CENTERED DIPOLE LATITUDE

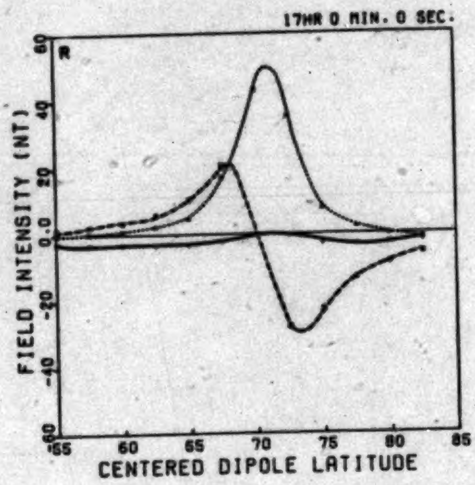
17HR 0 MIN. 0 SEC.
R
FIELD INTENSITY (NT)
60
40
20
0.0
-20
-40
-60
55
60
65
70
75
80
85
CENTERED DIPOLE LATITUDE

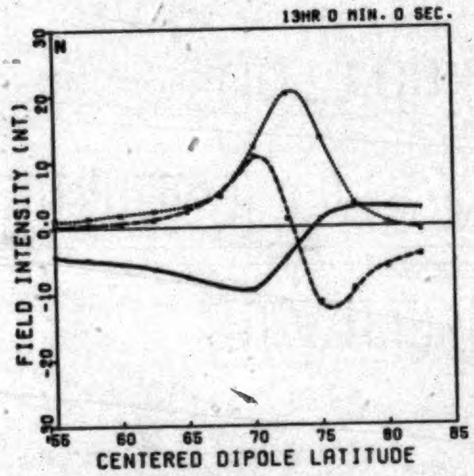
13HR 0 MIN. 0 SEC.
N
FIELD INTENSITY (NT)
30
20
10
0.0
-10
-20
-30
55
60
65
70
75
80
85
CENTERED DIPOLE LATITUDE

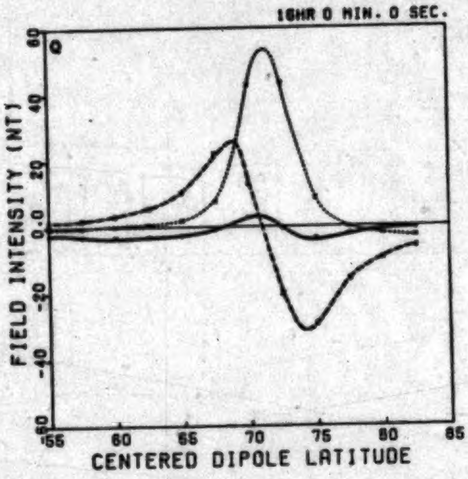
16HR 0 MIN. 0 SEC.
Q
FIELD INTENSITY (NT)
60
40
20
0.0
-20
-40
-60
55
60
65
70
75
80
85
CENTERED DIPOLE LATITUDE

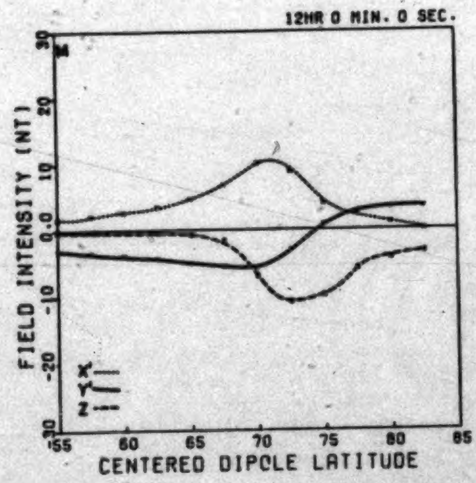
12HR 0 MIN. 0 SEC.
M
FIELD INTENSITY (NT)
30
20
10
0.0
-10
-20
-30
X
Y
Z
55
60
65
70
75
80
85
CENTERED DIPOLE LATITUDE

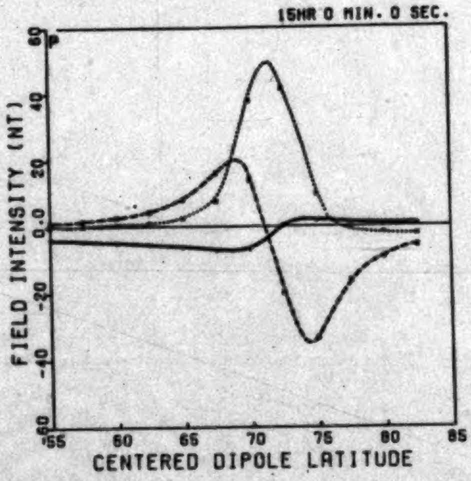
15HR 0 MIN. 0 SEC.
P
FIELD INTENSITY (NT)
60
40
20
0.0
-20
-40
-60
55
60
65
70
75
80
85
CENTERED DIPOLE LATITUDE

Figure 4.11 Model latitude profiles due to the complete eastward current system, to which has been added the corresponding north-south current system.

s) 1800 to 1900 MLT
t) 1900 to 2000 MLT
u) 2000 to 2100 MLT
v) 2100 to 2200 MLT
w) 2200 to 2300 MLT
x) 2300 to 2400 MLT

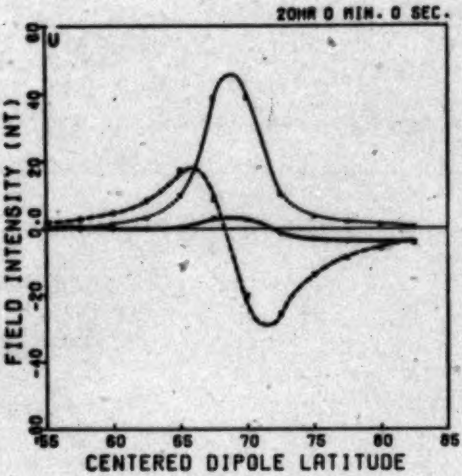
20HR 0 MIN. 0 SEC.
U
FIELD INTENSITY (NT)
60
40
20
0.0
-20
-40
-60
55
60
65
70
75
80
85
CENTERED DIPOLE LATITUDE

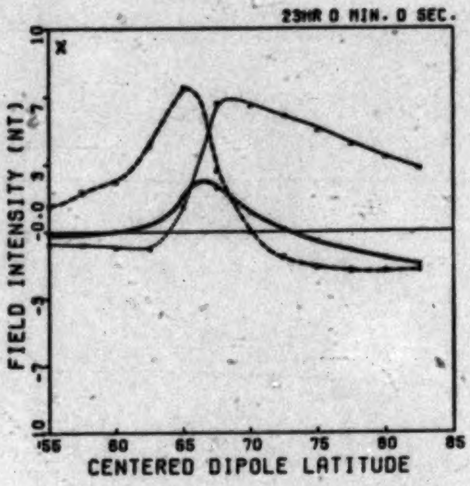
23HR 0 MIN. 0 SEC.
X
FIELD INTENSITY (NT)
10
7
3
0.0
-3
-7
-10
55
60
65
70
75
80
85
CENTERED DIPOLE LATITUDE

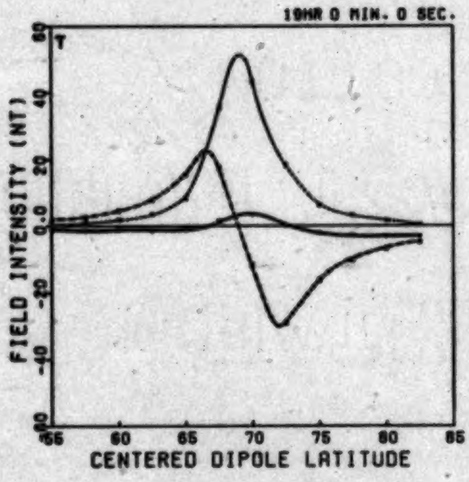
19HR 0 MIN. 0 SEC.
T
FIELD INTENSITY (NT)
60
40
20
0.0
-20
-40
-60
55
60
65
70
75
80
85
CENTERED DIPOLE LATITUDE

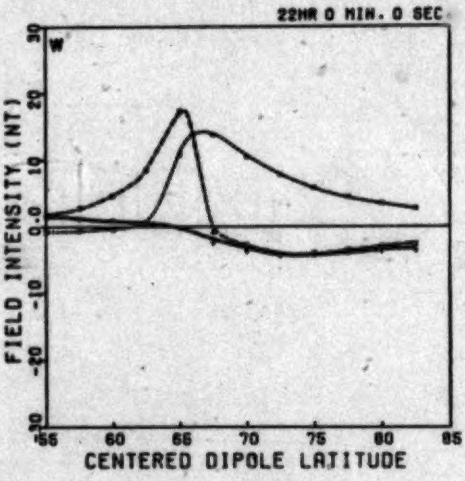
22HR 0 MIN. 0 SEC.
W
FIELD INTENSITY (NT)
30
20
10
0.0
-10
-20
-30
55
60
65
70
75
80
85
CENTERED DIPOLE LATITUDE

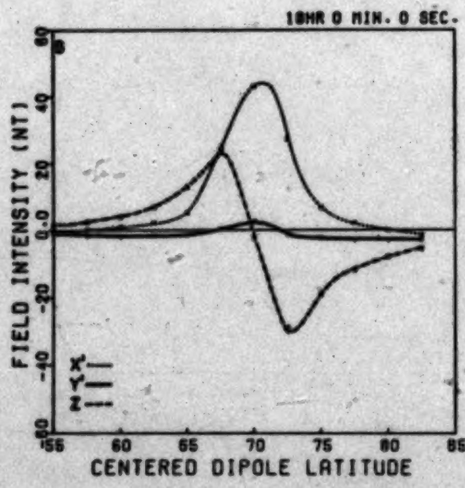
18HR 0 MIN. 0 SEC.
S
FIELD INTENSITY (NT)
60
40
20
0.0
-20
-40
-60
X
Y
Z
55
60
65
70
75
80
85
CENTERED DIPOLE LATITUDE

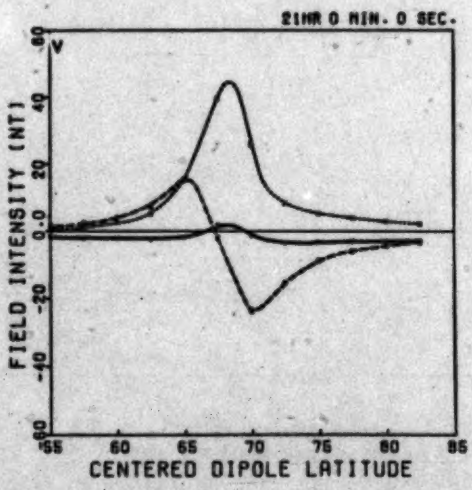
21HR 0 MIN. 0 SEC.
V
FIELD INTENSITY (NT)
60
40
20
0.0
-20
-40
-60
55
60
65
70
75
80
85
CENTERED DIPOLE LATITUDE

2300 MLT (Figure 4.11(v) to 4.11(x). In Figure 4.11(v) (2100 MLT) the Y'-component is altered by the poleward flowing current system so as to almost completely mask the effect of the tilted eastward current system. The same effect is seen in Figure 4.11(w) (2200 MLT), where as well, the level-shift in the Y'-component is reduced by the addition of the north-south current system. Also, in the 2200 MLT profile, the Z-component is changed so that the well-defined negative extremum shown in the profiles for the eastward current alone (Figure 4.10(w)) is all but lost. The profiles for 2300 MLT (Figure 4.10(x) and 4.11(x)) show that the north-south current system produces a marked change in all 3 components; the X'-component develops distinctly positive values at high latitude; the Y'-component takes on the character of a strongly tilted east-west current system; and the Z-component gains a marked positive extremum. Apart from this time period, little change is observed in the profiles which result from adding the poleward flowing current system to the eastward electrojet.

4.4.3 The North-South Current System

For the sake of completeness, the entire north-south current system is shown in Figure 4.12 (24 panels). This system is frequently neglected in auroral current models, at least in the case of polar magnetic substorms. Indeed, in these cases there may be some justification for considering only the east-west current systems inasmuch as the ratio of

Figure 4.12 Model latitude profiles due to the entire north-south current system.

a) 0000 to 0100 MLT
b) 0100 to 0200 MLT
c) 0200 to 0300 MLT
d) 0300 to 0400 MLT
e) 0400 to 0500 MLT
f) 0500 to 0600 MLT

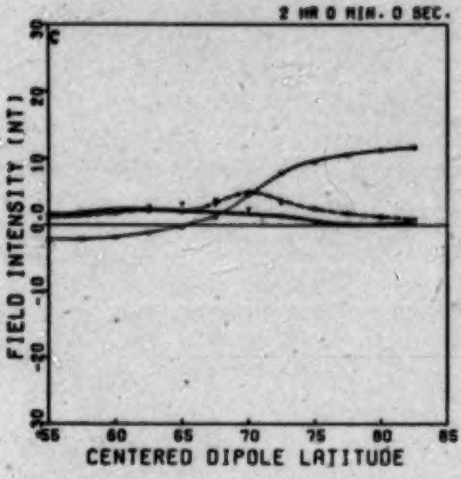
C
2 HR 0 MIN. 0 SEC.
FIELD INTENSITY (NT)
30
20
10
0.0
-10
-20
-30
55
60
65
70
75
80
85
CENTERED DIPOLE LATITUDE

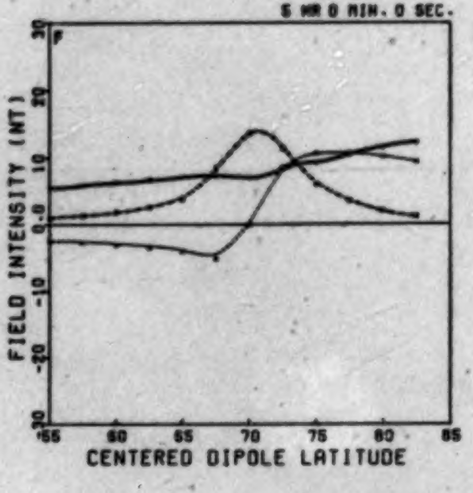
F
5 HR 0 MIN. 0 SEC.
FIELD INTENSITY (NT)
30
20
10
0.0
-10
-20
-30
55
60
65
70
75
80
85
CENTERED DIPOLE LATITUDE

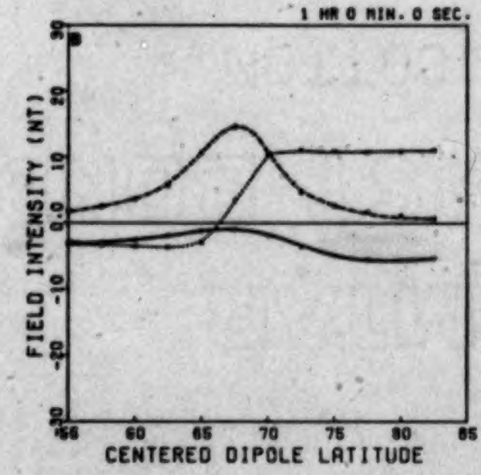
B
1 HR 0 MIN. 0 SEC.
FIELD INTENSITY (NT)
30
20
10
0.0
-10
-20
-30
55
60
65
70
75
80
85
CENTERED DIPOLE LATITUDE

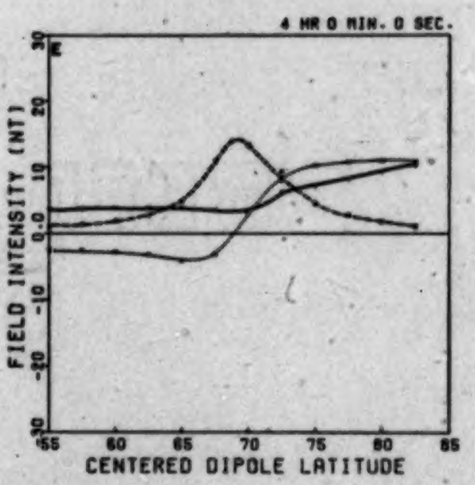
E
4 HR 0 MIN. 0 SEC.
FIELD INTENSITY (NT)
30
20
10
0.0
-10
-20
-30
55
60
65
70
75
80
85
CENTERED DIPOLE LATITUDE

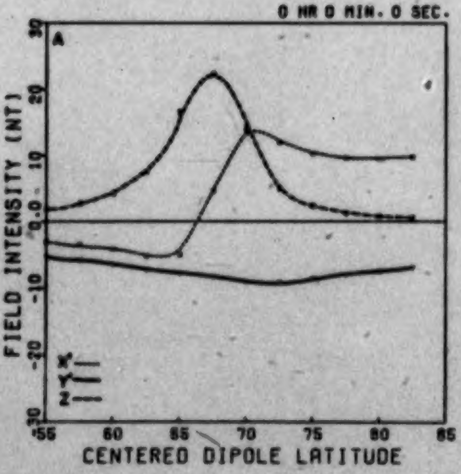
A
0 HR 0 MIN. 0 SEC.
FIELD INTENSITY (NT)
30
20
10
0.0
-10
-20
-30
X
Y
Z
55
60
65
70
75
80
85
CENTERED DIPOLE LATITUDE

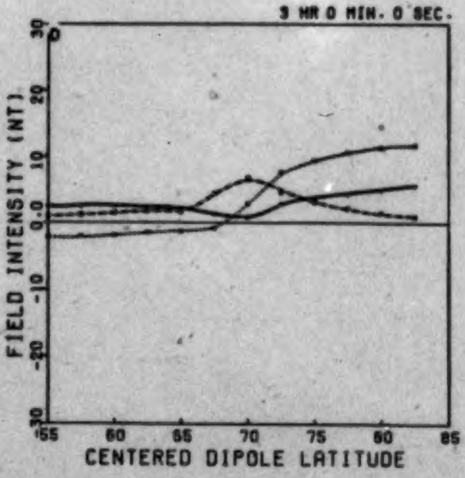
D
3 HR 0 MIN. 0 SEC.
FIELD INTENSITY (NT)
30
20
10
0.0
-10
-20
-30
55
60
65
70
75
80
85
CENTERED DIPOLE LATITUDE

Figure 4.12 Model latitude profiles due to the entire north-south current system.

g) 0600 to 0700 MLT
h) 0700 to 0800 MLT
i) 0800 to 0900 MLT
j) 0900 to 1000 MLT
k) 1000 to 1100 MLT
l) 1100 to 1200 MLT

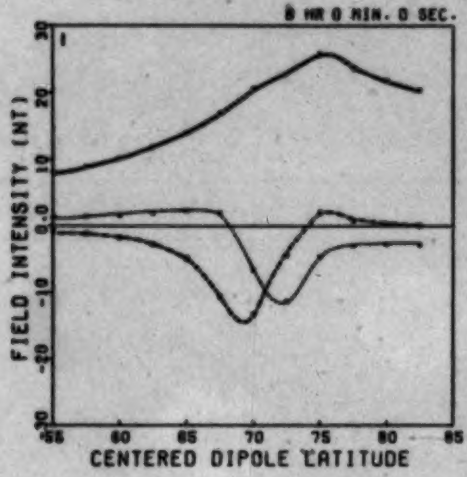
8 HR 0 MIN. 0 SEC.
I
FIELD INTENSITY (NT)
30
20
10
0.0
-10
-20
-30
55
60
65
70
75
80
85
CENTERED DIPOLE LATITUDE

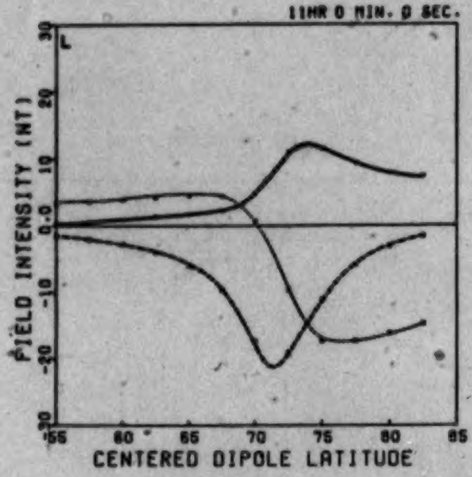
11HR 0 MIN. 0 SEC.
L
FIELD INTENSITY (NT)
30
20
10
0.0
-10
-20
-30
55
60
65
70
75
80
85
CENTERED DIPOLE LATITUDE

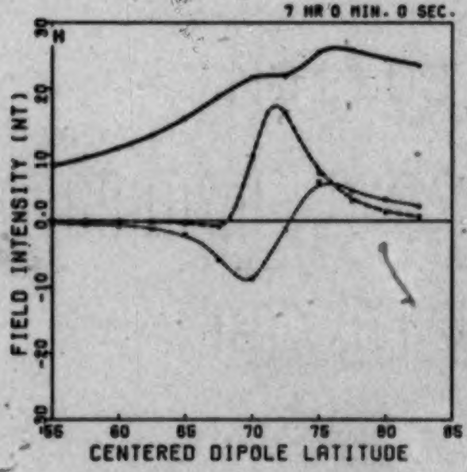
7 HR 0 MIN. 0 SEC.
H
FIELD INTENSITY (NT)
30
20
10
0.0
-10
-20
-30
55
60
65
70
75
80
85
CENTERED DIPOLE LATITUDE

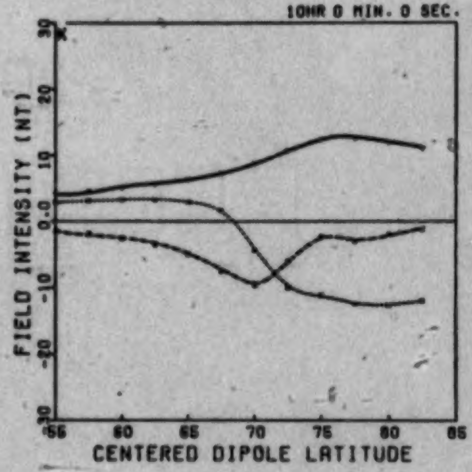
10HR 0 MIN. 0 SEC.
K
FIELD INTENSITY (NT)
30
20
10
0.0
-10
-20
-30
55
60
65
70
75
80
85
CENTERED DIPOLE LATITUDE

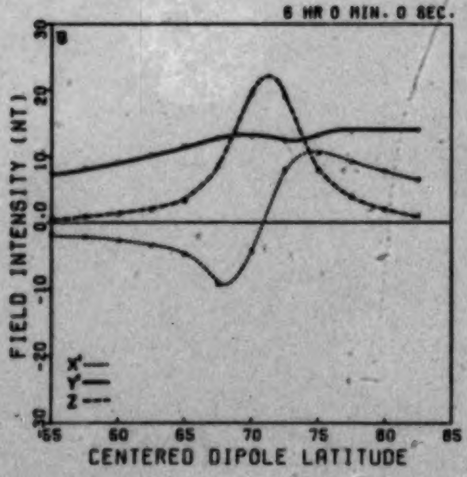
6 HR 0 MIN. 0 SEC.
G
FIELD INTENSITY (NT)
30
20
10
0.0
-10
-20
-30
X
Y
Z
55
60
65
70
75
80
85
CENTERED DIPOLE LATITUDE

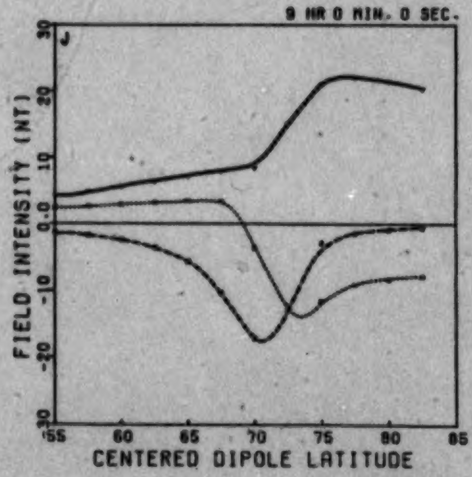
9 HR 0 MIN. 0 SEC.
J
FIELD INTENSITY (NT)
30
20
10
0.0
-10
-20
-30
55
60
65
70
75
80
85
CENTERED DIPOLE LATITUDE

Figure 4.12 Model latitude profiles due to the entire north-south current system.

m) 1200 to 1300 MLT
n) 1300 to 1400 MLT
o) 1400 to 1500 MLT
p) 1500 to 1600 MLT
q) 1600 to 1700 MLT
r) 1700 to 1800 MLT

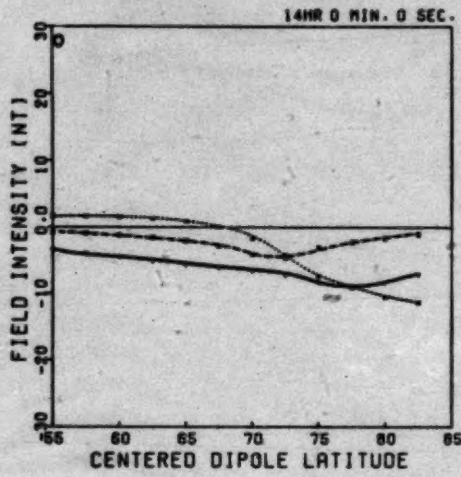
14HR 0 MIN. 0 SEC.
O
FIELD INTENSITY (NT)
30
20
10
0.0
-10
-20
-30
55
60
65
70
75
80
85
CENTERED DIPOLE LATITUDE

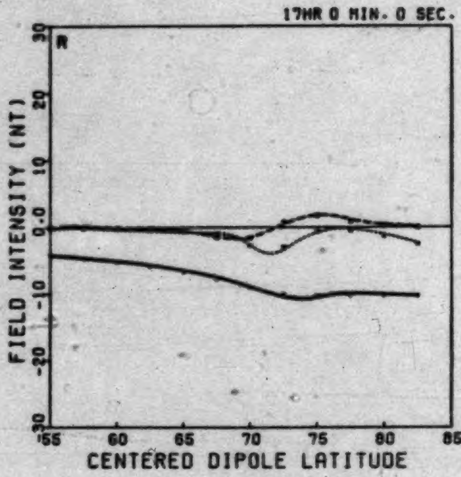
17HR 0 MIN. 0 SEC.
R
FIELD INTENSITY (NT)
30
20
10
0.0
-10
-20
-30
55
60
65
70
75
80
85
CENTERED DIPOLE LATITUDE

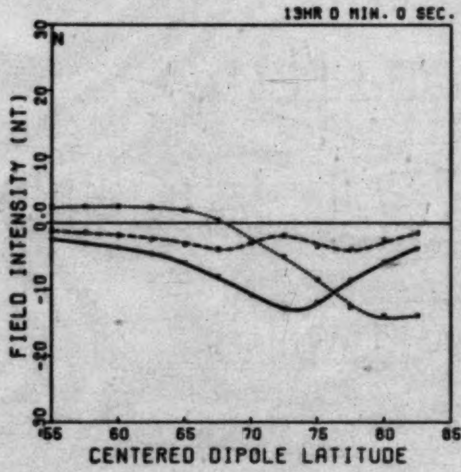
13HR 0 MIN. 0 SEC.
N
FIELD INTENSITY (NT)
30
20
10
0.0
-10
-20
-30
55
60
65
70
75
80
85
CENTERED DIPOLE LATITUDE

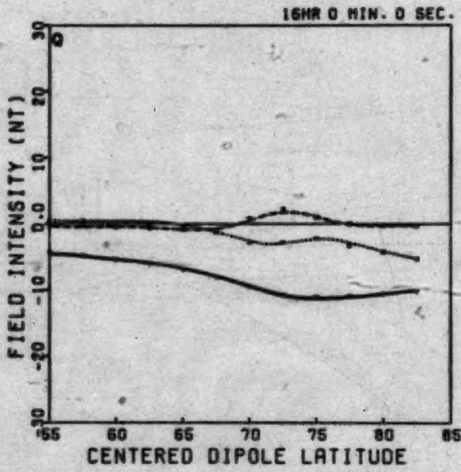
16HR 0 MIN. 0 SEC.
Q
FIELD INTENSITY (NT)
30
20
10
0.0
-10
-20
-30
55
60
65
70
75
80
85
CENTERED DIPOLE LATITUDE

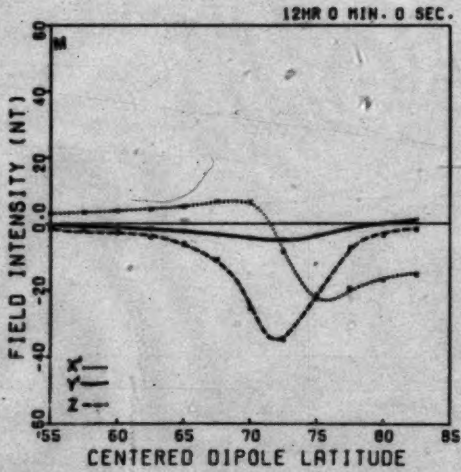
12HR 0 MIN. 0 SEC.
M
FIELD INTENSITY (NT)
60
40
20
0.0
-20
-40
-60
X
Y
Z
55
60
65
70
75
80
85
CENTERED DIPOLE LATITUDE

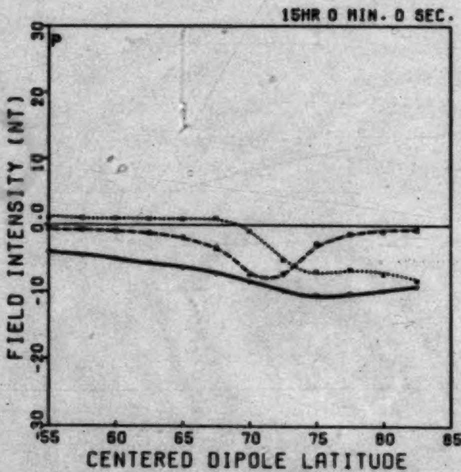
15HR 0 MIN. 0 SEC.
P
FIELD INTENSITY (NT)
30
20
10
0.0
-10
-20
-30
55
60
65
70
75
80
85
CENTERED DIPOLE LATITUDE

Figure 4.12 Model latitude profiles due to the entire north-south current system.

s) 1800 to 1900 MLT
t) 1900 to 2000 MLT
u) 2000 to 2100 MLT
v) 2100 to 2200 MLT
w) 2200 to 2300 MLT
x) 2300 to 2400 MLT

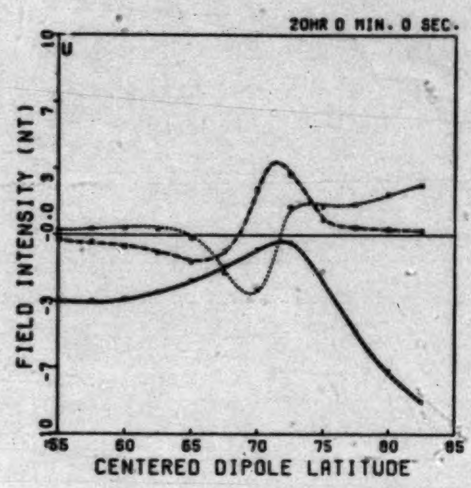
20HR 0 MIN. 0 SEC.
U
FIELD INTENSITY (NT)
10
7
3
0.0
-3
-7
-10
55
60
65
70
75
80
85
CENTERED DIPOLE LATITUDE

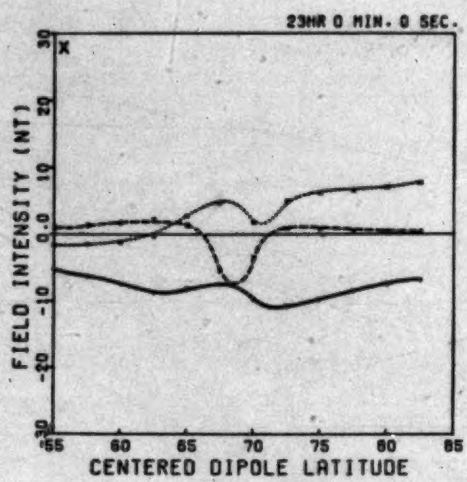
23HR 0 MIN. 0 SEC.
X
FIELD INTENSITY (NT)
30
20
10
0.0
-10
-20
-30
55
60
65
70
75
80
85
CENTERED DIPOLE LATITUDE

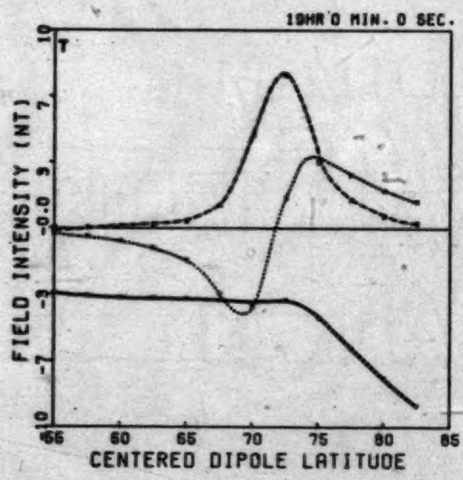
19HR 0 MIN. 0 SEC.
T
FIELD INTENSITY (NT)
10
7
3
0.0
-3
-7
-10
55
60
65
70
75
80
85
CENTERED DIPOLE LATITUDE

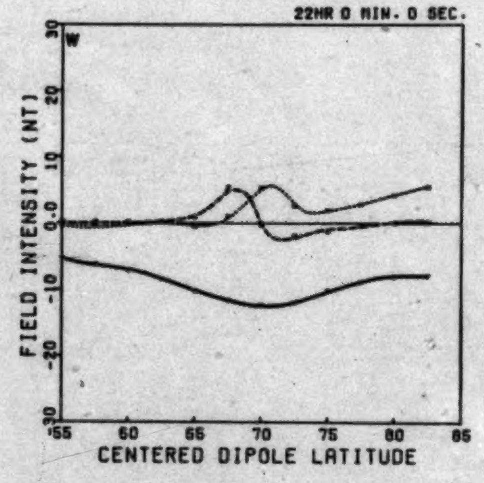
22HR 0 MIN. 0 SEC.
W
FIELD INTENSITY (NT)
30
20
10
0.0
-10
-20
-30
55
60
65
70
75
80
85
CENTERED DIPOLE LATITUDE

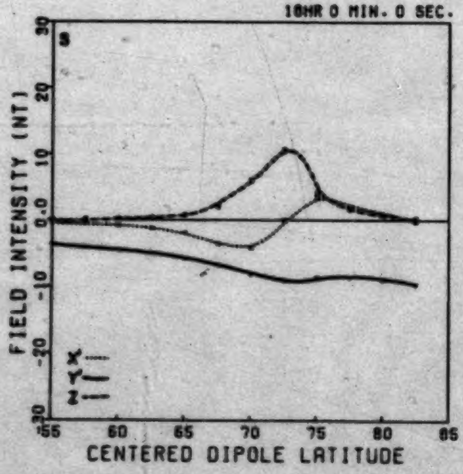
18HR 0 MIN. 0 SEC.
S
FIELD INTENSITY (NT)
30
20
10
0.0
-10
-20
-30
X
Y
Z
55
60
65
70
75
80
85
CENTERED DIPOLE LATITUDE

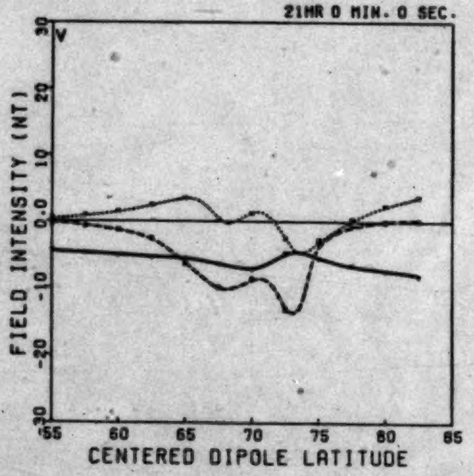
21HR 0 MIN. 0 SEC.
V
FIELD INTENSITY (NT)
30
20
10
0.0
-10
-20
-30
55
60
65
70
75
80
85
CENTERED DIPOLE LATITUDE

Σ_H to Σ_P increases to about 4 during periods of high magnetic activity (Brekke et al, 1974), so that the role of the north-south currents is relatively less important during substorms. Since the north-south currents are primarily Pedersen currents, their role in substorm modelling is possibly relatively small. Kisabeth (1972, 1975) and Bannister (1976) have successfully modelled substorms while ignoring north-south current systems. However, in this model, representing quiet to moderately disturbed periods the north-south current system becomes relatively important as may be seen in the model latitude profiles of Figure 4.12. In the first two profiles (Figure 4.12(a) and (b): 0000 and 0100 MLT), the effect of the northward flowing current in the midnight sector is seen as a strong positive ΔZ perturbation. It will be recalled that in the SPEA profiles from the post-midnight quadrant, the Z-component exhibited an asymmetry, with the positive extremum being greater than the norm of the negative extremum. In fact, this positive ΔZ profile continues in the model north-south system until about dawn. From 0400 to 1100 MLT (Figures 4.12(e) to 4.12(l)), the Y'-component is of greatest interest. It is evident that the total north-south system enhances the level-shift in $\Delta Y'$, as was seen in the comparison of Figure 4.8 and 4.9. In the 1100 and 1200 MLT model profiles (Figure 4.12(l) and (m)), the Z-component is distinctly negative. As will be seen in section 4.5, this effect is highly influential in the total model. As already noted, the north-south current system has only a minimal effect in the region of the eastward electrojet, from noon to dusk. However, the total system produces a fairly marked effect, in the post-dusk sector, on the $\Delta Y'$ profiles (Figures 4.12(t) to 4.12(v); 1900 to 2100 MLT) In this regime, the total north-south current system markedly enhances the negative going level-shift in the Y'-component.

Finally, the last two panels of Figure 4.12 (w and x; 2200 and 2300 MLT) show a negative Y'-component across the entire latitude profile, in keeping with the poleward flowing current in this region.

4.4.4. Other Contributing Current Systems

In addition to the current systems discussed up to this point, it was necessary to add two other current systems, although these are of relatively minor importance. The first of these was the eastward flowing current located immediately equatorward of the westward electrojet in the dawn sector. This current was made to flow anti-parallel to the westward electrojet in a 5° wide latitudinal strip whose poleward border coincided with the equatorward border of the westward electrojet. The current was limited to the longitude range of 60° to 165°; that is, eastward current flowed from 0400 MLT to 1100 MLT. For modelling purposes it was assumed that this current is fed from a downward field-aligned sheet current that diverges eastward. At dawn, the conductivity gradient described earlier (section 4.4.1) is encountered, and additional current flows into the ionosphere at this point. At 1100 MLT the current diverges back up a field-aligned current sheet to the magnetosphere. The maximum current flowing in this electrojet is 10^4 A, for a maximum height-integrated current density of 0.018 Am^{-1}. Latitude profiles for this current system possess no unusual features and are not presented here. The maximum positive $\Delta X'$ perturbation is about 5nT, occurring in the profile for 0900 MLT.

The final current system is also a relatively weak system when compared with either the westward or the eastward electrojet systems, but one which possesses useful features, from the point of view of the global model.

When this study was first undertaken, it was observed that the $\Delta Y'$ level-shift was not symmetric about the field intensity origin. (See, for example, Figure 4.3) However, an unbalanced, distributed field-aligned current produces a $\Delta Y'$ level-shift which is essentially symmetric about the origin (Figure 3.7). As well, it became evident that the inferences drawn from the ground-based magnetic data regarding unbalanced field-aligned currents were not in total agreement with the results obtained from the Triad magnetometer data (Sugiura and Potemra, 1976). That is, interpretation of the satellite data showed that net upward field-aligned current flowed in the post-noon sector, the exact opposite of the results of the ground-based data. Hughes and Rostoker (1977) offered an heuristic argument in an attempt to explain this discrepancy. This argument is as follows. Rostoker and Hron (1975) have pointed out that in the dawn sector there exists an equatorward-flowing Hall current, and it is assumed that this Hall current circulates through the low latitude ionosphere to the post-noon quadrant and then flows up field lines into the magnetosphere. Consider two infinite anti-parallel plane sheet currents separated by a finite distance (Figure 4.13(a)). The ionospheric equivalent current for the downward-flowing sheet current (I) is two horizontal sheets of strength I/2 flowing toward the vertical sheet. Similarly, the equivalent current for the upward-flowing current sheet (I) is two horizontal current sheets (I/2) flowing away from the vertical sheet. (This is simply an extension of the technique used by Fukushima (1969) for line currents). Connecting these two vertical sheets by a horizontal sheet current results in an equivalent current for the system of zero, so that no magnetic perturbation is observed on the ground.

If, as suggested above, there is a horizontal current flow into the region of Birkeland current flow associated with the auroral oval in the post-noon quadrant (Figure 4.13(b)), then there will be an unbalanced upward current flow (as observed by Triad), but no level-shift will occur in the east-west component as observed on the ground. However, Figure 4.13(b) shows that there will be a bias in the east-west component. A similar argument to this may be

Figure 4.13(a) Schematic drawing of equivalent ionospheric currents for infinite vertical current sheets and a pair of anti-parallel vertical current sheets connecting through a horizontal sheet. Equivalent currents from the downward-flowing current are shown by the dashed lines, and those from the upward-flowing current are shown by the dotted lines. Real currents are shown by the solid lines.

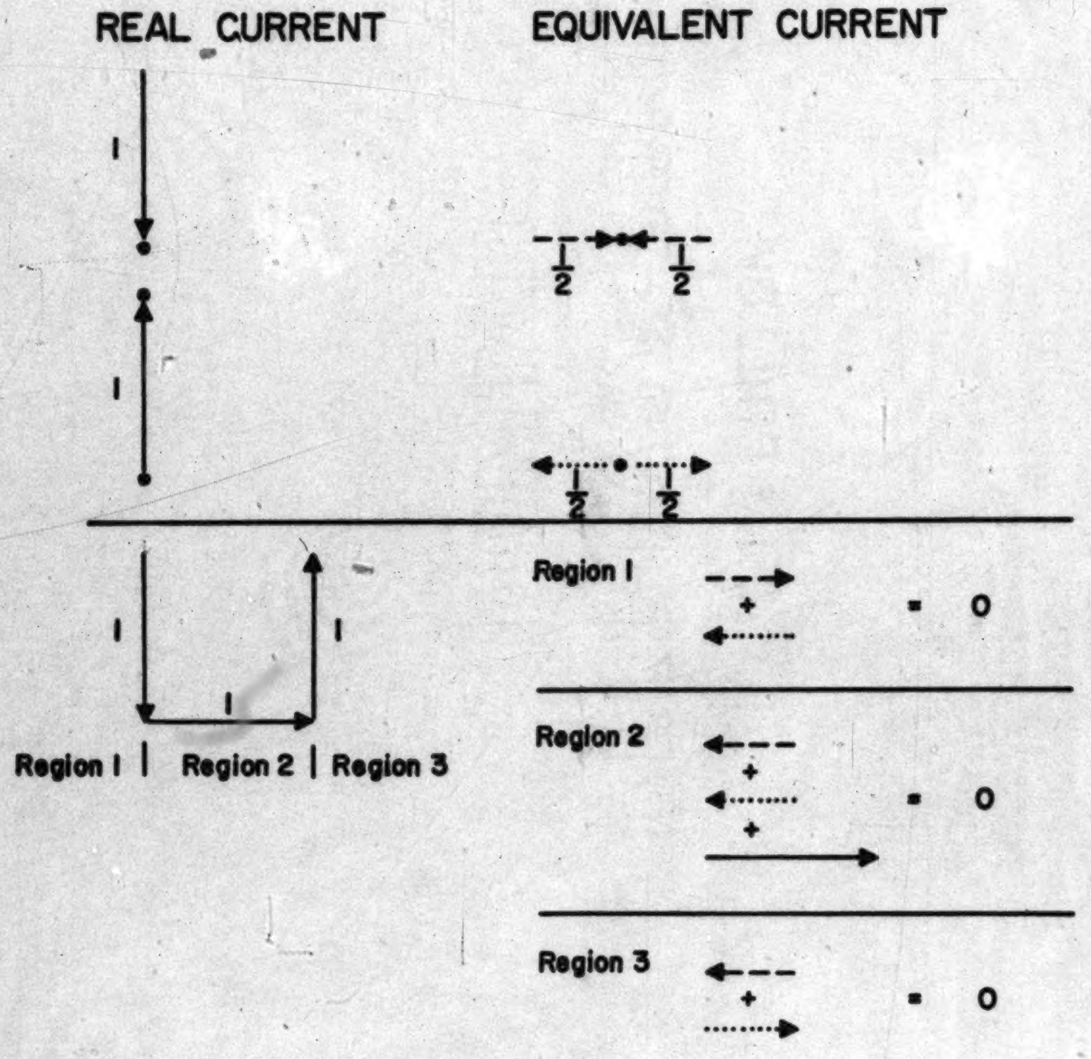
REAL CURRENT
EQUIVALENT CURRENT
I
I
$\frac{I}{2}$
$\frac{I}{2}$
$\frac{I}{2}$
$\frac{I}{2}$
I
I
I
Region I
Region 2
Region 3
Region I
+
= 0
Region 2
+
+
= 0
Region 3
+
= 0

Figure 4.13(b) Schematic drawing of equivalent ionospheric currents for a current system in which the upward current ($I_1 + I_2$) is greater than the downward current, I_1, because of an ionospheric current I_2 flowing into the system. The equivalent current I /2 is uniform across the current system and directed to the right.

REAL CURRENT

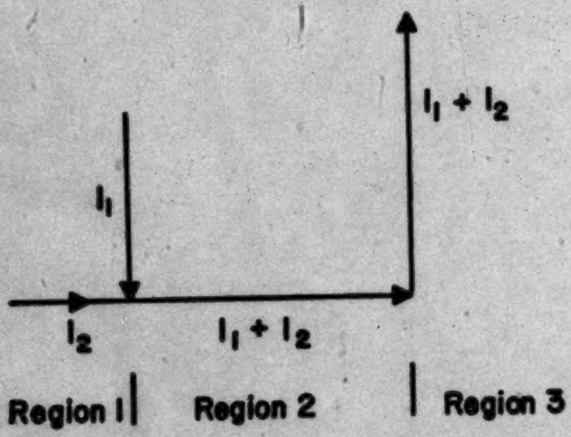
I_1
I_2
$I_1 + I_2$
$I_1 + I_2$
Region I
Region 2
Region 3

EQUIVALENT CURRENT

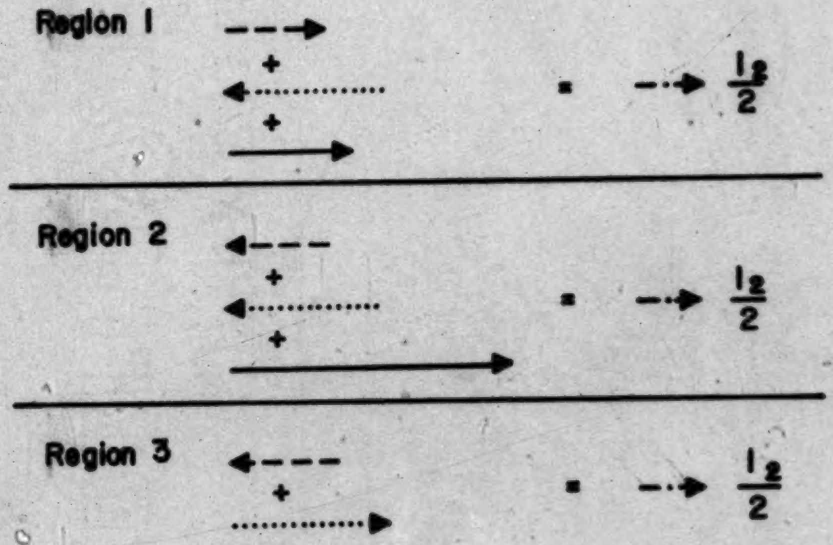
Region I
+
+
=
$\frac{I_2}{2}$
Region 2
+
+
=
$\frac{I_2}{2}$
Region 3
+
=
$\frac{I_2}{2}$

applied to the pre-noon quadrant to produce a bias in the east-west component. That is, downward current which diverges equatorward will produce a positive bias in the Y'-component. Thus, it is possible to explain the discrepancy between the ground data and the satellite data, as well as explain the observed bias in the Y'-component, with the same argument. Of course, in reality, this argument is not totally valid. The closure of the vertical currents is not complete, since closure currents in the outer magnetosphere are neglected, and also, the real currents are of finite extent. However, the argument was successful enough to lead to further investigation of such a current system.

These currents will be referred to as the low-latitude current system. The total current flowing in this system is 0.1875 x 10^5A, only 15% of the maximum westward flowing current. The low-latitude current system consists of field-aligned current flowing into the auroral oval within the 0600 to 1100 MLT sector. This current diverges equatorward and eventually into an eastward flowing current located between 0° to 40° latitude. In the post-noon quadrant, this eastward current in turn flows poleward and then diverges up field lines at the poleward border of the eastward electrojet. Note that in the pre-noon sector, the field-aligned current is distributed over the latitude range of the oval, whereas in the post-noon sector, the field-aligned current is confined to a sheet. From 0800 to 1100 MLT, the ionospheric current has an average height-integrated current density of $6 \times 10^{-4} Am^{-1}$. from 0800 to 0600 MLT, the height-integrated current density decreases to zero. At sub-auroral latitudes, the ionospheric current intensity is anti-symmetric about noon.

Schematically, this current system bears some resemblance to the Sq current system. However the model system is not completely closed in the ionosphere, as is the Sq system. This model system bears an even closer resemblance to the DP-2 system of Nishida (1968) although DP-2 is not symmetric, in its geometry, about noon. Akasofu et al (1973) have suggested that Nishida's DP-2 system may be due to an intensification of the S_q^p current system together with an expansion of the auroral oval (see Chapter 1). It is possible then that the low-latitude current system corresponds to DP-2 or S_q^p for the winter ionosphere, since no polar cap current flows in the model. This topic will be discussed somewhat further in section 4.7.1 of this chapter.

The 24 panels of Figure 4.14 are latitude profiles generated by the model low-latitude current system. It is evident from Figures 4.14(a) to 4.14(f) and Figures 4.14(t) to 4.14(x) that this system has little effect in the dark hemisphere. Note that in the 0600 MLT to 1800 MLT sector (Figure 4.14(g) to 4.14(s)) the Y'-component is biased as described in previous paragraphs, i.e. $\Delta Y'$ is positive in the pre-noon sector, and negative in the post-noon sector. However, unlike in the theoretical argument put forth earlier, there is an additional feature to the Y'-component,

Figure 4.14 Model latitude profiles due to the low-latitude current system.

a) 0000 to 0100 MLT
b) 0100 to 0200 MLT
c) 0200 to 0300 MLT
d) 0300 to 0400 MLT
e) 0400 to 0500 MLT
f) 0500 to 0600 MLT

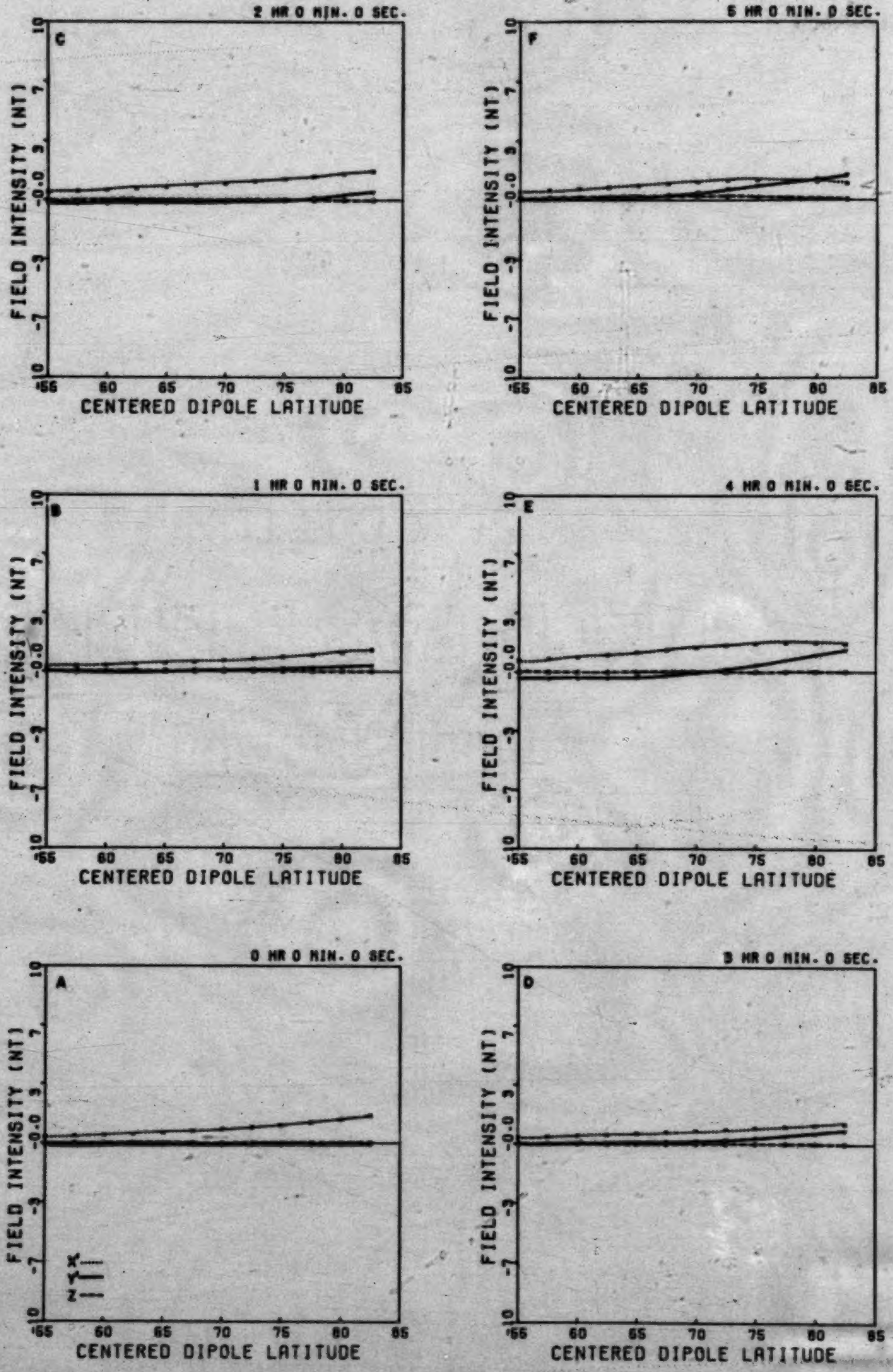
2 HR 0 MIN. 0 SEC.
C
5 HR 0 MIN. 0 SEC.
F
1 HR 0 MIN. 0 SEC.
B
4 HR 0 MIN. 0 SEC.
E
0 HR 0 MIN. 0 SEC.
A
3 HR 0 MIN. 0 SEC.
D
FIELD INTENSITY (NT)
10
7
3
0.0
-0.0
-3
-7
0
CENTERED DIPOLE LATITUDE
55
60
65
70
75
80
85
X
Y
Z

Figure 4.14 Model latitude profiles due to the low-latitude current system.

g) 0600 to 0700 MLT
h) 0700 to 0800 MLT
i) 0800 to 0900 MLT
j) 0900 to 1000 MLT
k) 1000 to 1100 MLT
l) 1100 to 1200 MLT

8 HR 0 MIN. 0 SEC.

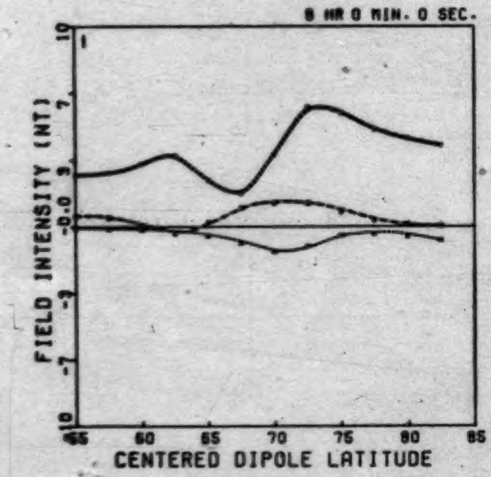

11HR 0 MIN. 0 SEC.

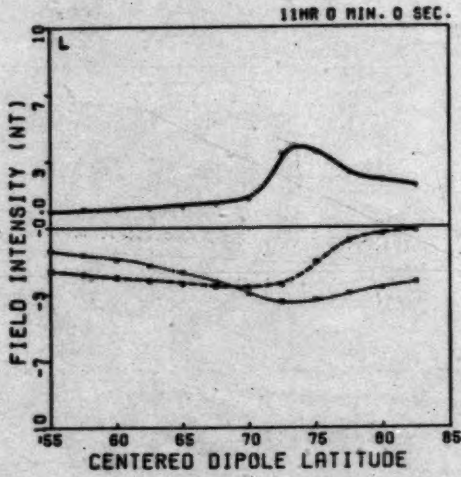

7 HR 0 MIN. 0 SEC.

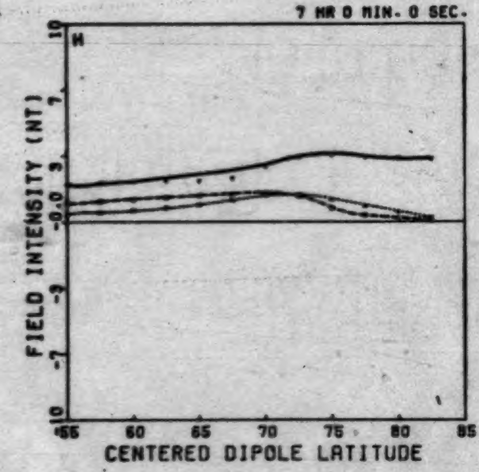

10HR 0 MIN. 0 SEC.

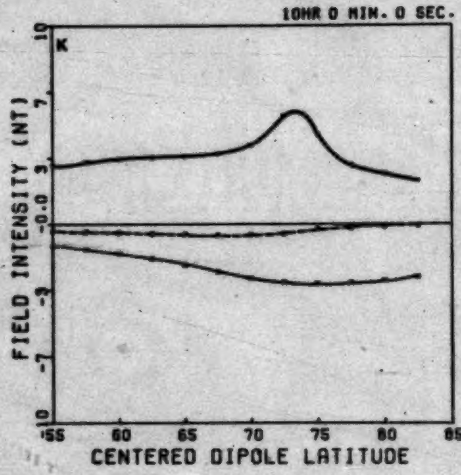

6 HR 0 MIN. 0 SEC.

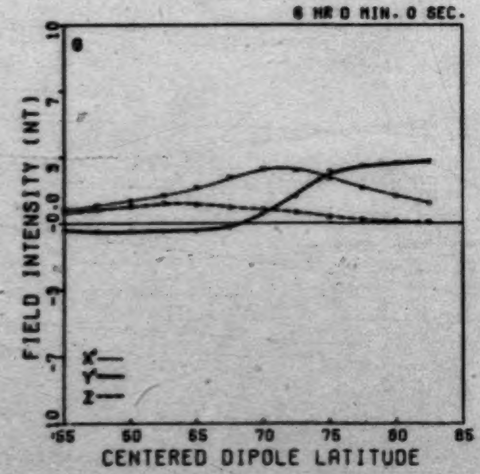

9 HR 0 MIN. 0 SEC.

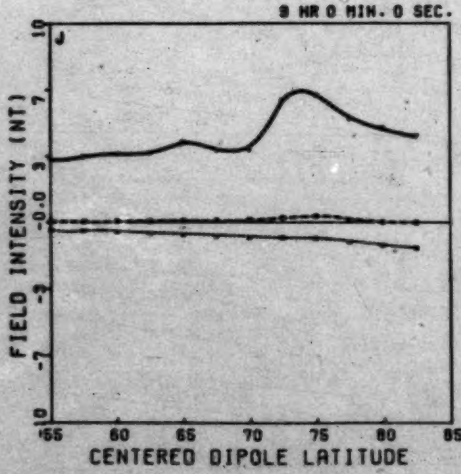

Figure 4.14 Model latitude profiles due to the low-latitude current system.

m) 1200 to 1300 MLT
n) 1300 to 1400 MLT
o) 1400 to 1500 MLT
p) 1500 to 1600 MLT
q) 1600 to 1700 MLT
r) 1700 to 1800 MLT

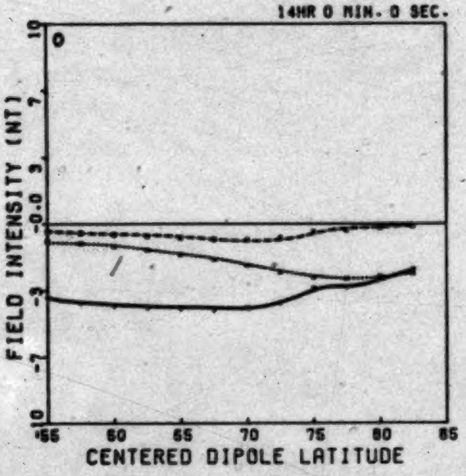
14HR 0 MIN. 0 SEC.
O
FIELD INTENSITY (NT)
10
7
3
-0.0
-3
-7
10
55
60
65
70
75
80
85
CENTERED DIPOLE LATITUDE

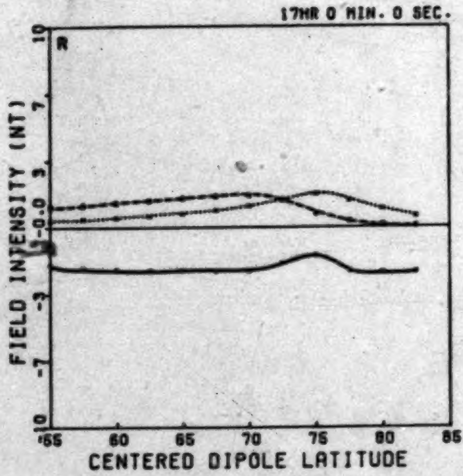
17HR 0 MIN. 0 SEC.
R
FIELD INTENSITY (NT)
10
7
3
-0.0
-3
-7
10
55
60
65
70
75
80
85
CENTERED DIPOLE LATITUDE

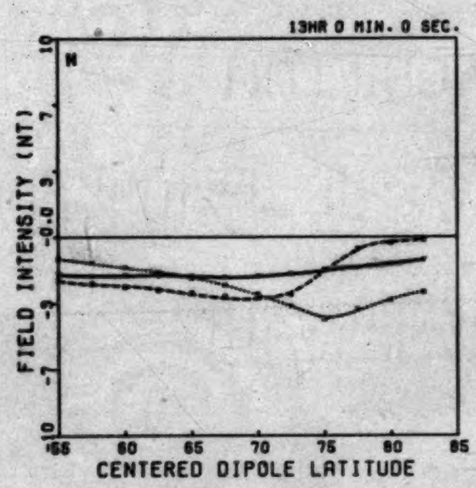
13HR 0 MIN. 0 SEC.
N
FIELD INTENSITY (NT)
10
7
3
-0.0
-3
-7
10
55
60
65
70
75
80
85
CENTERED DIPOLE LATITUDE

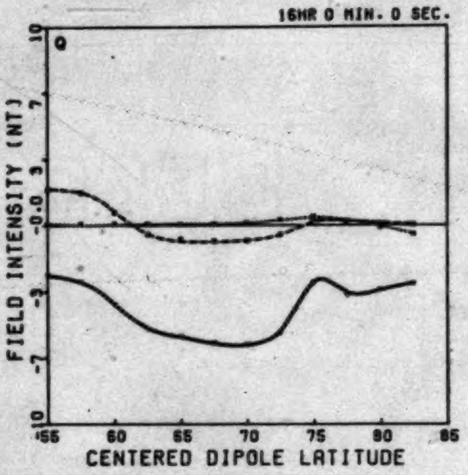
16HR 0 MIN. 0 SEC.
Q
FIELD INTENSITY (NT)
10
7
3
-0.0
-3
-7
10
55
60
65
70
75
80
85
CENTERED DIPOLE LATITUDE

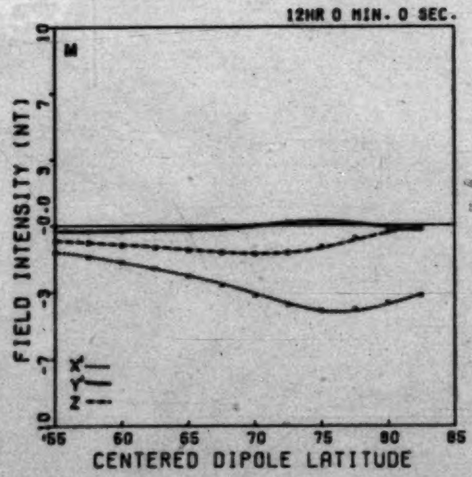
12HR 0 MIN. 0 SEC.
M
FIELD INTENSITY (NT)
10
7
3
-0.0
-3
-7
10
X
Y
Z
55
60
65
70
75
80
85
CENTERED DIPOLE LATITUDE

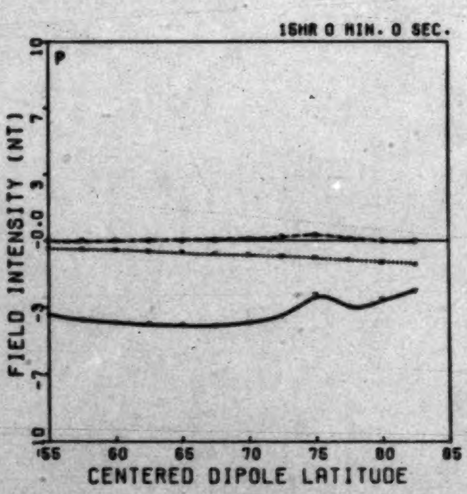
15HR 0 MIN. 0 SEC.
P
FIELD INTENSITY (NT)
10
7
3
-0.0
-3
-7
10
55
60
65
70
75
80
85
CENTERED DIPOLE LATITUDE

Figure 4.14 Model latitude profiles due to the low-latitude current system.

s) 1800 to 1900 MLT
t) 1900 to 2000 MLT
u) 2000 to 2100 MLT
v) 2100 to 2200 MLT
w) 2200 to 2300 MLT
x) 2300 to 2400 MLT

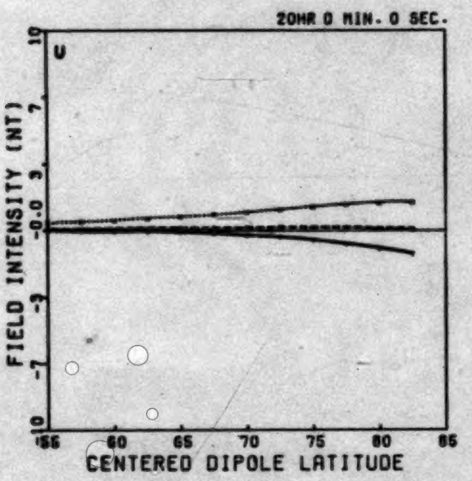
20HR 0 MIN. 0 SEC.
U
FIELD INTENSITY (NT)
10
7
3
0.0
-3
-7
CENTERED DIPOLE LATITUDE
55
60
65
70
75
80
85

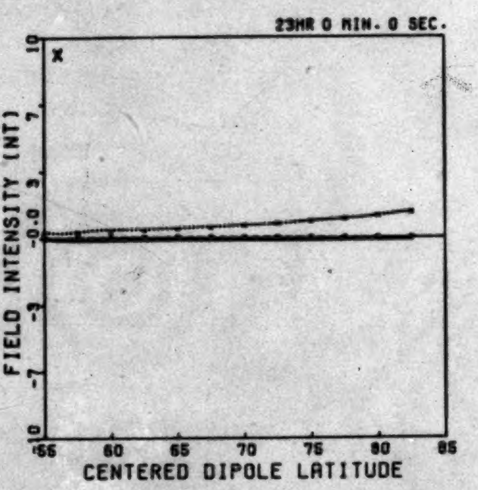
23HR 0 MIN. 0 SEC.
X
FIELD INTENSITY (NT)
10
7
3
0.0
-3
-7
CENTERED DIPOLE LATITUDE
55
60
65
70
75
80
85

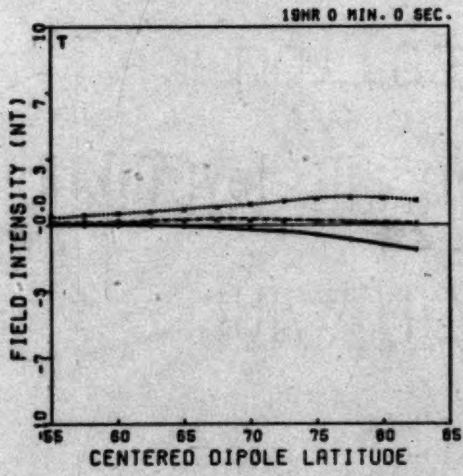
19HR 0 MIN. 0 SEC.
T
FIELD INTENSITY (NT)
10
7
3
0.0
-3
-7
CENTERED DIPOLE LATITUDE
55
60
65
70
75
80
85

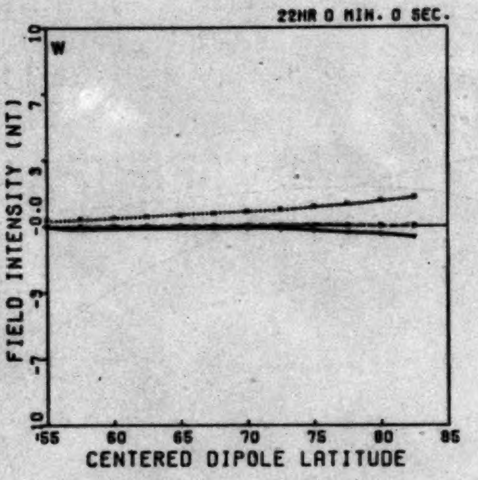
22HR 0 MIN. 0 SEC.
W
FIELD INTENSITY (NT)
10
7
3
0.0
-3
-7
CENTERED DIPOLE LATITUDE
55
60
65
70
75
80
85

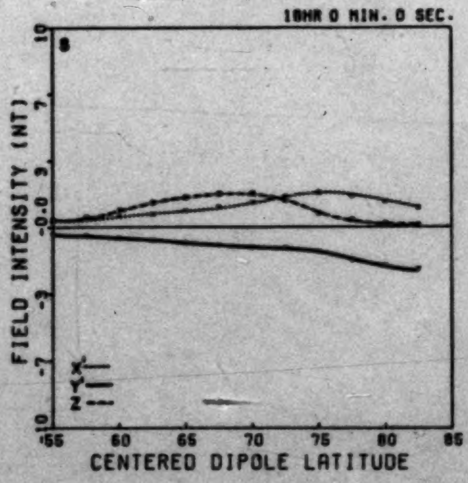
18HR 0 MIN. 0 SEC.
S
FIELD INTENSITY (NT)
10
7
3
0.0
-3
-7
X
Y
Z
CENTERED DIPOLE LATITUDE
55
60
65
70
75
80
85

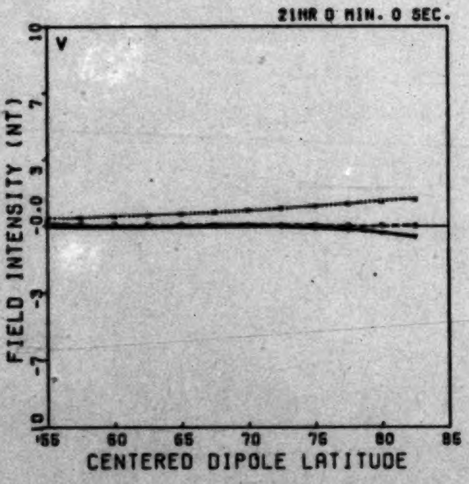
21HR 0 MIN. 0 SEC.
V
FIELD INTENSITY (NT)
10
7
3
0.0
-3
-7
CENTERED DIPOLE LATITUDE
55
60
65
70
75
80
85

in that the profile does not exhibit only a bias, but shows some structure as well. However, $\Delta Y'$ in these profiles is not easily interpreted in terms of unbalanced field-aligned current, so that in fact, as suggested by Hughes and Rostoker (1977), it is possible to have an unbalanced field-aligned current without there being a readily recognizable signature on the ground. In spite of this, the strength of the upward field-aligned current in the post-noon sector due to the low-latitude current system is insufficient to produce an overall net upward field-aligned current, so that the discrepancy between this model and the Triad observations remains. This will be dealt with further in section 4.7.1.

4.5 The Global Current Model

Figure 4.15 is a polar plot showing schematically the current systems used in this model. For the sake of clarity, the north-south current systems are not shown here. Neither relative widths of the arrows representing ionospheric currents nor the diameters of circles representing unbalanced field-aligned current are necessarily drawn to scale. However, most of the general features of the current systems used in this model are represented.

Figure 4.15 Schematic drawing of the complete model current system. Downward field-aligned currents are shown by , upward by . The width of the arrows is only an approximate indication of relative ionospheric current strength. Balanced field-aligned currents, and the corresponding north-south ionospheric currents have been omitted for the sake of clarity.

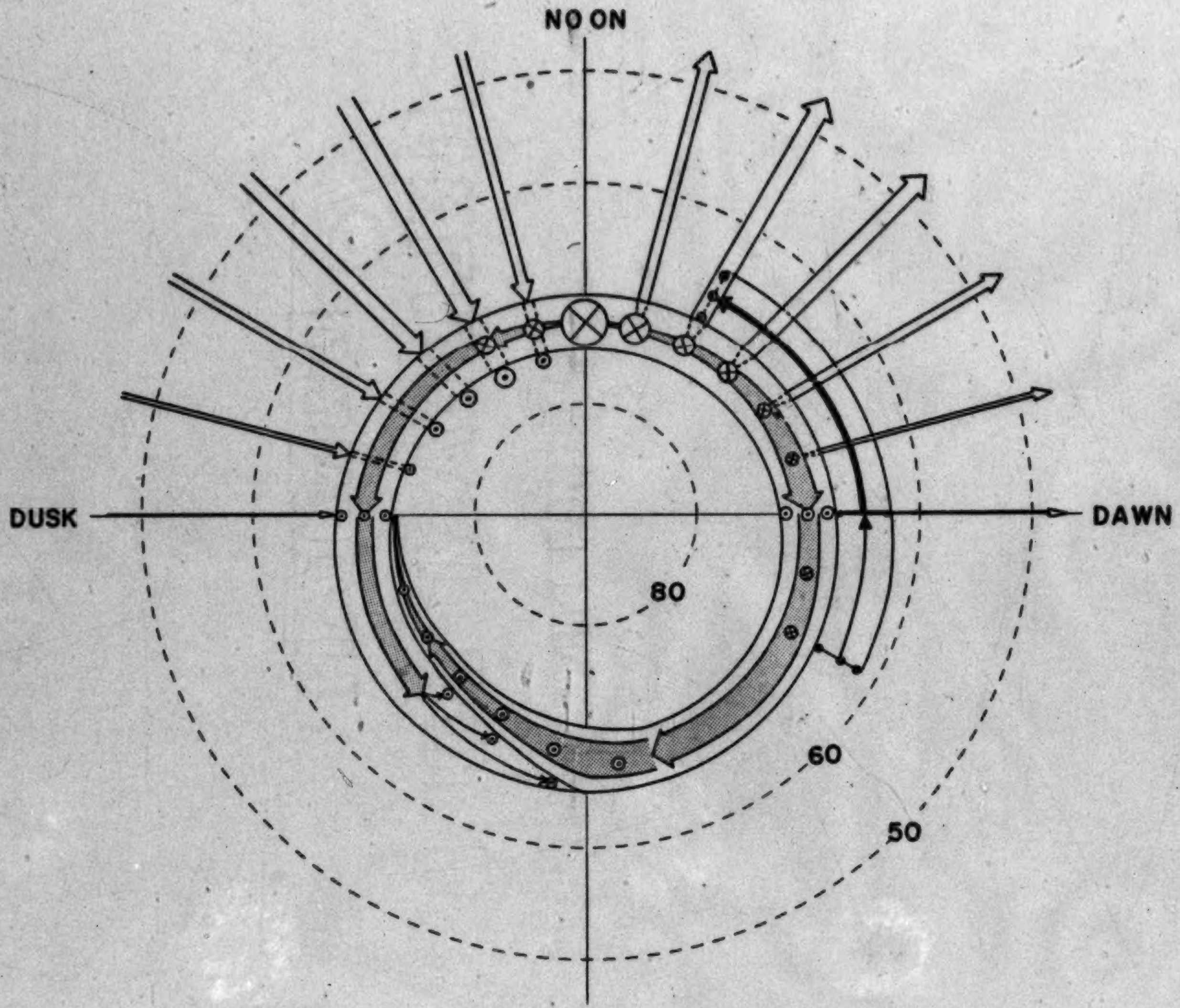
NOON
DUSK
DAWN
80
60
50

4.5.1 Qualitative Comparison of Model Latitude Profiles with SPEA Profiles

Figure 4.16 contains 48 separate panels in which the model latitude profile for a given hour is displayed next to the SPEA latitude profile for the same hour.

It is re-iterated at this point that the model has not been constructed to produce an exact fit to the data. The variations in the data from day to day are large. However, certain features do persist from day to day, and it is these features that the model has been designed to reproduce. Thus, a only a semi-quantitative comparison will be made between the model profiles and the SPEA profiles. In section 4.4.2, a statistical comparison of $\Delta X'_{peak}$ and $\Delta Y'_{step}$ for the model and SPEA profiles will be given.

Comparison of the 0000 MLT profiles shows a high degree of similarity between the model profiles and the data. The Y'-component is negative across the profile in both cases and has a similar step-like character. The X'-components are also similar. The model Z-component is asymmetric with the positive extremum being larger than the absolute value of the negative extremum, as is the case in the data. However, at high latitudes, the observed Z-component maintains relatively large values, whereas in the model, the Z-component decreases quite rapidly with increasing latitude beyond that at which the peak occurs. This is a persistent feature in the comparison of the model with the data in the post-midnight sector.

Figure 4.16 Comparison of the model latitude profiles, for the complete model, with the SPEA profiles. Note that the SPEA profiles are labelled in Universal Time, and the model profiles in Magnetic Local Time. Local magnetic midnight is at approximately 0800 UT.

EPOCH 8

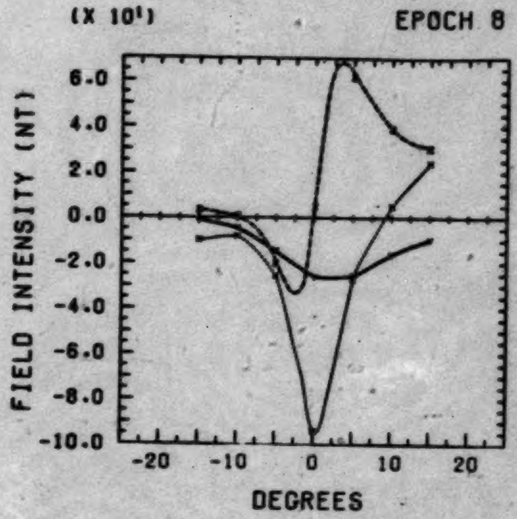

0 HR 0 MIN. 0 SEC.

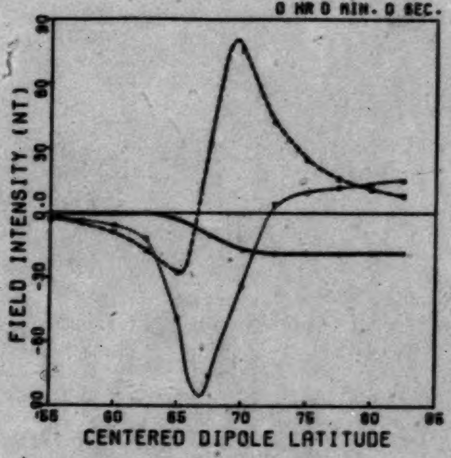

EPOCH 9

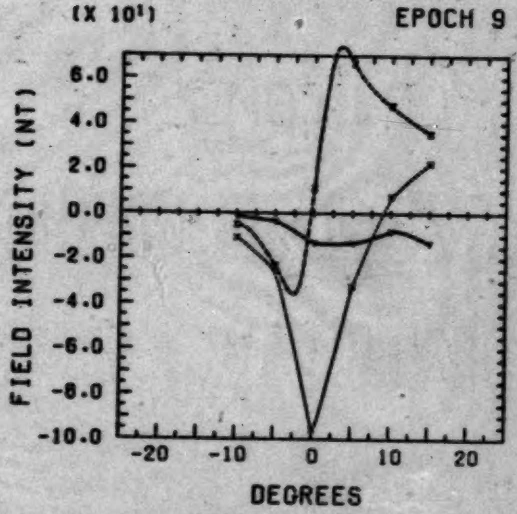

1 HR 0 MIN. 0 SEC.

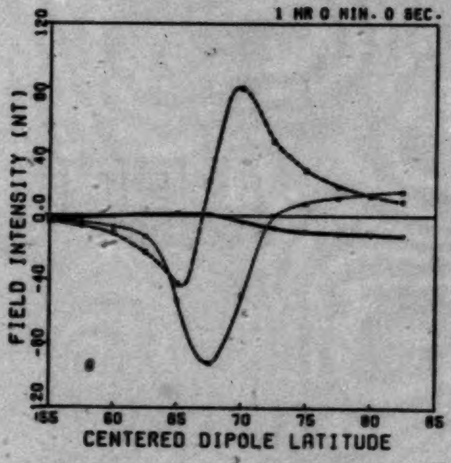

EPOCH 10

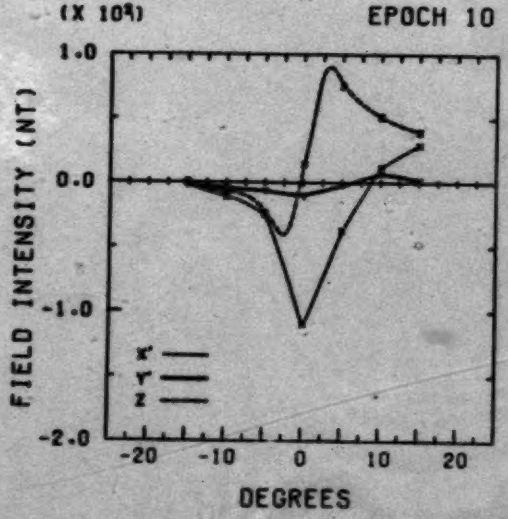

2 HR 0 MIN. 0 SEC.

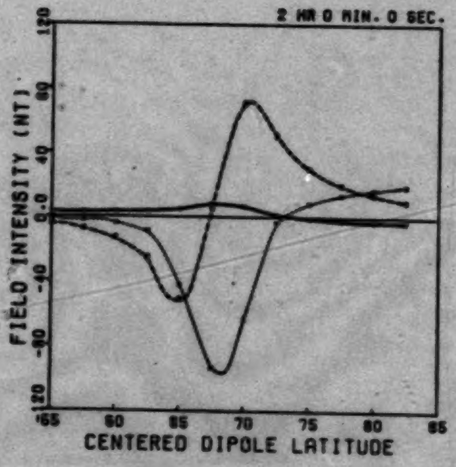

Figure 4.16 Comparison of the model latitude profiles, for the complete model, with the SPEA profiles. Note that the SPEA profiles are labelled in Universal Time, and the model profiles in Magnetic Local Time. Local magnetic midnight is at approximately 0800 UT.

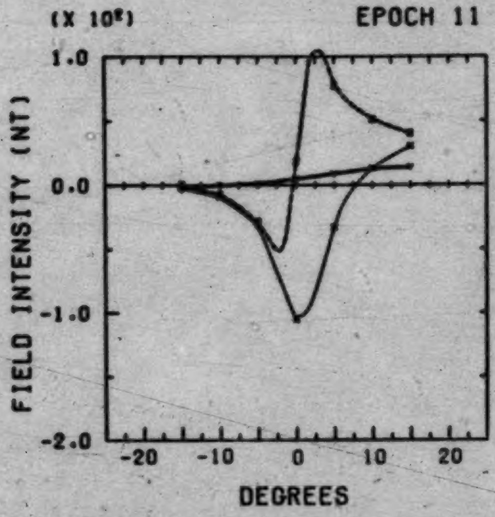
EPOCH 11

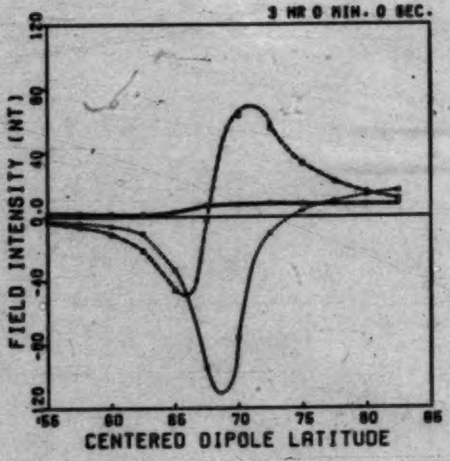
3 HR 0 MIN. 0 SEC.

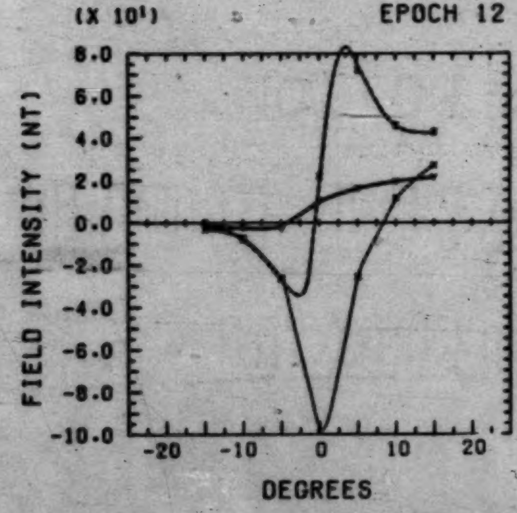
EPOCH 12

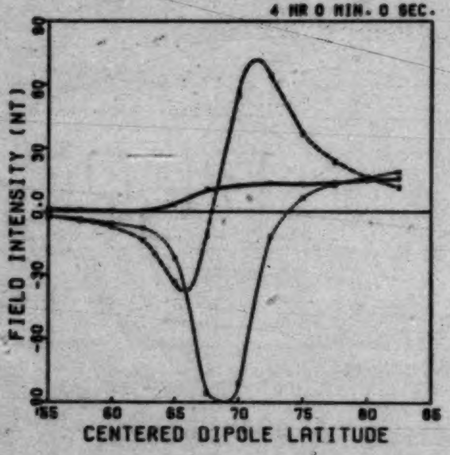
4 HR 0 MIN. 0 SEC.

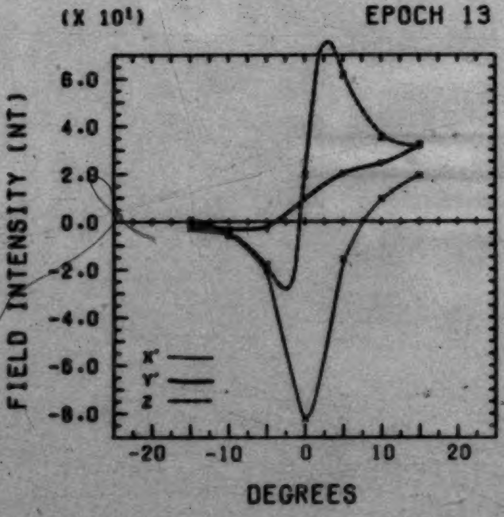
EPOCH 13

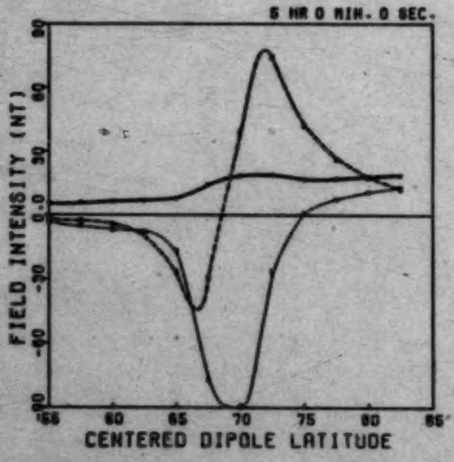
5 HR 0 MIN. 0 SEC.

Figure 4.16 Comparison of the model latitude profiles, for the complete model, with the SPEA profiles. Note that the SPEA profiles are labelled in Universal Time, and the model profiles in Magnetic Local Time. Local magnetic midnight is at approximately 0800 UT.

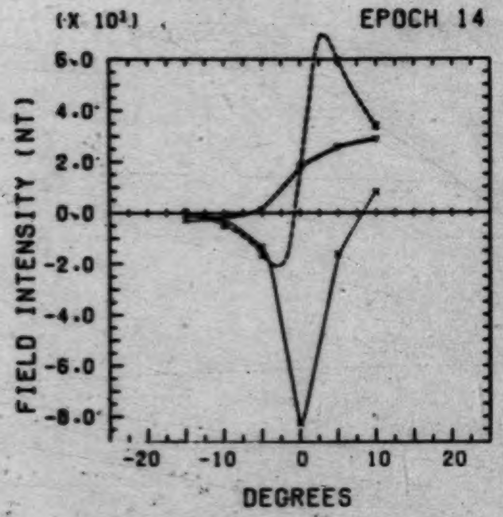
(X 10¹)
EPOCH 14
FIELD INTENSITY (NT)
6.0
4.0
2.0
0.0
-2.0
-4.0
-6.0
-8.0
-20
-10
0
10
20
DEGREES

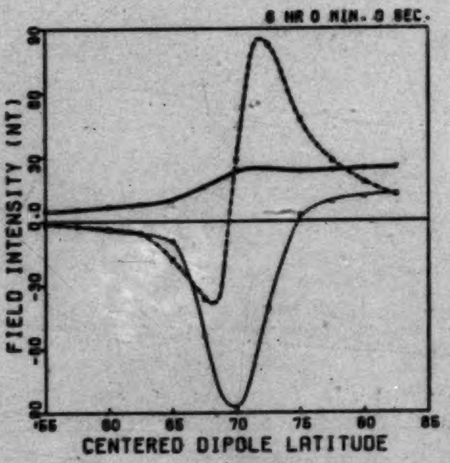
6 HR 0 MIN. 0 SEC.
FIELD INTENSITY (NT)
90
60
30
0.0
-30
-60
-90
55
60
65
70
75
80
85
CENTERED DIPOLE LATITUDE

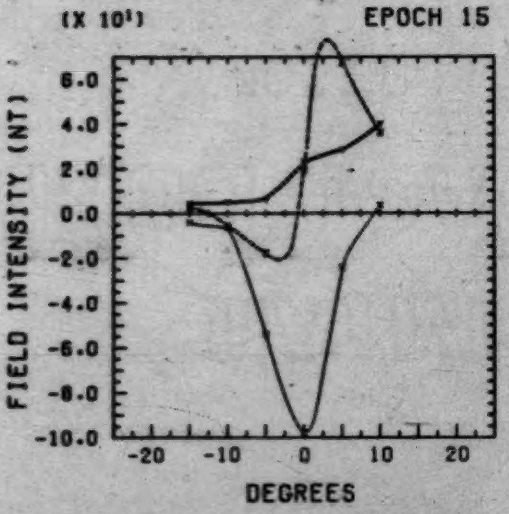
(X 10¹)
EPOCH 15
FIELD INTENSITY (NT)
6.0
4.0
2.0
0.0
-2.0
-4.0
-6.0
-8.0
-10.0
-20
-10
0
10
20
DEGREES

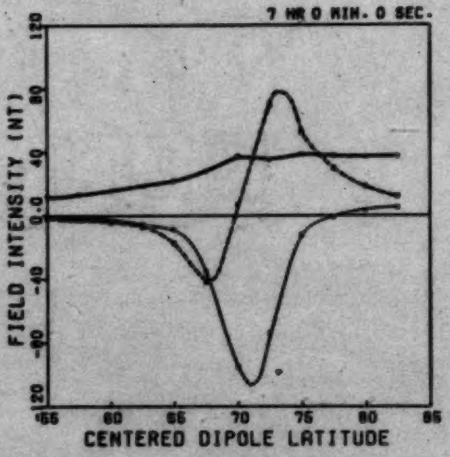
7 HR 0 MIN. 0 SEC.
FIELD INTENSITY (NT)
120
80
40
0.0
-40
-80
-120
55
60
65
70
75
80
85
CENTERED DIPOLE LATITUDE

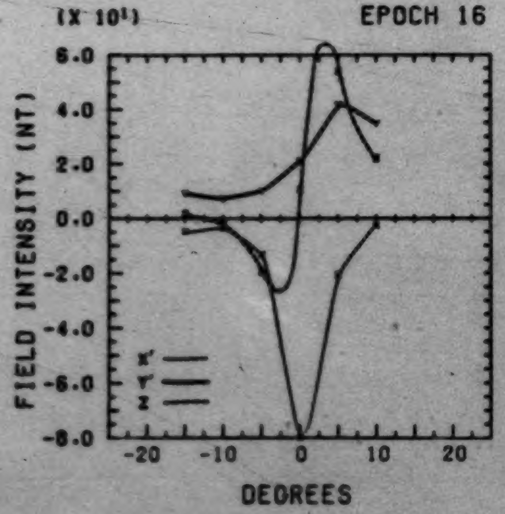
(X 10¹)
EPOCH 16
FIELD INTENSITY (NT)
6.0
4.0
2.0
0.0
-2.0
-4.0
-6.0
-8.0
-20
-10
0
10
20
DEGREES
X
Y
Z

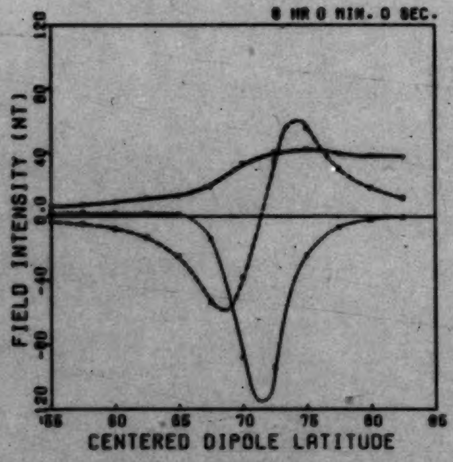
8 HR 0 MIN. 0 SEC.
FIELD INTENSITY (NT)
120
80
40
0.0
-40
-80
-120
55
60
65
70
75
80
85
CENTERED DIPOLE LATITUDE

Figure 4.16 Comparison of the model latitude profiles, for the complete model, with the SPEA profiles. Note that the SPEA profiles are labelled in Universal Time, and the model profiles in Magnetic Local Time. Local magnetic midnight is at approximately 0800 UT.

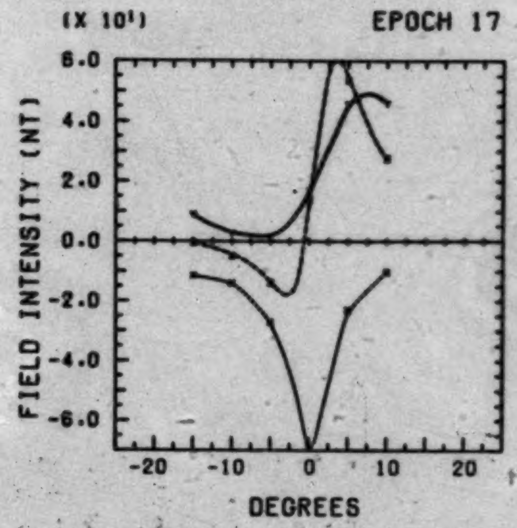
EPOCH 17

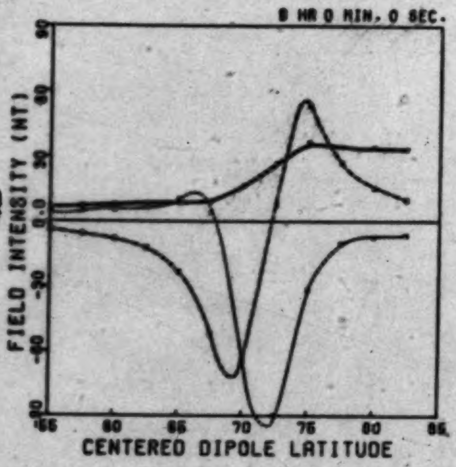
8 HR 0 MIN. 0 SEC.

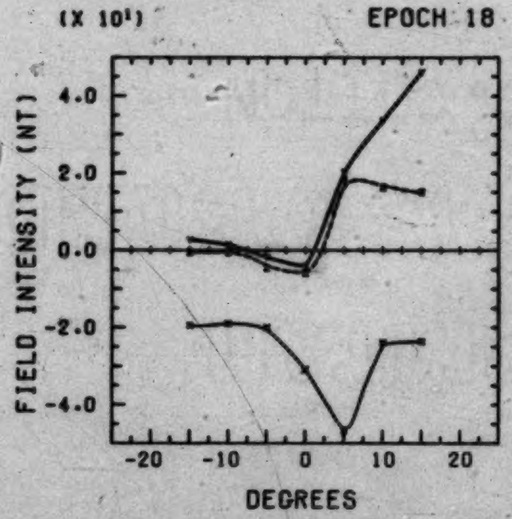
EPOCH 18

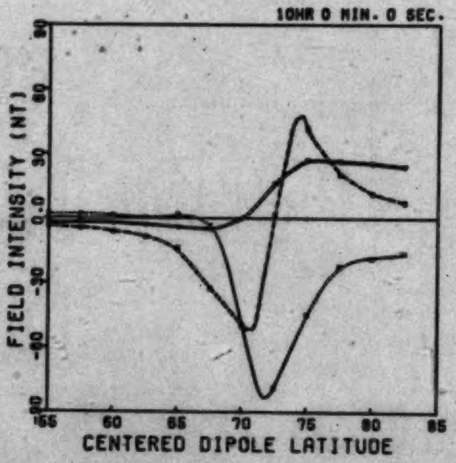
10HR 0 MIN. 0 SEC.

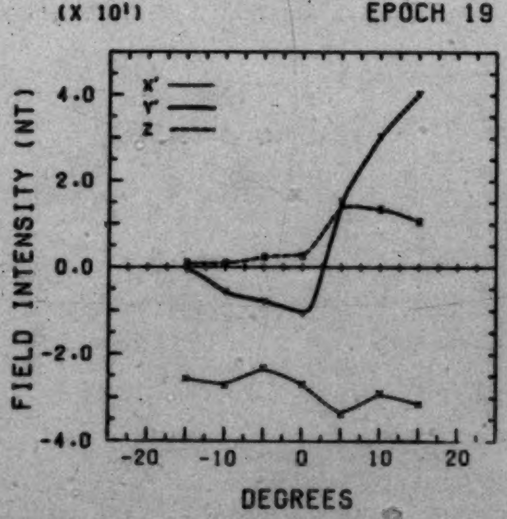
EPOCH 19

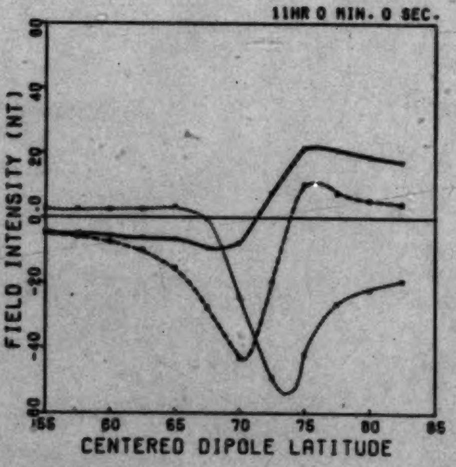
11HR 0 MIN. 0 SEC.

Figure 4.16 Comparison of the model latitude profiles, for the complete model, with the SPEA profiles. Note that the SPEA profiles are labelled in Universal Time, and the model profiles in Magnetic Local Time. Local magnetic midnight is at approximately 0800 UT.

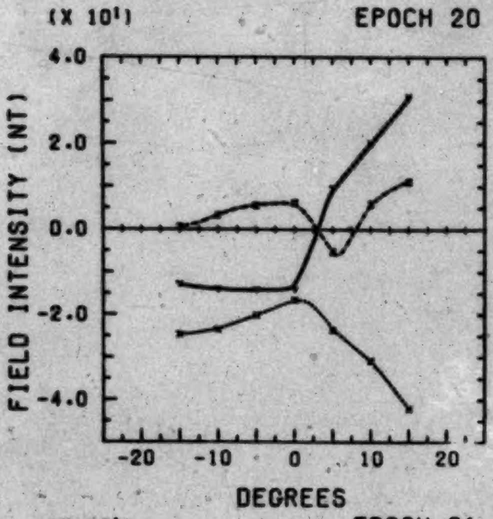
(X 10¹)
EPOCH 20
FIELD INTENSITY (NT)
4.0
2.0
0.0
-2.0
-4.0
-20
-10
0
10
20
DEGREES

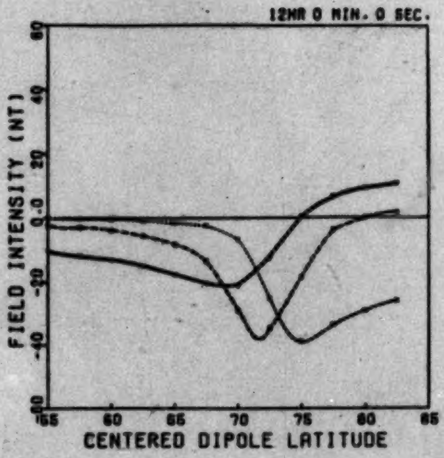
12HR 0 MIN. 0 SEC.
FIELD INTENSITY (NT)
60
40
20
0.0
-20
-40
-60
55
60
65
70
75
80
85
CENTERED DIPOLE LATITUDE

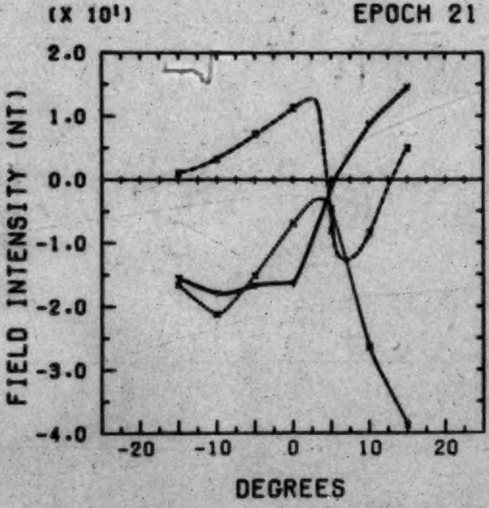
(X 10¹)
EPOCH 21
FIELD INTENSITY (NT)
2.0
1.0
0.0
-1.0
-2.0
-3.0
-4.0
-20
-10
0
10
20
DEGREES

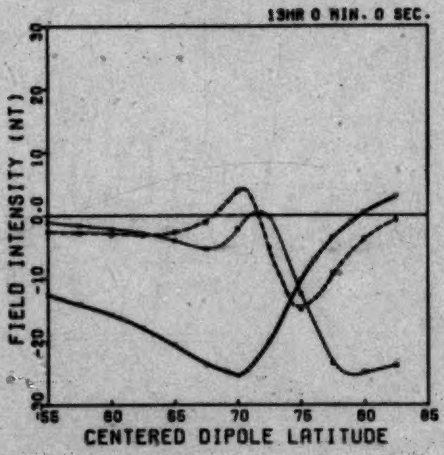
13HR 0 MIN. 0 SEC.
FIELD INTENSITY (NT)
30
20
10
0.0
-10
-20
-30
55
60
65
70
75
80
85
CENTERED DIPOLE LATITUDE

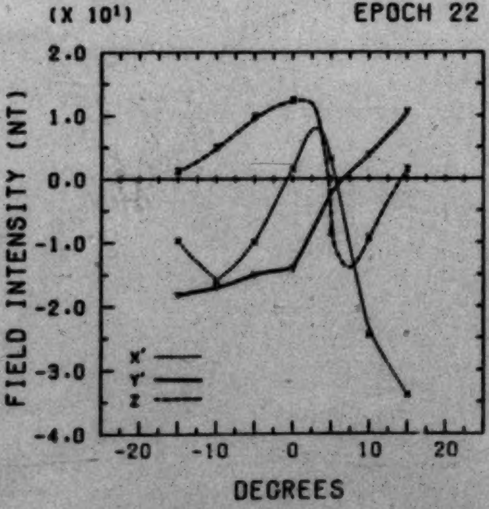
(X 10¹)
EPOCH 22
FIELD INTENSITY (NT)
2.0
1.0
0.0
-1.0
-2.0
-3.0
-4.0
X'
Y'
Z
-20
-10
0
10
20
DEGREES

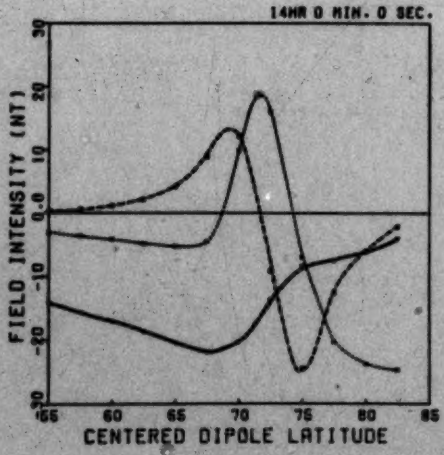
14HR 0 MIN. 0 SEC.
FIELD INTENSITY (NT)
30
20
10
0.0
-10
-20
-30
55
60
65
70
75
80
85
CENTERED DIPOLE LATITUDE

Figure 4.16 Comparison of the model latitude profiles, for the complete model, with the SPEA profiles. Note that the SPEA profiles are labelled in Universal Time, and the model profiles in Magnetic Local Time. Local magnetic midnight is at approximately 0800 UT.

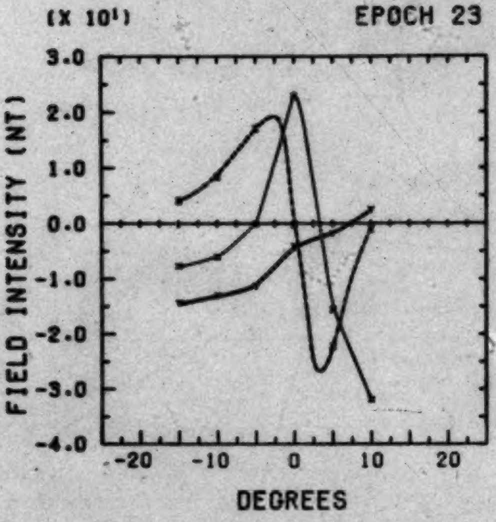
(X 10¹)
EPOCH 23
FIELD INTENSITY (NT)
3.0
2.0
1.0
0.0
-1.0
-2.0
-3.0
-4.0
-20
-10
0
10
20
DEGREES

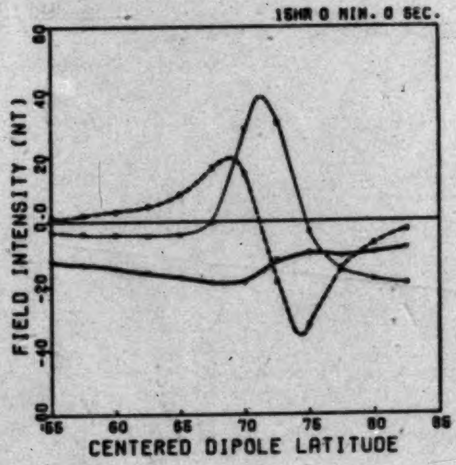
15HR 0 MIN. 0 SEC.
FIELD INTENSITY (NT)
60
40
20
0.0
-20
-40
-60
55
60
65
70
75
80
85
CENTERED DIPOLE LATITUDE

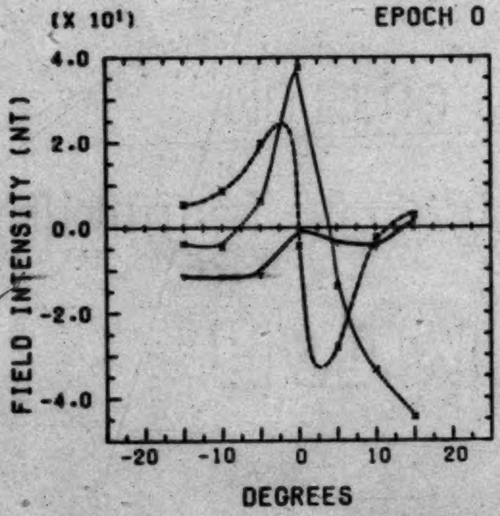
(X 10¹)
EPOCH 0
FIELD INTENSITY (NT)
4.0
2.0
0.0
-2.0
-4.0
-20
-10
0
10
20
DEGREES

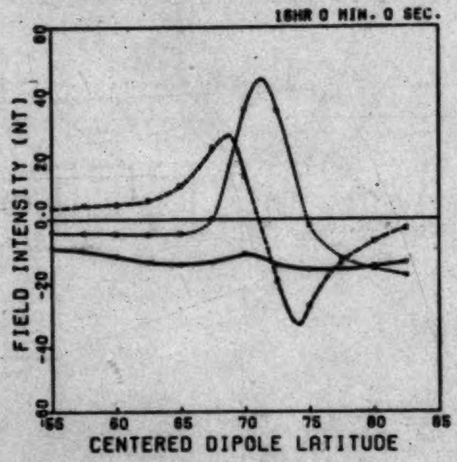
16HR 0 MIN. 0 SEC.
FIELD INTENSITY (NT)
60
40
20
0.0
-20
-40
-60
55
60
65
70
75
80
85
CENTERED DIPOLE LATITUDE

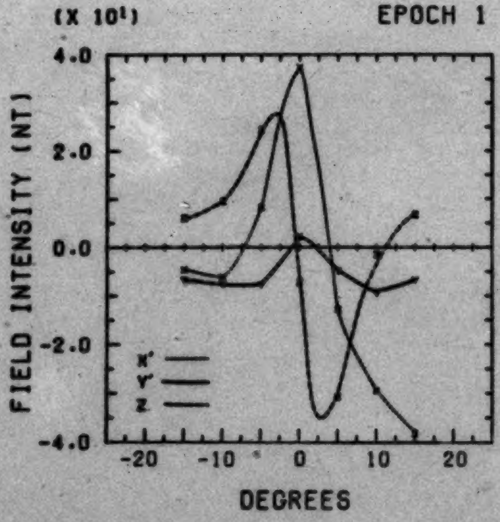
(X 10¹)
EPOCH 1
FIELD INTENSITY (NT)
4.0
2.0
0.0
-2.0
-4.0
X'
Y
Z
-20
-10
0
10
20
DEGREES

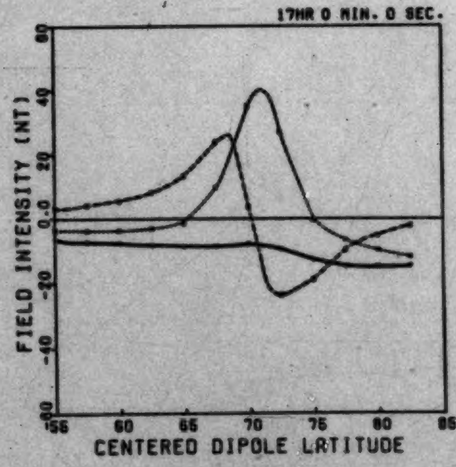
17HR 0 MIN. 0 SEC.
FIELD INTENSITY (NT)
60
40
20
0.0
-20
-40
-60
55
60
65
70
75
80
85
CENTERED DIPOLE LATITUDE

Figure 4.16 Comparison of the model latitude profiles, for the complete model, with the SPEA profiles. Note that the SPEA profiles are labelled in Universal Time, and the model profiles in Magnetic Local Time. Local magnetic midnight is at approximately 0800 UT.

EPOCH 2

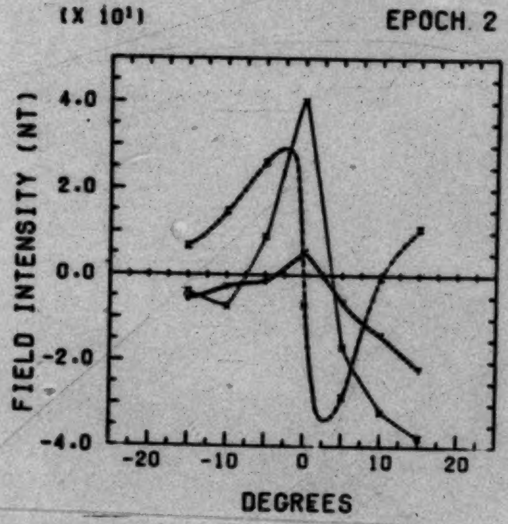

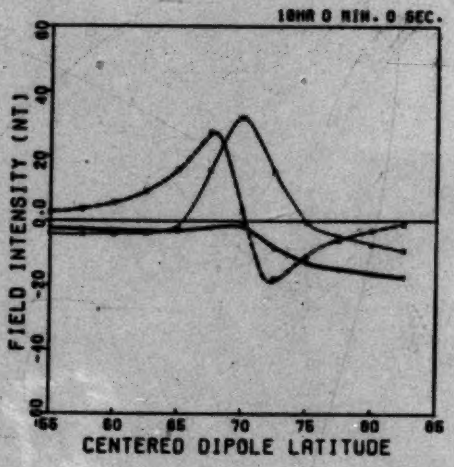

EPOCH 3

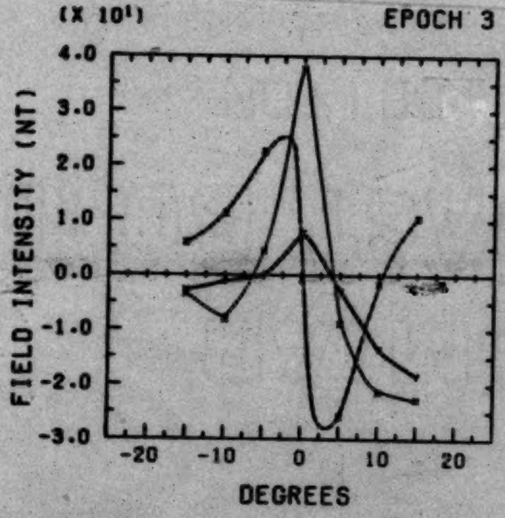

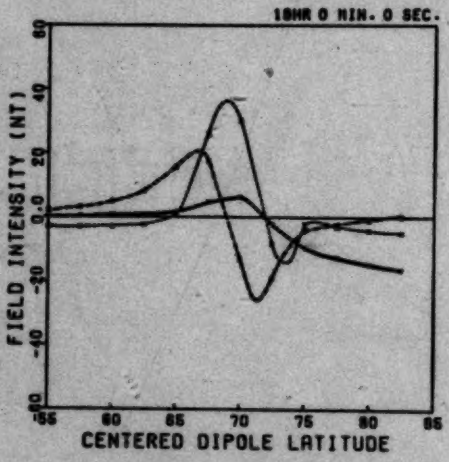

EPOCH 4

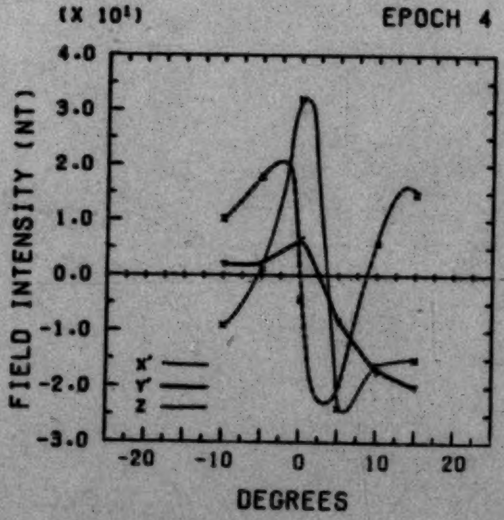

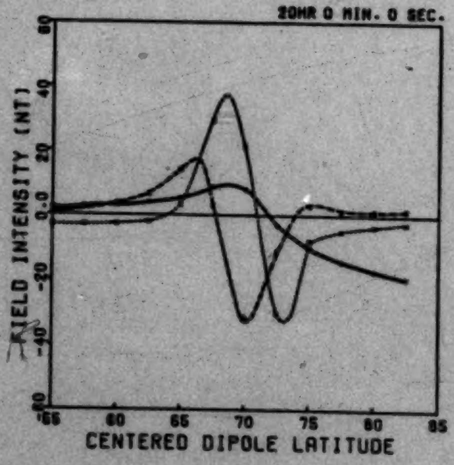

Figure 4.16 Comparison of the model latitude profiles, for the complete model, with the SPEA profiles. Note that the SPEA profiles are labelled in Universal Time, and the model profiles in Magnetic Local Time. Local magnetic midnight is at approximately 0800 UT.

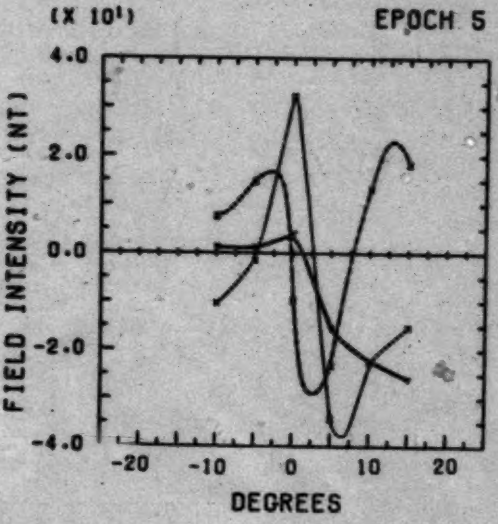
EPOCH 5

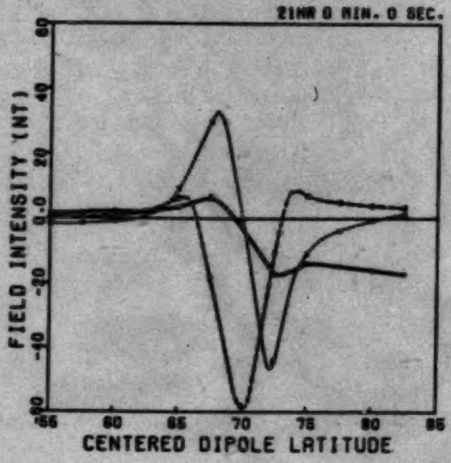
21HR 0 MIN. 0 SEC.

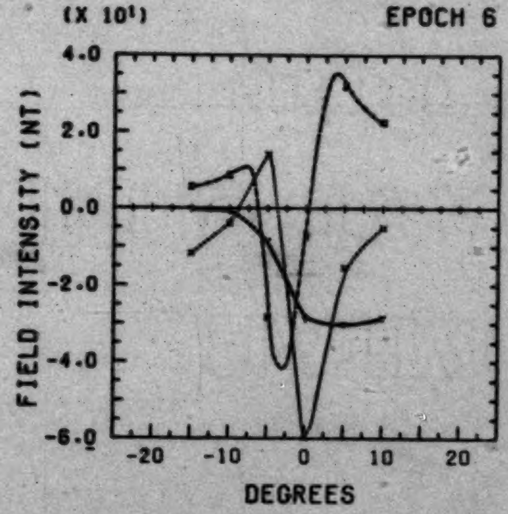
EPOCH 6

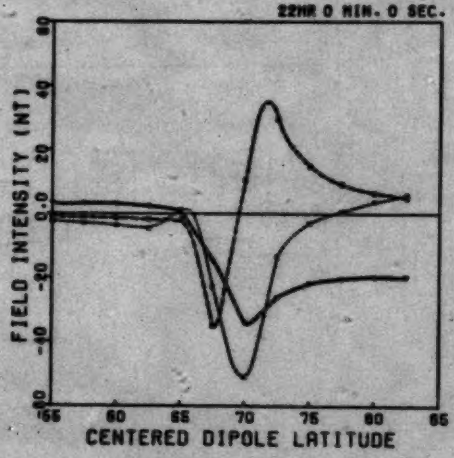
22HR 0 MIN. 0 SEC.

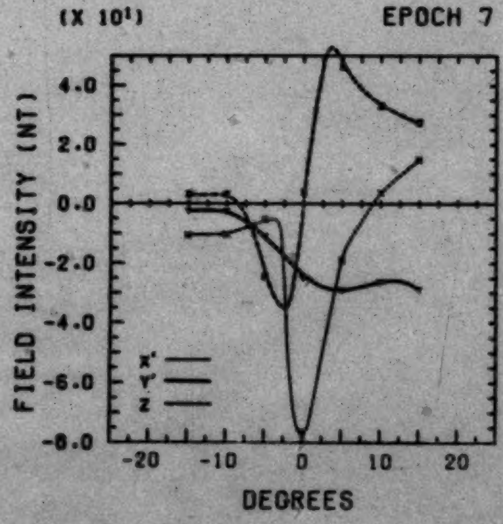
EPOCH 7

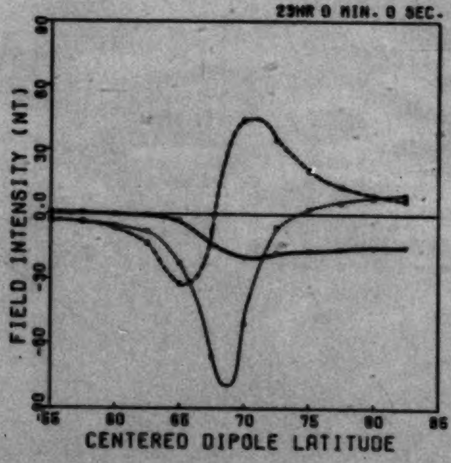
23HR 0 MIN. 0 SEC.

At 0100 MLT, all 3 components in the model profiles are in fair agreement with the character of the components in the SPEA profiles.

The 0200 MLT profiles also show good agreement in the X'- and Z-components. The Y'-component in the data shows evidence of a small positive going level-shift, perhaps superimposed on a slight, poleward tilted oval. ($\Delta Y'$ appears to follow $\Delta X'$). The model $\Delta Y'$ profile shows evidence of the opposite tilt, as indeed such is built into the model, and essentially no level-shift. However, in both cases, the magnitude of the Y'-component is relatively small, and these discrepancies are not major ones.

For 0300 MLT, the agreement between model and observation is quite good. The asymmetry in ΔZ is similar in both, and the values of the peak $\Delta X'$ are essentially the same in both cases. The Y'-component also shows the same qualitative features of a slight level-shift across the width of the electrojet.

The fifth set of panels in Figure 4.16 (0400 MLT) also show a good qualitive agreement between the observations and the model, although the magnitude of $\Delta Y'_{step}$ in the model is less than that observed. This difference is difficult to ascribe to the net field-aligned current component of the model, as increasing this necessitates increasing the westward flowing current. The westward current, however, produces peak values of $\Delta X'$ which are in good agreement with the observations. It is likely that this difference arises due to the choice of model north-south current. If the electric field during the observation period is not well modelled by the field shown in Figure 4.4, or if the height-integrated conductivity ratio shows variations away from the value of 2 in this sector, than the model north-south current system would differ from that used. However, lack of specific information about these factors for the data collection period have forced the use of the present north-south current model. Further refinements may improve the agreement between the observed and model $\Delta Y'_{step}$, but, as will be shown in section 4.4.2, the overall agreement is acceptable.

The comments of the above paragraph also apply to the comparison of model profiles with SPEA profiles for 0500 MLT through 0800 MLT. In addition, it will be noted that the model produces a more step-like Y'-component than is observed in the SPEA profiles. Indeed, as described in Chapter 3, the model $\Delta Y'$ profiles in this sector behave more like those observed in the individual hourly averaged latitude profiles than that in the SPEA profiles.

As the noon sector is approached, it becomes clear that the global current model fails to reproduce some features of the data. It will be recalled that the main feature described in the noon sector was the large positive-going level-shift in the Y'-component. This feature is reasonably well produced by the model. However, the magnitude of the X'-component is not well modelled by the current systems already described. From the superposed epoch analysis, it appears that there is little if any electrojet current flowing in the noon sector, whereas the end effects of the model westward current are evident in the model profiles as relatively large $\Delta X'$ perturbations. As well, the SPEA profiles in the noon sector show evidence of the Sq current system at the lower latitudes. That is, $\Delta X'$ is biased negatively at low latitudes, consistent with what would be expected for the Sq system. Although, as noted in section 4.4.4, the model low latitude current system might bear some resemblence to the Sq current, Sq circulates in the high-latitude sub-auroral ionosphere as a broad westward current. This feature has not been built into the model, and it would appear that the atmospheric dynamo current system is required to satisfy all the observed perturbations.

The inclusion of an Sq current system will not solve the entire problem in this sector. From 0900 to 1200 MLT, the observed $\Delta X'$ values across the profile are in general less than those in the model profiles, and at noon, the $\Delta X'$ SPEA profile does not indicate the presence of an electrojet. In an attempt to improve the model fit in this sector, the model westward electrojet was modified slightly, in that no current flow was permitted from noon to 1020 MLT. However, the westward electrojet was to grow to a maximum of 1.25×10^6 A by 0800 MLT, as in the original model. Thus, from 1020 MLT to 0800 MLT, the net downward field-aligned current was more intense than in the original model. The effect of this modification was limited to essentially the 1000 MLT to 1300 MLT sector, as shown in Figure 4.17(a,b,c,d). It is apparent that the model $\Delta X'$ profiles are improved, although the magnitude of $\Delta Y'_{step}$ is increased. It is suggested that the best possible model lies between the original and this modification.

Another possible explanation of this difficulty is the fact that the SPEA profiles in the noon sector have been constructed differently than elsewhere. At noon, the profiles were referenced to $\Delta Y'$ (see Chapter 2). It is possible that, had the noon sector data been sorted into cases which had distinctive eastward or westward electrojet signatures, then the correspondence between model and data would have been improved.

One additional alternative is that there may exist current systems in the noon sector other than those which have been modelled. Recently, Iijima and Potemra (1976) have published results showing field-aligned currents additional to and poleward of those shown in Figure 4.2 in the noon sector. It is not clear at this time how these currents connect, if at all, in the ionosphere, and further observations of the electric field and field-aligned currents in this region are necessary before conclusions may be drawn. At present, recourse to the variability in the data, from profile to profile, from this sector must be made to minimize the importance of this discrepancy between the model and SPEA X'-component profiles in the noon sector. As

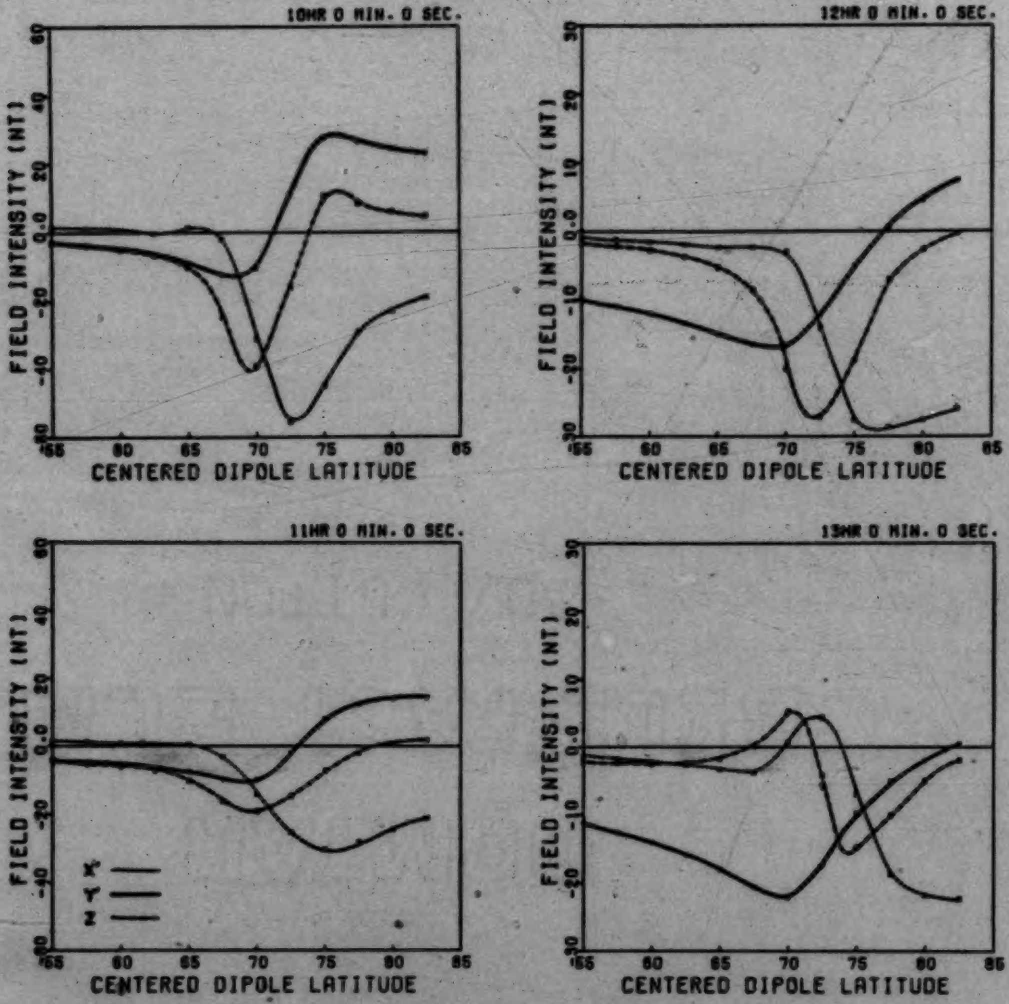

Figure 4.17 The model latitude profiles, for the 1000 MLT to 1300 MLT sector, that result from moving the origin of the westward current system from noon to 1020 MLT.

will be shown in section 4.4.2, if this variability is taken into account, the overall fit of the model to the data is quite acceptable.

From 1300 MLT onwards, the model reproduces the features of the observed profiles quite well. The positive-going step in $\Delta Y'$ is evident in the model profiles up to 1500 MLT, and the growth of the eastward current is visible through the increasing magnitude of the peak of the X'-component. The nature of the Y'-component for the model in the profiles for 1500, 1600 and 1700 MLT is not exactly the same as that observed. This is not believed to be a serious fault in that the model has been computed only at a single longitude for each epoch, whereas the SPEA profiles are superposed averages of hourly averaged profiles. Thus a boundary which changes from day to day (for example, the longitude beyond which the net downward field-aligned current ceases to flow) will introduce certain errors which cannot be accounted for in the model. The presence of the westward-current in the post-dusk sector of the model profiles is in good agreement with the observations.

Finally, the signature of poleward flowing current in the 2300 MLT SPEA profile (the negative Y'-component across the profile) is essentially reproduced in the model profile for 2300 MLT.

Another qualitative comparison may be made by considering a polar plot of the model results. Figure 4.18(a) is the polar plot of the model magnetic pertubations

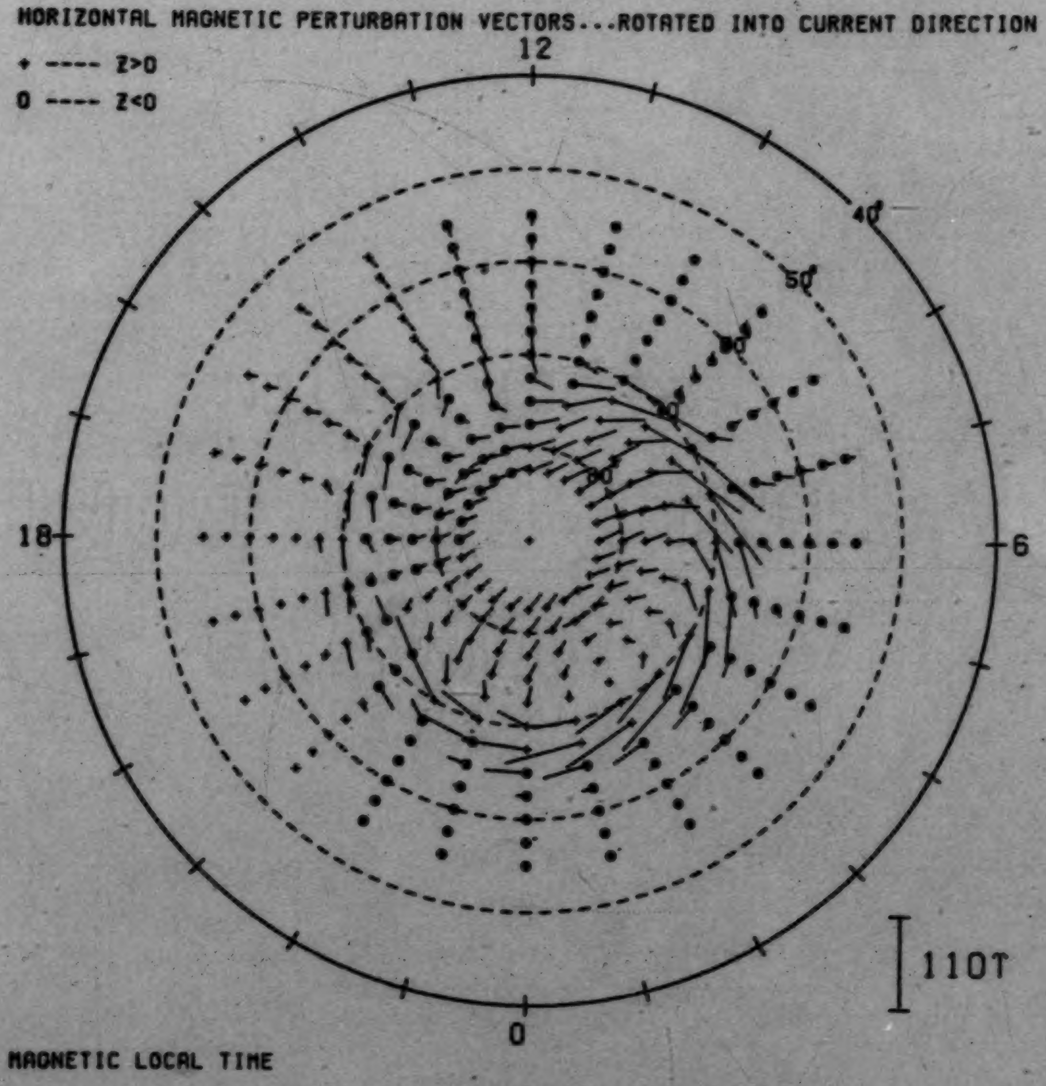

Figure 4.18(a) Polar plot in which the model horizontal magnetic perturbation vectors are rotated 90° clockwise to represent an equivalent current flow. The length of the vector is proportional to the horizontal magnetic perturbation.

rotated 90° clockwise to represent equivalent current flow. This figure is to be compared with Figure 4.18(b), taken from a recent publication of Friis-Christensen and Wilhjelm (1975). In this figure, high latitude average equivalent current vectors for ten winters of 1966-1968 are plotted, separated according to the value of B_z and B_y for the IMF. Although there is much more information in Figure 4.18(b) than in Figure 4.18(a), it is apparent that the model equivalent current vectors are very similar to those shown in the bottom three panels of Figure 4.18(b). Since the model has been developed from data during periods when B_z was both positive and negative, it would be expected that the model equivalent current vector field would agree with observations for which B_z was less than zero.

A final comparison may be made with the data shown in Figure 4.18(c), taken from Chen and Rostoker (1974). Although this plot is of data from a relatively disturbed period of time, the overall agreement between the model and the equivalent current vectors of Figure 4.18(a) is remarkable.

4.5.2 Quantitative Evaluation of the Model

As discussed previously, the model has not been compared to the data by, for example, doing a least-squares analysis on the latitude profile curves. Recalling that $\Delta X'_{peak}$ is related to the magnitude of the ionospheric Hall currents, and $\Delta Y'_{step}$ is related to the strength of net

Figure 4.18(b) Polar plot of the average high-latitude horizontal magnetic perturbation vectors, for winter data, in a format like that of Figure 4.18(a). The top row shows data for cases when $B_z = 0$, the bottom row shows data for $B_z < -1$. The data have also been arranged according to the azimuthal component of the IMF, as noted in the Figure. (From Friis-Christensen and Wilhjelm, 1975).

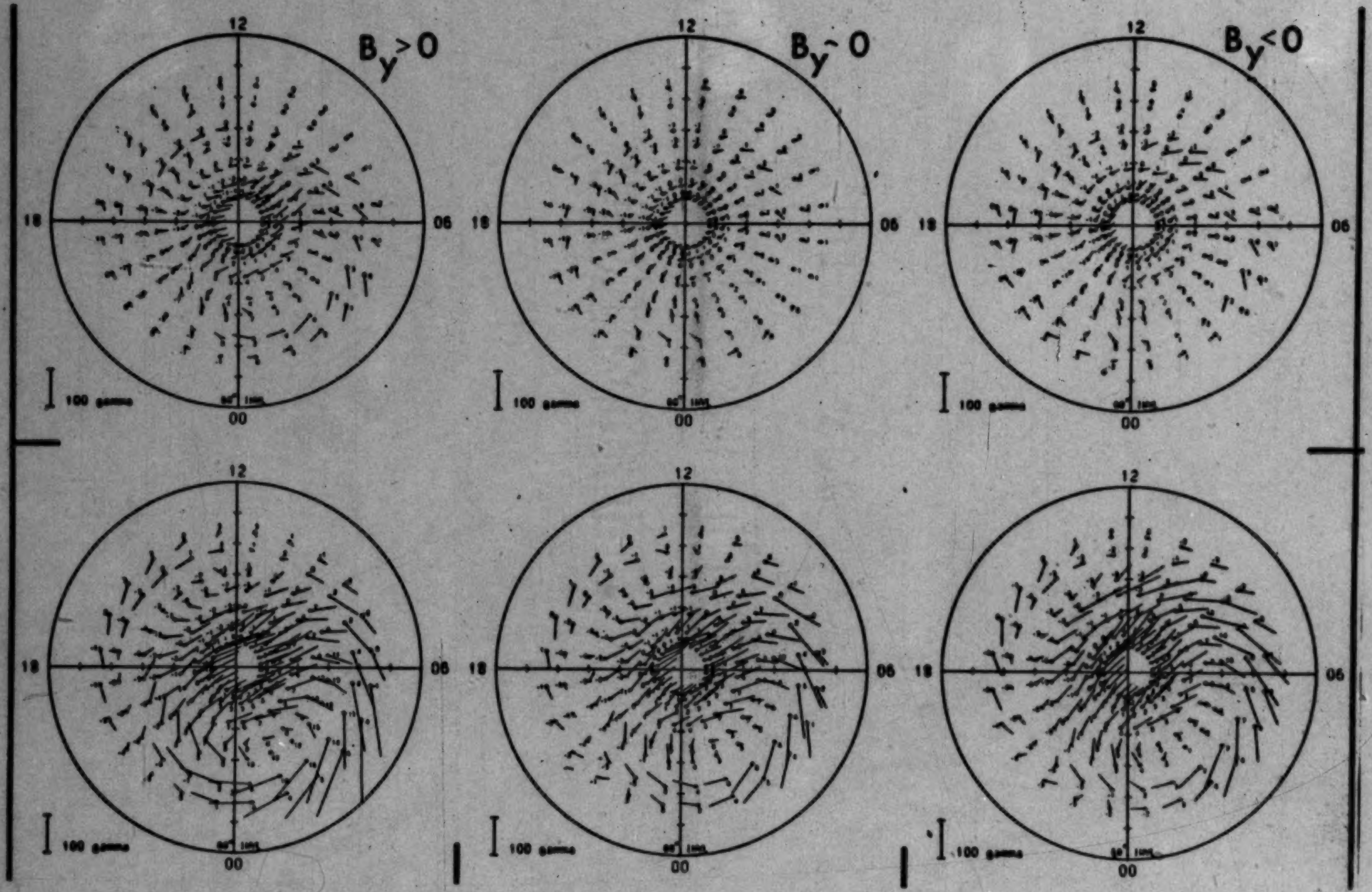
$B_y>0$
$B_y\sim 0$
$B_y<0$
12
06
18
00
100 gamma

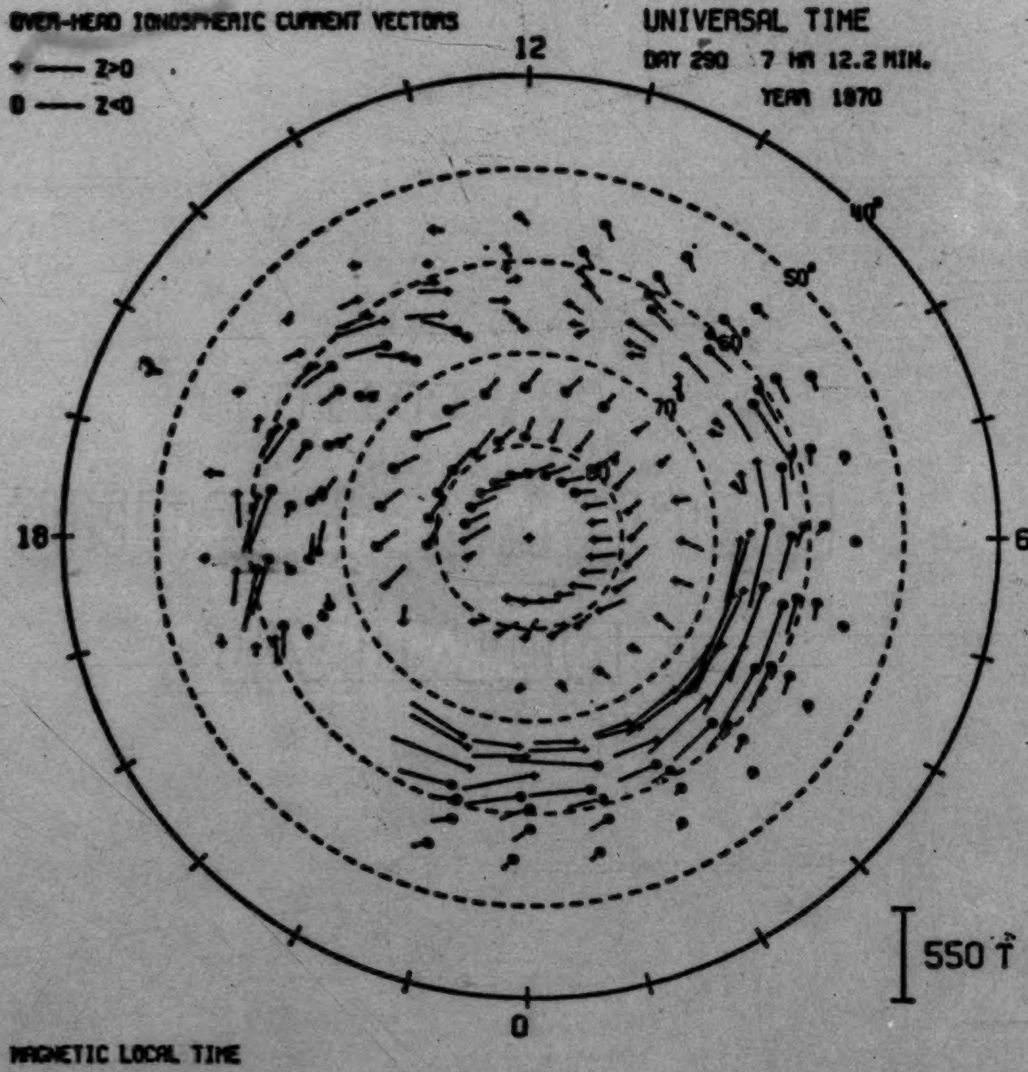

Figure 4.18(c). Overhead ionospheric current vectors for Day 290, 1970. The 22 hour interval shown starts at 0712.2 UT. (From Chen and Rostoker, 1974).

field-aligned current, the magnitudes of $\Delta X'_{peak}$ and $\Delta Y'_{step}$ produced by the model current system are compared to those observed. Figure 4.19 is a plot of $\Delta X'_{peak}$ and $\Delta Y'_{step}$ obtained from the model as a function of magnetic local time compared with the observed values. As described in Chapter 3, values near noon are not shown as it was difficult to determine a value for $\Delta X'$ in this regime. In the near midnight sector, values for $\Delta Y'$ were not well defined, and so data from this regime is also absent from Figure 4.19. The inset shows the values of $\Delta X'_{peak}$ for the pre-midnight sector westward electrojet.

The agreement between the model values of $\Delta X'_{peak}$ and $\Delta Y'_{step}$ and the observed values appears reasonably good in this figure. However, to demonstrate the agreement in a more qua~~l~~ntitative way, Figure 4.20 (a,b,c,d, and e) shows plots of the model values as functions of the observed values. For a perfect fit, the points plotted in these figures would fall on a straight line with unit slope. The straight line drawn through the points is the best fit straight line, except in the case of Figure 4.20(a). In this plot, the model $\Delta X'_{peak}$ is compared to the observed $\Delta X'_{peak}$, for the 0200-1000 MLT sector. It is in this sector that large discrepancies arise in the north-south component near noon, but it is also the sector in which the greatest variability in the X'-component was observed. To take advantage of this variability, a weighted linear least squares analysis for the best fit straight line was used, in which the weight of each data

Figure 4.19 Comparison of $\Delta X'_{peak}$ and $\Delta Y'_{step}$ from the model and the superposed epoch analysis. ■——■ represents $\Delta Y'_{step}$ as determined from the SPEA data, □--□ shows $\Delta Y'_{step}$ for the model. ●——● represents $\Delta X'_{peak}$ as found in the SPEA data, ○--○ is $\Delta X'_{peak}$ for the model. The insert is the comparison of $\Delta X'_{peak}$ for the pre-midnight westward electrojet.

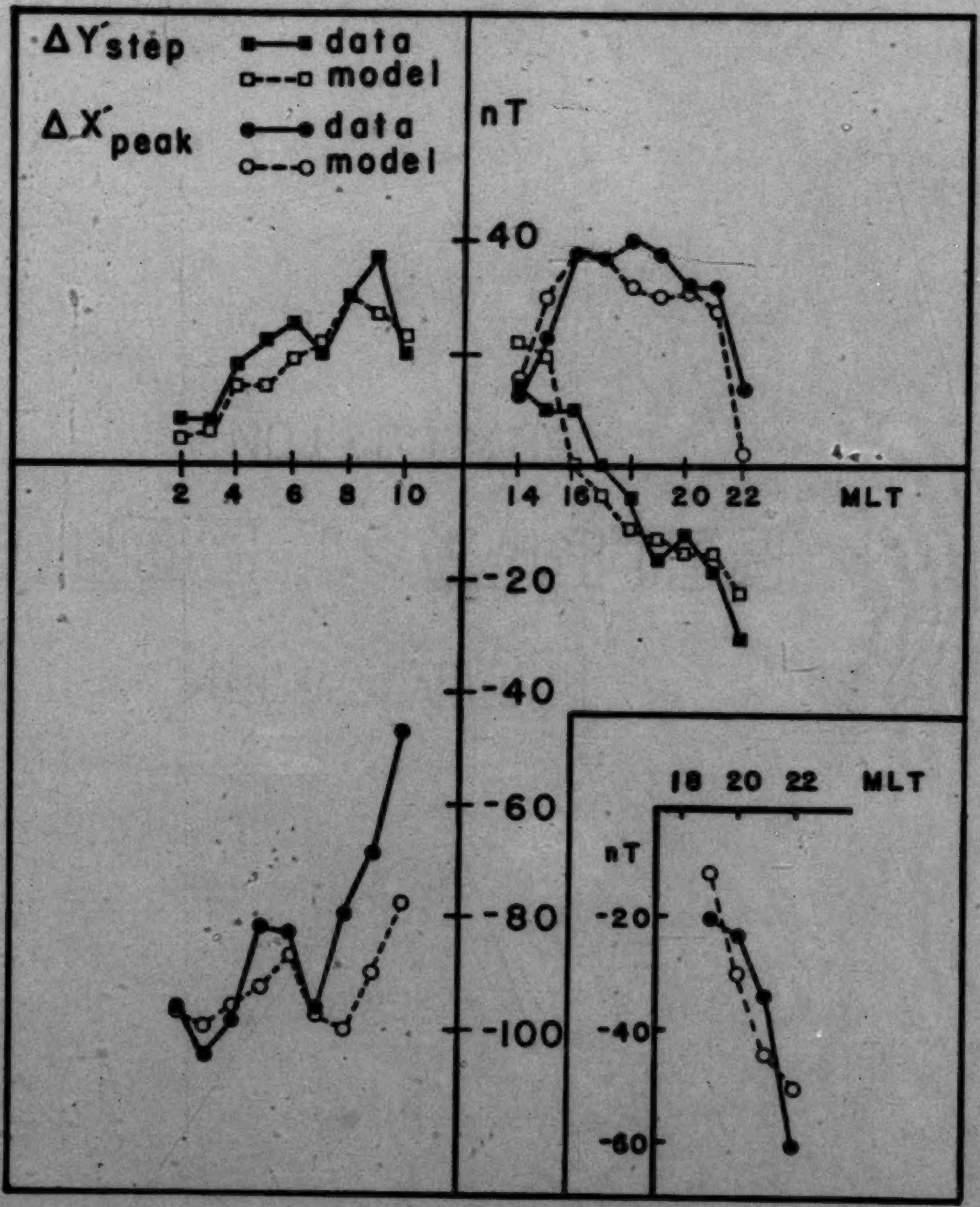
ΔY'step
data
model
ΔX'peak
data
model
nT
40
-20
-40
-60
-80
-100
2
4
6
8
10
14
16
20
22
MLT
18
20
22
MLT
nT
-20
-40
-60

Figure 4.20(a) Correlation between $\Delta X'_{peak}$ for the model and $\Delta X'_{peak}$ for the data for the period 0200-1000 MLT. The error bars indicate the standard deviation of the SPEA $\Delta X'_{peak}$ values. The solid line is the weighted regression line, as described in the text.

Figure 4.20(b) Correlation between $\Delta Y'_{step}$ for the model and $\Delta Y'_{step}$ for the data for the period 0200-1000 MLT. All data have been equally weighted.

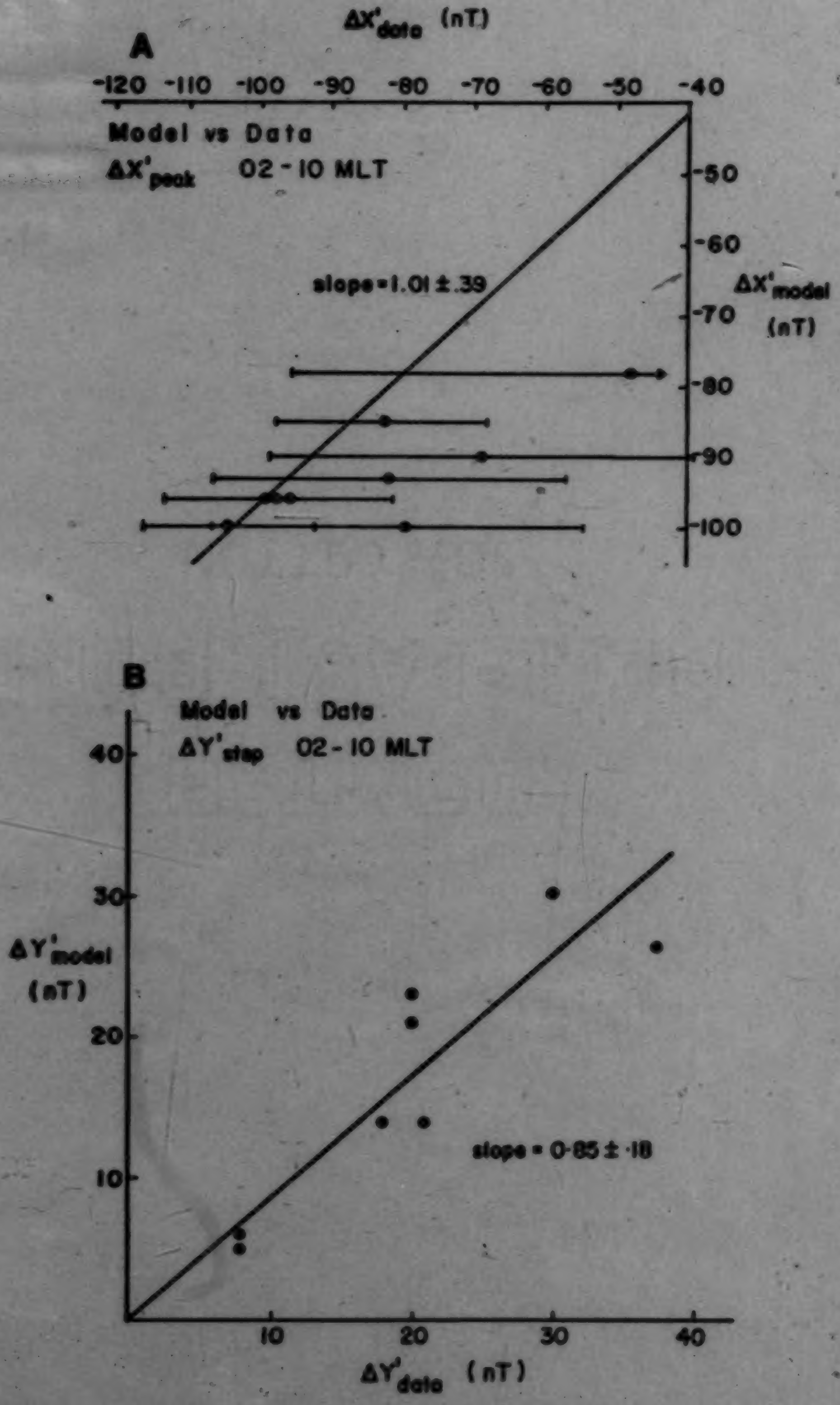
A
ΔX'data (nT)
-120 -110 -100 -90 -80 -70 -60 -50 -40
Model vs Data
ΔX'peak 02 - 10 MLT
slope = 1.01 ± .39
-50
-60
-70
-80
-90
-100
ΔX'model (nT)
B
Model vs Data
ΔY'step 02 - 10 MLT
40
30
20
10
ΔY'model (nT)
slope = 0·85 ± ·18
10
20
30
40
ΔY'data (nT)

Figure 4.20(c) Correlation between $\Delta X'_{peak}$ for the model and $\Delta X'_{peak}$ for the data for the period 1400-2200 MLT All data have been equally weighted.

Figure 4.20(d) Correlation between $\Delta Y'_{step}$ for the model and $\Delta Y'_{step}$ for the data for the period 1400-2200 MLT. All data have been equally weighted.

Figure 4.20(e) Correlation between $\Delta X'_{peak}$ for the model and $\Delta X'_{peak}$ for the data for the period 1800-2200 MLT. These data are for the pre-midnight westward electrojet. All data have been equally weighted.

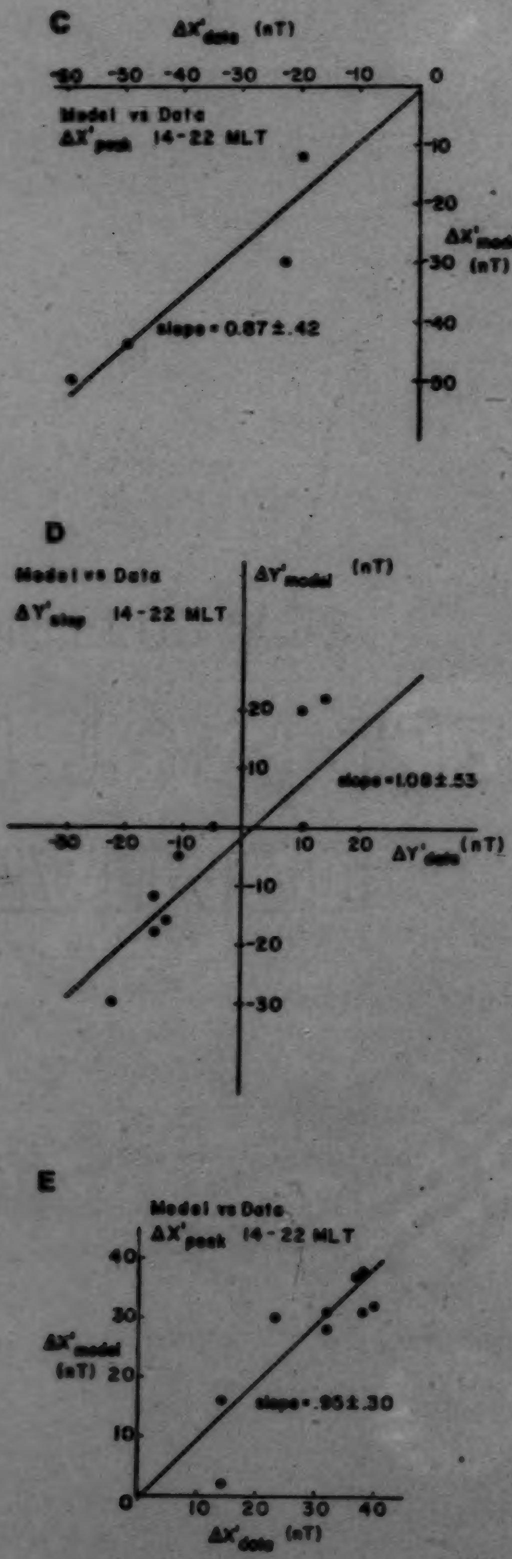
C
$\Delta X'_{data}$ (nT)
-60 -50 -40 -30 -20 -10 0
Model vs Data
$\Delta X'_{peak}$ 14-22 MLT
-10 -20 -30 -40 -50
$\Delta X'_{model}$ (nT)
slope = 0.87 ± .42
D
Model vs Data
$\Delta Y'_{step}$ 14-22 MLT
$\Delta Y'_{model}$ (nT)
20 10 -10 -20 -30
slope = 1.08 ± .53
-30 -20 -10 10 20
$\Delta Y'_{data}$ (nT)
E
Model vs Data
$\Delta X'_{peak}$ 14-22 MLT
40 30 20 10 0
$\Delta X'_{model}$ (nT)
slope = .95 ± .30
10 20 30 40
$\Delta X'_{data}$ (nT)

point was inversely proportional to the standard deviation of the data value. These standard deviations are shown as error bars in Figure 4.20(a). For the other comparisons, all data points were uniformly weighted.

Table 4.2 summarizes the results of the analysis. In all cases, the slope of the best fit line is unity within the error of the estimate. As well, all cases have a high correlation coefficient. In all but one case, Student's t-test indicates that the correlation is significant at the 1% level or better. In the case of $\Delta X'_{peak}$ for 1400-2200 MLT, only 4 data points are available, accounting for the low significance of the correlation.

On the basis of the statistics, as well as the good qualitative agreement of the model profiles with the SPEA profiles, it is concluded that the global current model is a reasonable model of the average three-dimensional current flow in the high latitude regions.

4.5.3 Preliminary Summary and Discussion

In summary to this point, the global current system consists of 5 ionospheric east-west current systems, each with appropriate field-aligned current connecting it to the outer magnetosphere, and appropriate north-south current systems. The eastward and westward convection electrojets grow in the noon sector, being fed by relatively intense inward field-aligned current distributed along the electrojet regions. In the sunlit auroral oval, the

Table 4.2

Statistical Analysis of the Comparison of the Global Model Profiles with the SPEA Profiles

Sector (MLT)	Parameter	Slope of Best Fit Line	Correlation Coefficient	Level of Significance*
0200-1000	X'	1.01±.39**	0.0985	0.1%
	Y'	0.85±.18	0.889	<1.0%
1400-2200	X'	0.95±.30	0.945	0.1%
	Y'	1.08±.53	0.874	<1.0%
1800-2200	X'	0.87±.42	0.919	5%

*Level at which the correlation coefficient is significant, using Student's t-test.

**A weighted best-fit; each point had a weight assigned which was inversely proportional to the standard deviation of that point.

conductivity arises due to solar UV radiation and particle precipitation. At or near dawn and dusk, the UV source of conductivity disappears, the electrojet strengths are reduced, and current flows upwards to the magnetosphere. The westward electrojet continues to grow slowly until 0100 MLT, at which time the current diverges both slightly poleward and up field lines. This westward current continues as a westward current in the region poleward of the eastward electrojet until 1800 MLT, at which time it has completely diverged up field lines. The eastward electrojet continues at constant strength beyond dusk to 2100 MLT, at which time it too diverges poleward. When this current reaches the equatorward boundary of the westward current, it flows up field lines.

In the pre-midnight sector, the $\Delta Y'_{step}$ is due to a combination of the upward current from the westward electrojet, the upward current from the eastward electrojet and the north-south current. Because of this mixture of contributing effects, it is thought that the correlation between $\Delta Y'_{step}$ and B_z of the IMF in this sector (Chapter 3) is not as strong as might have been expected. However, in the dawn sector, the $\Delta Y'_{step}$ is due essentially only to the single current system feeding the westward current. As has been shown by Hirshberg and Colburn (1969), the strength of the westward current is correlated with B_z of the IMF, so that the good correlation between $\Delta Y'_{step}$ and B_z is not unexpected.

As well as the two convection electrojets, a very weak eastward electrojet between 0400 and 1100 MLT has been put into the model, in accordance with the results of Rostoker and Hron (1975). Evidence of this current is not visible in the SPEA profiles. However, it is not always detectable in single averaged profiles so in all likelihood, its presence is averaged out in the SPEA data. The effect of this current system is minimal, although a slight positive perturbation is visible in the X'-component for the 0900 MLT model profile (Figure 4.16)

Finally, there is the so-called low-latitude current system which contributes slightly to the level-shift in the Y'-component but whose main purpose empirically is to bias that component in accordance with the observations. Although certain features of this current system are similar to Sq, it is more likely that the low-latitude current system represents winter S_q^p or DP-2.

A qualitative comparison of the profiles produced by the model with the SPEA profiles, profile by profile, indicates reasonable agreement except in the noon sector, where the $\Delta X'$ profiles show some disagreement. It has been shown however, that by incorporating a small change in the geometry of the westward electrojet in this sector, qualitative agreement in the X'-component is improved. However, even in this sector, the Y'-component shows good agreement. A statistical comparison between the SPEA and model $\Delta X'_{peak}$ and $\Delta Y'_{step}$ indicate that overall, there is excellent agreement.

As has been emphasized before, this model, as presented to this point, has been designed to reproduce only gross average features of the perturbation magnetic field as measured at ground level. The question naturally arises as to whether variations of this model may describe specific events. The next section gives three such examples.

4.6 Specific Events and the Average Current Model

To investigate the general applicability of the current model described in the previous sections, several instantaneous latitude profiles have been modelled using variations of the average model. It will be demonstrated in the following sections that the average model is well suited to act as a basis for modelling specific magnetospheric events.

4.6.1 Modelling of Two Unusual Dusk Sector Latitude Profiles

During a study of energetic particle precipitation into the high latitude ionosphere (Rostoker et al, 1978), several latitude profiles in the dusk sector attracted attention because they deviated markedly from the average latitude profiles in this sector. The deviation was most pronounced in the vertical component as may be seen in Figures 4.21(b) and 4.22(b). Figure 4.21(b) is the instantaneous latitude profile for Day 19, 1972, at 0332 UT. This profile would fall into the hourly averaged profile range of 1900-2000

5

Figure 4.21 Latitude profiles for Day 19, 1972, 0332 UT.
(a) the result of the model calculation
(b) the actual latitude profile

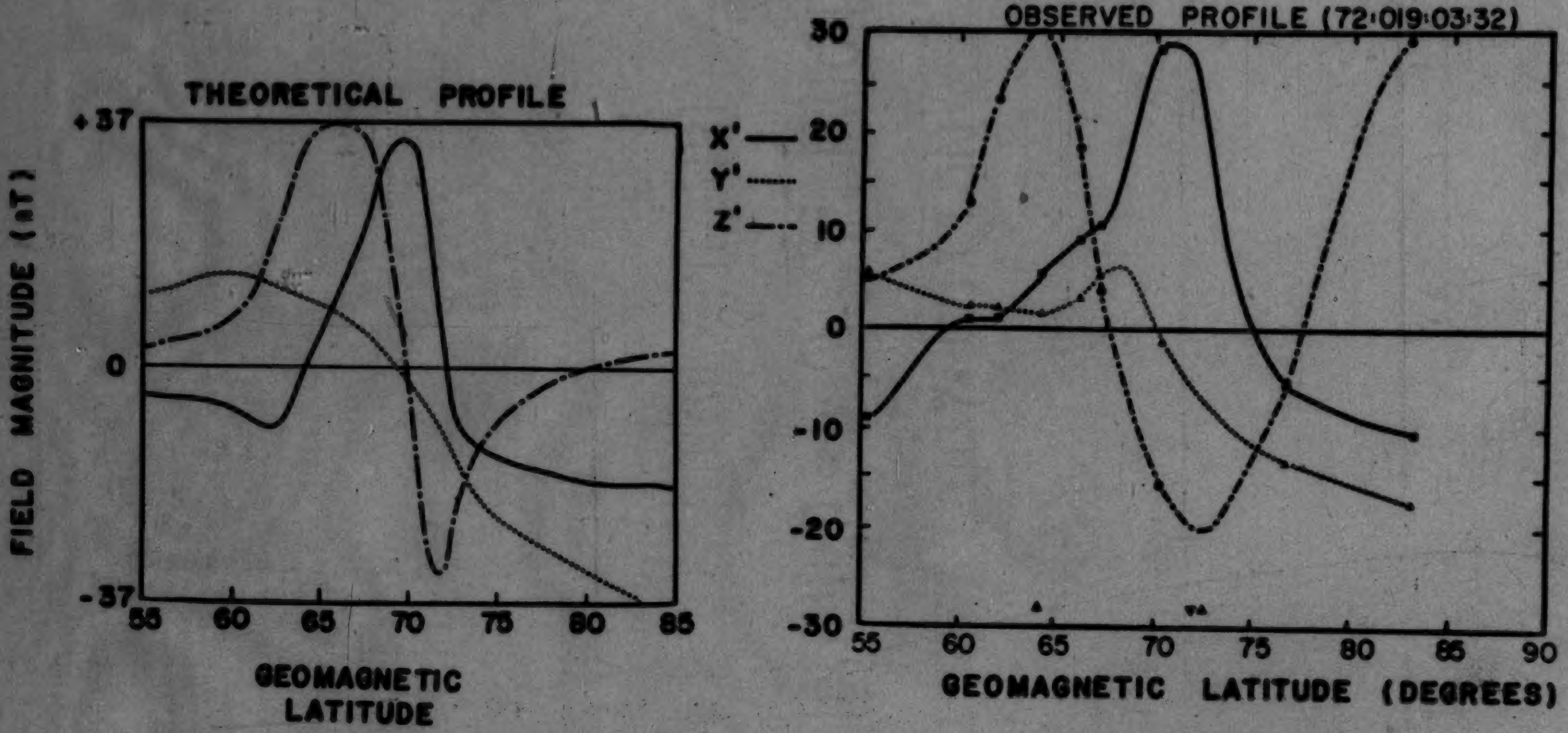
THEORETICAL PROFILE
OBSERVED PROFILE (72:019:03:32)
FIELD MAGNITUDE (nT)
+37
0
-37
55
60
65
70
75
80
85
GEOMAGNETIC LATITUDE
X' ——
Y' ·······
Z' —·—·
30
20
10
0
-10
-20
-30
55
60
65
70
75
80
85
90
GEOMAGNETIC LATITUDE (DEGREES)

Figure 4.22 Latitude profiles for Day 38, 1972, 02 UT.
(a) the result of the model calculation
(b) the actual latitude profile

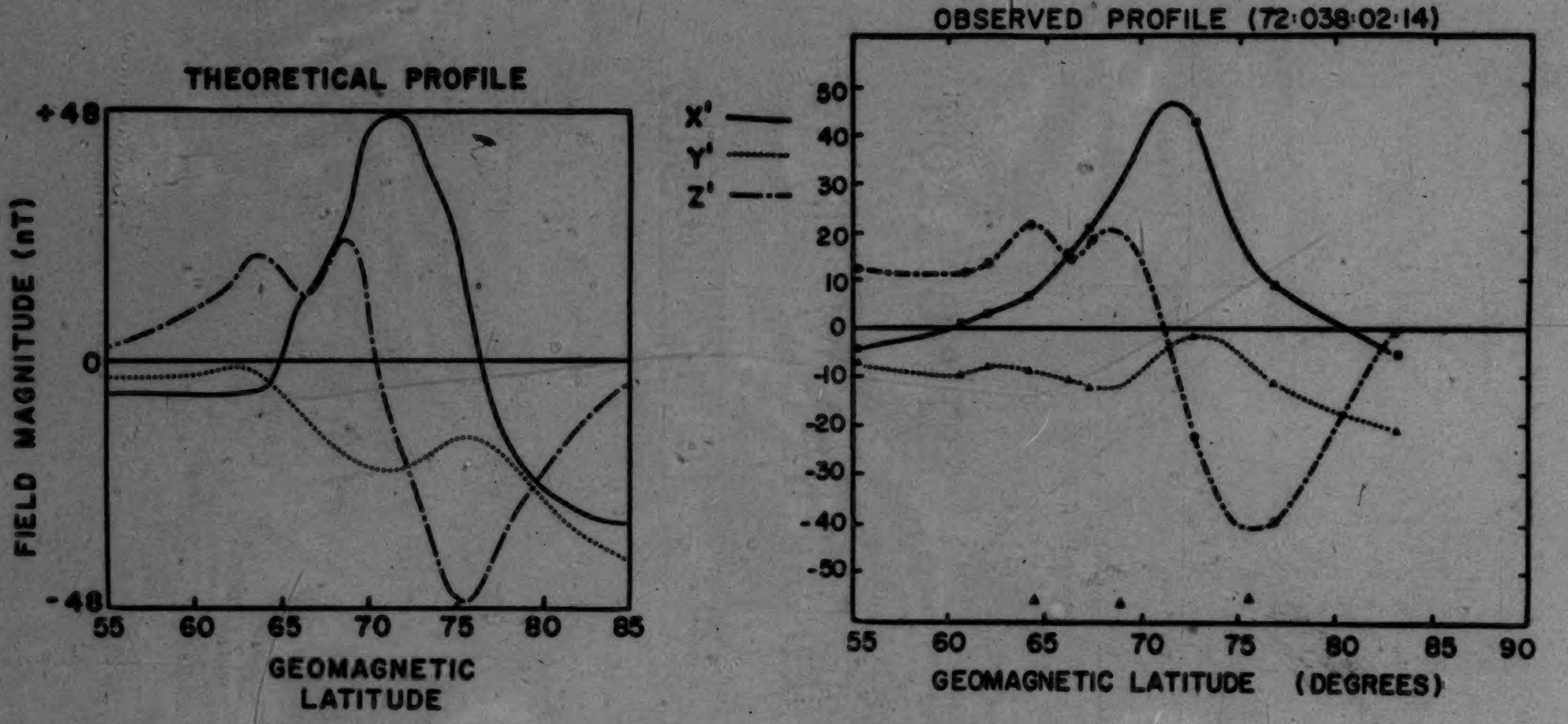
THEORETICAL PROFILE
FIELD MAGNITUDE (nT)
+48
0
-48
55
60
65
70
75
80
85
GEOMAGNETIC LATITUDE
X'
Y'
Z'
OBSERVED PROFILE (72:038:02:14)
50
40
30
20
10
0
-10
-20
-30
-40
-50
55
60
65
70
75
80
85
90
GEOMAGNETIC LATITUDE (DEGREES)

MLT. The feature of note in this profile is the behaviour of the positive Z-component at low latitudes. It is unusual in that the extremum is at least as large as the $\Delta X'$ extremum, and its location is displaced equatorward of the usual location of the ΔZ peak. In more usual latitude profiles, ΔZ peaks at the latitude where $\Delta X'$ is at about half of its peak value, and as well, the peak value of the Z-component is about half the peak $\Delta X'$ value. Also in this profile, two anomalous inflections occur in the X'-component, at latitudes of about 62°N and 67°N.

Figure 4.22(b) is the instantaneous latitude profile for Day 38,1972 at 0214 UT (corresponding to the averaged latitude profile range of 1800-1900 MLT). This profile is unusual because of the low latitude ΔZ behaviour as well. Although the values of Z-component extrema fall within normal ranges, ΔZ possesses a double peak at the equatorward side of the profile.

The above two profiles have certain characteristics in common. Both occur in the dusk sector, both are low amplitude profiles ($\Delta X' < 50$nt) indicating weak electrojet currents, and both exhibit abnormal behaviour near the equatorward edge of the electrojet. The nature of this behaviour suggested that a current other than a simple eastward electrojet was involved in producing these profiles.

To investigate the possibility of an anomalous structure in the eastward flowing current, Rostoker et al considered the electron and proton fluxes precipitating over the auroral zone in this sector. Soft particle spectrometer and energetic particle detector data were available from the ISIS-2 polar orbiting satellite during 0328-0336 UT on Day 19, 1972, when the satellite was within 1° - 3° of longitude of the meridian line of magnetometers, and during 0209-0217 UT, Day 38 1972, when the satellite was passing directly over the station line.

On Day 19, energetic electron fluxes (up to several keV) were observed in the latitudinal range of 69° to 73.5°, in close correspondence with the eastward electrojet. These fluxes dropped sharply at 69°N, so that no electron precipitation was present to produce conductivity at lower latitudes. There was also insufficient flux of high energy protons ($E > 150$ keV) to account for a conductivity high enough to produce ionospheric currents equatorward of 69°N. On Day 38, a similar pattern was observed, with electron fluxes (15 keV $> E >$ 10 eV) confined to the latitude range 74°N to 68.5°N. These latitudes correspond well to the latitudes at which the $\Delta X'$ perturbation is at half maximum, which in turn correspond to the approximate latitudinal limits of the eastward electrojet. Equatorward of this there was again insufficient precipitation to account for ionospheric currents.

It will be recalled from section 4.4.1 that the average current model contained provision for sunlit hemisphere electrojets which exist by virtue of conductivity produced by solar UV radiation. This feature of the model has been expanded upon to produce model latitude profiles very similar to those of Figure 4.21(b) and 4.22(b). Specifically, the unusual behaviour exhibited by ΔZ in these two profiles is believed to be the result of current which flows in the sunlit sector due to ionization generated by solar UV radiation. This current will be called the UV electrojet. This electrojet is superposed on an auroral (eastward) electrojet whose existence depends on the electric field and the conductivity generated by particle precipitation. The UV electrojet extends equatorward of the auroral electrojet because there is a significant poleward electric field (i.e., one which will drive eastward Hall current) equatorward of the southern border of the auroral oval as defined by energetic particle precipitation.

This model of current flow is appealing because of two features. The $\Delta X'$ associated with the UV electrojet may have values of the same order of magnitude as $\Delta X'$ for the auroral electrojet during quiet times. Thus, the enhancement of $\Delta X'$ seen in the equatorward latitudes of Fig 4.21(b) and 4.22(b) may be understood in terms of proximity of the observations to the UV electrojet. More importantly, the unusual ΔZ behaviour outlined above can be explained as an edge effect of the poleward Pedersen current flow which connects the Birkeland current sheets associated with the UV electrojet system.

To this end then, the model as already developed was modified to include a wider UV electrojet than was included in the average model. In addition, since the sun sets on the F-region about one hour later than it sets on the E-region, and the former is the location of significant Pedersen currents, the UV electrojet associated north-south system was extended one time zone further into the evening sector than the eastward UV electrojet. Figure 4.23 is a schematic drawing of the model as used for these examples.

Tables 4.3(a) and 4.3(b) display a complete summary of all the parameter values used. Note that equation 4.2 has been recast in the form:

$$\lambda = \lambda_{12} + 1/2\,(\lambda_{00} - \lambda_{12})(1 + \cos\varphi)$$

where λ_{12} and λ_{00} are the latitudes of the borders at 1200 and 0000 MLT respectively.

Figures 4.21(a) and 4.22(a) are the model latitude profiles obtained by calculating the magnetic perturbations on a meridian one hour towards midnight from the dusk terminator for Day 19, while for Day 38, the data were modelled on a meridian 4° away from the dusk terminator towards noon, the positions being those of the station line at the times that the anomalous profiles were recorded. The agreement between the observed and model profile is excellent in most respects. The positive ΔZ recorded at Resolute Bay on Day 19 is the main exception. This value was

Figure 4.23 Schematic of the current systems used to model the profiles of Figure 4.20(b) and Figure 4.21(b). Table 4.3(a) and Table 4.3(b) describe the model parameters in detail.

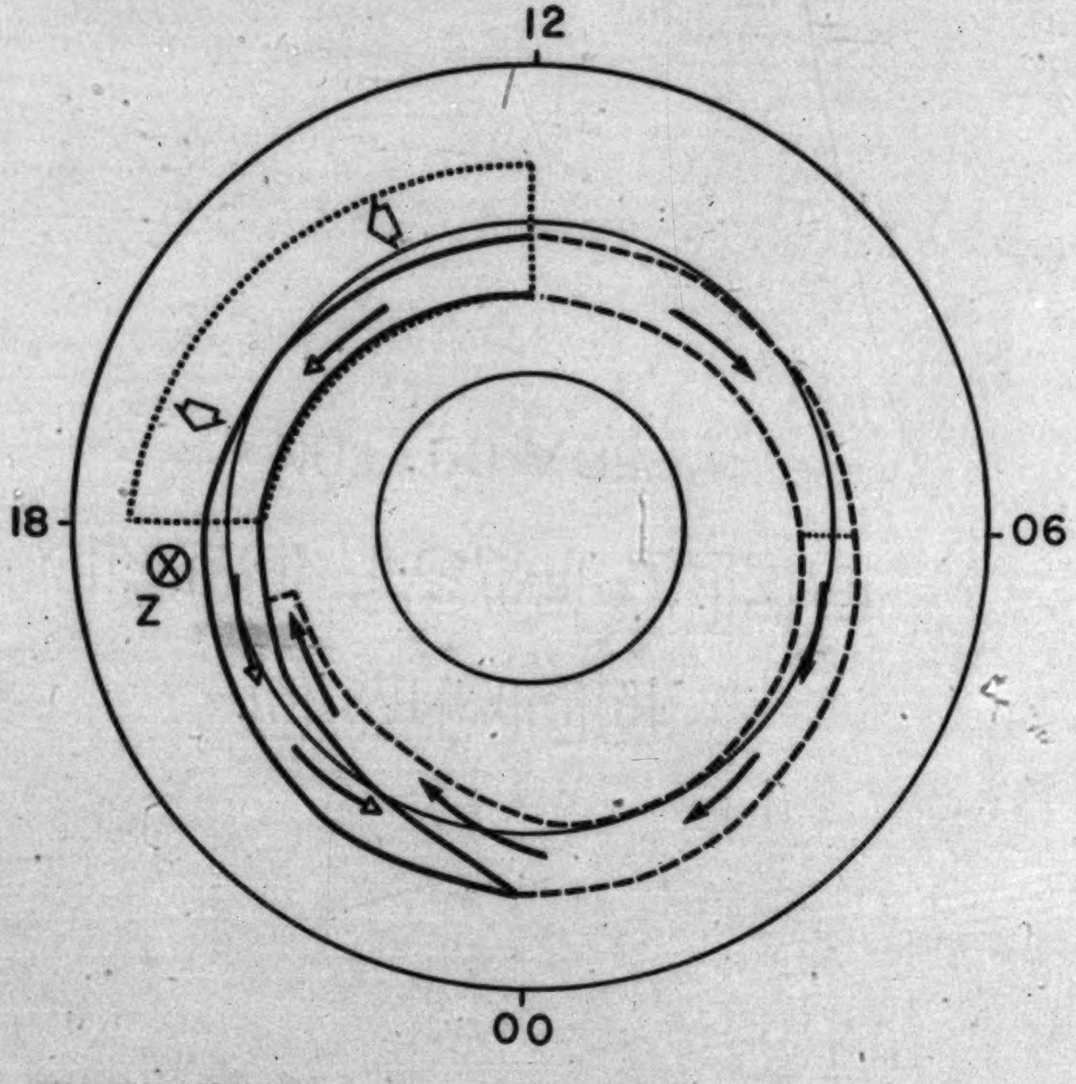
Z

Table 4.3(a)
Model Parameters for Day 38, 1972

System	Poleward Border (°N)		Equatorward Border (°N)		Longitudinal Extent	Current Intensity (A/m)	Total Current (A)
	λ_{12}	λ_{00}	λ_{12}	λ_{00}			
UV electrojet	77.5	72.5	67.5	62.5	180° $\le \varphi \le$ 270°	0.07	7.99×10^4
Auroral (eastward) electrojet	77.5	72.5	71.5	66.5	180° $\le \varphi \le$ 315°	0.25	1.72×10^5
Auroral (Westward) Electrojet in premidnight quadrant	80.5	75.5	77.5	72.5	285° $\le \varphi \le$ 315°	0.94*	2.64×10^5*
Auroral (westward) electrojet in dawn sector	77.5	72.5	71.5	66.5	15° $\le \varphi \le$ 180°	0.46**	2.64×10^5**

---

*maximum current intensity and total current. For this electrojet, peak intensity is at φ=315° decreasing in value to zero by φ=285°.

**Maximum current intensity and total current. For this electrojet peak intensity is at φ=37.5° decreasing in value to zero by φ=180°.

Table 4.3(b)
Model Parameters for Day 19, 1972

System	Poleward Border		Equatorward Border		Longitudinal Extent	Current Intensity (A/m)	Total Current (A)
	(°N) λ_{12}	(°N) λ_{00}	(°N) λ_{12}	(°N) λ_{00}			
Day 19, 1972 UV electrojet	75.0	70.0	62.0	57.0	$180° \leq \varphi \leq 270°$	0.06	$8.40x10^4$
Auroral (eastward) electrojet	75.0	70.0	72.0	67.0	$180° \leq \varphi \leq 315°$	0.22	$1.25x10^5$
Auroral (westward) electrojet in premidnight quadrant	77.5	72.5	75.0	67.0	$285° \leq \varphi \leq 315°$	0.66*	$1.87x10^5$*
Auroral (westward) electrojet in dawn sector	75.0	70.0	72.0	67.0	$15° \leq \varphi \leq 180°$	0.20**	$1.08x10^5$**

---

*maximum current intensity and total current. For this electrojet, peak intensity is at $\varphi=315°$ decreasing in value to zero by $\varphi=285°$.

**Maximum current intensity and total current. For this electrojet peak intensity is at $\varphi=37.5°$ decreasing in value to zero by $\varphi=180°$.

maintained steadily over several hours and therefore suggests the presence of a relatively steady state polar cap current system which is not accounted for in the model. All other differences are relatively minor and could have been minimized by further manipulation of the border locations and longitudinal and latitudinal variations in height-integrated current density. In view of the fact that no model based on a finite number of data is unique, it was felt that such "fine-tuning" was not warranted. It is contended that the model does account for the observed features, and it is concluded that a significant portion of the ionospheric current flow in the afternoon sector is diverted up the field lines at a conductivity discontinuity between the dark and sunlit ionospheres.

4.6.2 The Substorm of Day 23, 1972.

Although the current model that has been developed in the previous sections is intended to be a generalization of the currents flowing during quiet to moderately disturbed times, occasionally certain features in data from disturbed periods appear to be similar to features in the hourly averaged data. An example of such an event is provided by data from 0107 UT on Day 23, 1972. Although this day falls into the day range from which data has been taken to construct the hourly averaged latitude profiles, it was not used because it was an extremely active day. Figure 4.24 is a display of magnetograms from each station, with the

Figure 4.24 Magnetograms for the stations in the University of Alberta magnetometer chain, for Day 23, 1972, 0000 to 0200 UT.

DAY23,1972

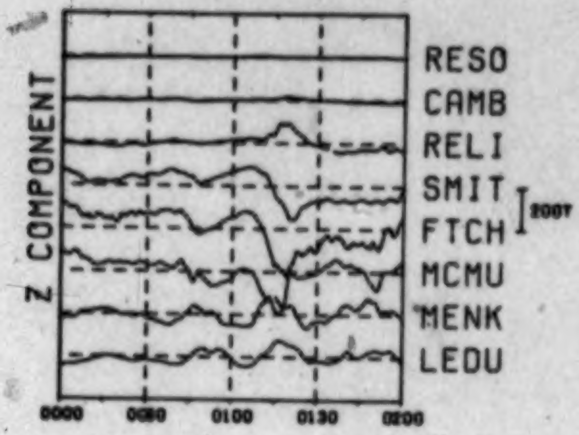
Z COMPONENT
RESO
CAMB
RELI
SMIT
FTCH
MCMU
MENK
LEDU
200γ
0000
0030
0100
0130
0200

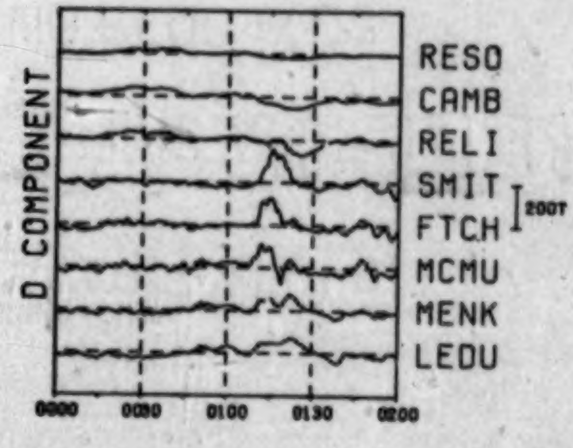
D COMPONENT
RESO
CAMB
RELI
SMIT
FTCH
MCMU
MENK
LEDU
200γ
0000
0030
0100
0130
0200

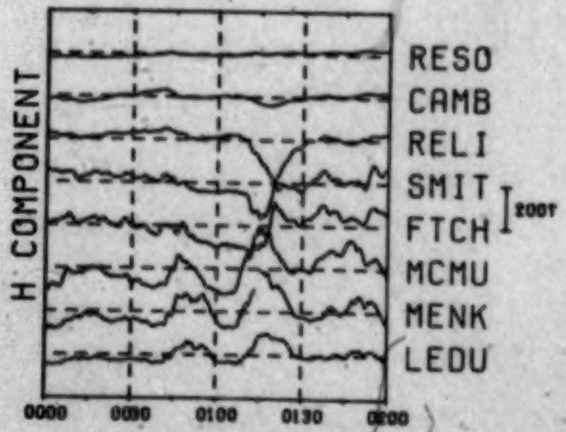
H COMPONENT
RESO
CAMB
RELI
SMIT
FTCH
MCMU
MENK
LEDU
200γ
0000
0030
0100
0130
0200

stations arranged north to south from the top of the page, for the UT hour 0100 to 0200. Note that near 0107 UT that the north-south component becomes increasingly positive at low latitudes, but increasingly negative-going at higher latitudes (north of SMIT). During the time that this is occurring, the east-west component is strongly positive-going in the mid-latitudes of the magnetometer line. Figure 4.25 (a,b,c,d) shows four latitude profiles, beginning at 01 hours, 7 min, 34 sec UT and spaced 123 sec apart. These show a growth of the X'-component indicating an increasing eastward current flow, and in Figure 4.25(c) and (d), an increasingly negative $\Delta X'$ poleward of about 66°N. As well, the Z-component is consistent with an increasing eastward current and, as the negative $\Delta X'$ develops, the Z-component is consistent with an increasing westward flowing current in the poleward part of the profiles. The Y'-component is remarkable for its double peak in the first two profiles (Figure 4.25(a) and (b)) which merge into a single well defined peak during the later two profiles (Figure 4.25(c) and (d)).

Figure 4.26 (a,b,c,d) show linear mappings of all-sky camera (ASCA) photographs for 0900 to 0112 UT, taken from Fort Smith. These indicate an auroral structure (a westward travelling surge) which advances westward towards Fort Smith and then remains overhead (Figure 4.26(c) and (d)). While overhead, the structure moves slightly poleward. Figure 4.27 is a north-south magnetogram from College, Alaska. College

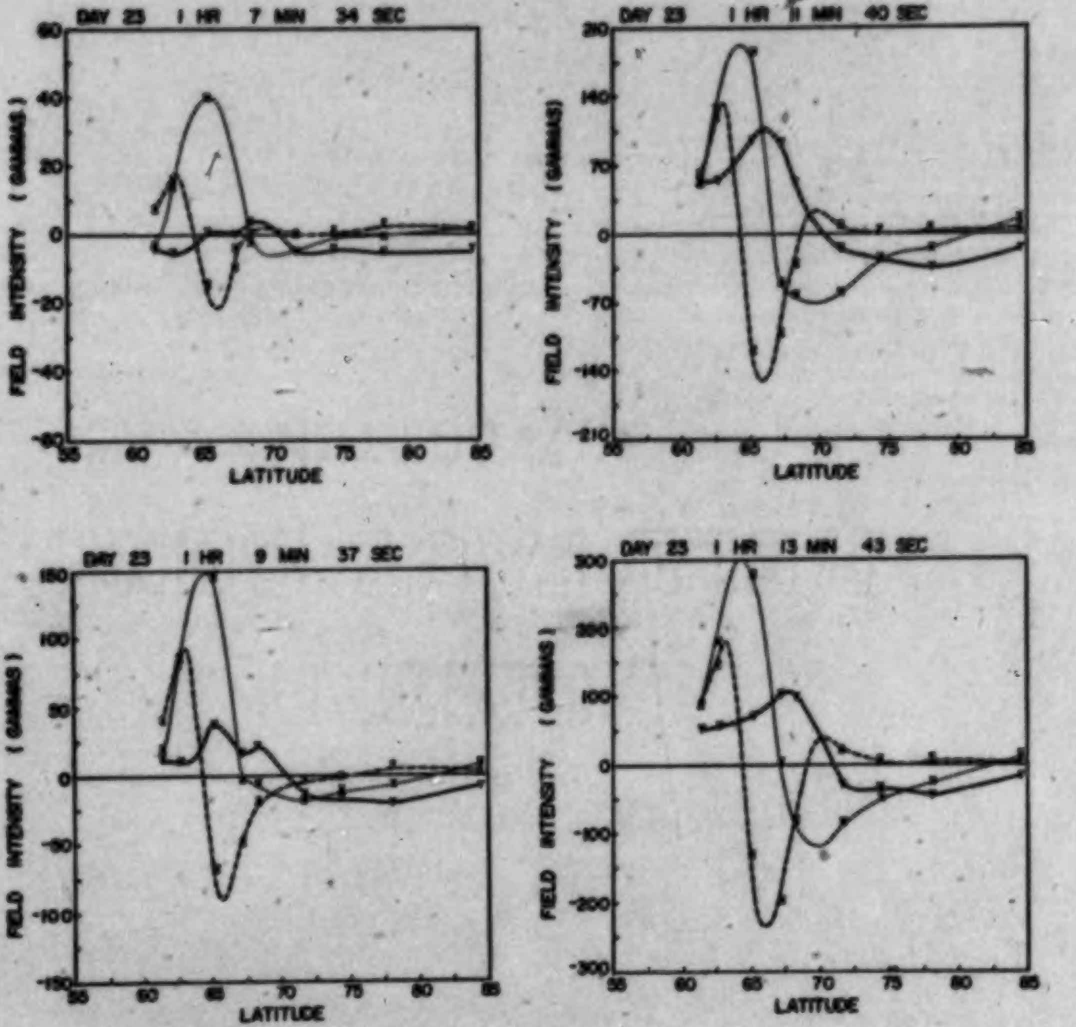

Figure 4.25 Latitude profiles for Day 23, 1972.

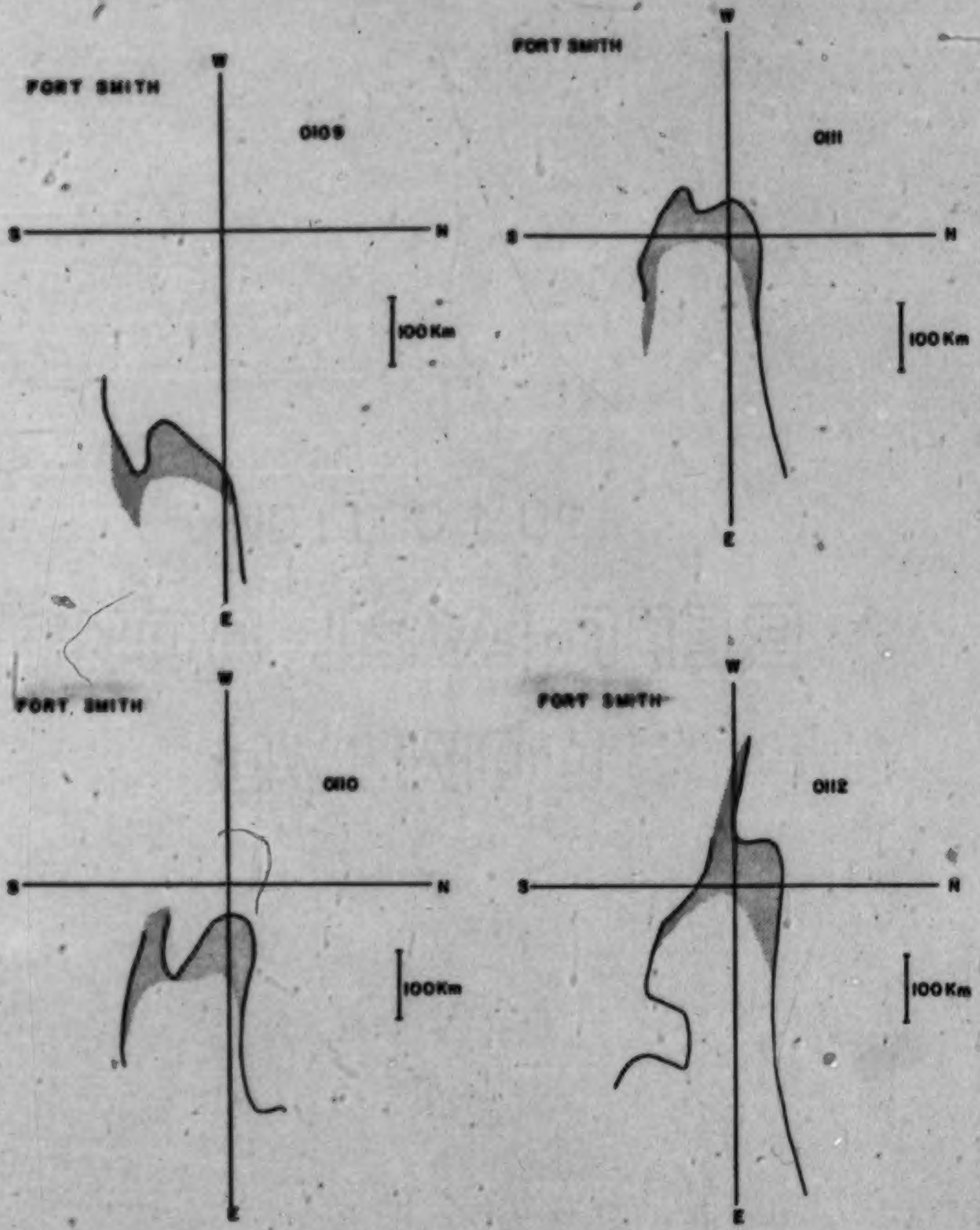
FORT SMITH
W
0109
S
N
100Km
E
FORT SMITH
W
0111
S
N
100Km
E
FORT SMITH
W
0110
S
N
100Km
E
FORT SMITH
W
0112
S
N
100Km
E

Figure 4.26 Linear mappings of the auroral forms visible on all-sky camera pictures taken at Fort Smith on Day 23, 1972, at the times indicated.

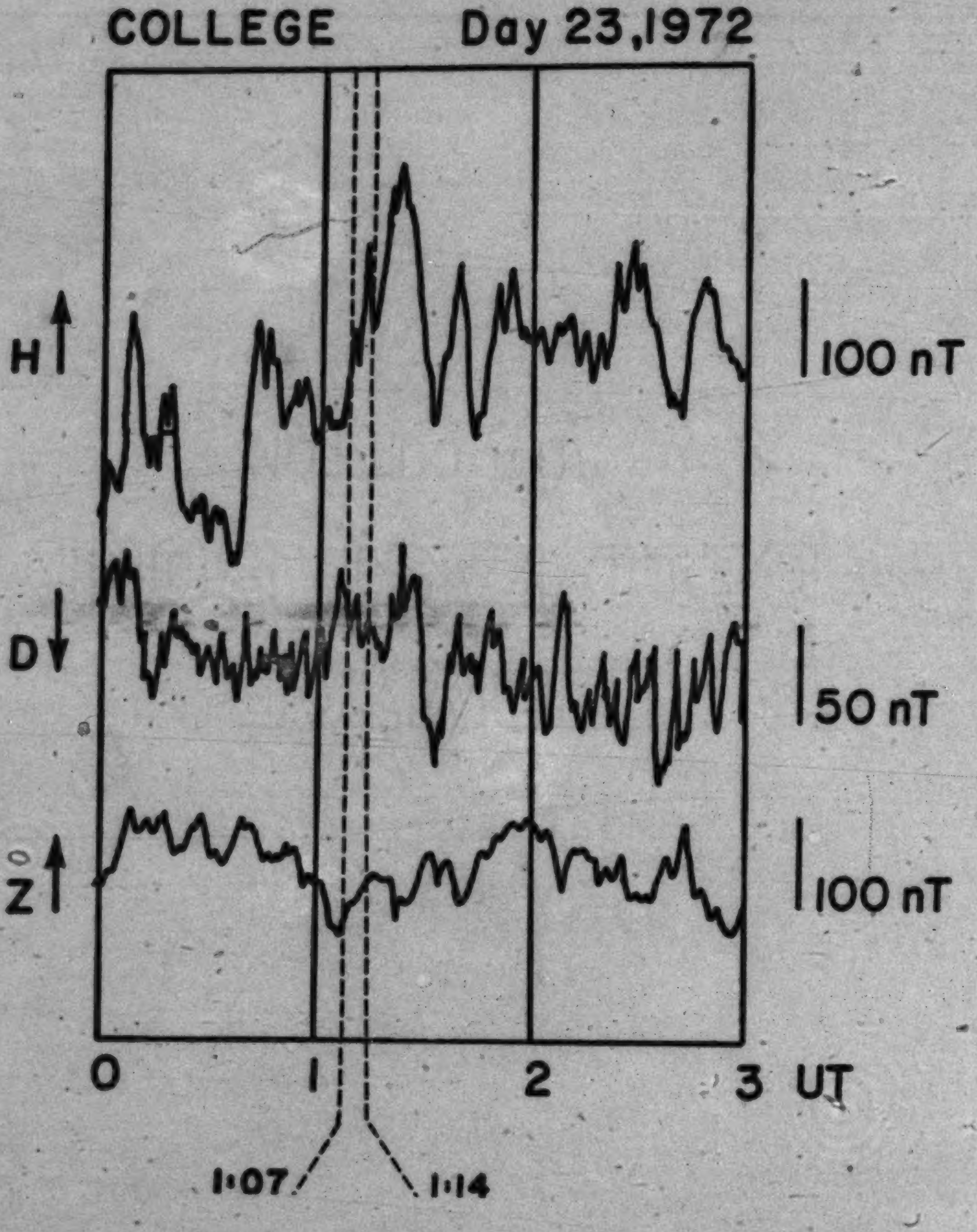

Figure 4.27 Magnetogram from College, Alaska, for Day 23, 1972. The vertical dashed lines delineate the time period of interest.

is situated about three time zones west of the magnetometer line. The magnetogram indicates an increasingly positive north-south component, indicative of a growing eastward current. This actual growth of the eastward electrojet is emphasized, because, as shown by Kisabeth (1972) it is possible to generate a north-south component of the magnetic field which appears to indicate both eastward and westward current flow by introducing a shear in a purely westward flowing current. Such is not the case during the period of interest here.

Up to this point, then, from the $\Delta X'$ and ΔZ profiles, combined with the ASCA data and the observations from College, it appears that the profiles of Figure 4.25 are produced by an eastward current that is growing in strength, combined with a westward flowing current that is advancing from east of the magnetometer line to a position overhead.

The Y'-component is not unlike those seen in the post-1800 MLT averaged latitude profiles. That is, the $\Delta Y'$ profiles are consistent with the existence of locally unbalanced upward-flowing field-aligned currents in that $\Delta Y'$ shows a negative-going level-shift. However one additional feature is present in that the earlier $\Delta Y'$ profiles (Figure 4.25(a) and (b)) are double-peaked, and the last two (Figure 4.25(c) and (d)) show a pronounced peak superimposed upon the level-shift. The proposed explanation for this structure is given in the following description of the model.

In order to model these profiles, differential latitude profiles were constructed. That is, it was assumed that the phenomenon of interest was primarily the structure shown in Figure 4.26 (a) through (d), and that this structure was superimposed upon an existing system of currents. Thus, the profile for Day 23, 1 hour, 7 min, 34 sec was taken as a reference level, and was subtracted from the other profiles. This has the advantage of removing uncertainties in the model of the relatively quiet profile of Figure 4.25(a). The resulting three profiles, then, were modelled.

A schematic diagram of the model is shown in Figure 4.28 (a,b,c,d). The small circles represent the location of the station line, i.e., the meridian along which model calculations were made. Figure 4.28(a) represents the baseline current system, and consists of a basic eastward current (46,125 A) with boundaries at 62°N and 66°N, and longitudinal boundaries identical with the average model. East of the observation meridian is a westward current, which terminates 15° east of the observation points. This current, as in the average model, is linearly decreasing in strength as a function of longitude, (as shown by the shaded area), with a maximum integrated current of 2.05×10^5 A flowing at 315° longitude (i.e. 60° east of the observation meridian) and between 66°N and 72°N latitude. Superimposed on both of these systems is a north-south current system consistent with the electric field and conductivity models used in the average current model. As well, an intensified

Figure 4.28 Schematic diagram showing the currents used to model the event of Day 23, 1972. (a) represents the baseline system, and (b), (c) and (d) the development of the currents, in time, in order to model the latitude profiles of Figure 4.25. The open-circles represent the locations of the magnetometer sites. The shaded area at the leading edge of the of the westward electrojet indicates the region of intensified equatorward current flow.

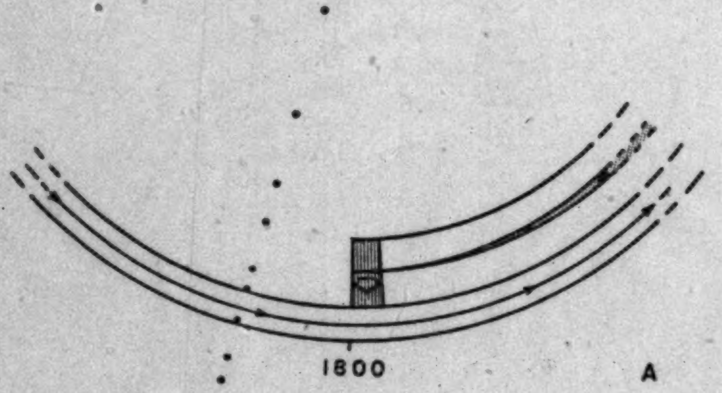
1800
A

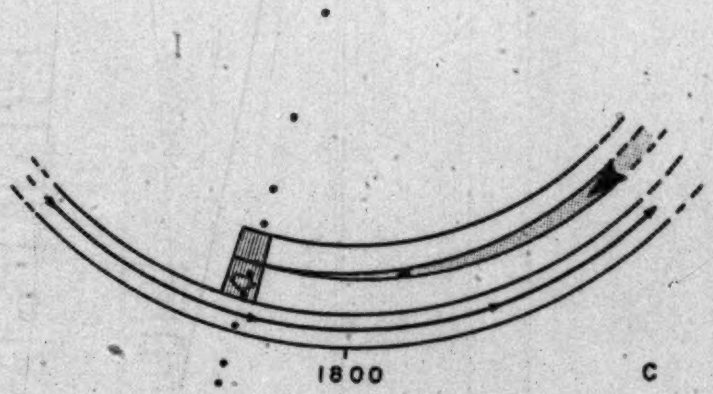
1800
C

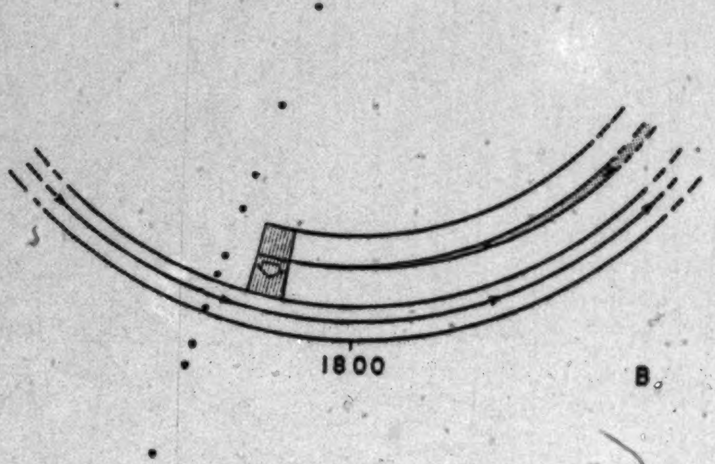
1800
B

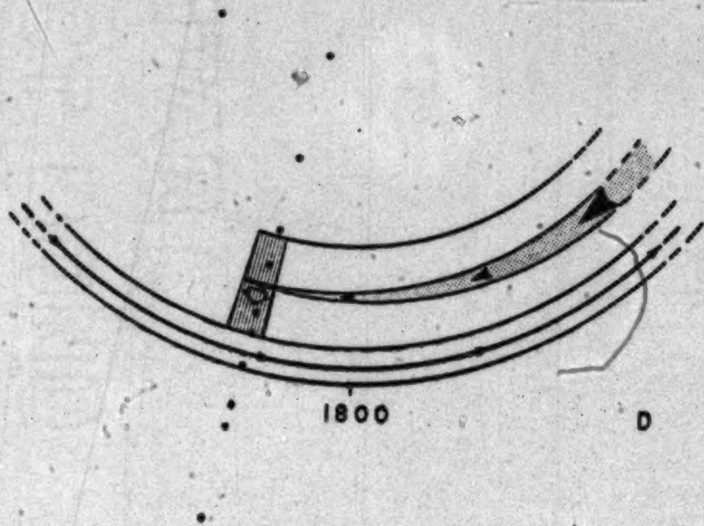
1800
D

region of equatorward current flow has been added to the western-most 5° of the westward current. The total current flowing equatorward in this region is 2.03×10^5 A, so that, in effect, the current at the leading edge of the model westward electrojet is primarily equatorward. This intense north-south system is necessary in this model to reproduce the double-peaked nature of the $\Delta Y'$ profile. That is, the Y'-component profiles exhibit a double-peak when the observations are made at long distances beyond the longitudinal extremes of a north-south current system (Kisabeth, 1972).

Figure 4.28(b) shows the time development of the model representing the changes seen in the profile of Figures 4.25(b) (1 hour, 9 min, 37 sec). The eastward electrojet has increased in strength by a factor of 3.5 to 1.614×10^5 A. The westward electrojet has not changed in maximum strength, but simply advances 11° westward. Figure 4.28(c) is the current system corresponding to the time of 1 hr, 11 min 40 sec (Figure 4.25(c)). The eastward current has increased in strength again, by a factor of 1.6 from the previous figure, to 4.214×10^5 A. The westward current has continued to advance until its leading edge is now 3° west of the observation meridian, so that the observation points now lie slightly to the east of the center of the north-south intensification. As well, the westward current increases in strength to a maximum value of 8.2×10^5 A, while the total current in the intensified north-south system remains constant.

Finally, Figure 4.28(d) represents the currents giving rise to the latitude profile at 1 hour, 13 min, 43 sec. The eastward current again grows in strength to a total current of 3.23×10^5 Amps. No further westward expansion of the westward electrojet occurs, but this system expands poleward 2°, so that the poleward boundary is at 74°N latitude. Simultaneously, the maximum current strength increases by a factor of 2 to 1.64×10^6 Amps. The intensified north-south system expands poleward also, but undergoes no increase in total current strength. Table 4.4 summarizes the model parameters.

In this model, the UV electrojet plays no role inasmuch as it undergoes no changes in time and therefore does not appear in the differential profiles. The pre-noon westward current, and the current flow across the midnight-sector have been constructed to be commensurate with the main systems described in the preceding paragraphs.

The model latitude profiles generated from these current models (and referenced to the baseline system of Figure 4.28(a)) are shown in Figure 4.29(a,b,c). (In this figure, the symbols H,D refer to X',Y' respectively). It is evident that the fit is extremely good. In particular the unusual behaviour of the Y'-component is reproduced very well. This is achieved due to two features of the model. First, the double peak in $\Delta Y'$ is the distant effect of the north-south intensification associated with the westward

Table 4.4

Model Parameters for the Substorm of Day 23,1972

TIME (Hr:Min:Sec)	EASTWARD CURRENT		WESTWARD CURRENT*		
	Strength (x 10^5A)	Borders λ_{∞} $\lambda_{1/2}$ (°N)	Maximum Strength (x 10^6A)	Borders λ_{∞} $\lambda_{1/2}$ (°N)	Leading Edge** (°W)
1:07:34	.46125	62,66	.205	66,72	90
1:09:37	1.614	62,66	.205	66,72	101
1:11:40	2.214	62,66	.82	66,72	108
1:13:43	3.23	62,66	1.64	66,74	108

*Superposed on the leading edge of this is an equatorward flowing current of 2.03 x 10^5A, and 5° in longitudinal extent. See text for details.

**Model profiles were calculated along the 105°W longitude meridian.

Figure 4.29 Comparison of the differential profiles with the model calculations. The data points are indicated by H,D, and Z (corresponding to X', Y', and Z), and the model results by the continuous curves.

(a) Comparison of the differential profile for 01:09:37 UT with the model calculation.

(b) Comparison of the differential profile for 01:11:40 UT with the model calculation.

(c) Comparison of the differential profile for 01:13:43 UT with the model calculation.

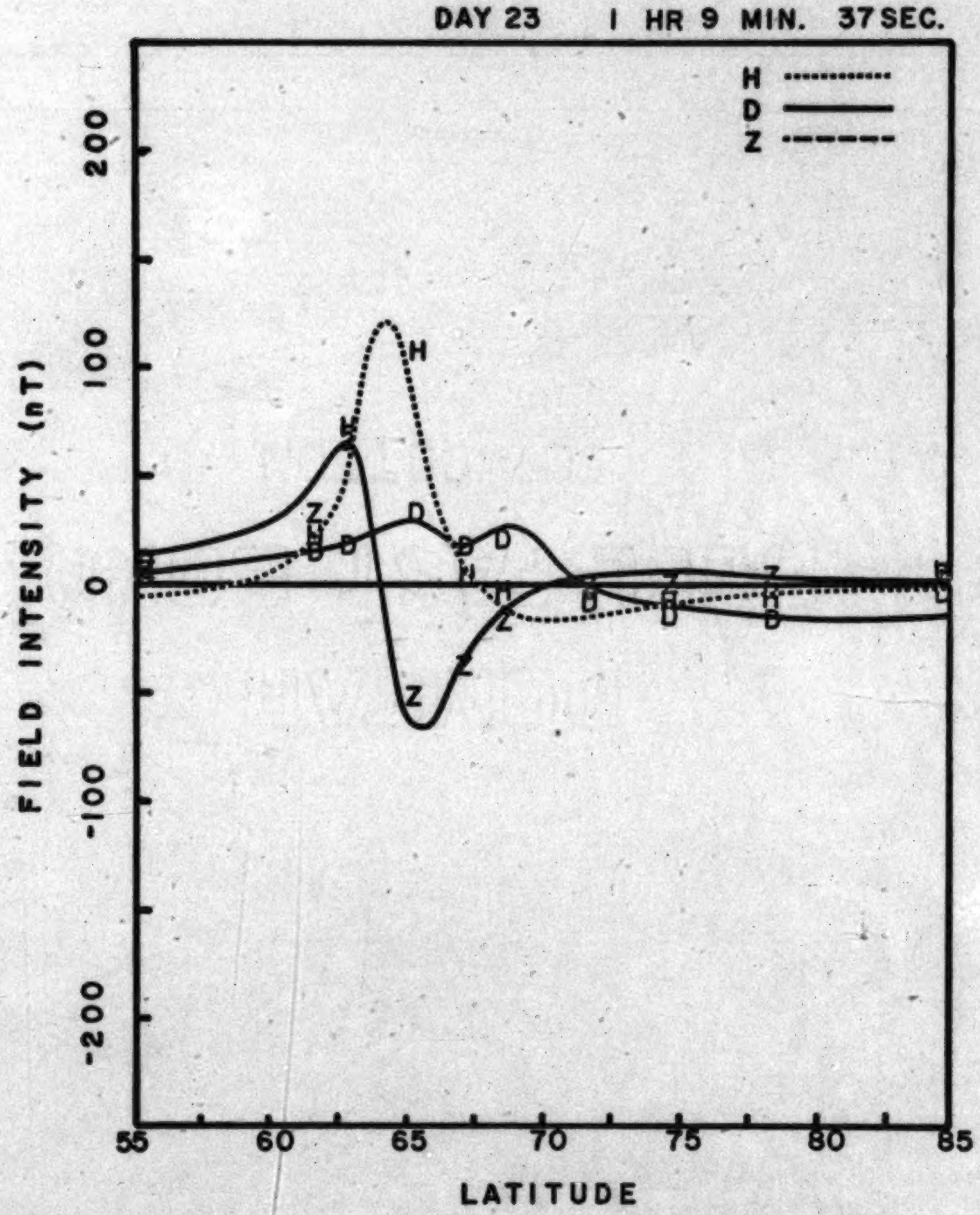
DAY 23 1 HR 9 MIN. 37 SEC.
H
D
Z
FIELD INTENSITY (nT)
200
100
0
-100
-200
55
60
65
70
75
80
85
LATITUDE
H
D
Z

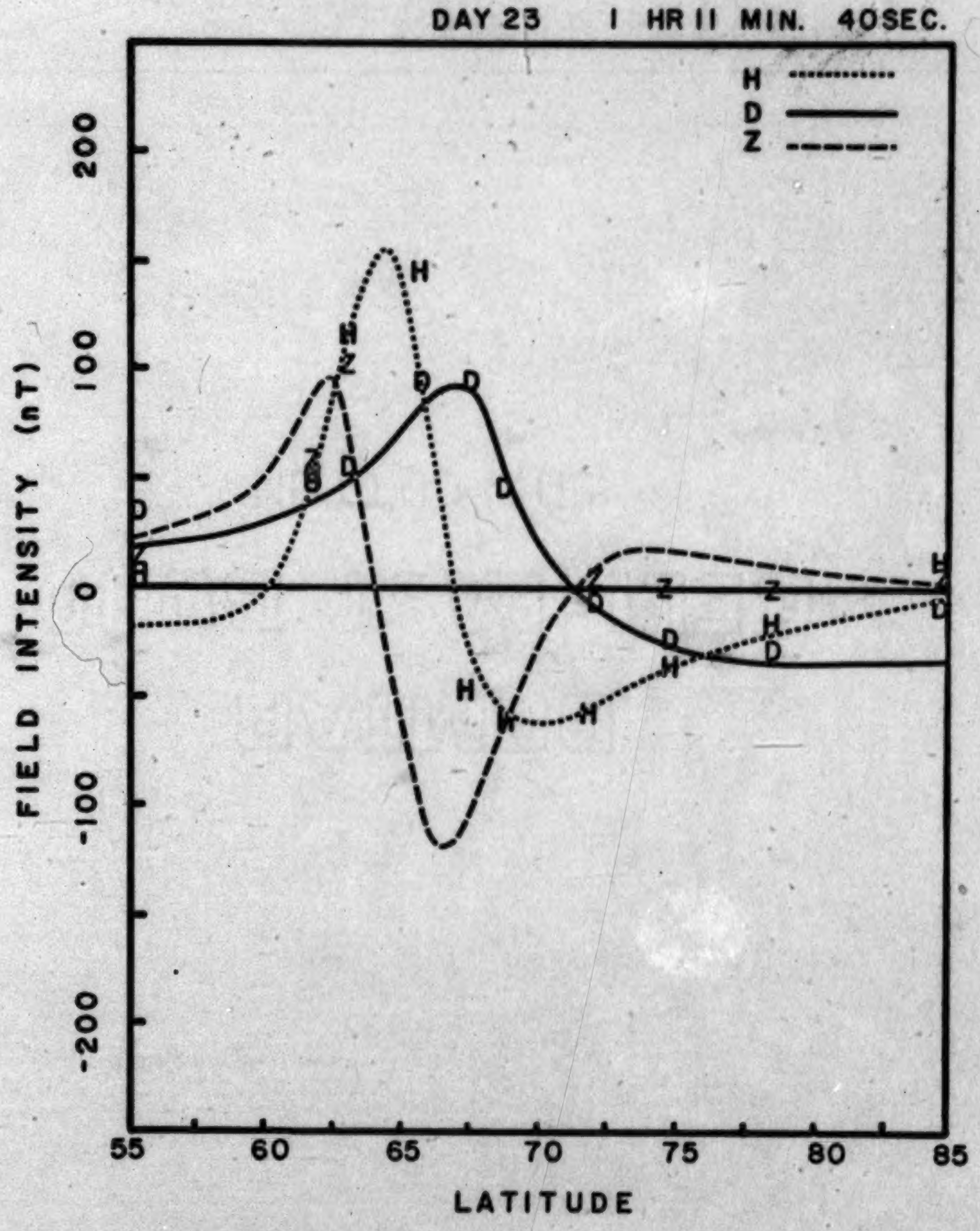
DAY 23 I HR 11 MIN. 40SEC.
H
D
Z
FIELD INTENSITY (nT)
200
100
0
-100
-200
55
60
65
70
75
80
85
LATITUDE

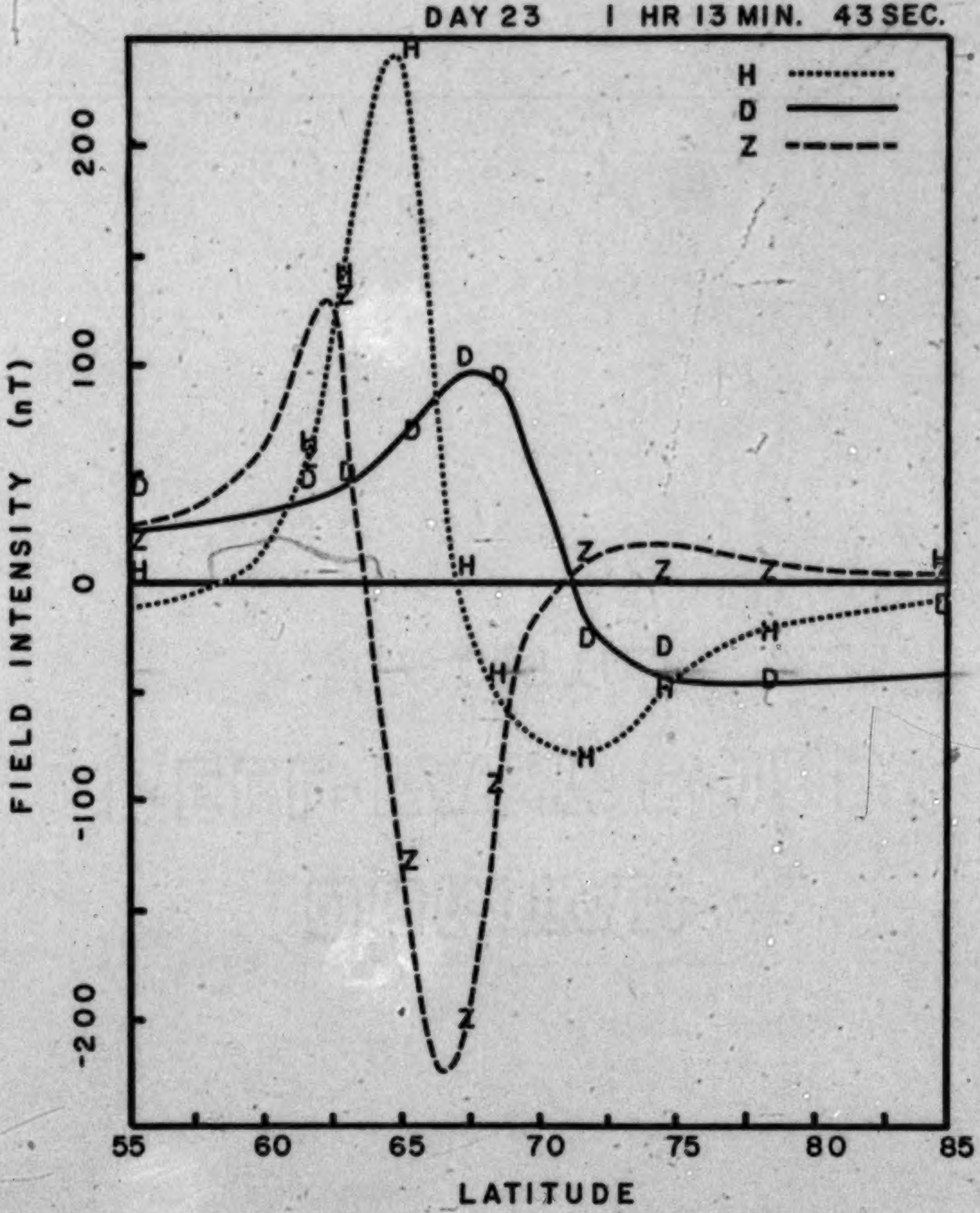
DAY 23 1 HR 13 MIN. 43 SEC.
H
D
Z
FIELD INTENSITY (nT)
200
100
0
-100
-200
55
60
65
70
75
80
85
LATITUDE

current. This intensification is also responsible for the positive peak in the same component of the later profiles (Figure 4.29(b) and (c)). Second, the negative-going level-shift in the Y'-component is due to the upward-flowing net field-aligned current associated with the westward electrojet. Thus it appears that this disturbance is a pertubation of the quiet-time model current system.

Basically, the quiet-time model is altered by increasing the current in the auroral electrojet and both increasing the current in the westward electrojet and letting it expand westward from the nominal position assigned to the westward electrojet in the quiet-time model. The westward current probably expands due to an enhanced particle precipitation into the region poleward of the eastward electrojet thus providing a Hall conductivity where little or none existed before. The intensification of the intense equatorward flowing current at the leading edge of the westward current is probably due to an enhanced Pedersen conductivity in this region, i.e., an increase in relatively soft particles, although an enhancement of the equatorward electric field in this regime would also bring about a north-south current enhancement. Such a change in the electric field would also cause an enhancement of the westward flowing Hall current in this same sector, although the magnetic field has been successfully modelled without invoking such a localized enhancement in the westward current. However, in view of the lack of corroborating particle and electric field data, it is not possible to apply a unique physical interpretation to this disturbance model. One can only interpret the results in terms of equivalent current flow. This model has been presented here only to show that, indeed, a variation in the model for average conditions is remarkably successful in modelling a variation in real substorm current systems.

4.7 Comparison of the Model for Average Conditions with Satellite Observations of Field-Aligned Currents

Reference has been made in preceding sections of this chapter to the fact that the global current model of section 4.5 has a field-aligned current distribution that does not compare well in all aspects with the interpretation of some polar-orbiting satellite observations, specifically, data from the Triad satellite (Sugiura and Potemra, 1976; Iijima and Potemra, 1976). Statistical characteristics of the field-aligned current flow as inferred from the Triad satellite data have been shown in Figure 4.2. As well, Figure 4.30 shows the most recently determined average characteristics of the upward and downward field-aligned current densities as a function of latitude. Combination of the data in these two figures indicates that although the satellite observations imply a strong unbalanced downward current flow in the pre-noon hours, there is a similarly strong net upward flow in the immediate post-noon hours. It is in this latter region that the disagreement between the

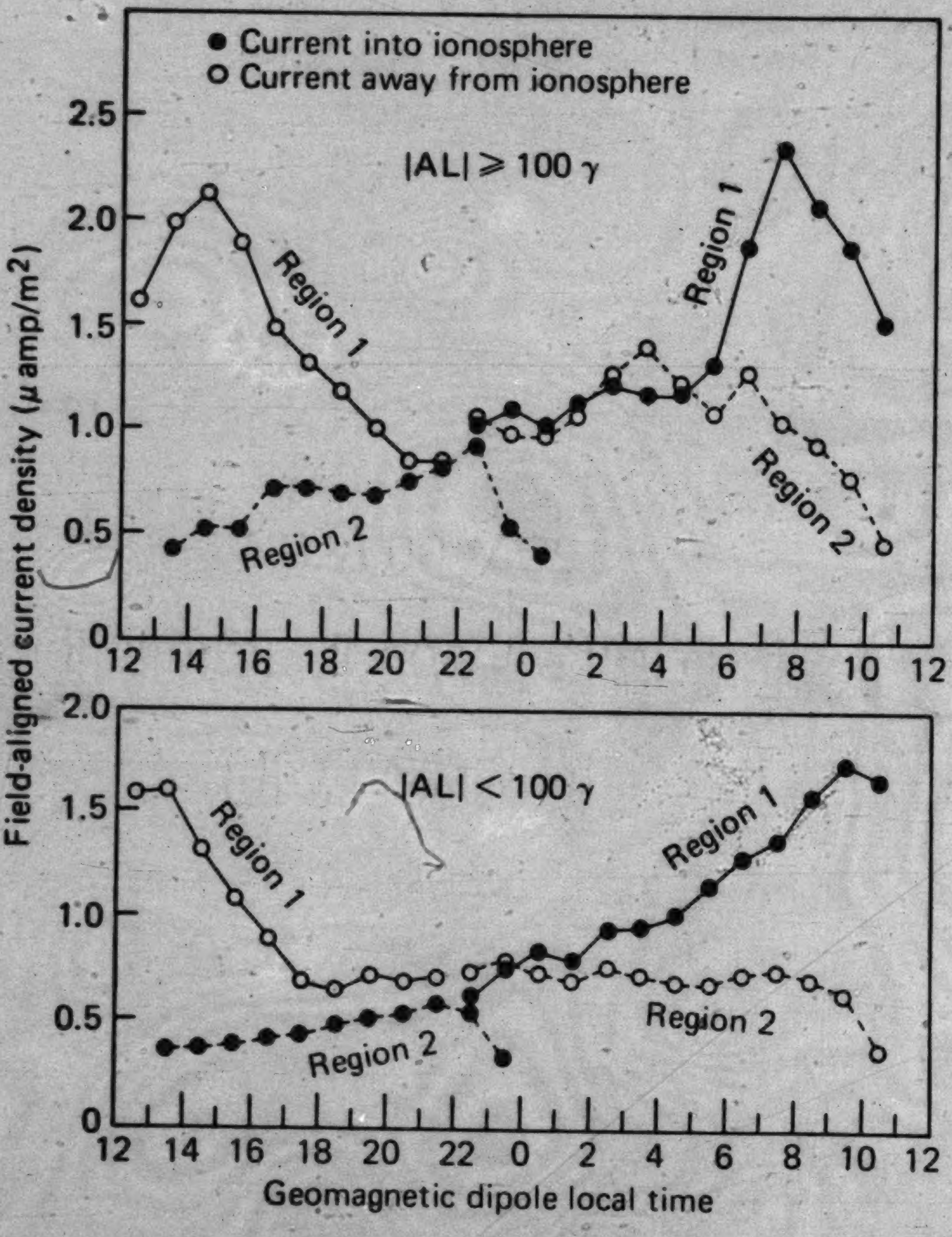

Figure 4.30 Diurnal distribution of average field-aligned current densities during active periods in the upper panel, and weakly disturbed periods in the lower panel (after Iijima and Potemra, 1978).

satellite observations and ground based observations arise.

Elsewhere, the two data suites are in good general agreement although the ground based data indicates that a pair of east-west aligned field-aligned current sheets may extend as far into the dusk sector as 1800 MLT, whereas the satellite data shows such a structure only until about 2200 MLT. This discrepancy is not fully understood. Iijima and Potemra (1977) present a figure similar to Figure 4.2 for more disturbed periods and show that even then, the field-aligned current pair that would be associated with westward current flow only extend up to 2200 MLT as well, although Kamide and Akasofu (1976) present Triad data in which the substorm westward electrojet and the associated field-aligned currents extend to 1900 MLT. As well, the latitudinal extent of this westward electrojet is small and the associated field-aligned currents occupy a narrow region, so that, on a statistical basis, these currents are not evident in average pictures of field-aligned current flow developed from Triad data.

4.7.1 An Hypothesis to Explain the Post-Noon Discrepancy

As discussed earlier, a polar-cap current system has not been included in the model developed for this thesis because it is not believed that there is, on average, sufficient conductivity in the polar cap to support a significant current flow during the winter months. However, almost all the Triad data that has been published has been from the summer months when one might expect ionospheric polar cap current systems to exist. The average features of polar cap and auroral zone magnetic perturbations in the summer are markedly different from those in the winter. For example, when one compares Figure 4.31 showing the average magnetic perturbation vectors (rotated into equivalent current directions) for the summer months of 1966 through 1968 (Friis-Christensen and Wilhjelm, 1975), with Figure 4.17(b). it is evident that the high latitude equivalent current vectors are rotated sunward in the summer, relative to their direction in the winter months.

As well as much of the published Triad data being from summer months, these published data are also found to be confined to periods during which B_y of the IMF is less than zero. This is not to say that all the Triad data that has been analyzed has been from times when $B_y < 0$. Indeed, the data have not been selected on this basis (Potemra, 1977(b)). This observation is pointed out because when $B_y < 0$, in the summer, the Svalgaard effect is indicative of a counter-clockwise polar cap current on the dayside. That is, there is a pre-noon to post-noon current flow across the polar cap.

A possible explanation for the difference between the Triad summer data and the ground-based winter data can be developed based on the existence of a cross polar cap current system, particularly when $B_y < 0$. Figure 4.32 is reproduced from the paper of Iversen and Madsen (1977). This

Figure 4.31 Polar plot of average high-latitude horizontal magnetic perturbation vectors, for summer data. (From Friis-Christensen and Wilhjelm, 1975)

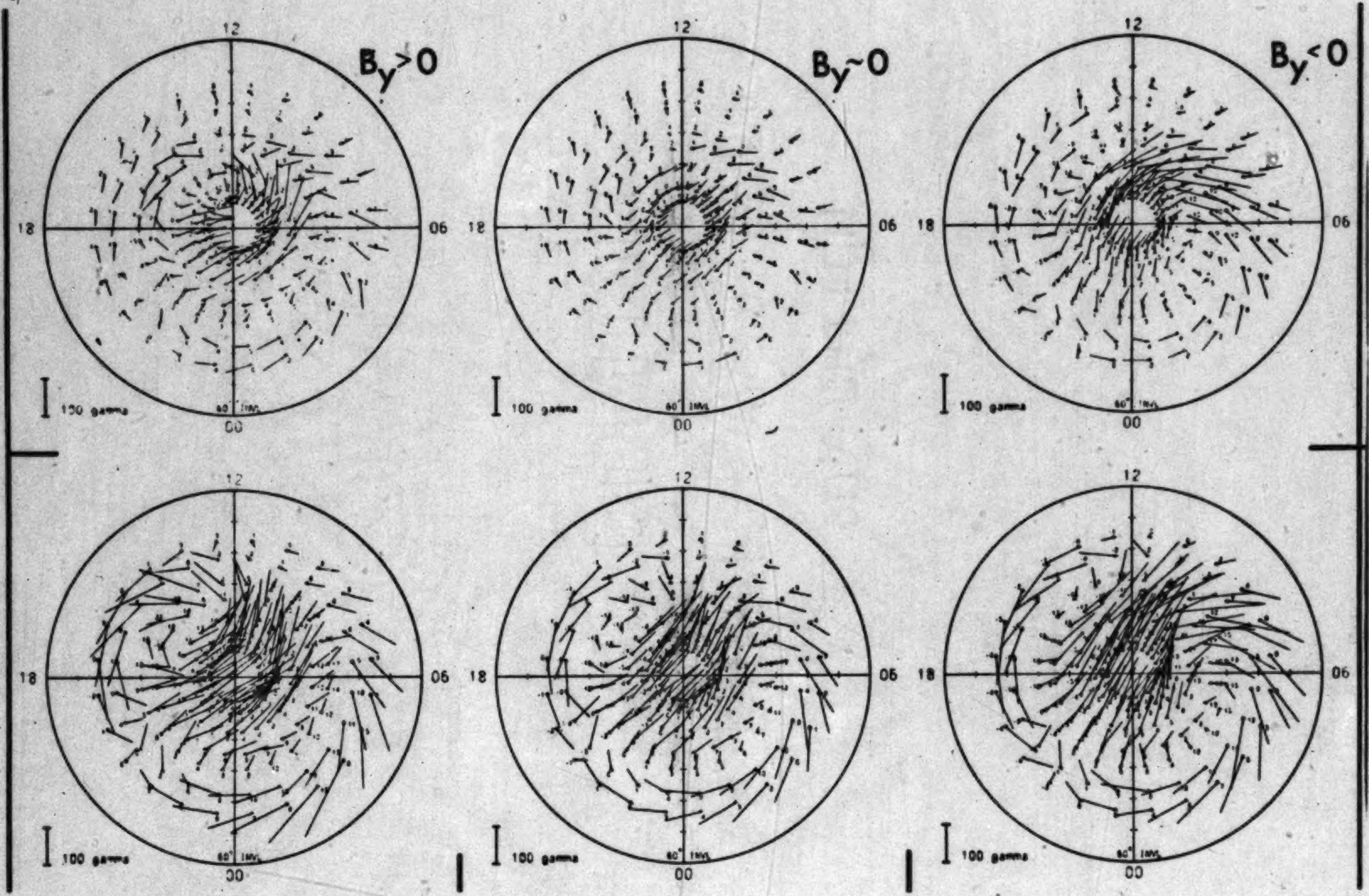
$B_y > 0$
$B_y \sim 0$
$B_y < 0$
12
18
06
00
60° INVL
100 gamma
150 gamma

Figure 4.32 Average ionospheric electric field vectors for times when $B_y < 0$. (After Iversen and Madsen, 1977).

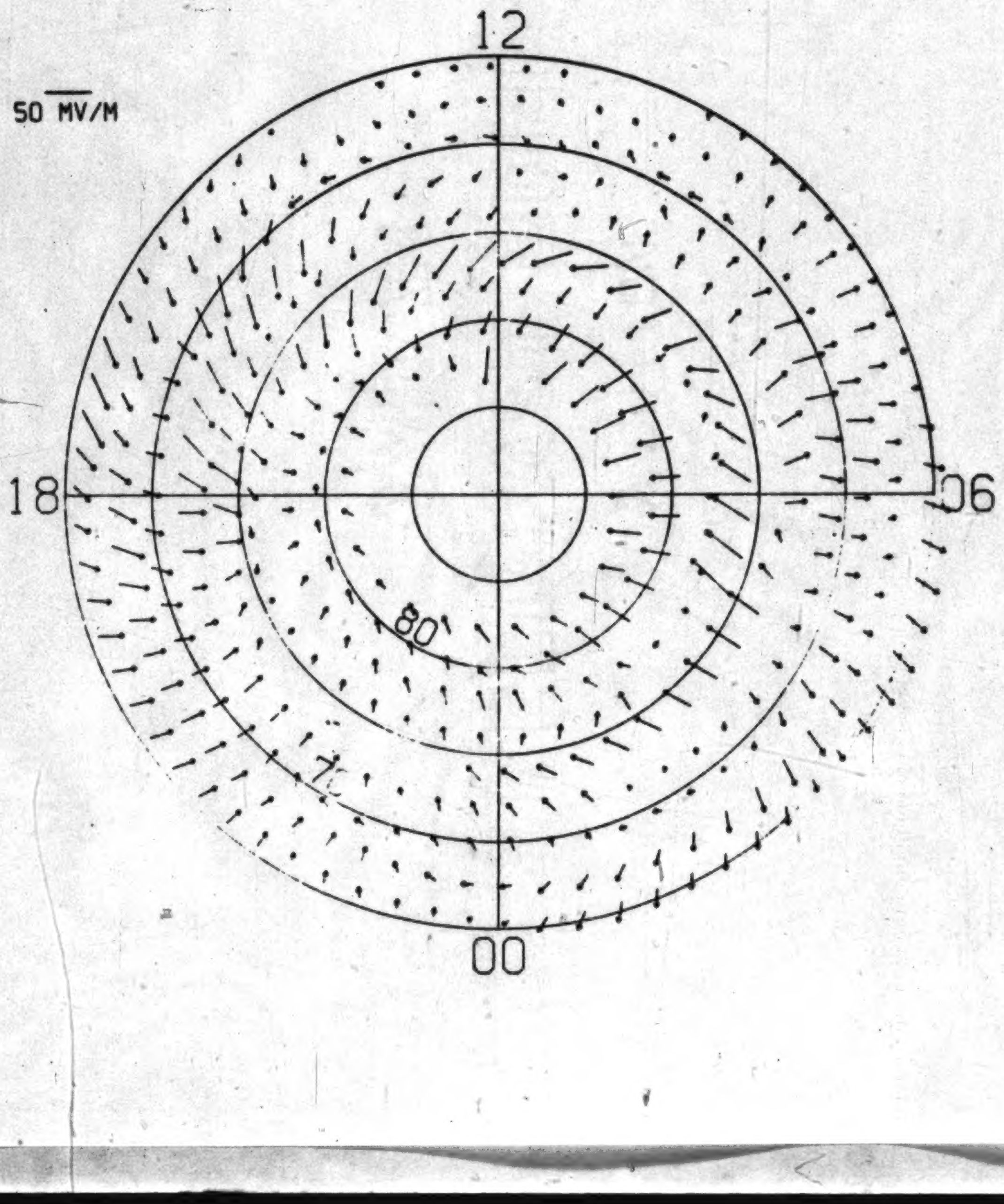
50 MV/M
12
18
06
80
70
00

is a plot of the average electric field for $B_y < 0$. The noon-sector, high latitude average electric field is consistent with a cross-polar cap current. Recent work by McDiarmid et al (1978), using data from the ISIS-2 polar-orbiting satellite, shows that, for $B_y < 0$, there is a region of downward current immediately after local magnetic noon and well poleward of the field-aligned current sheets observed by Triad (e.g. see Figure 4.2). (This current has also been observed by Iijima and Potemra (1976), but the relationship to B_y was not elucidated). This is also consistent with a cross-polar cap current, of somewhat limited extent, but the right sense, if this field-aligned current connects to the upward current sheet at the poleward edge of the auroral oval in the post-noon sector. Thus, there is sufficient evidence to justify examining the effect of a morning-to-afternoon cross polar cap current system.

The cross-polar cap current system that will be developed is very similar to the S_q^p current model of Kawasaki and Akasofu (1973). These authors used a flat-earth approximation, but allowed field-aligned current to flow along dipole field lines. In the present model, a spherical earth has been used, and also field-aligned current has been allowed to flow along dipole field lines. Cross polar cap flow is modelled by current flowing along great circles. (see Appendix I). This current is connected to field-aligned current sheets which are placed symmetrically about noon, and along lines of constant latitude. A uniformly distributed current flows into the ionosphere on the morning side of the polar cap, and out of the ionosphere on the afternoon side (see Figure AI.2). As well, a strictly ionospheric current which circulates around the field-aligned current sheets has been included. The current densities have been adjusted to give a Hall to Pedersen conductivity ratio of 2, consistent with the value used throughout this thesis. It is emphasized at this point that this polar cap model has not been developed in an attempt to model real data, but simply to provide a possible explanation of the Triad/ground-based data discrepancy. Indeed, it is believed that this discrepancy is probably a summertime feature, and ground-based summer data were not available in sufficient quantity at the time of this study to permit a detailed analysis..

For the purpose of this discussion, the polar-cap has been defined as the region poleward of 75°N latitude. The field-aligned current sheets were positioned on the 75°N latitude circle, over longitude ranges from 0700-1100 MLT for downward current, and 1300-1700 MLT for upward current. A total of 5×10^{4} A flowed across the polar cap connecting the field-aligned current sheets (Figure AI.2).

The computed perturbation magnetic field for this current system is shown in Figure 4.33. This system has not been added to the quiet-time model since the specification of the borders in the two systems is not identical. However, it is evident that a current system like that shown in

Figure 4.33 Polar plot of the magnetic field perturbation vectors due to the polar cap current system described in the text, rotated into the equivalent current direction.

HORIZONTAL MAGNETIC PERTURBATION VECTORS...ROTATED INTO CURRENT DIRECTION

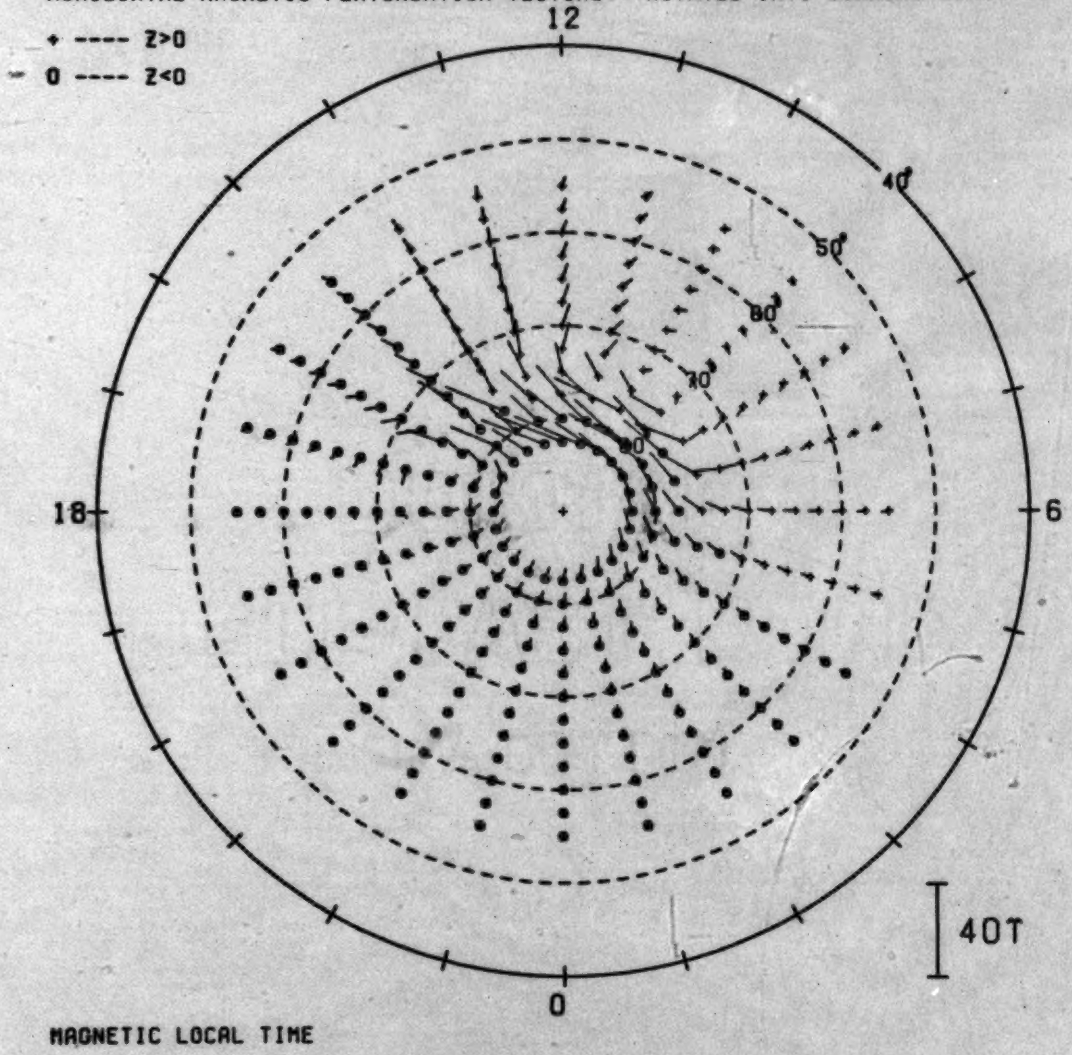

Figure 4.33, if added to a system like that of the quiet time model (Figure 4.18(a)), would rotate the equivalent current vectors of Figure 4.18(a) into a pattern very similar to that observed, for summer, by Friis-Christensen and Wilhjelm (1975) (Figure 4.31). As well, and this is of greatest importance, the polar-cap current system produces latitude profiles in the post-noon sector which could be interpreted as signature of net downward field-aligned current. The Y'-component shows a positive-going level-shift (Figure 4.34 (a,b,c,d)) and this occurs where it is known, from the model, that the field-aligned current is actually directed upward. This result occurs primarily because the magnetic perturbations due to the ionospheric current flow are larger than the perturbations due to field-aligned current.

It is suggested, then, that during the summer, when $B_y<0$, current flows across the polar cap from the morning sector to the afternoon sector, and that this current is most intense when $B_y<0$. This current is connected to the magnetosphere via field lines which lie along the poleward border of the auroral oval. During times of moderate activity, the field-aligned current associated with the cross polar cap current could be sufficiently strong to cause the satellite to measure a magnetic signature consistent with a net upward current in the post-noon quadrant. The existence of this current however does not preclude the existence of a downward field-aligned current

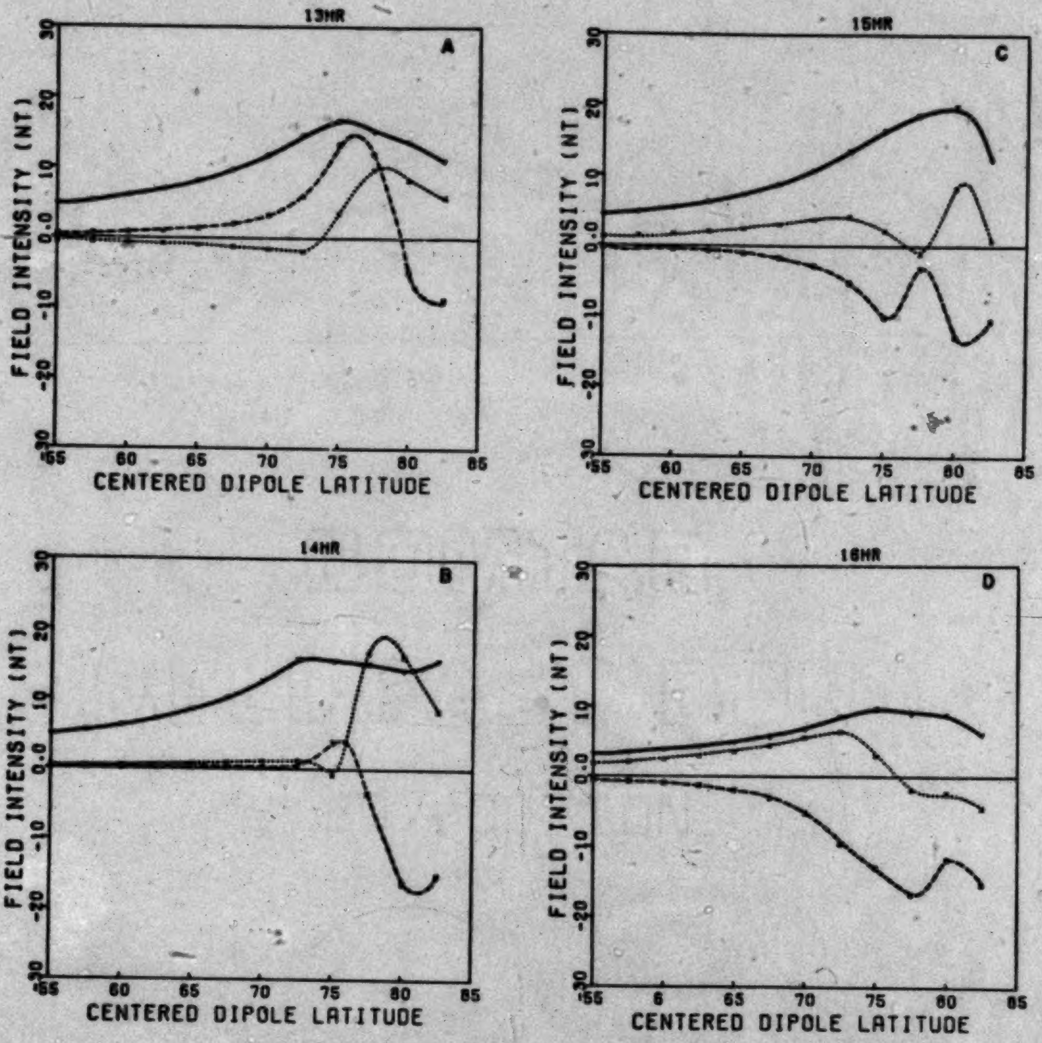

Figure 4.34 Model latitude profiles calculated for the polar cap current system.

(a) 1300 MLT
(b) 1400 MLT
(c) 1500 MLT
(d) 1600 MLT

in this sector, feeding the eastward electrojet.

CHAPTER 5 POSSIBLE SOURCE MECHANISMS

5.1 Sources of Field-Aligned Currents

Up to this point in this thesis, nothing specific has been said regarding the mapping of the field-aligned currents to the outer magnetosphere. Indeed, this is still a topic of active discussion. This section will briefly outline some of the thoughts from the literature concerning sources of field-aligned currents.

Sato (1974) has given a theoretical overview of possible field-aligned current sources. Assuming frozen field conditions, i.e., $\underset{\sim}{E} + \underset{\sim}{V} \times \underset{\sim}{B} = 0$, where $\underset{\sim}{E}$, $\underset{\sim}{V}$, and $\underset{\sim}{B}$ are the electric field, velocity field, and magnetic induction field vectors respectively, he obtains,

$$\nabla \cdot \underset{\sim}{E} = \underset{\sim}{V} \cdot (\nabla \times \underset{\sim}{B}) - \underset{\sim}{B} \cdot (\nabla \times \underset{\sim}{V}) \qquad 5.1$$

The first term of this is often zero, but has non-zero values if a shear exists in the magnetic field component normal to the plasma flow. Such can arise on a boundary separating regions of relative motion of open and closed field lines. Thus, $\underset{\sim}{V} \cdot (\nabla \times \underset{\sim}{B}) \neq 0$ if a current flows in the same direction as the plasma flow.

The second term of equation 5.1 is thought, in general, to be the most important since there is a shear in the velocity component normal to the magnetic field at the boundary between open and closed field lines.

Thus, $\nabla \cdot \underset{\sim}{E} \neq 0$ on this boundary, implying a charge accumulation on this boundary. Sato states a theorem concerning field-aligned current, based on equation 5.1:

> "If the plasma convects around a point in the same sense as the proton gyration, positive charges accumulate there, so that a field-aligned current flows out from that point. On the other hand, if the plasma convection is in the same sense as the electron gyration motion, negative charges (electrons) accumulate, a field-aligned current thereby flowing into the center of the vortex. In other words, if the vorticity vector is parallel to the magnetic vector, a field-aligned current flows in, but if it is anti-parallel, a field-aligned current flows out." (Sato, 1974).

For the actual case of the magnetosphere, in the region of open field lines above the polar cap where the field lines are directed downward, the above theorem predicts a downward field-aligned current on the dawn side of the polar cap, and an upward field-aligned current on the dusk side. This dynamo or magnetohydrodynamic (MHD) generator has been discussed by Akasofu (1974,1975,1977) as a possible mechanism for driving substorms. Figure 5.1 is a schematic of this, and in particular, panel (b) shows the operation of the dynamo. Solar wind plasma is driven in the +y direction, across the magnetic field (B), oriented in the +z direction. This results in the generation of the $-\underset{\sim}{V} \times \underset{\sim}{B}$ electric field in the -x direction. Current flows down the field lines on the left of the figure, and the entire system constitutes a generator. Akasofu (1975) has also pointed out how such a system can explain, at least in part, why auroral activity

Figure 5.1 A schematic diagram indicating the processes associated with the solar wind - magnetospheric dynamo. Panel (a) shows the location of the dynamo, (b) indicates the basic processes, and (c) shows the connecting circuits. (After Akasofu, 1977).

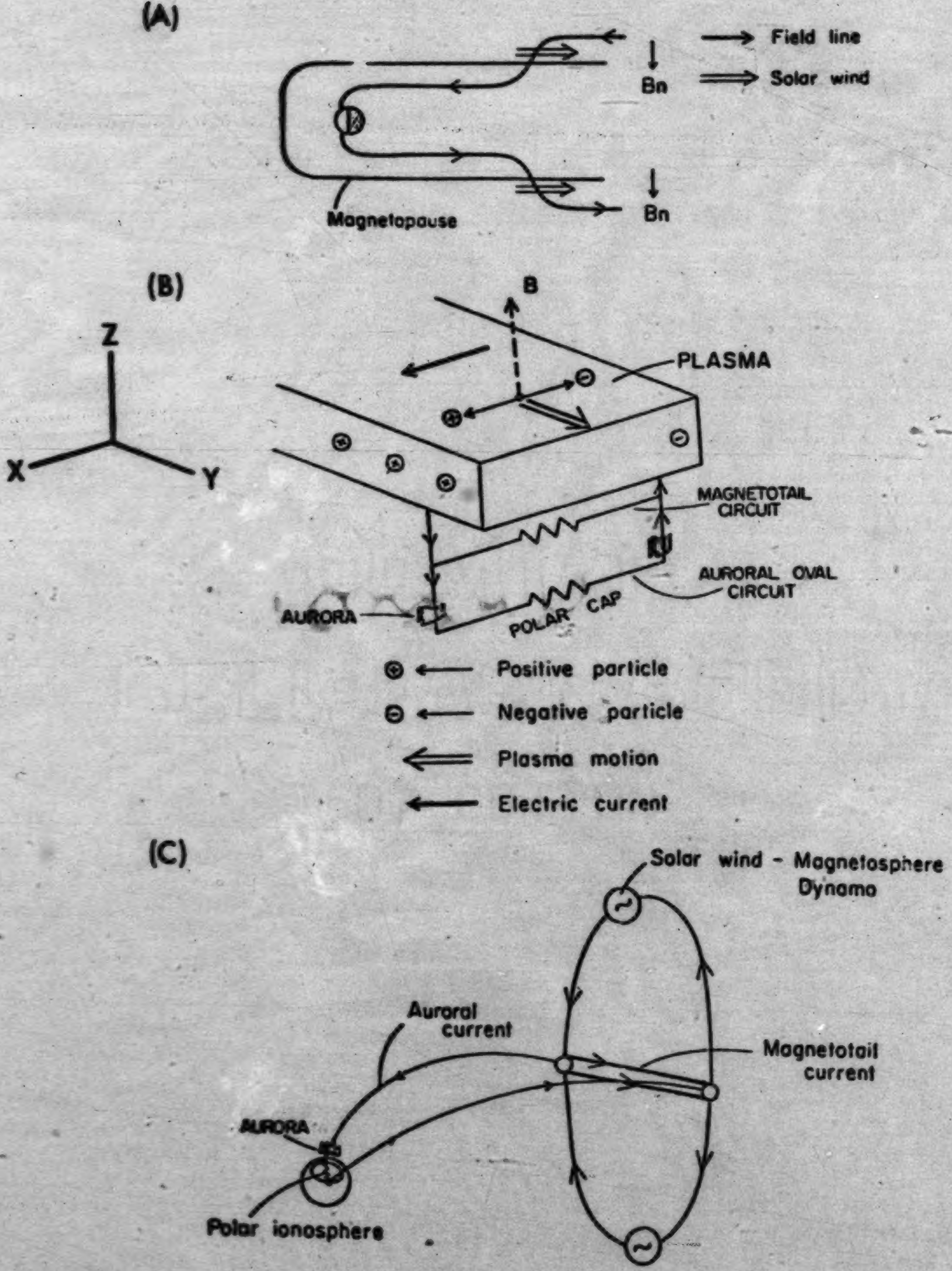
(A)
Field line
Solar wind
Bn
Bn
Magnetopause
(B)
B
Z
X
Y
PLASMA
MAGNETOTAIL CIRCUIT
AURORAL OVAL CIRCUIT
AURORA
POLAR CAP
Positive particle
Negative particle
Plasma motion
Electric current
(C)
Solar wind - Magnetosphere Dynamo
Auroral current
Magnetotail current
AURORA
Polar ionosphere

occurs in a particular region (the auroral oval) around the earth. For example, when the IMF is directed southward, then a "neutral line" surrounds the magnetosphere in the equatorial plane (Figure 5.2). The morning half of this line acts as a positive terminal of the dynamo, the afternoon half as the negative terminal. Thus current flows into the ionosphere in the morning half, and out of the ionosphere in the evening half, as pointed out above.

In the magnetosphere, the plasma sheet is filled with hot plasmas which may give rise to intense drift currents. The drift current can be described by

$$\mathbf{J}_{\perp} = \mathbf{J}_{mag} + \mathbf{J}_{\nabla B} + \mathbf{J}_{curv} + \mathbf{J}_{pol} \qquad 5.2$$

where

$$\mathbf{J}_{mag} = -\nabla \times \frac{P_{\perp}}{B^2}\mathbf{B}$$

$$\mathbf{J}_{\nabla B} = \frac{P_{\perp}}{B^3}\hat{b} \times \nabla B$$

$$\mathbf{J}_{curv} = \frac{P_{\parallel}}{B}\hat{b} \times (\hat{b}\cdot\nabla)\hat{b}$$

$$\mathbf{J}_{pol} = \frac{\rho}{B^2}\frac{d\mathbf{E}}{dt}$$

ρ being the charge density, $\hat{b}\,(=\mathbf{B}/B)$ the unit vector in the direction of the magnetic field, and $P_{\perp}$ and $P_{\parallel}$ the components of the pressure tensor perpendicular and parallel to $\mathbf{B}$ respectively. Taking the divergence of equation 5.2

Figure 5.2 A schematic diagram showing how the "terminals" of the solar wind dynamo connect through the ionosphere. (After Akasofu, 1975).

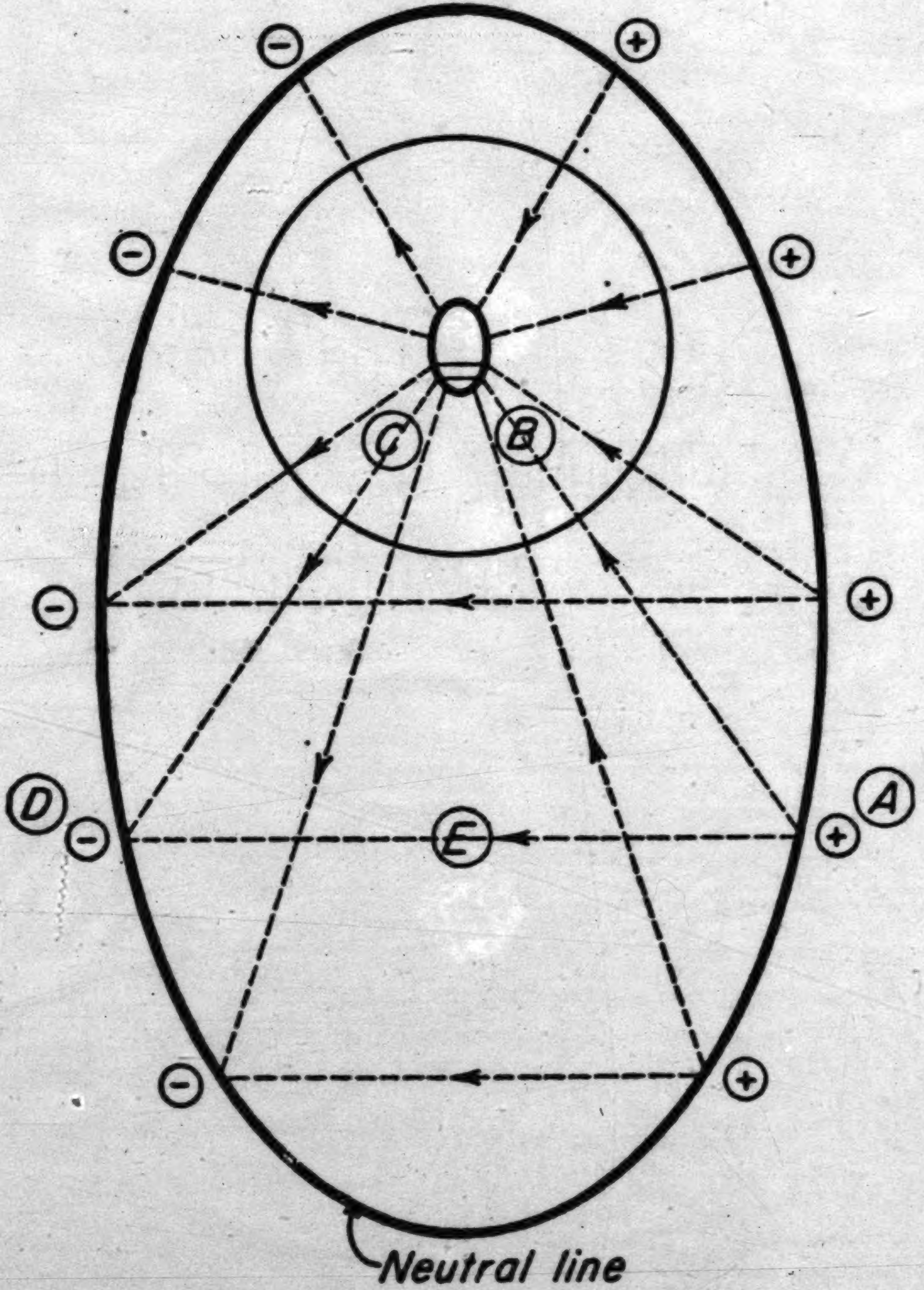
−
+
−
+
C
B
−
+
D
−
A
+
E
−
+
Neutral line

leads to

$$\nabla\cdot\underset{\sim}{J}_{\perp} = \nabla\cdot\underset{\sim}{J}_{curv} + \nabla\cdot\underset{\sim}{J}_{\nabla B} + \nabla\cdot\underset{\sim}{J}_{pol} \tag{5.3}$$

$$\nabla\cdot\underset{\sim}{J}_{\perp} = \left(\frac{\nabla P_{\parallel}}{B} - \frac{P_{\parallel}-P_{\perp}}{B^2}\nabla B\right)\cdot\left(\hat{b}\times\hat{b}\cdot\nabla\right)\hat{b} + \frac{\hat{b}}{B^2}\cdot\left(\nabla B\times\nabla P_{\perp}\right) + \nabla\cdot\frac{\rho}{B^2}\frac{d\underset{\sim}{E}}{dt}$$

The polarization term in general opposes charge accumulation due to the other terms. Thus, a current divergence in the magnetosphere may arise if the plasma pressure has a gradient in the direction of either the curvature current and/or the ∇B current. It is interesting to note in passing that the vortex-like generator has the nature of a voltage generator, whereas the source due to curvature and gradients in B is a current generator.

Finally, if the ionosphere has gradients in plasma density, it no longer acts as a passive closure path for field-aligned currents, but behaves as a field-aligned current source due to the development of polarization electric fields. Height-integrated ionospheric current density is given by

$$\underset{\sim}{I} = \Sigma_P\underset{\sim}{E} - \Sigma_H\frac{\underset{\sim}{E}\times\underset{\sim}{B}}{B} \tag{5.4}$$

where Σ_P and Σ_H are the height-integrated Pedersen and Hall conductivities respectively. If it is assumed that E is irrotational, then

$$\nabla\cdot\underset{\sim}{I} = -J_{\parallel} = \Sigma_P\nabla\cdot\underset{\sim}{E}_{\perp} + \underset{\sim}{E}\cdot\nabla_{\perp}\Sigma_P - \frac{\underset{\sim}{E}\times\underset{\sim}{B}}{B}\cdot\nabla_{\perp}\Sigma_H \tag{5.5}$$

In the case of an homogeneous ionosphere, field-aligned currents arise only because of gradients in $\underline{E}$, and $\underline{E}$ has its origin in the magnetosphere. In this case then, the source of $J_{\parallel}$ is the magnetosphere, and the field-aligned currents are connected to the ionospheric Pedersen currents. In the case of an inhomogeneous ionosphere however, gradients in Σ_P and $\Sigma_{\parallel}$ will lead to $J_{\parallel}$ also.

As described earlier, the solar wind dynamo produces field-aligned current sheets around the polar cap. These sheets correspond to the poleward side of the north-south current system in the model of Chapter 4. Sato argues that the current sheets on the equatorward side of the auroral oval arise from ionospheric conductivity gradients, and that therefore, the ionosphere regulates magnetospheric convection. The gradients in ionospheric conductivity govern the field-aligned current closure with the result that polarization electric fields are set up. These electric fields map to the outer magnetosphere and drive convection.

Cole (1961,1974,1976) has discussed a model in which field-aligned currents are connected to a dynamo which is located in a boundary layer of plasma inside the magnetopause. He has shown that solar wind protons may penetrate the magnetopause on the morning side, and solar wind electrons may do so on the evening side, thus generating charged boundary layers which may act as a source of field-aligned currents. He also points out that the dynamo action of ionospheric winds may generate electrostatic fields or gradients of ionization, and that these fields may map to the magnetopause (Cole, 1976). Eastman *et al*(1976) have also discussed a boundary layer MHD generator as the source of the field-aligned currents which bound the polar cap.

Potemra (1977) has remarked that, due to the statistical stability of the poleward field-aligned current sheets, as inferred from the Triad satellite magnetometer data, these field-aligned currents constitute the *primary* or *driven* current system, and are associated with boundaries of the plasma sheet far distant from the earth where bulk plasma convection may act as a generator. Further, he suggested that the equatorward field-aligned current sheets are secondary currents, which map to the inner edge of the plasma sheet. These currents exist in *response* to localized variations in, for example, ionospheric conductivity.

An alternative driving mechanism has been discussed by Rostoker and Boström (1976). They confined their attention to field-aligned current flow in the dark hemisphere only. Based on the work of Frank (1971), Lassen (1974), and Rostoker *et al*, (1975), they assumed that the plasma sheet maps into the auroral oval, and that the poleward edge of the oval maps to the boundary of the tail lobe and plasma sheet (see Figure 1.1). Thus, field-aligned currents map into the plasma sheet, and flow on *closed field lines*. Rostoker and Boström assume that static forces in the tail are unbalanced, and that these forces lead to an outflow of plasma from the center of the plasma sheet to its flanks. This outflow leads to a potential difference between high and low latitude field lines, which in turn drives field-aligned currents in pairs. Figure 5.3 shows the resulting field-aligned current flow.

It is clear from the above discussion that one would expect downward field-aligned current on the morning side of the polar cap and upward field-aligned current on the afternoon side. It is not, however, patently clear how the field-aligned current pattern determined in this thesis fits into the above source mechanisms. Certainly, in the model, the north-south current system with its associated balanced field-aligned current flow satisfies, in general, the pattern of downward current flow on the morning side of the polar cap, and the reverse on the afternoon side. However, the existence of a relatively intense inward current flow in the noon sector, and a similarly intense outward flow in the pre-midnight sector is not explained in terms of the above models. Figure 5.4 is a schematic in which only certain features of the model current system are shown. The eastward and westward electrojets are indicated as Hall currents (I_H), connected to downward field-aligned current near noon, and upward field-aligned current near midnight. Across the midnight sector, the westward current is represented as a separate current system, with the ionospheric part being a Pedersen current (I_P), and connected to separate field-aligned currents. Combined, the

Figure 5.3 A schematic of the field-aligned current flow generated by the Rostoker-Bostrom dynamo. The view is from down-tail towards the earth. The field-aligned currents are indicated by and and are confined to the plasma sheet. (After Rostoker and Boström, 1976).

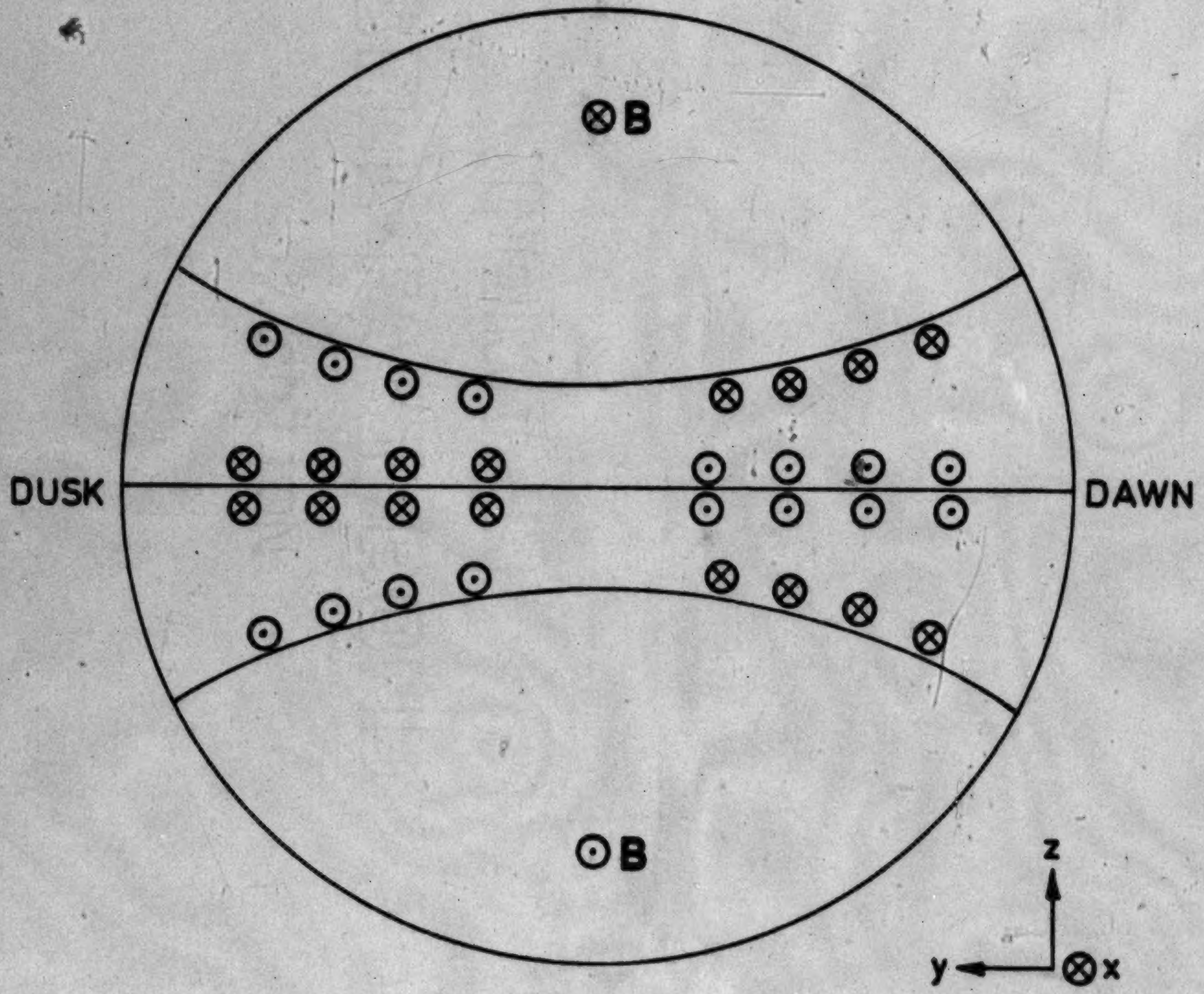
⊗B
DUSK
DAWN
⊙B
z
y
⊗x

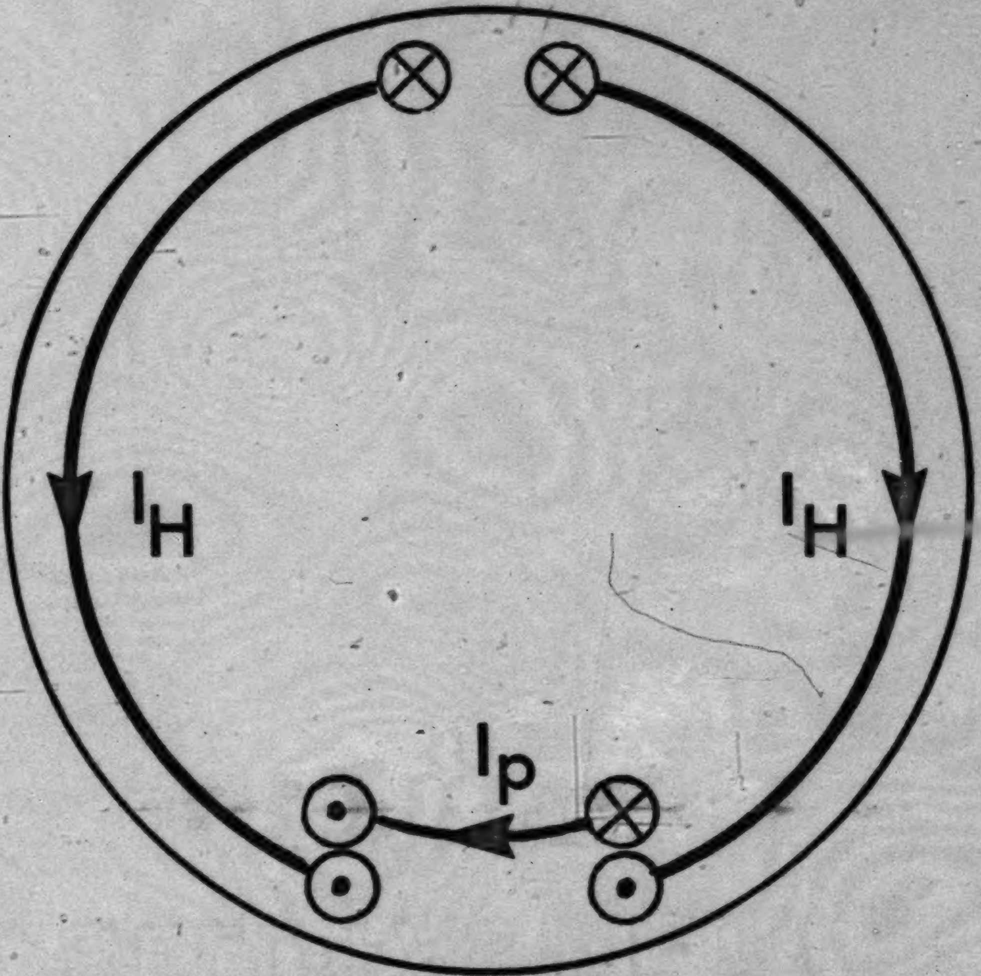

Figure 5.4 A simplified schematic of the global current model. The main eastward and westward electrojets are shown as Hall currents(I_H). The westward electrojet in the midnight sector is shown as a Pedersen current(I_P), consistent with the westward electric field in this sector. The Hall currents are fed by downward field-aligned current (⊗) concentrated primarily in the noon sector. These Hall currents return to the magnetosphere as upward field-aligned current (⊙) in the midnight sector. The westward current in the midnight sector (I_P) is fed by a downward current to the east equal in strength to the upward field aligned current shown in the same sector, so that there is no net field-aligned current in the immediate post-midnight sector.In the pre-midnight sector, the upward flowing current connected to the eastward Hall current and the westward Pedersen current add to give the observed net upward field-aligned current.

three current systems represent the major currents of the model, less the north-south current system.

This breakdown into a Hall and Pedersen component is somewhat appealing, at least in part, because it permits one to account for the known potental drop across the polar cap of 30 to 40 kV (Axford et al,1965). In the model, there is no polar cap current system for the winter months so that the current flowing into the ionosphere in the pre-noon hours, and around the oval into the pre-midnight sector cannot be purely Hall current. However, in the midnight sector, the electric field has a westward component, as does the current. Thus, in the midnight sector, the westward electrojet has the nature of a Pedersen current, and is therefore capable of dissipating power. Indeed,if the value of 10 mV m^{-1} is taken as a representative value of the westward component of the electric field, and it is assumed that this Pedersen current flows across four time zones at an average latitude of 70°N, then the potential drop is approximately 38 kV. This requires that the field-aligned current be connected to a magnetospheric generator, and the mechanism such as that described by Akasofu (1977) and as outlined earlier in this chapter, may be invoked.

To explain the pattern of field-aligned current flow connected with the Hall current electrojets, the following model is proposed. Figure 5.5 is a schematic drawing of a possible plasma convection pattern in the equatorial plane, or equivalently, an electric equipotential pattern. This

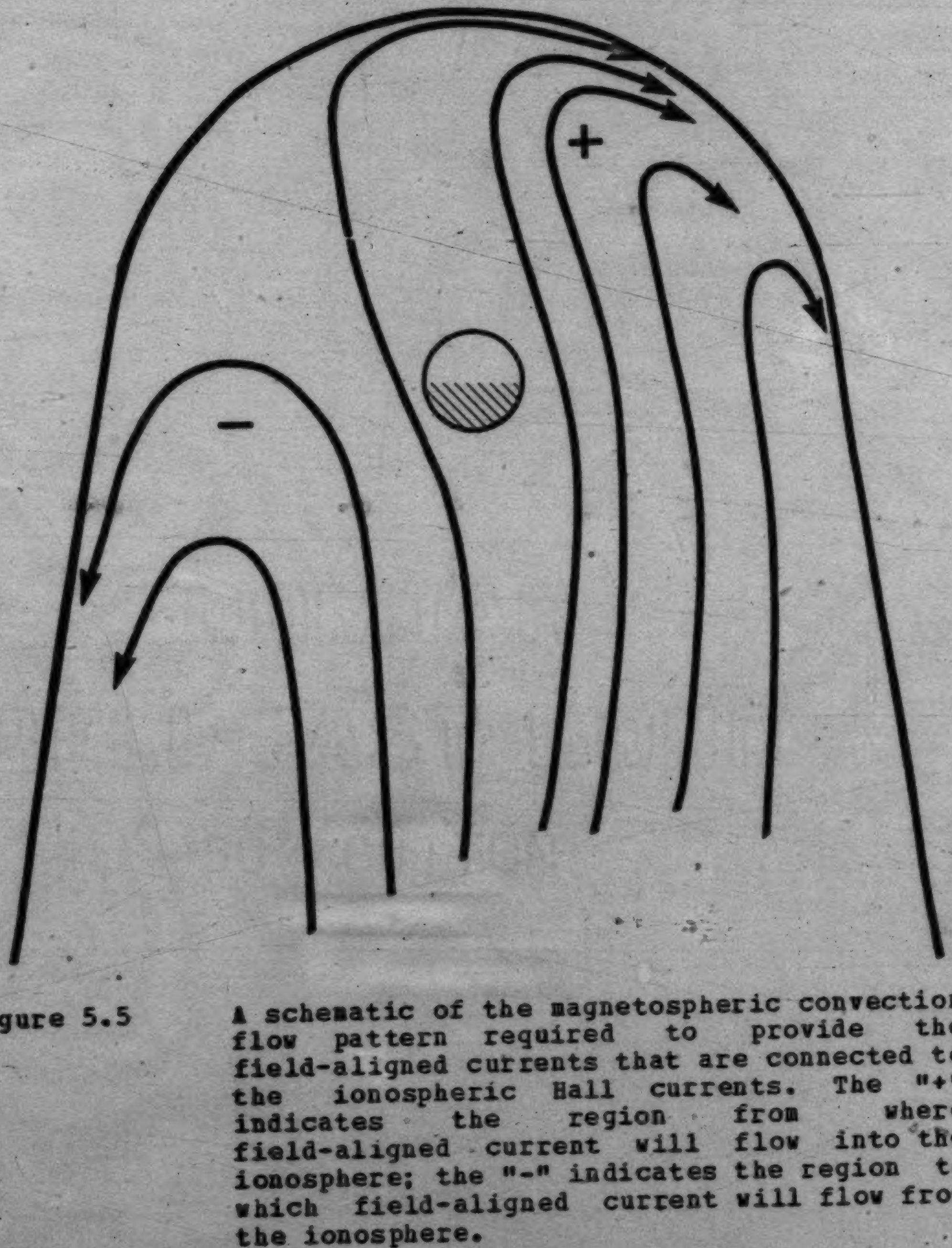

Figure 5.5 A schematic of the magnetospheric convection flow pattern required to provide the field-aligned currents that are connected to the ionospheric Hall currents. The "+" indicates the region from where field-aligned current will flow into the ionosphere; the "-" indicates the region to which field-aligned current will flow from the ionosphere.

pattern is not unlike one given by Harel and Wolf (1976), and is reasonably consistent with the average high-latitude electric field pattern (see Figure 3.13(b)). Plasma is convected earthward from the tail and diverges to flow around the earth. In the evening sector, most of the plasma is turned toward the nearest flank long before it reaches the dayside regions of the magnetopause. However, some of the plasma flowing around the dusk side penetrates into the noon sector where it is deflected to flow towards dawn. As well, all the plasma which flows around the dawn side of the earth returns to the tail along the dawn flank of the magnetosphere. In the regions where $\underset{\sim}{V}$ is not curl-free, equation 5.1 predicts a divergence of the electric field such that a positive charge would build up in the region labelled + in Figure 5.5, and a negative charge would build up in the region labelled -. These charge concentrations are dissipated via field-aligned current into the ionosphere from the + region, and out of the ionosphere in the - region.

An equivalent way of describing this has been given by Vasyliunas (1972(a), 1972(b)). He shows that azimuthal pressure gradients result in field-aligned current flow. In the regions where the plasma is being diverted back down tail, there is an enhanced particle pressure which result in field-aligned currents which flow in the directions described above. Vasyliunas (1972(b)) also shows that these pressure gradient field-aligned currents may arise from the interaction of the ring current (see below) with an electric field, and that these field aligned currents can be related to an ionospheric Hall current.

In section 1.3.2 of this thesis, the presence of a westward flowing extra-terrestrial ring current was mentioned in connection with Dst. Frank (1967) first detected this current directly from an analysis of particle data from the Ogo 3 satellite. As well as this symmetric current, there is an asymmetric ring current (Cahill, 1966; Frank, 1970), and several authors (Fejer, 1961; Swift, 1967, 1968; Akasofu and Meng, 1969) have suggested that both the auroral electrojets are connected to the partial ring current. It has also been proposed that the westward electrojet connects to a partial ring current which lies at a greater distance from the earth than the one to which the eastward electrojet connects (Crooker and McPherron, 1972).

Thus, it is suggested in this thesis that the field-aligned currents connected to the Hall currents (Figure 5.5) arise from within the magnetosphere in the manner outlined above. Further, it is suggested that these field-aligned currents are connected to the partial ring current to form a closed loop. More details of the actual convective motions in the dayside of the magnetosphere than are currently available are required to test the consistency of the above hypothesis. In the absence of this, the above description provides a mechanism whereby the convection electrojets are connected to the magnetosphere through field-aligned currents.

5.2 Concluding Remarks

A detailed study of ground-based magnetometer data has been carried out using the superposed epoch analysis technique of Chree and linear inversion techniques. Based on this study, a comprehensive three-dimensional model of ionospheric-magnetospheric current flow has been developed. The data and the results of the model calculations have been parameterized on the basis of the peak value in the X'-component of the magnetic field, and the level shift in $\Delta Y'$, and these parameters have been compared statistically. Within the margin of error in the data, the fit of the model to the data is excellent.

Although many features of the model are not new, certain new results have come to light. The presence of both eastward and westward electrojet components dependent on conductivity caused by solar UV radiation has been detected. The existence of westward flowing current poleward of the eastward convection electrojet in the pre-midnight sector has been demonstrated by using linear inverse techniques, and, by forward modelling, it is shown that this westward current is associated with upward-flowing, locally unbalanced field-aligned current.

Finally, it has been shown that both the eastward and westward electrojets are connected, in the noon sector, to the outer magnetosphere through locally unbalanced field-aligned currents. It is suggested that these field-aligned currents arise from asymmetric convection of plasma on the dayside of the magnetosphere. It is further suggested that the ionospheric Hall currents are connected through these field lines to the ring current, as described by, for example, Vasyliunas (1972(b)).

It is believed that the current model developed in this thesis is important for several reasons. First, it has been tested against a real data suite, and shown to be consistent with that data on average. Further, the model has demonstrated that, for low-level magnetic activity, the UV electrojet can be important to the complete description of ionospheric-magnetospheric current systems. Also, when perturbed appropriately, the model can be used to describe substorm current systems. Thus, a generalized current model has been developed which may be used as a base system for modelling real current flow for many levels of auroral activity. Finally, field-aligned current in the noon sector to feed the eastward and westward electrojets has never before been included in an ionospheric-magnetospheric current model. The success of the model in reproducing the nature of the $\Delta Y'$ level-shift indicates that these currents are required.

The model described in this thesis is not presented as the ultimate in ionospheric-magnetospheric current models, as all current models are subject to revision until the entire underlying physics is understood. It is hoped that the work described in this thesis will serve the role of providing one more step in this search.

REFERENCES

Akasofu,S.-I., The aurora and the magnetosphere: The Chapman Memorial Lecture, Planet. Space Sci.,22, 885, 1974.

Akasofu,S.-I., The solar wind-magnetosphere dynamo and the magnetospheric substorm , Planet. Space Sci., 23, 817,1975.

Akasofu, S.-I., Physics of Magnetospheric Substorms, D.Reidel Publishing Co., Boston, 1977.

Akasofu, S.-I. and S. Chapman, Solar Terrestrial Physics University Press, Oxford, 1972.

Akasofu, S.-I., S. Chapman, and C.-I.Meng, The polar electrojet, J. Atmospheric Terrest, Phys., 30, 227, 1965.

Akasofu, S.-I., and C.-I. Meng, Intense negative bays inside the auroral zone, 1, The evening sector, J.Atmos. Terr. Phys., 29, 965, 1967.

Akasofu, S.-I., F. Yasuhara, and K. Kawasaki, A note on the DP-2 variation, Planet. Space Sci., 21, 2232, 1973.

Allen, J. H., and H. W. Kroehl, Spatial and temporal distributions of magnetic effects of auroral electrojets as derived from AE indices, J. Geophys. Res., 80, 3667, 1975.

Armstrong, J., C., and A. J. Zmuda, Field-aligned current at 1000 km in the auroral region measured by satellite, J. Geophys. Res., 75, 7122, 1970.

Armstrong, J. C., and A. J. Zmuda, Triaxial magnetic measurements of field-aligned currents at 800 kilometers in the auroral region: initial results, J. Geophys. Res., 78, 6802, 1973.

Axford, W. I., and C. O. Hines, A unifying theory of high latitude geophysical phenomena and geomagnetic storms, Can. J. Phys., 39, 1433, 1961.

Axford, W. I., H. E. Petschek, and G. L. Siscoe, Tail of the magnetosphere, J. Geophys. Res., 70, 1231, 1965.

Backus, G., and F. Gilbert, Numerical applications of a formalism for geophysical inverse problems, Geophys. J. Roy. Astr. Soc., 13, 247, 1967.

Backus, G. and F. Gilbert, Uniqueness in the inversion of inaccurate gross earth data, Phil. Trans. R. Soc., A266, 123, 1970.

Bannister, J. R., A magnetometer array study of polar magnetic substorms, Ph.D. Thesis, University of Alberta, Edmonton, Canada, 1977.

Bartels, J., The standardized index, Ks, and the planetary index, Kp, Int. Union Geod. Geophys., IATME Bull., no. 12b, 97, 1949.

Berko, F. W., Distributions and characteristics of high-latitude field-aligned electron precipitation, J. Geophys. Res., 78, 615, 1973.

Berko, F. W., Hoffman, R. A., Burton, R. K., and Holzer, R. E., Simultaneous particle and field observations of field-aligned currents, J. Geophys. Res., 80, 37, 1975.

Biermann, L., Komentschwerfe and solare Korpuskularstrallung, Z. Astrophys., 29, 274, 1951.

Birkeland, K., The Norwegian Aurora Polaris Expedition, 1902-1903, Vol. 1, Sect. 1, Christiania, Norway, 1908.

Birkeland, K., The Norwegian Aurora Polaris Expedition, 1902-1903, Vol. 1, Sect. 2, Christiania, Norway, 1913.

Boström, R., A model of the auroral electrojets, J. Geophys. Res., 69, 4983, 1964.

Boström, R., The magnetic field of three-dimensional magnetospheric model current systems and currents induced in the ground, Acta. Poly. Scand., 77, 1, 1971.

Brekke, A., J. R. Doupnik, and P. M. Banks, Incoherent scatter measurements of E-region conductivities in the auroral zone, J. Geophys. Res., 79, 3773, 1974.

Cahill, L. J.,Jr., Inflation of the inner magnetosphere during a magnetic substorm, J. Geophys. Res., 71, 4505, 1966.

Cauffman, D. P., and D. A. Gurnett, Satellite measurements of high latitude convection electric fields, Space Sci. Rev., 13, 369, 1972.

Chapman, S., and V. C. A. Ferraro, A new theory of magnetic storms, Terr. Magn. Atmos. Elect., 36, 77, 1931.

Chen, A. J., and G. Rostoker, Auroral-polar currents during periods of moderate magnetospheric activity, Planet. Space Sci., 22, 1101, 1974.

Chree, C., Some phenomena of sunspots and terresrial magnetism at Kew observatory, Phil. Trans. London (A), 212, 75, 1912.

Chree, C., Some phenomena of sunspots and terresrial magnetism at Kew observatory, Phil. Trans. London (A), 213, 245, 1913.

Cole, K. D., On solar wind generation of polar geomagnetic disturbance, Geophys. J. Roy. astr. Soc., 6, 103, 1961.

Cole, K. D., Outline of a theory of solar wind interaction with the magnetosphere, Planet. Space Sci., 22, 1075,1974.

Cole K. D., The magnetospheric dynamo for geomagnetic disturbance, presented at AGU Chapman Symposium, Yosemite, USA, 1976.

Crooker, N. U., and R. L. McPherron, On the distinction between the auroral electrojet and partial ring current systems, *J*. *Geophys*. *Res*., *77*, 6886, 1972.

Davis, T. N., and M. Sugiura, Auroral electrojet activity index AE and its universal time variations, *J*. *Geophys*. *Res*., *71*, 785, 1966.

Dungey, J. W., Interplanetary magnetic field and the auroral zone, *Phys*. *Rev*. *Lett*., *6*, 47, 1961.

Eastman, T. E., E. W. Hones, Jr., S. J. Bame, and J. R. Asbridge, The magnetospheric boundary layer: site of plasma, momentum and energy transfer from the magnetosheath into the magnetosphere, *Geophys*. *Res*. *Lett*., *3*, 685, 1976.

Fejer, J. A., Semidiurnal currents and electron drifts in the ionosphere, *J*. *Atmospheric* *Terrest*. *Phys*., *4*, 184, 1953.

Fejer, J. A., The effects of energetic trapped particles on magnetospheric motions and ionospheric currents, *Can*. *J*. *Phys*., *39*, 1409, 1961.

Feldstein, Y. I., Some problems concerning the morphology of auroras and magnetic disturbances at high latitudes, *Geomag*. *Aeron*, *3*, 183, 1963.

Feldstein, Y. I., and A. N. Zaitsev, Magnetic field variations at high latitudes on quiet days in summer during the IGY, *Geomag*. *Aeron*., *7*, 160, 1967.

Fennel, J. F., Access of solar protons to the earth's polar caps, *J*. *Geophys*. *Res*., *78*, 1036, 1973.

Frank, L. A., On the extra-terrestrial ring current during geomagnetic storms, *J*. *Geophys*. *Res*., *72*, 3753, 1967.

Frank, L. A., Direct detection of asymmetric increases of extraterrestrial 'ring current' proton intensities in the outer radiation zone, J. Geophys. Res., 75, 1263, 1970.

Frank, L. A., Plasma in the earth's polar magnetosphere, J. Geophys. Res., 76, 5202, 1971.

Friis-Christensen, E., K. Lassen, J. Wilhjelm, J. M. Wilcox, W. Gonzalez, and D. S. Colburn, Critical component of the interplanetary magnetic field responsible for large geomagnetic effects in the polar cap, J. Geophys. Res., 77, 3371, 1972.

Friis-Christensen, E., and J. Wilhjelm, Polar cap currents for different directions of the interplanetary magnetic field in the Y-Z plane, J. Geophys. Res., 80, 1248, 1975.

Fukushima, N., Eqivalence in ground geomagnetic effect of Chapman-Vestine's and Birkeland-Alfven's electric current systems for polar magnetic storms, Rep. Ionosph. Space Res., Japan, 23, 219, 1969.

Goldstein, H., Classical Mechanics, Addison-Wesley Publishing Company, Reading, Mass., 1950, Chapter 2.

Harang, L., The mean field of disturbance of polar geomagnetic storms, Terr. Magn. Atmos. Elect., 51, 353, 1946.

Harel, M., and R. A. Wolf, Convection, Proceedings of the International Symposium of Solar-Terrestrial Physics, Boulder, USA, 1976.

Heelis, R. A., W. B. Hanson, and J. L. Burch, Ion convection velocity reversals in the dayside cleft, J. Geophys. Res., 81, 3803, 1976.

Heikkila, W. J., Penetration of particles into the polar cap and auroral regions, in Critical Problems of Magnetospheric Physics, IUCSTP Secretariat, Nat. Acad. Sci., Washington, 1972.

Hess, W. N., The Radiation Belt and Magnetosphere, Blaisdell Publishing Co., Waltham, Mass., 1968.

Hirshberg, J., and D. S. Colburn, Interplanetary field and geomagnetic variations - a unified view, Planet. Space Sci., 17, 1183, 1969.

Hughes, T. J., and G. Rostoker, Current flow in the magnetosphere during periods of moderate activity, J. Geophys. Res., 82, 2271, 1977.

Iijima, T., and T. A. Potemra, The amplitude distribution of field-aligned currents at northern high latitudes observed by Triad, J. Geophys. Res., 81, 2165, 1976.

Iijima, T., and T. A. Potemra, Large scale characteristics of field-aligned currents associated with substorms. J. Geophys. Res., , in press, 1978.

Iversen, I. B., and M. M. Madsen, Auroral zone electric field measurements with ballons. COSPAR, Varna, Bulgaria, 1977.

Kamide, Y., and S.-I. Akasofu, The auroral electrojet and field-aligned currents, Planet. Space Sci., 24, 203, 1976.

Kamide, Y., and A. Brekke, Altitude of the eastward and westward auroral electrojets, J. Geophys. Res., 82, 2851, 1977.

Kamide, Y., and N. Fukushima, Spatial extent of the return current of the auroral-zone electrojet, Rep. Ionosph. Space Res., Japan, 24, 115, 1970.

Kawasaki, K., and S.-I. Akasofu, Polar solar daily geomagnetic variations on exceptionally quiet days, J. Geophys. Res., 72, 5363, 1967.

Kawasaki, K., and S.-I. Akasofu, A possible current system associated with the Sq variation, Planet. Space Sci., 21, 329, 1973.

Kern, J. W., A charge separation mechanism for the production of polar auroras and electrojets, J. Geophys. Res., 67, 2649, 1962.

Kisabeth, J. L., The dynamical development of the polar electrojets, Ph.D. Thesis, University of Alberta, Edmonton, Canada, 1972.

Kisabeth, J., L., Substorm fields in and near the auroral zone, Phys. Earth Planet. Int., 10, 241, 1975.

Kisabeth, J. L., The use of magnetic charge in the calculation of magnetic fields due to magnetospheric current systems and induced current systems within the earth, In preparation, 1978.

Kisabeth, J. L., and G. Rostoker, Modelling of three-dimensional current systems associated with magnetospheric substorms, Geophys. J. R. astr. Soc., 49, 655, 1977.

Langel, R. A., Near-earth magnetic disturbance in total field at high latitudes, 1, Summary of data from Ogo 2, 4, and 6, J. Geophys. Res., 79, 2363, 1974.

Langel, R. A., Near-earth magnetic disturbance in total field at high latitudes, Interpretation of data from Ogo 2, 4, and 6, J. Geophys. Res., 79, 2373, 1974.

Langel, R., and N. Brown, Average high latitude magnetic field: variation with interplanetary sector and with season - II Comparison with disturbance levels and discussion of ionospheric currents, Planet. Space Sci., 22, 1611, 1974.

Lassen, K., Relation of the plasma sheet to the nighttime auroral oval, J. Geophys. Res., 79, 3857, 1974.

Maeda, H., and K. Maekawa, A numerical study of polar ionospheric currents, *Planet. Space Sci.*, *21*, 1287, 1973.

Mansurov, S. M., New evidence of a relationship between magnetic fields in space and on earth, *Geomagn. Aeron.*, *9*, 622, 1969.

Matsushita, S., Dynamo currents, winds and electric fields, *Radio Sci.*, *4*, 771, 1969.

McDiarmid, I. B., and J. R. Burrows, Latitude profiles of low-energy solar electrons, *J. Geophys. Res.*, *75*, 3910, 1970.

McDiarmid, I. B., J. R. Burrows, and M. D. Wilson, Magnetic field perturbation in the dayside cleft and their relationship to the IMF, submitted to J. Geophys. Res., 1978.

Meng, C.-I., and S.-I. Akasofu, Polar magnetic substorms in conjugate areas, *Radio Sci.*, *3*, 751, 1968.

Mozer, F. S., and P. Lucht, The average auroral zone electric field, *J. Geophys. Res.*, *79*, 1001, 1974.

Nagata, T., and S. Kokubun, An additional geomagnetic daily variation in field (S_q^p-field) in the polar region on geomagnetically quiet days, *Rep. Ionosph. Space Res., Japan*, *16*, 256, 1962.

Ness, N. F., K. W. Behannon, C. S. Cantarano, and C. S. Scearce, Observations of the earth's magnetic tail and neutral sheet at 510,000 kilometers by Explorer 33, *J. Geophys. Res.*, *72*, 927, 1967.

Nishida, A., Geomagnetic DP-2 fluctuations and associated magnetospheric phenomena, *J. Geophys. Res.*, *73*, 1795, 1968.

Nishida, A., Coherence of geomagnetic DP-2 fluctuations with interplanetary magnetic variation, *J. Geophys. Res.*, *73*, 5549, 1968.

Nishida, A., DP-2 and polar substorms, *Planet. Space Sci.*, *19*, 205, 1971.

Obayashi, T., *Solar Terrestrial Physics*, J. W. King and W. S. Newman, editors, Academic Press, London, 1967.

Oldenburg, D. W., Ionospheric current structure as determined from ground based magnetometer data, *Geophys. J.*, *46*, 41, 1976.

Parker, R. L., Linear inference and underparameterized models, *Rev. Geophys. Space Sci.*, *15*, 446, 1977.

Piddington, J. H., *Cosmic Electrodynamics*, John Wiley and Sons, Inc., New York, 1969.

Potemra, T., Large scale characteristics of field-aligned currents determined from the Triad magnetometer experiment, presented at the *NATO Advanced Study Institute on Dynamical and Chemical Coupling of Neutral and Ionized Atmosphere*, Spatinal Mountain Hotel, Norway, 1977(a).

Potemra, T., personal communication, 1977(b).

Roederer, J. G., *Dynamics of Geomagnetically Trapped Radiation*, Springer-Verlag, New York, 1970.

Rosenbauer, H., H. Grunwaldt, M. D. Montgomery, T. Paschmann, and N. Schopke, Heos 2 plasma observations in the distant polar magnetosphere: The plasma mantle, *J. Geophys. Res.*, *80*, 2723, 1975.

Rostoker, G., Geomagnetic indices, *Rev. Geophys. Space Sci.*, *10*, 951, 1972.

Rostoker, G., and R. Bostrom, A mechanism for driving the gross Birkeland current configuration in the auroral zone, *J. Geophys. Res.*, *81*, 235, 1976.

Rostoker, G., and M. P. Hron, The eastward electrojet in the dawn sector, Planet. Space Sci., 23, 1377, 1975.

Rostoker, G., and J. L. Kisabeth, Response of the polar electrojets in the evening sector to polar magnetic substorms, J. Geophys. Res., 78, 5559, 1973.,

Rostoker, G., J. L. Kisabeth, R. D. Sharp, and E. G. Shelley, The expansive phase of magnetospheric substorms, 2, The response at synchronous altitude of particles of different energy ranges, J. Geophys. Res., 80, 3557, 1975.

Rostoker, G., J. D. Winningham, K. Kawasaki, J. R. Burrows, and T. J. Hughes, Energetic particle precipitation into the high latitude ionosphere and auroral electrojets. 3. Eastward electrojet and field-aligned current flow at the dusk meridian, in preparation, 1978.

Sato, T., Possible sources of field-aligned currents, Rep. Ionosph. Space Res., Japan, 28, 179, 1974.

Siscoe, G. L., A unified treatment of magnetospheric dynamics with applications to magnetic substorms, Planet. Space Sci., 14, 947, 1966.

Stone, E. C., Local time dependence of non-Stormer cutoff for 1.5 MeV protons in quiet geomagnetic field, J. Geophys. Res., 69, 3577, 1964.

Sugiura, M., and T. A. Potemra, Net field-aligned currents observed by Triad, J. Geophys. Res., 81, 2155, 1976.

Svalgaard, L., Sector stucture of the interplanetary magnetic field and daily variation of geomagnetic field at high latitude, Geophys. Pap. R-6, Dan. Meteorol. Inst., Copenhagen, Denmark, 1968.

Svalgaard, L., Polar cap magnetic variations and their relationship with the interplanetary magnetic structure, J. Geophys. Res., 78, 2064, 1973.

Swift, D. W., Possible consequences of the asymmetric development of the ring current belt, *Planet. Space Sci.*, *15*, 835, 1967.

Swift, D. W., Further possible consequences of the asymmetric development of the ring current belt - effect of variations of ionospheric conductivity, *Planet. Space Sci.*, *16*, 239, 1968.

Vampola, A. L., Access of solar electrons to closed field lines, *J. Geophys. Res.*, *76*, 36, 1971.

Vasyliunas, V., Discussion of paper by Harold E. Taylor and Edward W. Hones, Jr., 'Adiabatic motion of auroral particles in a model of the electric and magnetic fields surrounding the earth', *J. Geophys. Res.*, *73*, 5805, 1968.

Vasyliunas, V., Mathematical models of magnetospheric convection and its coupling to the ionosphere, in *Particles and Fields in the Magnetosphere*, edited by B. M. McCormac, Springer-Verlag, New York, 1972(a).

Vasyliunas, V., The interrelationship of magnetospheric processes, in *Earth's Magnetospheric Processes*, edited by B. M. McCormac, D. Reidel Publishing Company, Dordrecht, Holland. 1972(b).

Wilcox, J. M., and N. F. Ness, Quasi-stationary corotating structure in the interplanetary medium, *J. Geophys. Res.*, *70*, 5793, 1965.

Yasuhara, F., Y. Kamide, and S.-I. Akasofu, Field-aligned and ionospheric currents, *Planet. Space Sci.*, *23*, 1355, 1975.

Zmuda, A. J., J. C. Armstrong, and F. T. Heuring, Characteristics of transverse magnetic disturbances observed at 1100 kilometers in the auroral oval, *J. Geophys. Res.*, *75*, 4757, 1970.

Zmuda, A. J., and J. C. Armstrong, The diurnal flow of field-aligned currents, *J. Geophys. Res.*, *79*, 4611, 1974.

Zmuda, A. J., J. H. Martin, and F. T. Heuring, Transverse magnetic disturbances at 1100 km in the auroral region, _J. Geophys. Res._, _71_, 5033, 1966.

Zmuda, A. J., F. T. Heuring, and J. H. Martin, Dayside magnetic disturbances observed at 1100 kilometers in the auroral oval, _J. Geophys. Res._, _72_, 1115, 1967.

APPENDIX I MODELLING OF THE CURRENT SYSTEMS

AI.1 The magnetic field due to a three-dimensional current system

Kisabeth(1972) has developed equations which facilitate calculation of a three-dimensional current system. This appendix summarizes the develcpment of these equations.

Figure AI.1 defines the vectors used in spherical coordinates for the calculations. The Biot-Savart Law is formulated as:

$$\underset{\sim}{B} = \frac{\mu_o}{4\pi} \iiint \frac{\underset{\sim}{J} \times (\underset{\sim}{r}_o - \underset{\sim}{r})}{|\underset{\sim}{r}_o - r_o|} d^3r \qquad \text{AI.1}$$

where

μ_o is the permittivity of free-space

$\underset{\sim}{J}$ is the current density in Am^{-2}

$\underset{\sim}{r}_o = (r_o, \theta_o, \varphi_o)$ = observer coordinate vector

and $\underset{\sim}{r} = (r, \theta, \varphi)$ = source coordinate vector.

The coordinate directions at the source $(\hat{r}, \hat{\theta}, \varphi)$ are different than those at the observation point $(\hat{r}_o, \hat{\theta}_o, \hat{\varphi}_o)$, but they are related by:

$$\begin{pmatrix} \hat{r}_o \\ \hat{\theta}_o \\ \hat{\varphi}_o \end{pmatrix} = \underset{\approx}{A} \begin{pmatrix} \hat{r} \\ \hat{\theta} \\ \hat{\varphi} \end{pmatrix} \qquad \text{AI.2}$$

where $\underset{\approx}{A}$ is an orthogonal matrix with components:

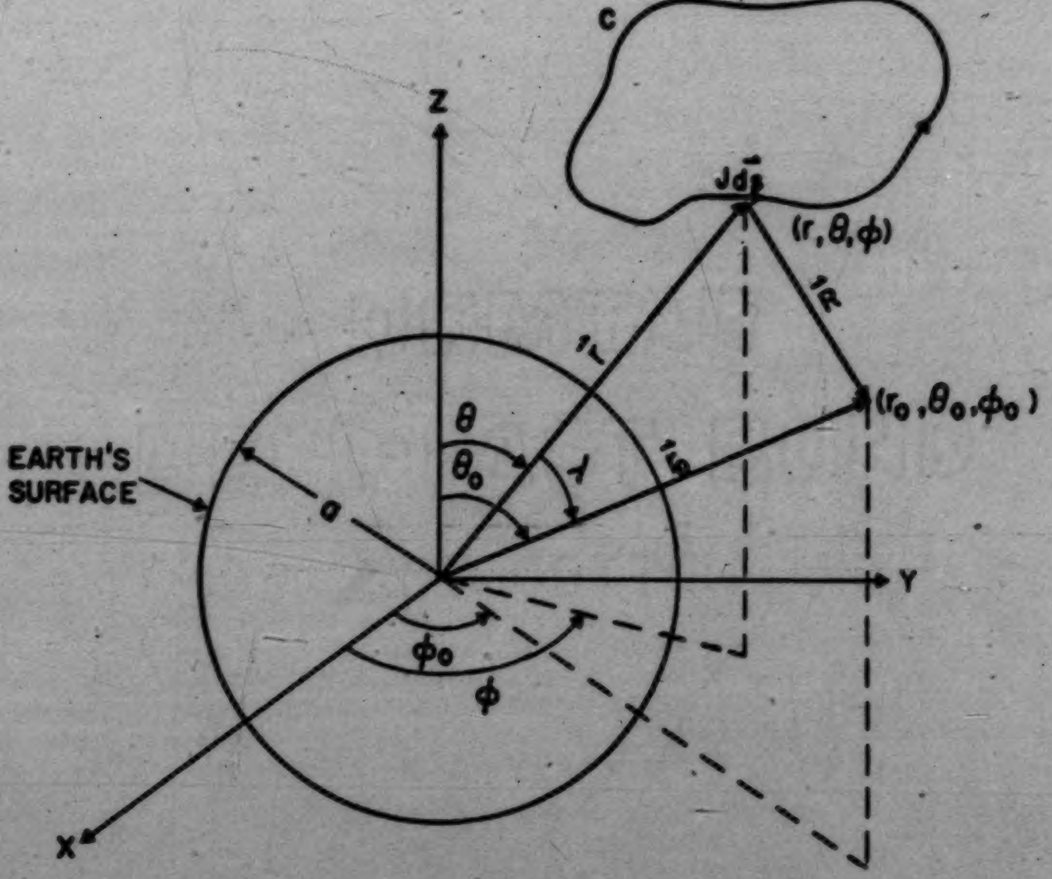
C
Z
Jd$\vec{s}$
(r, θ, φ)
1R
1r
(r_0, θ_0, ϕ_0)
θ
θ_0
λ
$1r_0$
EARTH'S SURFACE
a
Y
ϕ_0
φ
X

Figure AI.1 Diagram defining the vectors in spherical coordinates used in the magnetic field calculations.

$$A_{11} = \sin\theta_0 \sin\theta \cos(\varphi_0 - \varphi) + \cos\theta_0 \cos\theta$$
$$A_{12} = \sin\theta_0 \cos\theta \cos(\varphi_0 - \varphi) - \sin\theta \cos\theta_0$$
$$A_{13} = \sin\theta_0 \sin(\varphi_0 - \varphi)$$
$$A_{21} = \cos\theta_0 \sin\theta \cos(\varphi_0 - \varphi) - \sin\theta_0 \cos\theta$$
$$A_{22} = \cos\theta_0 \cos\theta \cos(\varphi_0 - \varphi) + \sin\theta_0 \sin\theta$$
$$A_{23} = \cos\theta_0 \sin(\varphi_0 - \varphi)$$
$$A_{31} = -\sin\theta \sin(\varphi_0 - \varphi)$$
$$A_{32} = -\cos\theta \sin(\varphi_0 - \varphi)$$
$$A_{33} = \cos(\varphi_0 - \varphi)$$

At a point (a, θ_0, φ_0), the magnetic field from a line current can be expressed as

$$B_j(a, \theta_0, \varphi_0) = \frac{\mu_0 J}{4\pi} \int_{\Gamma} \sum_{i=1}^{3} dC_{ij} \qquad \text{AI.3}$$

where B_j =Z, X', or Y' as j takes on values of 1,2, or 3 respectively; and Γ is the curve defining the current path. The matrix $\underline{\underline{dC}}$ has components:

$$\underline{\underline{dC}} = \begin{pmatrix} 0 & -A_{31} e_2 ds_1 & -A_{21} e_2 ds_1 \\ -rA_{13} e_0 ds_2 & -(rA_{23} e_1 + e_2 A_{32}) ds_2 & (rA_{33} e_1 - A_{22} e_2) ds_2 \\ rA_{12} e_0 ds_3 & -(A_{33} e_2 - rA_{22} e_1) ds_3 & -(A_{23} e_2 + rA_{32} e_1) ds_3 \end{pmatrix}$$

where

$$\ell_0 = \frac{1}{|R|^3} - \frac{1}{|R'|^3}\left(\frac{b}{a}\right)^3$$

$$\ell_1 = \frac{1}{|R|^3} + \frac{1}{|R'|^3}\left(\frac{b}{a}\right)^3 - \frac{I_1}{ab}$$

$$\ell_2 = \frac{r_0}{|R|^3} + \frac{r_0'}{|R'|^3}\left(\frac{b}{a}\right)^3 - \frac{I_2}{ab}$$

a = radius of the earth

b = radius of the superconducting sphere

$$r_0' = b/a$$

$$|R|^2 = r^2 + r_0^2 - 2 r r_0 \cos\lambda \qquad (\cos\lambda = A_{11})$$

$$|R'|^2 = r \quad + (r_0')^2 - 2 r r_0' \cos\lambda$$

$$I_1 = \frac{(r_0')^2}{rR'} \frac{1}{R' + r - r_0'\cos\lambda}$$

$$I_2(\cos\lambda \le 0) = rI_1\cos\lambda - \frac{r_0'}{R} + \ln\left[\frac{R' + r' - r\cos\lambda}{r(1-\cos\lambda)}\right]$$

$$I_2(\cos\lambda > 0) = rI_1\cos\lambda - \frac{r_0'}{R} + \ln\left[\frac{r(1-\cos\lambda)}{R' - r_0' + r\cos\lambda}\right]$$

and $\underset{\sim}{ds} = (ds_1, ds_2, ds_3)$ depends on the current path. For example, for current flowing along a path given by

$$\theta = \theta_1 + 1/2(\theta_2 - \theta_1)(1 + \cos\varphi) \qquad \text{AI.4}$$

which describes the locus of the auroral oval as used in Chapter 4, $\underline{ds}$ is found as follows. Rewriting equation AI.4 as

$$\theta = c + d\cos\varphi$$

where

$$c = \tfrac{1}{2}(\theta_2 + \theta_1)$$

$$d = \tfrac{1}{2}(\theta_2 - \theta_1)$$

and defining $f = \theta - c - d\cos\varphi$.

Then, a unit vector perpendicular to the current path is given by

$$\begin{aligned}\hat{i}_\perp &= \frac{\nabla f}{|\nabla f|}\\ &= \frac{\sin\theta\,\hat{\theta} + d\sin\varphi\,\hat{\varphi}}{(\sin^2\theta + d^2\sin^2\varphi)^{1/2}}\end{aligned}$$

The unit vector parallel to $\underline{ds}$, $\hat{i}_\parallel$, is given by

$$\begin{aligned}\hat{i}_\parallel &= \hat{i}_\perp \times \hat{r}\\ &= \frac{-d\sin\varphi\,\hat{\theta} + \sin\theta\,\hat{\varphi}}{(\sin^2\theta + d^2\sin^2\varphi)^{1/2}}\end{aligned}$$

The differential path length, ds, is given by

$$\begin{aligned}ds &= r(d\theta^2 + \sin^2\theta\, d\varphi^2)^{1/2}\\ &= r(\sin^2\theta + d^2\sin^2\varphi)^{1/2} d\varphi\end{aligned}$$

from which

$$\underset{\sim}{ds} = \hat{i}_{\parallel} ds$$
$$= r(-d\sin\varphi\,\hat{\theta} + \sin\theta\,\hat{\varphi})d\varphi$$

and

$$ds_1 = 0$$
$$ds_2 = -rd\sin\varphi(d\varphi) = -\frac{r}{2}(\theta_2 - \theta_1)\sin\varphi\, d\varphi$$
$$ds_3 = r\sin\theta\, d\varphi$$

For current flowing along a field line,

$$ds_1 = 2r\cot\theta\, d\theta$$
$$ds_2 = r\,d\theta$$
$$ds_3 = 0$$

AI.2 A Cross-Polar Cap Current system

In Chapter 4, the magnetic field due to current flowing across the polar cap is discussed. To calculate this field, the method outlined in the first section of this appendix is used, but first an expression for the current path must be formulated. It is assumed that the ionospheric part of the current is confined to great circles across the polar cap, and further, that these are symmetric about the noon meridian and perpendicular to it (Figure AI.2).

The equation of a geodesic is found by minimizing the arc length, i.e., minimize

$$I = \int_1^2 ds \qquad \text{AI.5}$$

where ds is the differential arc length, and the integral is carried out from points 1 to 2 on the curve.

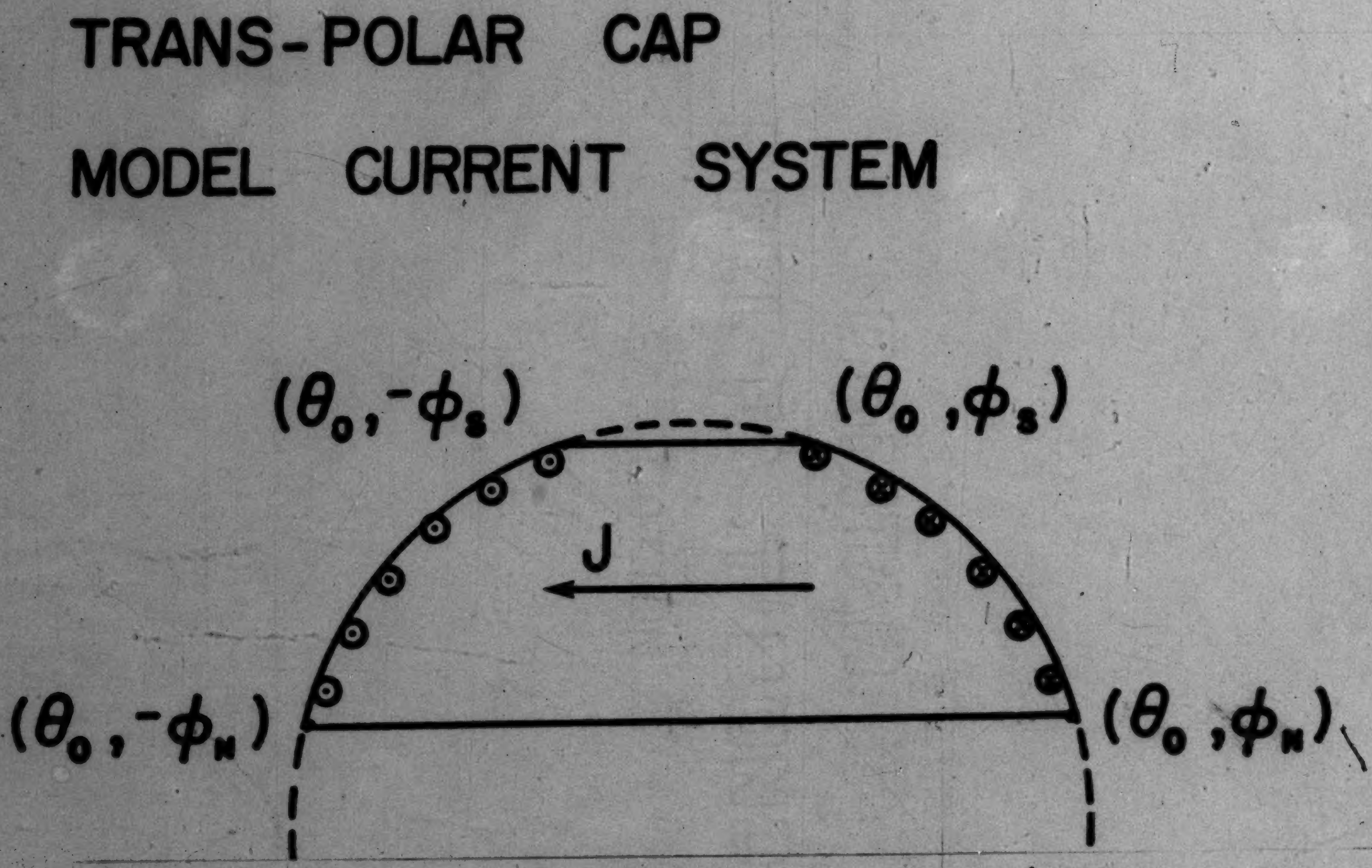
TRANS-POLAR CAP
MODEL CURRENT SYSTEM
$(\theta_0,-\phi_S)$
(θ_0,ϕ_S)
J
$(\theta_0,-\phi_N)$
(θ_0,ϕ_N)

Figure AI.2 Diagram illustrating the cross polar cap current system.

For a sphere, $ds = r(1+\dot{\varphi}^2\sin^2\theta)^{1/2}d\theta$, where $\dot{\varphi} = d\varphi/d\theta$

Then,

$$I = \int_{\theta_1}^{\theta_2} r(1+\dot{\varphi}^2\sin^2\theta)^{1/2}d\theta$$

$$= \int_{\theta_1}^{\theta_2} f(\theta,\dot{\varphi})d\theta$$

Taking the variation δI and setting it equal to zero leads to the result (Goldstein, 1950)

$$\frac{\partial f}{\partial \varphi} - \frac{d}{d\theta}\frac{\partial f}{\partial \dot{\varphi}} = 0 \qquad \text{AI.6}$$

But $\frac{\partial f}{\partial \varphi} = 0$, and $\frac{\partial f}{\partial \dot{\varphi}} = \frac{\dot{\varphi}\sin\theta}{(1+\dot{\varphi}^2\sin^2\theta)^{1/2}}$.

Therefore,

$$\frac{d}{d\theta}\left[\frac{\dot{\varphi}^2\sin^2\theta}{(1+\dot{\varphi}^2\sin^2\theta)^{1/2}}\right] = 0$$

or, after some manipulation,

$$\dot{\varphi} = \frac{c\csc^2\theta}{\sin^2\theta(1-c^2-c^2\cot^2\theta)^{1/2}} \qquad \text{AI.7}$$

where C is a constant.

Integration of equation AI.7 (see Margeneau and Murphy, 1956) gives

$$\varphi = \alpha - \sin^{-1}(k\cot\theta) \qquad \text{AI.8}$$

which is the equation of a great circle.

For the case shown in Figure AI.2 , two points on the great circle are (θ_0, φ_N) and $(\theta_0, -\varphi_N)$, or (θ_0, φ_S) and $(\theta_0, -\varphi_S)$. Substitution of these into AI.8 permits the definition of α and k, with the result that

$$\cot\theta = \frac{\cot\theta_0}{\cos\varphi_N}\cos\varphi$$

$$\cot\theta = \frac{\cot\theta_0}{\cos\varphi_S}\cos\varphi \qquad \text{AI.9}$$

Equations AI.9, together with $\theta = \theta_0$, define the boundaries between which the current flows across the polar cap, as discussed in Chapter 4.

APPENDIX II LINEAR INVERSE THEORY

One of the most important methods of analysis developed in recent years to aid in the definition of parameter variations in regions not assessable by direct measurements is the technique of linear inversion. While a complete description of this technique is not possible in a few pages, a brief description of the principles of linear inversion theory will be outlined here. For a more detailed presentation of the technique, the reader is referred to the pioneering papers of Backus and Gilbert (1967,1970), the recent applications of Oldenburg (1976), and a general review by Parker (1977).

The three-dimesional east-west current system (Kisabeth,1972) (see Appendix I of this thesis also) is used as the forward model to obtain height-integrated ionospheric current densities. Once the parameters defining the geometry of the current system (longitude of the eastern and western field-aligned current sheets, and the northern and southern latitudinal boundaries of the ionospheric current) have been specified, the magnetic field observations at the surface of the earth (r=R), colatitude θ_0, and longitude φ_0 are obtained from

$$B_j^{EW}(R,\theta_0,\varphi_0) = \int_{\theta_1}^{\theta_2} J_{EW}(\theta)\,G_j^{EW}(R,\theta_0,\varphi_0;\theta)\,d\theta \qquad j = 1,23 \qquad \text{AII.1}$$

where B_j^{EW} is the j^{th} measurement of any component of the magnetic field due to the east-west current system, $J_{EW}(\theta)$

is the height-integrated current density, in Am^{-1}, and θ_1, and θ_2 are the colatitudinal limits of the ionospheric current. G_j^{EW} is the Fréchet kernel or Green's function for the problem, and is a function of the current system geometry and the position of the observer. In particular,

$$G_j^{EW} = r\int_{\Gamma} \sum_{i=1}^{3} dC_{ij} \qquad \text{AII.2}$$

where Γ and dC_{ij} are defined in Appendix I.

The magnetic contribution for a north-south current system may be calculated in a similar manner, viz,

$$B_j^{NS}(R,\theta_o,\varphi_o) = \int_{\theta_1}^{\theta_2} J_{NS}(\theta)\, G_j^{NS}(R,\theta_o,\varphi_o;\theta)\, d\theta \qquad j=1,2,3 \qquad \text{AII.3}$$

as has been shown by Kisabeth (1978).

In any realistic modelling of current systems, both north-south and east-west current systems exist simultaneously in any region, so that the datum B_j is given by

$$B_j = B_j^{EW} + B_j^{NS} \qquad \text{AII.4}$$

The height-integrated ionospheric current is given by

$$\begin{aligned} J_{NS} &= \Sigma_P E_{NS} - \Sigma_H E_{EW} \\ J_{EW} &= \Sigma_H E_{NS} + \Sigma_P E_{EW} \end{aligned} \qquad \text{AII.5}$$

where Σ_P and Σ_H are the height-integrated Pedersen and

Hall conductivities respectively. E_{EW} and E_{NS} are the east-west and north-south components of the ionospheric horizontal electric field, and where northward and eastward are taken as positive directions.(Anderson and Vondrak,1975).

If it is assumed that the electric field is purely northward, then

$$J_{NS} = \Sigma_P E_{NS}$$

$$J_{EW} = \Sigma_H E_{NS}$$

and

$$J_{NS} = \frac{\Sigma_P}{\Sigma_H} J_{EW} \qquad \text{AII.6}$$

Combining equations AII.1 and AII.2, and substituting for J_{NS} from equation AII.6 gives:

$$B_j = \int_{\theta_1}^{\theta_2} J_{EW}\left(G_j^{EW} + \frac{\Sigma_P}{\Sigma_H} G_j^{NS}\right) d\theta \qquad \text{AII.7}$$

$$= \int_{\theta_1}^{\theta_2} J(\theta)\, G_j(R,\theta_o,\varphi_o;\theta)\, d\theta \qquad j = 1,2,3$$

where $J(\theta)$ has been written for $J_{EW}(\theta)$ and $G_j = G_j^{EW} + \frac{\Sigma_P}{\Sigma_H} G_j^{NS}$ is the complete kernel for the problem. This approach requires either that Σ_P/Σ_H be known, or that Σ_P/Σ_H may be treated as a free parameter. In the latter case, the ratio may be adjusted until discrepancies between the model and the observations are minimized. in this study, several values of Σ_p/Σ_H were used initially, ranging from 2.0 to 0.5. The value of 0.5 was found to yield the best-fitting results, and this is a reasonable value based on the results of Brekke et al (1974).

The inverse problem that was to be solved can be stated as follows: "given n measurements, B_j ($j=1,2,\ldots,n$), of the perturbation magnetic field, what can be said about $J(\theta)$, the height-integrated current density, in some colatitudinal region, $\theta_1 < \theta < \theta_2$?" Linear inverse theory shows that only linear combinations of the data are available to answer this question. That is,

$$\langle J(\theta_0)\rangle = \sum_{j=1}^{N} a_j(\theta_0)\, B_j = \int_{\theta_1}^{\theta_2} J(\theta)\, A(\theta,\theta_0)\, d\theta \qquad \text{AII.8}$$

where $A(\theta,\theta_0) = \sum_{j=1}^{N} a_j(\theta_0)\, G_j(\theta)$ and $\langle J(\theta_0)\rangle$ is the estimate of J at θ_0.

$A(\theta,\theta_0)$ is the "averaging function" and is effectively a window through which the height-integrated current density is viewed. Note that if it is possible to find a set of a_j's such that $A(\theta,\theta_0)$ is a Dirac-delta function, then,

$$\langle J(\theta_0)\rangle = \int_{\theta_1}^{\theta_2} J(\theta)\, \delta(\theta-\theta_0)\, d\theta = J(\theta_0)$$

Thus, if $A(\theta,\theta_0)$ is constructed so that it is narrow and peaked at $\theta = \theta_0$, the $\langle J(\theta_0)\rangle$ will be a localized estimate of the height-integrated density in the neighbourhood of $\theta = \theta_0$.

The important feature of this technique is a theorem proved by Backus and Gilbert (1970) in which it is shown that all possible current densities, $J(\theta)$, which give rise to the observations will provide the same estimate, $<J(\theta_0)>$, when averaged with $A(\theta, \theta_0)$. As Oldenburg (1976) has described, observational errors, or those incurred by a departure of the real current system from the assumed forward model, may also be included in the analysis to provide estimates of the standard deviation, $\sigma(\theta_0)$, of $<J(\theta_0)>$. If it is assumed that the errors in the data are Gaussian distributed with zero mean, Then,

$$\sigma^2[<J(\theta_0)>] = \sum_{i=1}^{N} a_i^2(\theta_0)\sigma_i^2 \qquad \text{AII.9}$$

where σ_i^2 is the variance of the i^{th} datum.

Ideally, it is desirable to minimize this quantity, while at the same time, it is also preferable to minimize the width of $A(\theta, \theta_0)$ to give the maximum resolution of the height-integrated current density. Backus and Gilbert (1970) have shown that it is not possible to minimize both these quantities simultaneously. It thus becomes necessary to formulate the expression

$$\Phi = D(\theta_0)\cos\psi + \sigma^2(\theta_0)\sin\psi \qquad \text{AII.10}$$

where $D(\theta_0)$ is the width of $A(\theta, \theta_0)$ and ψ is called the trade-off parameter. The functional Φ is then minimized for a given value of ψ. Thus, for $\psi = 0$, the a_i's determined from minimizing Φ produce a very narrow averaging function, so the resolution of the estimate $<J(\theta_0)>$ is maximized, but at the same time, σ is also maximized. Thus, equation AII.10 expresses a form of uncertainty principle that operates whenever imperfect data is inverted.

Although there are infinitely many current densities that will recreate the observations of the magnetic field (Backus and Gilbert, 1967), the estimate $< J(\theta) >$ will not in general do so. There thus exists the possibility that a model current density which does reproduce the data might be of some assistance in the interpretation of the results of an inversion. Such models are found by minimizing a specific functional, subject to the constraint that the observations be reproduced.

If the model is constrained further such that the current density is zero at the specified latitudinal limits of the current (θ_1 and θ_2), then there is a set of constraints that can be used to define the current density. Specifically, from equation AII.7,

$$\theta_j = \int_{\theta_1}^{\theta_1} J(\theta)\, G_j(\theta)\, d\theta \qquad j = 1,2,3 \qquad \text{AII.11}$$

and

$$J(\theta_1) = J(\theta_2) = 0 \qquad \text{AII.12}$$

If the so-called "flattest-model" of height-integrated current density is chosen as the model that fits the data, then the functional

$$\phi = \int_{\theta_1}^{\theta_2} \left[\frac{dJ(\theta)}{d\theta} \right]^2 d\theta \qquad \text{AII.13}$$

must be minimized with respect to $J(\theta)$.

To minimize equation AII.13 subject to the constraints AII.11 and AII.12, AII.13 is recast in the form

$$\phi = \int_{\theta_1}^{\theta_2} (J')^2 d\theta + 2\sum_j \lambda_j \left[\theta_j + \int_{\theta_1}^{\theta_2} J' H_j(\theta) d\theta \right] + 2\eta \int_{\theta_1}^{\theta_2} J' d\theta \qquad \text{AII.14}$$

where $J' = \frac{dJ}{d\theta}$ and λ_j (j=1,2,...n) and η are Lagrange multipliers. The coefficients of η and the λ_j's are reformulations of the constraint equations. Note that, by definition,

$$J(\theta_2) - J(\theta_1) = \int_{\theta_1}^{\theta_2} J'(\theta) d\theta$$

so that equation AII.12 is equivalent to

$$\int_{\theta_1}^{\theta_2} J'(\theta) d\theta = 0$$

Also, define

$$H_j(\theta) = \int_{\theta_1}^{\theta} G_j(u) du$$

and integrating AII.11 by parts:

$$\begin{aligned} \theta_j &= J(\theta) H_j(\theta) \Big|_{\theta_1}^{\theta_2} - \int_{\theta_1}^{\theta_2} J'(\theta) H_j(\theta) d\theta \\ &= -\int_{\theta_1}^{\theta_2} J'(\theta) H_j(\theta) d\theta \end{aligned}$$

$$B_j + \int_{\theta_1}^{\theta_2} J'(\theta) H_j(\theta) d\theta = 0$$

This describes the set of coefficients for the λ_j's.

To minimize AII.14, consider the variation,

$$\delta\phi = 0 = \int_{\theta_1}^{\theta_2} \left[J'(\theta) + \sum_j \lambda_j H_j(\theta) - \eta\right] \delta J'(\theta) d\theta \qquad \text{AII.15}$$

This must hold for arbitrary $\delta J'$, so that

$$J'(\theta) = \eta - \sum_j \lambda_j H_j(\theta) \qquad \text{AII.16}$$

Substitution of this into AII.14 leads to

$$B_j = -\eta \int_{\theta_1}^{\theta_2} H_j(\theta) d\theta + \sum_{i=1}^{N} \lambda_i \int_{\theta_1}^{\theta_2} H_i(\theta) H_j(\theta) d\theta \qquad \text{AII.17}$$

and from AII.16,

$$\int_{\theta_1}^{\theta_2} J'(\theta) d\theta = 0 = \int_{\theta_1}^{\theta_2} \eta d\theta - \int_{\theta_1}^{\theta_2} \sum_j \lambda_j H_j(\theta) d\theta$$

which defines η as

$$\eta = \frac{1}{\theta_2 - \theta_1} \sum_j \lambda_j \int_{\theta_1}^{\theta_2} H_j(\theta) d\theta \qquad \text{AII.18}$$

Equations AII.17 and AII.18 constitute a set of linear equations to be solved for η and λ_j $(j=1,2,\ldots,n)$. Substitution of these into AII.16 then gives $J'(\theta)$, which can then be integrated to find the $J(\theta)$ which satisfies all the constraints.